$304 \cdot P \not\! z \, 5, 6c$

U. S. ARMY
TRANSPORTATION RESEARCH COMMAND
FORT EUSTIS, VIRGINIA

TRECOM TECHNICAL REPORT 64-10

PRELIMINARY STUDIES OF THE APPLICATION OF
PERIPHERAL FANS TO GROUND EFFECT MACHINES

FINAL REPORT

Task 1D021701A04814
(Formerly Task 9R99-01-005-14)
Contract DA 44-177-AMC-5(T)

April 1964

prepared by:

FROST ENGINEERING DEVELOPMENT CORP.
Englewood, Colorado

DISCLAIMER NOTICE

Performance of existing annular jet air cushion vehicles (ACV) is limited by the substantial loss in efficiency between the fan and the nozzle. Because of the performance and design data available, axial flow fans were used on most early ACV in spite of the inefficiency of the axial fan in high payload to gross weight applications. The peripheral fan showed promise of correcting these two major shortcomings of current vehicles. A study was initiated to investigate the performance of several types of transverse flow fans to determine if any were suitable for an air cushion vehicle lift system.

Experimental investigation demonstrated that a flexible blade peripheral fan not only provided a relatively constant efficiency throughout its operating range but also promised increases in system efficiency of from 30 to 40 percent. While such an increase in performance can be considered as a technical breakthrough, mechanical problems in producing a practical fan of the type envisioned are still to be solved.

WILLIAM E. SICKLES
Leader
Ground Effect Research Group

APPROVED.

FOR THE COMMANDER:

LARRY M. HEWIN
Technical Director

FINAL REPORT

Task 1D021701A04814
(Formerly Task 9R99-01-005-14)
Contract DA 44-177-AMC-5(T)
TRECOM Technical Report 64-10

April 1964

PRELIMINARY STUDIES OF THE APPLICATION OF
PERIPHERAL FANS TO GROUND EFFECT MACHINES

Frost Report No. 142-18

Prepared by
Frost Engineering Development Corporation
3910 S. Kalamath St., Englewood, Colorado

for
U. S. ARMY TRANSPORTATION RESEARCH COMMAND
FORT EUSTIS, VIRGINIA

By

P. R. Payne
Vice President, Engineering
Frost Engineering Development Corporation

Approved:

R. H. Frost

Richard H. Frost
President
Frost Engineering Development Corporation

CONTENTS

ILLUSTRATIONS

LIST OF SYMBOLS

A_c = cushion area

or A_c = case area

A_f = fan area

A_i = inlet area

A_J = jet exit area

A_{JN} = nominal (100 per cent) jet nozzle area

A_L = total mean effective leakage area

A_{LN} = nominal leakage area

A_T = total plan area

ΔA = area change between inlet and exit between two blades of a Frost Fan

a = lift curve slope, $a = \dfrac{\partial C_L}{\partial \alpha}$

b = width of a fan, measured normal to plane being considered

or b = width of a two-dimensional GEM, measured normal to the plane being considered

C = mean circumference of jet

C_D = drag coefficient

C_{SF} = skin friction coefficient

C_L = lift coefficient

c = a constant

or c = blade chord

D = overall length of a two-dimensional GEM

or D = drag force

or	D	=	diameter of fan
	D_c	=	length of cushion of a two-dimensional GEM
	d	=	depth of GEM structure
	E	=	power required
	E_J	=	power in jet
	e	=	base of natural logarithms, $e = 2.3026....$
	F	=	a force
or	F	=	symbol denoting "a function of"
	f	=	symbol denoting "a function of"
	ΔH	=	fixed total head increment
	h	=	manometer reading
or	h	=	height of GEM base above ground
	h_c	=	hover height
	J	=	momentum flux in jet, $J = \dot{m}_J V_J$
	J_I	=	momentum flux in incoming jet
	J_H	=	horizontal momentum flux
	K	=	a constant
	L	=	lift force
	$\bar{m}$	=	mass flow parameter
	m_o	=	blade mass
	m_p	=	blade point mass
	$\dot{m}$	=	mass flow/sec./unit jet length
	$\dot{m}_J$	=	jet mass flow
	$\dot{m}_o$	=	ideal jet mass flow for zero slippage

$\dot{m}_L$ = leakage mass flow

$\bar{\dot{m}}_L$ = $\dot{m}_L / A_L$

$\dot{m}_Z$ = mass flow across blade plane

N = fan speed in r.p.m.

N_S = specific speed

n = number of blades

or n = number of fans

P = absolute total pressure, $P = p + \frac{1}{2}\rho V^2$

P_J = total pressure in jet

P_υ = total pressure loss in cavity region

P_e = total pressure at jet exit

P_S = static back-pressure

ΔP = $P - P_a$

ΔP_i = total pressure rise behind inlet blades, measured normal to local tangent

ΔP_{iS} = incremental total head rise due to swirl behind inlet blades

ΔP_{iT} = resultant total head rise behind inlet blades

ΔP_J = total head over-pressure in jet

or ΔP_J = pressure loss in jet

ΔP_{sr} = pressure loss due to skin friction

$\Delta P_{\upsilon D}$ = pressure loss due to diffusion

p = absolute static pressure

p_a = ambient static pressure of the air

p_c = cushion static pressure

$$\Delta P \; = \; P - P_a$$

ΔP_c = cushion overpressure

ΔP_J = mean static overpressure in jet exit

or ΔP_J = jet back-pressure

ΔP_v = back-pressure within cavity

Q = flow rate

q = dynamic pressure, $q = \frac{1}{2}\rho V^2$

q_T = dynamic pressure associated with circumferential velocity of fan blade tips

R = radius of case

Re = Reynold's number

r = a radius

r_D = minimum effective radius of a Frost Fan

t = jet or nozzle thickness

t_i = inlet depth, $t_i = \frac{A_i}{b}$

t_J = jet thickness

t_1 = width of inlet nozzle

t_2 = width of exit nozzle

or t_2 = a constant, $t = \frac{1}{2}\left(1 - x_0^2\right)$

$\hat{t}_i$ = t_i / R

$\hat{t}_J$ = t_J / R

$\hat{t}_L$ = A_L / bR

V = forward (translational) velocity

V_{RI} = resultant inlet velocity

V_{Sn} = swirl velocity at station n

V_T = fan circumferential tip speed

U_1 = axial velocity through fan at intake plane

U_2 = velocity component across plane of blade

U_i = velocity at intake plane

U_c = mean effective velocity through fan case

U_J = velocity in the jet

U_{Jc} = velocity at center of jet exit

U_{Jv} = jet velocity measured at stations along a vertical centerline at the jet exit plane

U_{JH} = jet velocity measured at stations along a horizontal centerline at the jet exit plane

U_L = leakage velocity at leakage gap

U_{swirl} = swirl velocity

U_v = velocity within vortex

ω_b = total hinged blade weight per foot run

x = $\frac{t}{h}\left(\sin\theta + \sin\alpha\right)$

$\quad$ = $\frac{t}{h}\left(\sin\theta + 1\right)$ under equilibrium conditions

x_o = hinge radius in a Frost Fan

z = distance across a jet

α = angle of attack

or α = angle at which a jet strikes the ground plane, relative to local vertical

α_1, α_2 = angles defined in Figure 46

β_1, β_2 = angles defined in Figure 46

Δ = prefix denoting "relative to ambient"

δ = incremental value

ζ = blade lag or lead angle

λ = mass flow

or λ = fan inflow ratio, $\lambda = V_1 / V_T$

μ = eccentricity ratio, $\mu = 1 - \left(\dfrac{r_0}{R}\right)^2$

or μ = viscosity coefficient

μ_R = rolling friction coefficient

ν = kinematic viscosity, $\nu = \dfrac{\mu}{\rho}$

ξ = ratio of local tip velocity to V_T (that is, slip factor)

ρ = mass density of air

σ = fan solidity, $\sigma = \dfrac{nc}{2\pi R}$

$\bar{\sigma}$ = $\dfrac{a\sigma}{2}$

η = efficiency

η_F = total fan efficiency

η_D = duct loss

η_{KE} = kinetic efficiency

Θ = angle at which jet is pointed in towards the cushion, measured from the vertical relative to structural axes

or Θ = angle defined in Figure 88

or Θ = fan blade angle relative to local tangent line on the fan cylinder

Θ_1, Θ_2 = angles defined in Figure 144

ϑ = blade pitch angle, measured from plane of rotation

ϕ = inflow angle, $\tan \phi = \dfrac{V}{\Omega r}$

or ϕ = loss coefficient

or ϕ = ratio of effective radius of air cylinder to maximum radius

xxiv

or ϕ = angle defined in Figure 102

Φ = overall non-dimensional flow factor

Φ_V = flow factor evaluated by pressure readings along vertical axis of the exit nozzle

Φ_H = flow factor evaluated by pressure readings along horizontal axis of the exit nozzle

ψ = pressure coefficient

ψ_2 = effective fan exit width

Ω = rotational speed of fan

Subscripts:

a denotes ambient condition

i denotes inlet condition

j denotes condition within jet

max denotes maximum value

nom denotes nominal value

o denotes condition with zero slippage

opt denotes optimum condition or value

s denotes condition within separation bubble

v denotes condition within vortex

SUMMARY

In Ground Effect Machines developed to date, generation of the lifting cushion pressure has generally been accomplished by use of axial- or centrifugal-type fans. Substantial reductions in efficiency result from the elaborate ducting required with these, particularly from turning losses; moreover, these installations require expensive, complicated structure and much of the potential deck area and cargo volume is rendered unuseable. Considerable improvement in all these aspects, as well as in stability and control, is offered through use of vane- or crossflow-type fans installed around the periphery of rectangular planform GEM's. This is the Frost Fan concept with which the project described in this report was concerned.

This report presents the results of a program conducted to develop and evaluate the Frost Fan concept. The data obtained from comprehensive test programs made with small-scale models and full-scale fan assemblies are discussed in detail. A theory has been developed to explain satisfactorily the performance of the Frost Fan. The theoretical work accomplished and the comparison between theory and experiment are presented together with a study of recirculation theory. An elementary theory of the crossflow fan is developed using concepts already well established in fan aerodynamics.

Organization of this report is on the basis of presenting the most significant and interesting information first. Thus, in view of the importance and funding of research projects concerned with energy recovery in ground effect machines through recirculation of the lift cushion air, Section One deals with this subject. Both experimental results and newly developed theory are presented in evidence of the need for a fresh look at the potential of recirculation.

Section Two is concerned with the evaluation of crossflow fans as a means for generating lift cushion pressure with potentially high efficiency. This relatively new type of blower lends itself well to the peripheral fan GEM configuration that underlies the Frost Fan concept.

Finally, Sections Three, Four, and Five describe the small-scale model testing performed, the development of theory pertinent to the Frost Fan, and the results of full-scale testing of the first generation version of this configuration.

1

CONCLUSIONS

1. The good agreement between the theory developed herein and ex-
   perimental results indicates that a satisfactory basis for de-
   signing lift fan systems for ground effect machines has been
   established.

2. In general, the results obtained with the full-scale Frost Fan
   assemblies are considered to be satisfactory. Despite the
   losses attributable to tip roller friction, blade leakage and
   end losses, efficiencies as high as 55 per cent were measured
   with these fans. This is substantially better than the system
   efficiencies reported thus far for any existing GEM.

3. It is concluded that the Frost Fan and the crossflow fan may be
   capable of giving efficiencies in the order of 80 per cent
   after the completion of additional development programs.

4. Finally, it is concluded that the recirculation system for
   GEM's as it is presently envisaged, is inferior to the conven-
   tional annular jet, requiring more power to generate a given
   lift and being markedly unstable in heave at low hover heights.

RECOMMENDATIONS

1. The proof of the effectiveness of a component or principle is whether it enables a more effective system to be built. For this reason it is suggested that the knowledge of the performance characteristics of the Frost Fan acquired in this program now be applied to a design study for a specific vehicle, intended to perform a specific mission.

2. Since friction and leakage losses are of considerable importance it is logical to look for a design concept which will minimize these factors. A revised Frost Fan configuration is presented in this report which eliminates tip rollers altogether and minimizes end-plate and blade-tip leakage. In addition, this revised configuration permits the use of flexible plastic or sheet metal blades, thus considerably reducing total fan weight. It is strongly recommended that a follow-on study be conducted to develop and evaluate this new configuration.

3. Despite all the work that has been done in study and application of recirculation principles for GEM air cushions, this phenomenon is sufficiently complicated for past efforts to be regarded as negligible in relation to the amount of theoretical work yet to be done. It is suggested that effort would most profitably be spent on fundamental experimental and theoretical investigations into the basic aerodynamic phenomena involved in recirculation.

INTRODUCTION

SOME REMARKS ON COMPONENT AND SYSTEM EFFICIENCY

The process of producing the optimum design for any vehicle is concern-
ed mainly with optimizing the most important operational parameters.
In designing a transport aircraft, for example, great stress is laid
upon achieving a minimum figure for the total operating cost per seat-
mile over the operational ranges for which it is designed, and nearly
all other requirements are subordinate to this.

The important performance parameters for a Ground Effect Machine (GEM)
are not easy to define. First, there seem to be innumerable opera-
tional roles open to GEM's and the question of which are the most im-
portant parameters will differ with mission characteristics. Secondly,
GEM technology is so new that only fairly simple performance criteria
can be justified, because of the relative inaccuracy involved in making
performance estimates. It would be very rash, for example, to place
much emphasis on second order optimizations based on cruising speed,
because the methods available for estimating drag are still very inac-
curate, and there is not even general agreement as to the parameters
against which experimental results should be correlated.

A fairly obvious efficiency parameter is the power required per pound
of payload to hover at a given height above the ground plane. Provided
that the known effects of body shape on drag, together with the effects
of jet geometry and momentum flux, are kept in mind, it seems reason-
able to believe that a configuration optimized for this hover criterion
will also be close to optimum in cruise.

The determination of optimum configurations is often attempted without
extensive design layouts on the drawing board and without stress anal-
yses of the various structural configurations to determine the sizes of
the structural elements and their associated weights. Experience with
older types of airborne vehicles indicates that without such layouts
and analyses those design studies are often valueless and usually plat-
itudinous. Although such design studies are often based on reasonably
valid approximations such as relating structural weight to the vehicle's
overall dimensions, for example, they miss the point that design is
still very much a creative art. That is to say, the number of compro-
mises is so vast, and many of them are so ill-defined in terms of quan-
titative effect, that the choice between them cannot be programmed on a
computer, but must be made by an experienced design engineer. The most
that can be expected from a design study alone is the optimum geometry
for a vehicle of one particular and rigidly defined configuration, and
even here human ingenuity and inventiveness can often obsolete the re-
sults before the ink is dry.

With these reservations in mind, it is reasonable to assume that the
optimum GEM components are those which result in maximum payload for a
given hover height and power consumption. For example, a single,
centrally located axial fan may be more efficient than a number of
small ones mounted around the periphery and may also be lighter when
the transmission weights are taken into account. However, if the duct
losses dissipate half the power supplied, the more complex peripheral
fan system could be the optimum of the two.

The most usual GEM configuration is based upon one or more centrally
located fans and ducting which channels the air from these fans to the
peripheral jet nozzle. In general, the wetted area of these ducts will
be in the order of twice the plan area of the vehicle, even without in-
cluding frames and turning vanes. Moreover, this ducting usually in-
volves two right-angled bends, each involving losses of the order of
50 per cent of the local dynamic head, and some diffusion. It is not
surprising then that 40-50 per cent of the energy put into the airflow
by the fan is typically dissipated before the air reaches the exhaust
nozzle. Thus a fan which is 80 per cent efficient at its design opera-
ting point is really only 40 per cent efficient when the necessary
ducting is taken into account.

If we could eliminate duct losses by some form of peripheral fan, it
would only have to be 40 per cent efficient to break even with an effi-
cient centrally located fan. Moreover, we could afford a somewhat
greater weight penalty for a peripheral fan, since we should be saving
the weight of the ducting.

It was these considerations which resulted in the original concept of
the peripheral fan, and it was soon found that no loss in efficiency
need be accepted and that under the right conditions such a fan could,
in fact, be as efficient as its axial flow equivalent. On the score of
weight also, it was found that the area of skin needed to form the fan
case was comparable with the amount of material required for ducting
the air from a centrally located fan. Moreover, since the peripheral
fan case can be used as the basic structure of a GEM, it is serving two
purposes and enables a substantial overall saving in structural weight
to be made.

It was felt that these considerations were sufficient to warrant a de-
tailed examination of the peripheral fan concept. As the investigation
proceeded, however, it became evident that such a system had other po-
tential advantages, some of which might possibly be of more far-
reaching importance to GEM technology than the original features of
high system efficiency and low weight.

SOME DISADVANTAGES OF AXIAL FANS

We start with the assumption that an annular jet GEM is initially resting on the ground or water and that its jet nozzle exit is therefore close to or in contact with the surface. Thus, the air mass flow through the system will be negligible when the fans are started up and will remain so until the vehicle starts to raise itself to its operating hover height. Once it is hovering, the airflow relative to an element of one blade will be as depicted in Figure 1.
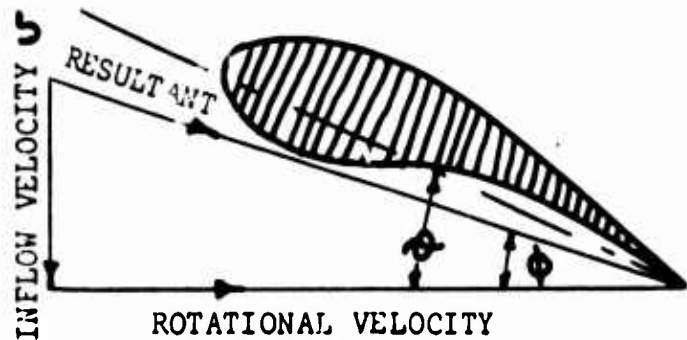
Figure 1. Blade Angle of Attack.

θ is the blade pitch angle, measured from the plane of rotation

ϕ is the inflow angle defined by $\tan \phi = U/\Omega r$

Ωr is the rotational velocity, Ω being the rotational speed in radians per second and r being the radius of the blade element from the shaft centerline

U is the inflow velocity, or the speed at which the air is sucked through the fan.

Some very simple relationships can be written down immediately from the geometry of Figure 1, and these equations are the basis for all axial fan theory and, incidentally, for helicopter rotor theory as well. First of all, the lift on the blade element can be obtained from the relationship

Section lift coefficient = (lift curve slope) x (angle of attack)

or
$$C_L = a\alpha \tag{1}$$

The angle of attack is

$$\alpha = \text{(pitch angle)} - \text{(inflow angle)}$$
$$= \theta - \phi \tag{2}$$

6

If the blade pitch angle ϑ is small - say less than 25° - then the inflow angle will be even smaller. This means that we can use small angle approximations and say that

$$\tan \phi \approx \sin \phi \approx \phi$$

$$\cos \phi \approx 1.0$$

If we do this, then equation (1) becomes

$$C_L = a\alpha = a(\vartheta - \phi) = a\left(\vartheta - \frac{U}{\Omega r}\right) \tag{3}$$

This simplification enables us to obtain closed form solutions for fan performance and efficiency, resulting in a considerable reduction in the amount of computation needed to optimize an axial fan design and to determine its performance for off-design-point conditions. It also enables us to determine more precisely the contribution of the fan to the dynamic stability of a GEM, an effect which has hitherto had to be neglected in stability analysis. It is of interest to note that a theory developed along these lines (References 1 and 2) was used in the design of the Frost Mine Search Head Carrier GEM for U. S. Army Transportation Research Command and that the full-scale vehicle performance gives exceptionally good agreement with theoretical predictions.

We now go back and consider the problems of take-off, when the air mass flow through the system is zero, so that the inflow velocity (U) is zero. For this case the lift coefficient is

$$C_L = a\vartheta$$

The maximum lift coefficient obtainable under full-scale conditions is about $C_L = 1.6$ (and for model GEM's it can be very much less, of the order of 0.5 - 0.8, depending on the blade section used). So, if the blade pitch angle is greater than

$$\vartheta = \frac{C_{L_{MAX}}}{a} = \frac{1.6}{0.1} = 16°$$

- then the blade will be stalled and the vehicle may not be able to take off at all.

In practice, the fan
will induce swirl under
conditions of zero mass
flow, as shown in Fig-
ure 2, and this will
further reduce tne
pressure rise generated
by the fan.

For these reasons, it
is often necessary to
have variable pitch
blades on an axial fan
or else to mount the
blades at an angle of
16° or less.
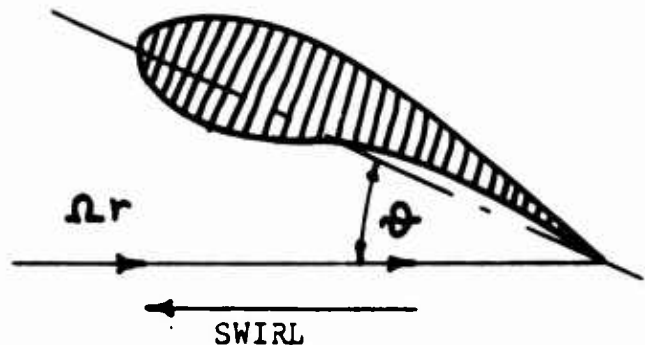
Figure 2. Conditions at Blade
Element for Zero Mass Flow.

When the GEM is flying at its operating height the inflow velocity will
be equal to the air volume flow rate divided by the fan area. Now the
airflow rate, or the mass inflow, is fixed by the operating height and
jet nozzle geometry, for a given vehicle weight, so the only way we
have of varying the inflow velocity in practice is by varying the work-
ing area of the fan.

For maximum fan efficiency in cruise, we need to get maximum lift or
pressure rise from the blades for a minimum power loss, and it can be
shown that this occurs when the ratio

$$\frac{C_L}{C_D} = \frac{\text{blade section lift}}{\text{blade section drag}}$$

is a maximum. This maximum occurs at an angle of attack which varies
with the camber of the aerofoil section and certain geometrical proper-
ties of the fan, but a typical value might be α_{opt} = 9°. Thus, if the
blade pitch angle is 16°, the inflow angle, ϕ, must be 16° - 9° = 7°.
Since the air mass flow is fixed, as explained above, the only way we
can obtain this optimum inflow angle is by using an appropriate combina-
tion of fan area and rotational speed. Moreover, the fan rotational
speed - or more specifically, the circumferential tip speed - is limit-
ed by aerodynamic compressibility, so that the considerations outlined
above define quite precisely the working area of the fan.

The optimum fan size is quite large when a large hover height is re-
quired and immediately poses problems of where to put the payload,
since the fans and their associated inlet ducting assemblies account
for a major portion of the GEM's upper deck. Also, if only one fan is
used, the problem of torque reaction assumes some importance and can
only be remedied at the expense of additional pressure losses in the

8

jet air supply. These compromises can be very serious, although they have often been neglected because of the very low operating height-to-diameter ratios, and therefore low specific mass flows, of the experimental vehicles presently flying.

So far, we have only considered design point operation, but in practice any real vehicle is often operated away from its optimum design condition. For example, the need for maximum terrain clearance under certain conditions will usually make this the design point, in association with maximum engine cruise power output and maximum all-up weight. Thus, design point fan speed will correspond with point A in Figure 3.
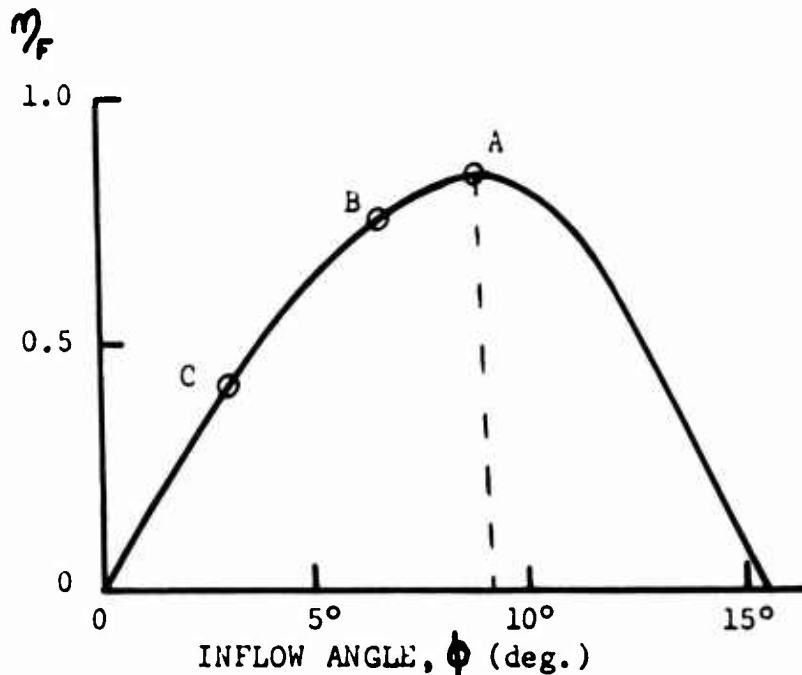
Figure 3. Variation of Fan Efficiency With Inflow Angle.

If we now wish to operate at an all-up weight which is less than the design point value, the mass flow required will be less, and therefore so will the overall efficiency, corresponding to point B in Figure 3. If we now decide to extend our range by reducing the ground clearance, such as in traveling over flat terrain or smooth water, for example, we find that the inflow angle is further reduced, and the efficiency drops to point C in Figure 3. Indeed, in some configurations it is possible to drop to half the hover height and yet to suffer an increase in the power required.

To a certain extent these adverse effects can be minimized when an internal combustion engine is used if the engine is capable of maintaining output through a wide range of operating speeds. For a gas turbine, on the other hand, where there is very little engine shaft speed variation available, no relief is possible without use of a complicated and expensive transmission.

In the realm of stability,
an axial fan also suffers
from a number of disabili-
ties. In steady pitch,
for example, as illus-
trated in Figure 4, the
increased back pressure
in the jet nozzle close to
the ground causes the
greater part of the air-
flow to be diverted to
the higher nozzle, thus
greatly reducing the
pitching stability. This
effect, which is also a
possible cause of high
speed, nose-down pitch,
can only be eliminated
by using a multiplicity
of fans.
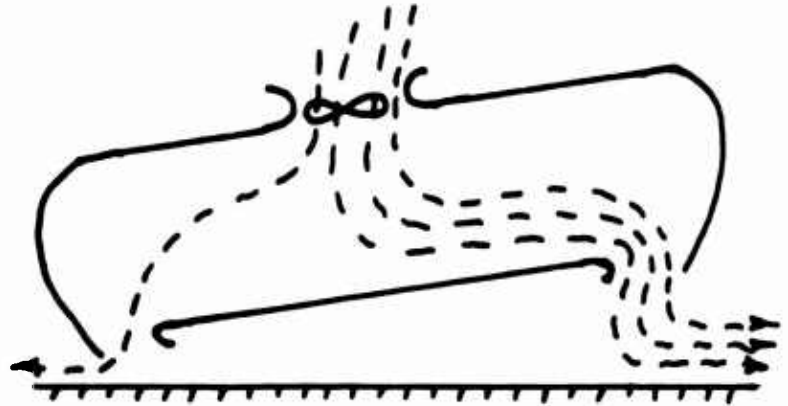
Figure 4. Asymmetrical Airflow Effect.

Typical experimental curves for a small axial fan with a relatively high
blade pitch angle are given in Figure 5. When the blade angle is lower,
the stall shown in Figure 5 can be avoided, but the efficiency falls off
much more sharply as the back pressure is reduced.
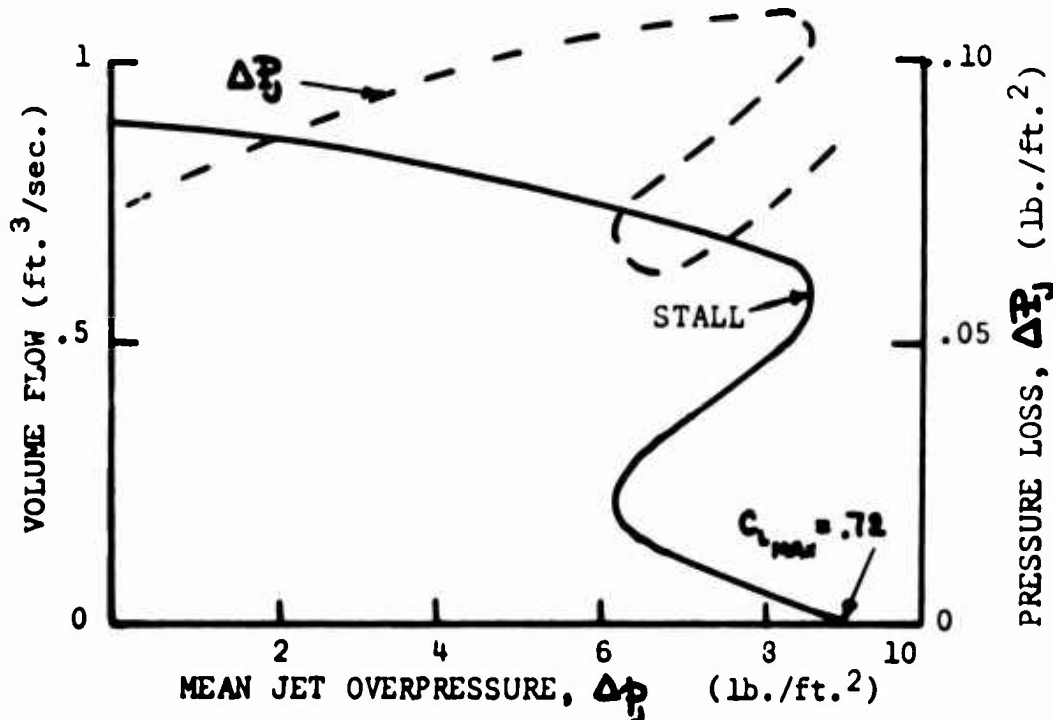
Figure 5a. Variation of Air Volume Flow With Back Pressure
for VAX-2-MM Vaneaxial Blower at 26 V.D.C.
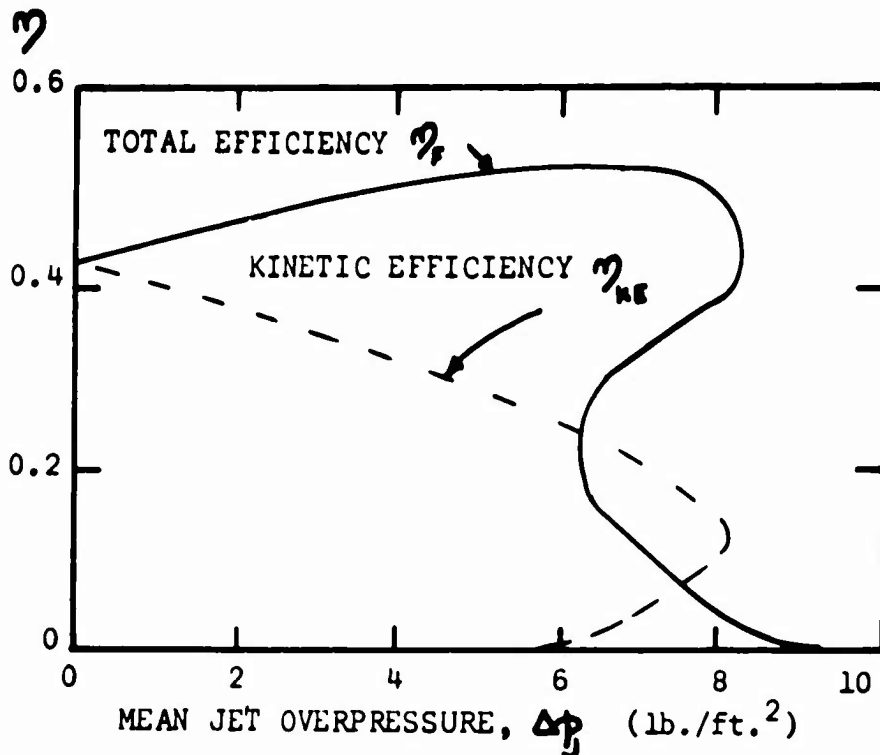
Figure 5b. Efficiency of VAX-2-MM Vaneaxial Blower,
Assuming a Constant Motor Efficiency of 70 Per Cent.

In heave oscillations another effect takes over, and in this case the
number of fans used is unimportant. It is usual to assume that the jet
total head remains constant during a heave perturbation, and to calcu-
late the change in momentum flux caused by the change in jet exit static
pressure. In some analyses the still simpler (and less accurate) as-
sumption of constant momentum flux is made. When a real fan is con-
sidered, however, we find that the total head varies with mass flow,
the relationship for constant chord blades being approximately

$$\frac{\partial \Delta P}{\partial h} = -\frac{1}{2} \rho \, V_T^2 \, a \, \sigma \, t_2 \qquad (5)$$

where the constant $t_2 = \int_{x_0}^{1.0} x \, dx = \frac{1}{2}(1 - x_0^2) \qquad (6)$

11

This effect considerably modifies both the period and damping of a heave motion, of course. In addition, if the fan and engine inertia are low enough for an appreciable variation in their speed to occur during a heave oscillation, then this fluctuation of fan rotational speed can introduce destabilizing coupling terms, which are physically manifested by a heave oscillation with negative damping - a phenomenon analogous to helicopter ground resonance.

Finally, as shown in Reference 3, it is possible for the fan characteristics to be such that heave instability occurs, even at constant fan speed.

We have already mentioned that duct losses are a serious objection to the use of centrally located axial fans, since they can result in the dissipation of up to half the power input. For example, if the back pressure were negligible and the ducting involved no diffusion, the pressure loss would be
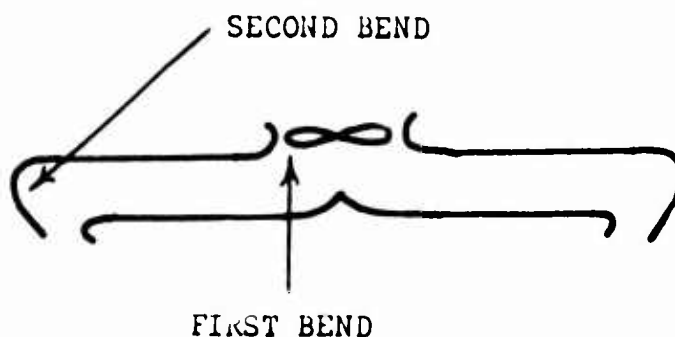
Figure 6. Idealized Duct Geometry for Centrally Located Fan.

$$\Delta P = C_f \frac{1}{2} \rho v^2 \left(\frac{A_2}{A_F}\right) + \text{turning losses} \tag{7}$$

Thus, if the fan area is 10 per cent of the cushion area and C_f = .004, the pressure loss due to skin friction will be

$$\Delta P_{sf} = .004 \times 30 \times \frac{1}{2} \rho v^2 = 0.12 \times \frac{1}{2} \rho v^2$$

The lowest pressure loss around a well-designed bend is about 0.2 $(1/2 \rho v^2)$, so that on these assumptions, two right-angled bends (Figure 6) plus skin friction losses would account for little more than half the total head rise due to the fan.

If we introduce a diffuser after the fan, the skin friction and the second bend pressure loss are reduced, but because of practical space limitations, the additional diffuser losses just about balance this gain.
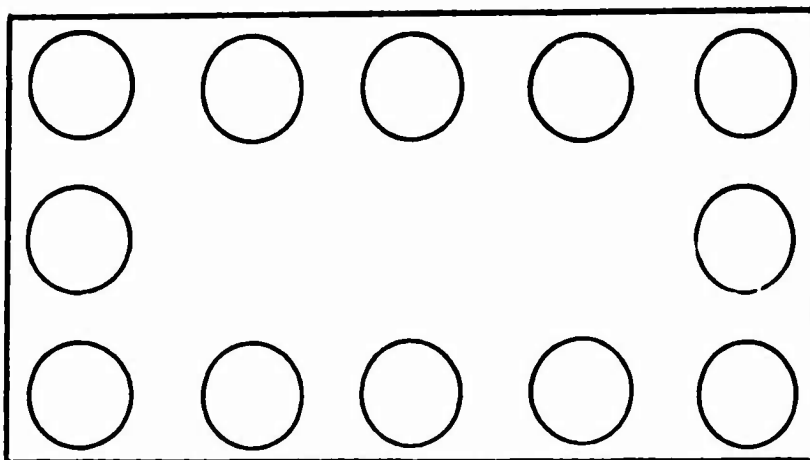
Some of these duct losses can be avoided by installing a multiplicity of fans around the periphery of a GEM, as illustrated in Figure 7, although at the expense of considerable mechanical complication so far as the transmission is concerned. Unless a large number of fans is used, however, a rapidly changing duct shape is needed behind the fan to give a continuous jet curtain. This will result in substantial pressure drops in the regions marked X in Figure 7, so that the overall performance will not necessarily be better than for a centrally located fan.
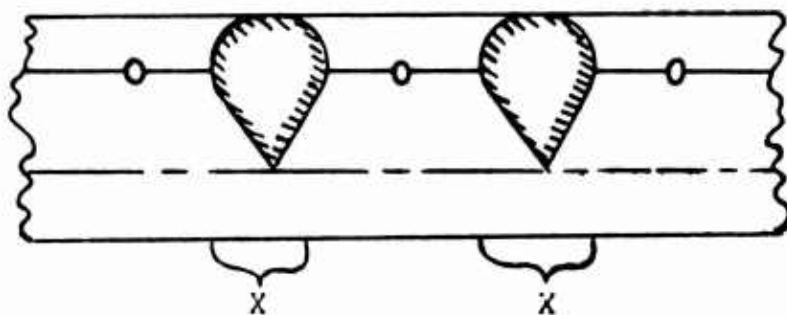
Figure 7. Axial Fans Mounted Around the Periphery.

SOME DISADVANTAGES OF CENTRIFUGAL IMPELLERS

Since a centrifugal (CF) impeller embodies the first bend in Figure 6, it has sometimes been considered as a possible substitute for an axial fan when the back-pressure is relatively high and the mass flow is relatively low. However, a detailed examination shows that a CF impeller usually has to be larger than an equivalent axial fan and that its efficiency will always be substantially lower. Moreover, apart from eliminating the losses in the first bend, which is more than nullified by its lower efficiency and higher weight, a CF impeller suffers from all the disadvantages itemized for the axial fan.

13

THE ADVANTAGES OF PERIPHERAL FAN INSTALLATIONS

Since the jet exit nozzle of an annular jet GEM is around its periphery, it is logical to place the necessary fans also around the periphery and thus minimize both the ducting length and the directional changes applies to the air. One way of doing this is illustrated in

Figure 7, but the transmission weight and complexity penalties are likely to be important, due to the fairly radical change in the duct cross section below each fan. A more logical approach is to use a fan which operates on a horizontal shaft and which would approximate the ideal configuration of Figure 8.

There are two practical methods of achieving this requirement; a transverse flow fan and a positive displacement pump, the last of which has been called the Frost Fan in this application.

A typical transverse flow design is illustrated in Figure 9. At first sight it is difficult to believe that such an assembly of fixed-pitch blades can pump air in one direction, but on a closer analysis it is seen that the duct induces a form of

Figure 8. Ideal Peripheral Fan.
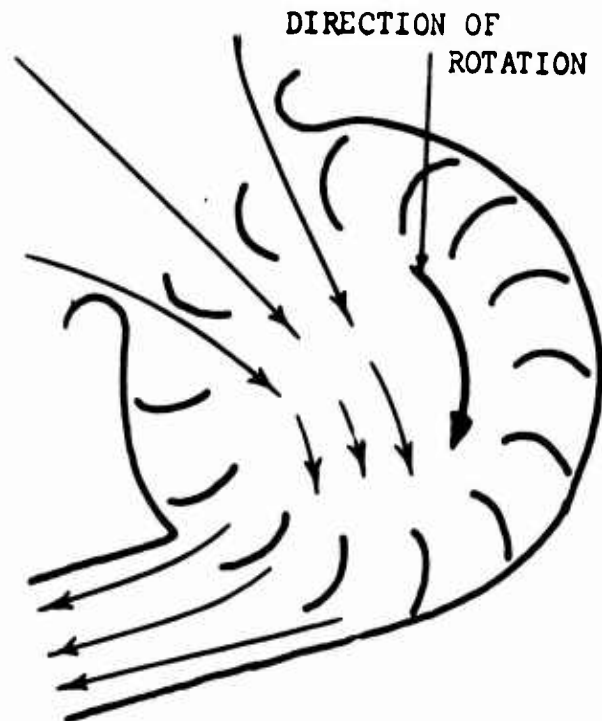
Figure 9. Transverse Flow Fan.

aerodynamic feather-
ing. As shown in
Figure 10, the in-
take airflow relative
to a blade is similar
to the picture for
an axial flow fan,
and air is accord-
ingly forced into
the center of the
rotor, with a mark-
ed swirl velocity
component.

At the exit, the air
passes out of the
rotor with only a
small angle of
attack relative to
the blades, so that
they offer little
impediment to it.
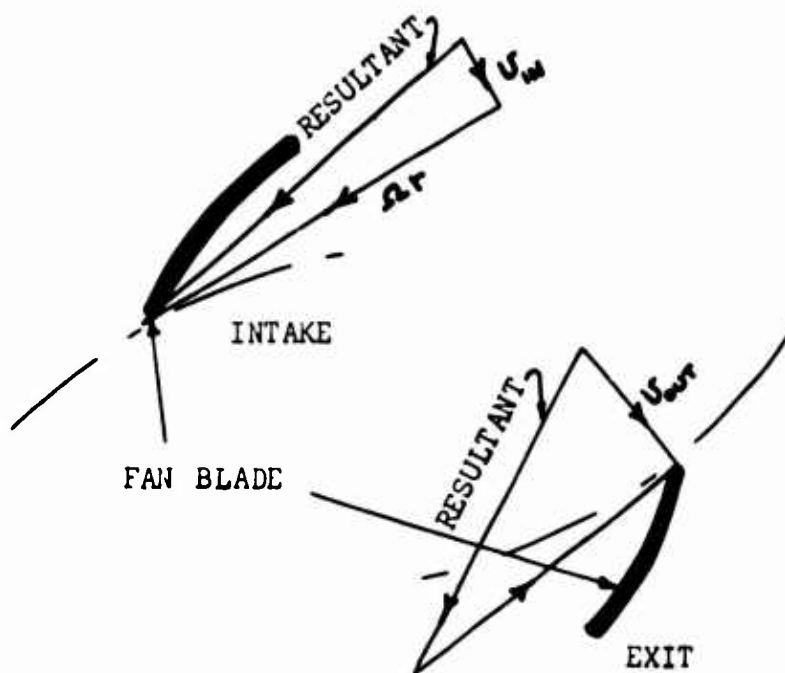
Figure 10. Airflow Relative to
Transverse Flow Fan Blades.

THE FROST FAN

The Frost Fan is a positive displacement device, as shown in Figure 11,
and is similar to the rotary fluid pumps that have been used in hydrau-
lic engineering for many years. Although it has the same short duct
length as the transverse flow fan, it does not suffer from some of its

disadvantages, being es-
sentially an unstallable
constant mass flow pump.
Thus, one of its unique
features is that an in-
crease in nozzle back
pressure does not re-
sult in a reduced
momentum flux until
the increased power
requirement has caused
a reduction in fan
speed. Additional fea-
tures of the Frost Fan
will be discussed in
the next two sections.

DIRECTION OF
ROTATION
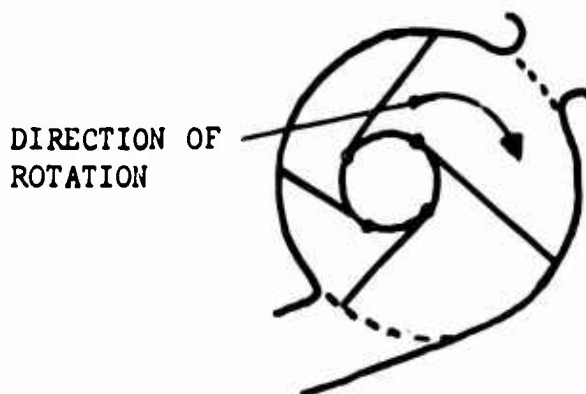
Figure 11. Frost Fan.

15

So far, we have only discussed the performance advantages of peripheral fans, which result from a reduction in losses. Following are a number of secondary advantages, however, some of which may well prove to be of greater operational importance than performance (some of these are indicated in Figure 12):

1. The separation bubble in front of the vehicle (below Walker's second critical speed) may be sucked into the front intake, thus reducing the drag and cleaning up the flow over the upper surface. It may even be possible to establish a form of vortex flow in the bubble, thus reducing the power required by the front jet.

2. A fairly high percentage of the free-stream dynamic pressure should be recoverable in the front jet, so that Walker's second critical speed need never be reached.

3. By varying the rotational speed or nozzle exit area of the front and rear fans, the machine can be readily trimmed when the C.G. is off center. The same is true for lateral trim, of course.

4. In pitching and rolling motions the internal cross flow sketched in Figure 4 can never occur, and the machine will therefore be much stiffer in these directions.

5. Heave instability due to fan coupling terms [equation (5)] cannot occur, as is shown by the theory of Reference 3.

6. Nose-up pitching moments in forward flight will be a minimum, because the change in height of the air passed through the vehicle is a minimum.

7. High-speed nose-down pitch will probably be avoided.

8. The rear fan intake can act as a form of boundary layer suction device and will clean up the flow over the rear portions of the machine, thus reducing its drag.
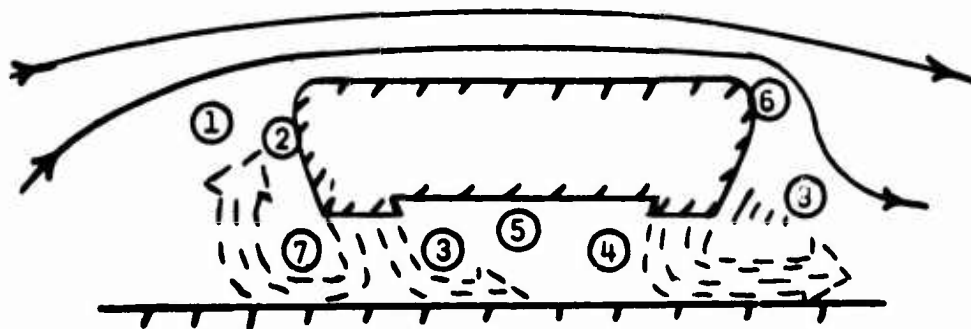
Figure 12. Forward Flight Flow Over a GEM Equipped With Peripheral Fans.

In addition to these aerodynamic features, there are a number of other advantages which can be cited for a peripheral fan, some of which are as follows:

1. The deck is left clear for payload.

2. Since the fans are paired and rotate in opposing directions around horizontal axes, there is no torque reaction.

3. The rotational speed of the fan shafts is relatively high so that there is generally no need for a reduction gear between the engine and its drive. This results in some saving in gearbox and transmission weights.

4. The fan case can double as the backbone of the GEM structure so that the remaining structure required is relatively lightweight.

5. A peripheral fan can be used to generate a vortex flow field, as explained in a following section concerning the Frost Fan in a full-scale recirculation GEM, thus introducing the possibility of additional savings in the power required to support the vehicle.

THE FROST FAN IN A FULL-SCALE ANNULAR JET GEM

In a practical application, the horizontal shaft of a peripheral fan needs to be supported by bearings at regular intervals. In designing a practical application of the Frost Fan principle, these bearings provice an opportunity to segment the fan, in the interests of both serviceability and reduction in cost of initial development. As shown in Figure 13, each segment is 2-feet long and can be rapidly disconnected from the vehicle by removing two external bolts and reaching inside the intake to activate a simple mechanical linkage. Obviously, such a feature is desirable in an operational vehicle and, particularly in one which may be subjected to enemy fire, if all the segments are identical, it also has obvious logistical advantages.

From a development point of view, the prospect of refining a relatively small fan segment, utilizing a relatively modest power supply, is obviously attractive if we can be confident that the results will be applicable to the complete vehicle. One of the problems with existing GEM test beds has been the sheer magnitude of the task of debugging and refining the maze of ducting, where the airflow in each sector poses a unique problem.

NO. 2 FAN ASSEMBLY
PARTIALLY WITHDRAWN

NO. 3 FAN ASSEMBLY

NO. 2 FAN ASSEMBLY

NO. 1 FAN ASSEMBLY

FAN ROTOR

ROTOR
BEARING

PLUNGER RETRACTED
FREEING NO. 2 FAN
ROTOR

UNLOCKED

PLUNGER EXTENDED
ENGAGING NO. 2
FAN ROTOR

LOCKED

18
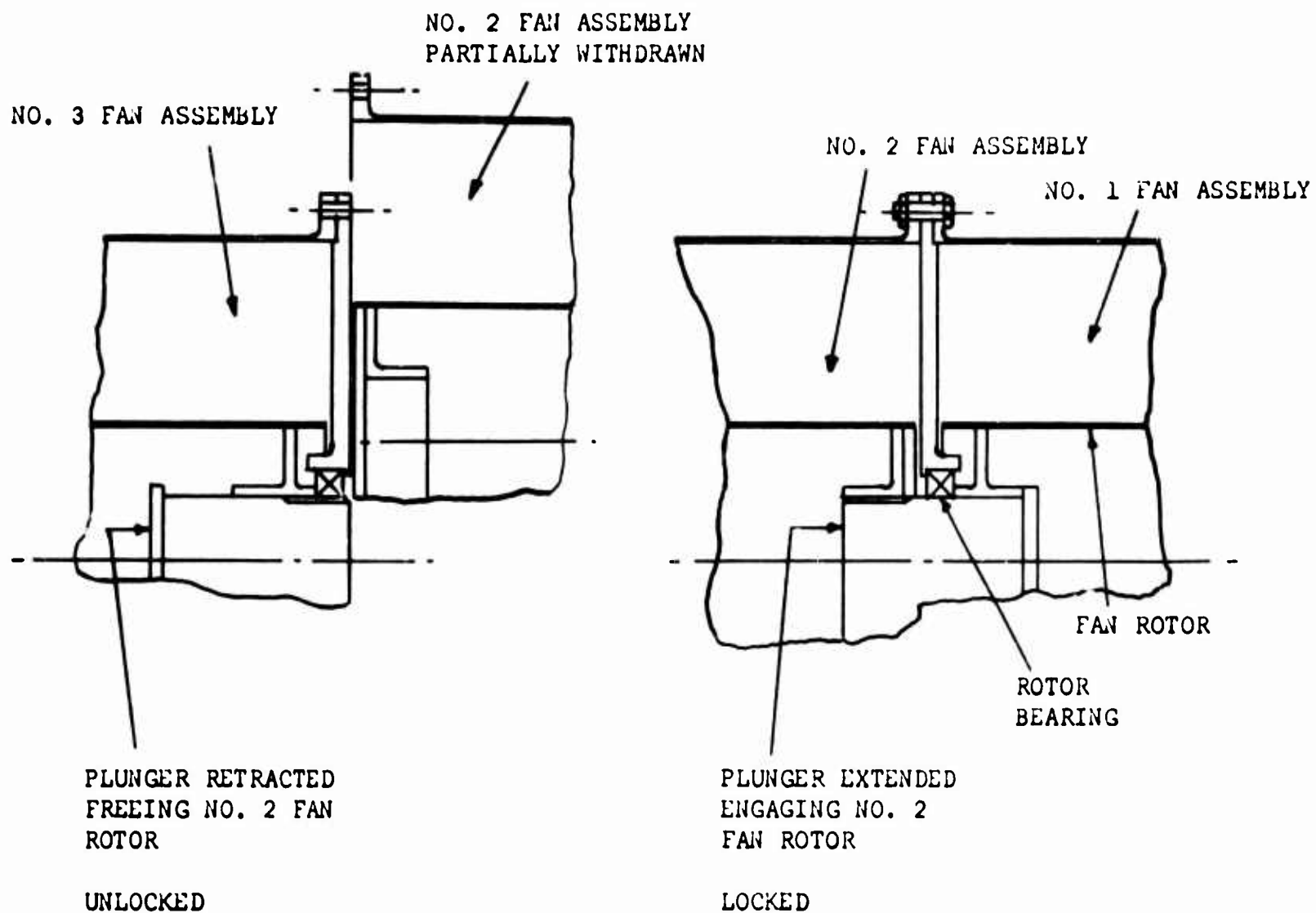
Figure 13. Frost Fan Installation - Modular Arrangement.

BLANK PAGE

THE FROST FAN IN A FULL-SCALE RECIRCULATION GEM

So far, we have confined our discussion to conventional annular jets, where the power required is primarily needed to accelerate the airflow and to force it out of the jet nozzle against the back pressure

In the recirculation principle, the function of the fan is to establish a vortex which seals the ground cushion, as illustrated in Figure 14, and which, in an ideal fluid, would require no power to maintain it. In practice, air entrainment and leakage occur on both sides of the vortex, while both skin friction and

Figure 14.   Vortex Flow.

turbulence losses occur in the ducts, so that some power is required. Nevertheless, a great deal of interest is currently focused on the recirculation principle.
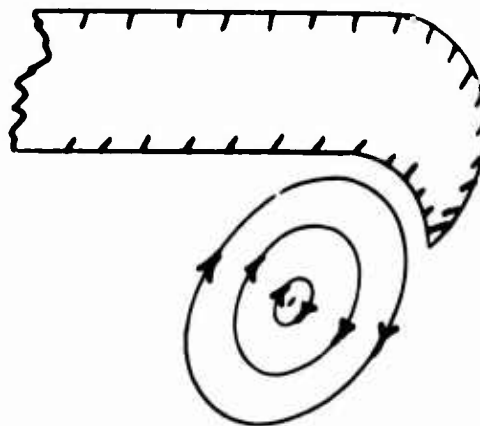
We can expect a considerable amount of dust and other solid particles to be entrained in a vortex flow of this type, so that it is probably out of the question to maintain the flow with any form of conventional fan. The "Ejectijet" solution proposed by the Martin Company avoids this difficulty by using an ejector pump to maintain the vortex, so that there are no moving parts in contact with the airflow. Unfortunately, jet pumping is so inefficient that the losses involved largely cancel any performance gains achieved by establishing vortex flow, and no great overall gains in the performance of such a system can be seen.

The use of a Frost Fan to maintain a vortex does not involve substantial pumping losses, however, and when suitably designed for this application, it is still highly resistant to abrasion and damage by water and solid objects.

The version illustrated in Figure 15 retains the hinged blades of the annular jet fan, but operates with them lagging to maintain the correct angle of attack at the inlet. This is a fortunate aerodynamic requirement, since if a large solid object enters the fan case, its impact upon a fan blade will cause it to swing backwards, thus minimizing the chance of structural damage.
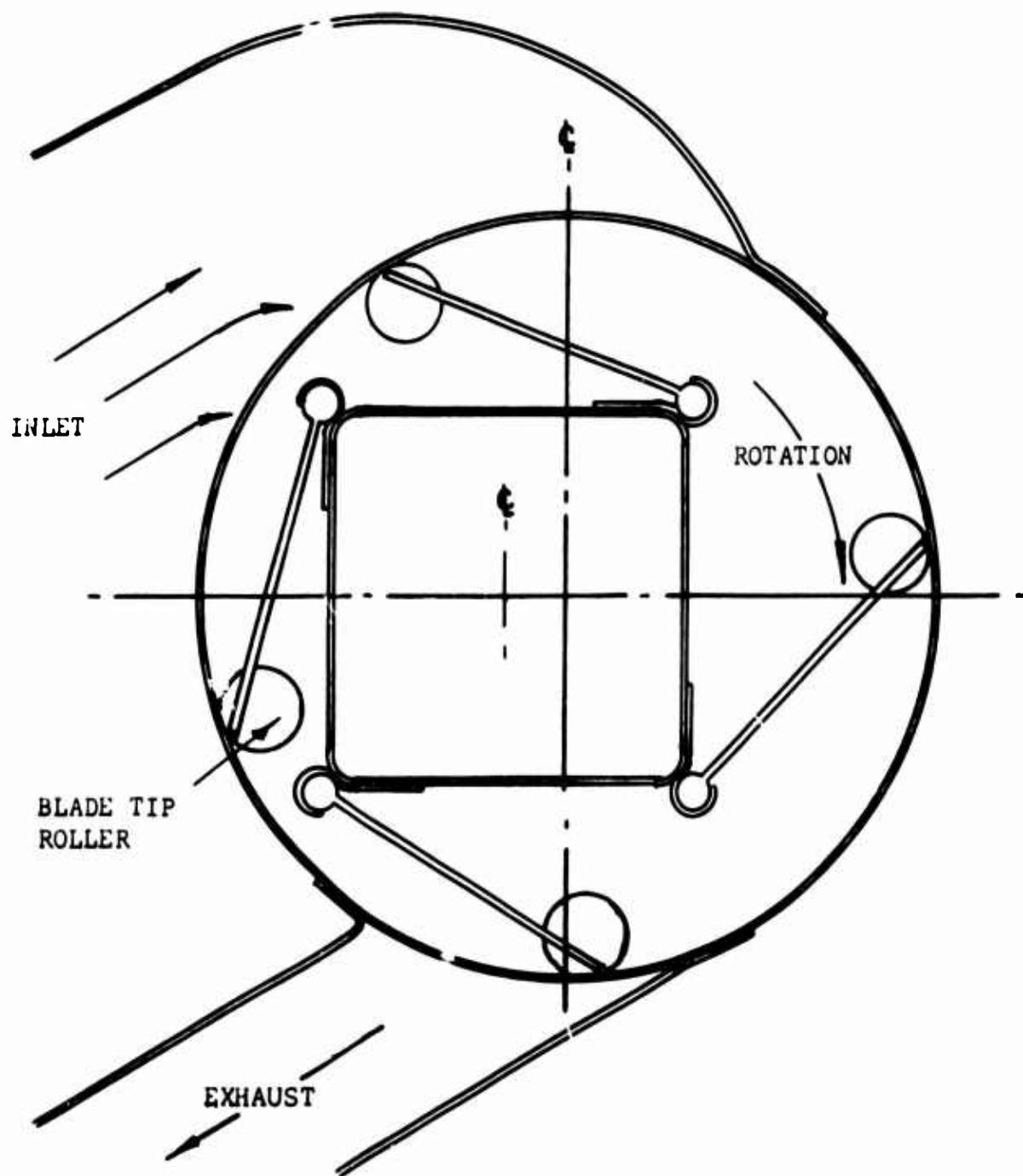
Figure 15.   Frost Fan - Cross Section

A REVISED FROST FAN CONFIGURATION

In Reference 4, the tip roller friction was measured, by using a separate test rig, and it was found that the friction coefficient was roughly four times the value originally selected as the target. This was very serious because roller friction is the main cause of power loss in the Frost Fan configuration, and a friction coefficient of .04 reduces the efficiency to about 30 per cent. The friction is also found to be very variable as might be expected, and with essentially the same configuration, full-scale efficiency measurements vary from as low as 20 per cent to as high as 55 per cent.

Faced with this problem, it would have been logical to embark on a study of the effects of high rolling friction and its variability, with a view to reducing both effects and thus to increasing the fan efficiency. However, Mr. F. Tallentire of Frost Engineering attacked the problem from the alternative standpoint of eliminating the tip rollers altogether and, hence, of reducing this source of loss to essentially zero. His final configuration is shown in Figure 16 and the calculated efficiency for this is plotted in Figure 17. It is now believed that this is the most satisfactory solution to the problem and a follow-on in which the development work can be continued with this new configuration is strongly recommended.

A SUMMARY OF SOME GENERAL OBSERVATIONS AND STUDIES MADE DURING THE PROGRAM

Corner Losses

The junction of two jet or vortex sheets at the corners of a rectangular GEM has been suggested as the cause of cushion pressure loss due to a "hole" in the jet sheets. This was investigated experimentally for both annular jet and recirculation systems and the results were reported in Reference 5. It was found that cushion pressure increased rather than decreased, and it was shown that this is what should be expected from theoretical considerations. It is therefore concluded that if corner losses do exist (and no evidence for this has yet been put forth so far as we are aware), then they can be rectified by proper attention to duct design at the corners.

21

ROTATING END PLATE

FAN CASE

FAN AXIS

ROTOR AXIS

ROTOR

FLEXIBLE
BLADE

ROTATION

FIXED HUB
SUPPORTING
ROTOR BEARING

BLADE TIP
SUPPORTS
(ATTACHED TO
END PLATE)
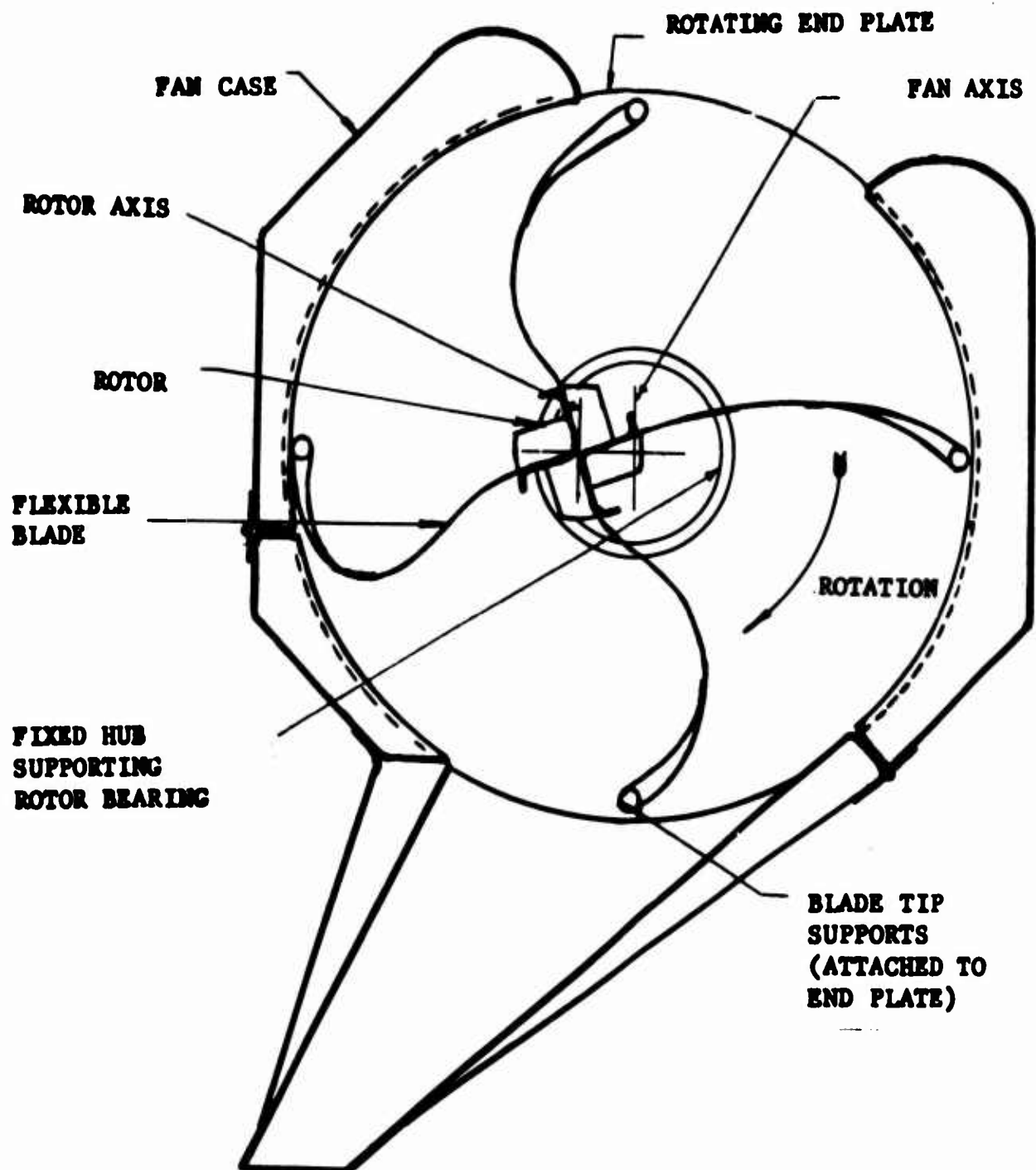
Figure 16.   Revised Configuration of Frost Fan.

22
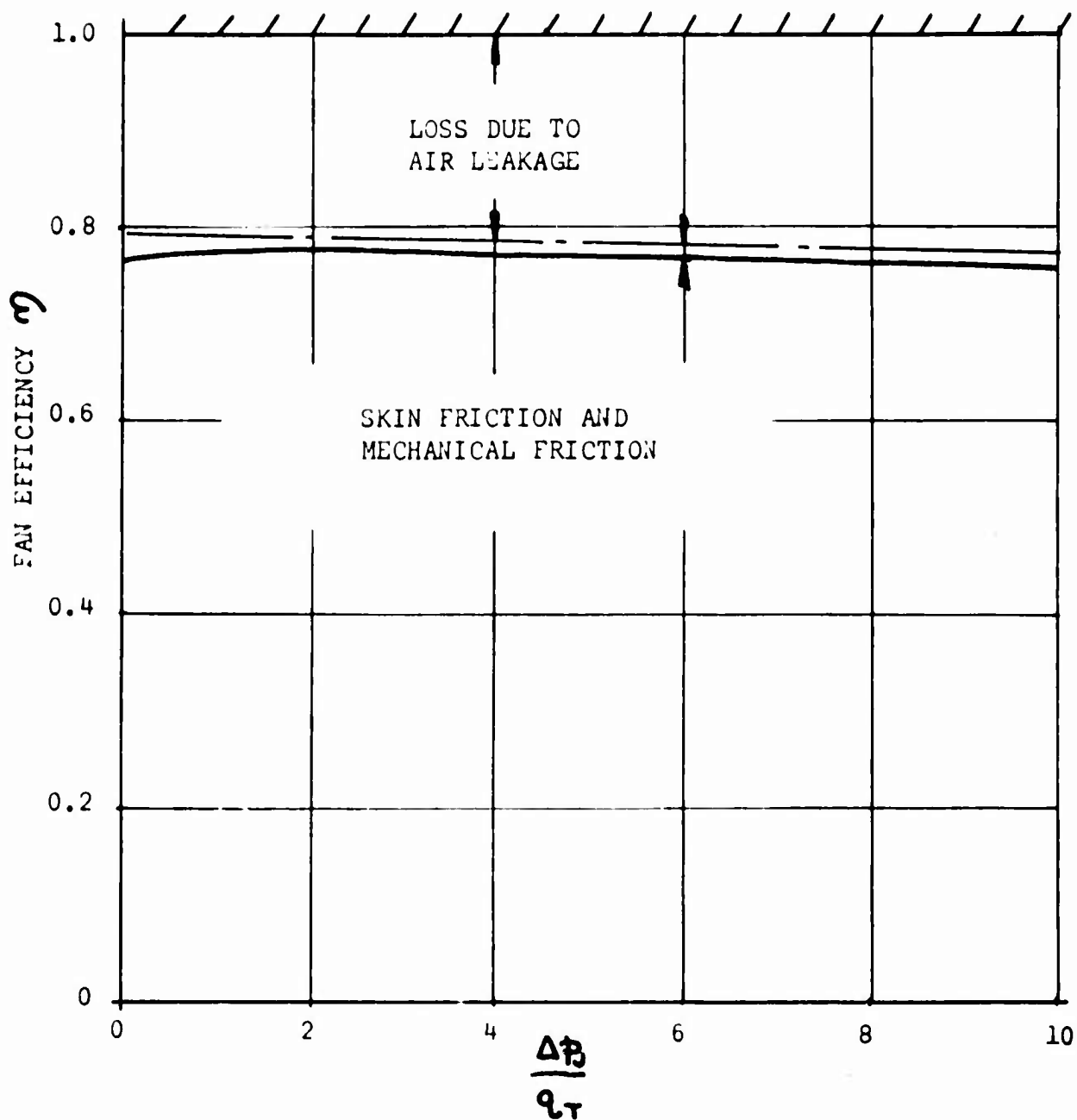
Figure 17. Fan Efficiency (η) Versus $\Delta P_{B} / q_{T}$
For Revised Configuration of Frost Fan.

Optimum Jet Thickness

Reference 6 examined the effect of jet thickness upon GEM performance
in hover. Prior to the publication of this report, it was generally
accepted that the height parameter x should have a value of unity for
optimum operation. In Reference 6, it was shown that the correct value
of x for optimum performance was 1.45 and that for any given configura-
tion there was also an optimum value for the jet angle of inclination.

Arising out of this work, Reference 7 used the optimum performance
equations for an annular jet as a basis for a method of assessing the
performance of any practical system, a process which hitherto had been
so indefinite that the desires of an investigator could have altogether
too large an effect on his conclusions.

A Comparison Between Annular Jets and Plenum Chamber Machines

The concept of a truly optimum GEM established in the reports mentioned
in the previous paragraph led naturally to the comparison between an
optimum annular jet GEM and an optimum plenum chamber machine. Ob-
viously, one of the reasons for studying the Frost Fan is the belief
that it will result in superior performance, and this would not neces-
sarily be so if the plenum chamber machine were, on an overall system
basis, comparable in efficiency with an annular jet. Reference 8 con-
cluded that the annular jet had some superiority in hover, and probably
more under forward flight conditions. Nevertheless, the efficiency of
the plenum chamber machine was such that work with it should definitely
be continued, since there are probably many applications where its
greater simplicity more than offsets the relatively small performance
advantage of the annular jet.

To clarify this point, the performance of most existing plenum chamber
machines is very poor. However, it was shown in Reference 9, Appendix
III, that efficiency could conceivably be raised to as high as 80 per
cent. The poor performance of most existing machines is due to the
fact that the importance of fan optimization was not sufficiently under-
stood at the time of their design. In contrast to this, the Frost Mine
Search Head Carrier plenum chamber machine developed for the U. S. Army
Transportation Research Command (USATRECOM) by Frost Engineering Devel-
opment Corporation was found to be very good and certainly better than
could be achieved with an annular jet machine of the same scale.

Contributions to Annular Jet Theory

Any program connected with annular jet GEM's is naturally vitally con-
cerned with the theory of annular jets, and Reference 10 was written in
an effort to clear up some of the misunderstandings which have arisen
with regard to the various theories promulgated for the calculation of

cushion pressure. It was shown that layered jet theory is by far the most accurate statement of the true flow picture, so long as the total head distribution across the nozzle is reasonably uniform, and that alternative theories are merely less successful approximations of this solution.

It was also shown that the work of Cross in England has conclusively demonstrated that layered jet theory automatically allows for most of the effects of viscous mixing and that attempts to make additional corrections are quite inappropriate. The viscous mixing corrections to thin jet theory certainly improve the accuracy of thin jet theory to some extent; however, this is only of academic interest, when more accurate theories are available.

Heave Stability

Reference 3 discusses heave stability in order to give insight into the effect of the substantially constant mass-flow delivery of the Frost Fan in comparison with the characteristic of conventional fans, where the mass flow varies inversely with the static pressure of the nozzle. It is believed that this investigative report is more detailed than previously published ones; of particular interest is the fact that the theory presented shows a possibility of two types of instability, both of which depend upon fan characteristics and neither of which can occur with the Frost Fan. It is also of interest to note that Mr. Norman K. Walker has demonstrated heave instability experimentally in the course of model experiments for USATRECOM.

In general, a constant mass-flow machine is stiffer in heave and also has greater damping. Since many GEM configurations appear to be marginal in these respects, this characteristic is extremely important, of course.

SECTION ONE

THEORY OF ENERGY RECOVERY BY RECIRCULATION

INTRODUCTION

Although the Work Statement of the contract called only for the application of the Frost Fan to a recirculation system, it was felt that it would be necessary to understand recirculation theoretically before this could be done effectively. A very small amount of work had previously been published by Martin in this regard, but this was obviously insufficient to permit optimization of a recirculation configuration.

The first Frost study of recirculation theory was reported in Reference 11 and was based upon the various experimental observations reported by the Martin Company. The design of the Frost Fan recirculation rig was based upon the theory developed in this Reference, but subsequent work showed that a number of the assumptions made were invalid and that the problem was very much more complicated than had perhaps hitherto been supposed.

Recirculation as presently understood is inferior in both stability and performance to the conventional annular jet configuration and little hope can be offered of useful operational applications with existing configurations. It may prove possible, when we have the necessary understanding of the phenomenon, to design optimum configurations which will greatly surpass the efficiency of an annular jet configuration.

It was not until Reference 5 was published that a satisfactory explanation for the heave instability at low hover heights was established. The heave instability will pose a severe operational problem unless the machine is flown well above its critical height, where its efficiency will be further reduced.

Although experimental verification could not be made in the present program, it appears that heave instability can be reduced by the use of a constant displacement air mover such as the Frost Fan. When eductors or aerodynamic reaction fans are used, however, heave instability appears to be fundamental to the system at low hover heights.

The effect of a right-angled junction between jet sheets was investigated experimentally. For both annular jet and recirculation configurations it was found that a corner increased cushion pressure rather than reduced it as had been suggested in the past. It is shown that this result is in conformity with basic momentum theory.

26

A start has been made in the problem of calculating the power required by a recirculation system and in identifying the individual loss components. The fact that some energy conservation is theoretically possible with recirculating flow indicates that it has more development potential than the annular jet configuration, even though this potential may never be recognized in practice.

POWER REQUIREMENTS

Recirculation in GEM applications has been characterized as a standing vortex around the periphery of a machine which seals in the cushion overpressure. Because the vortex velocity has only to be maintained and no acceleration of the air is involved, it is generally assumed that the power required by a recirculation system will be less than for an annular jet system. Unfortunately, this is not so.

Although there is little experimental work available upon which we can base estimates of power required, we know that to maintain a given cushion pressure a recirculation system requires between twice and three times the momentum flux of an annular jet in the useful operating range (as shown in Figure 18, for example); that is, other factors being the same, its mean jet velocity will be about $\sqrt{2}$ times as much. Thus the jet power will be greater in the ratio ($\sqrt{2}$)^3 : 1, or roughly three times as great. It follows that the energy ratio must be greater than three for the system to break even. And in Reference 12 it is pointed out that even a good open-jet wind tunnel can only just achieve such a figure, despite the fact that its mixing surface per unit mass flow is many orders of magnitude less than for a GEM recirculation system.

We can also reach the same conclusion from the Martin experimental data, such as that given in Reference 13, for example. Here the total pressure recovery at the intake is seen to be quite small in relation to the exit total pressure, and the addition of 10 per cent - 20 per cent total pressure loss in the ducts results in essentially zero energy conservation. Thus, on this basis, we should expect two or three times the annular jet power requirement because of the greater jet momentum flux needed to maintain the cushion pressure.

It does not necessarily follow from these observations that the recirculation principle should be abandoned, of course. The truth is that we are still so ignorant of the basic flow mechanisms that it is quite impossible to predict the full potential of the system. Further research directed towards a more thorough and accurate theoretical description of present recirculation configurations will undoubtedly lead to more efficient configurations; but how efficient these will be cannot be guessed.

27
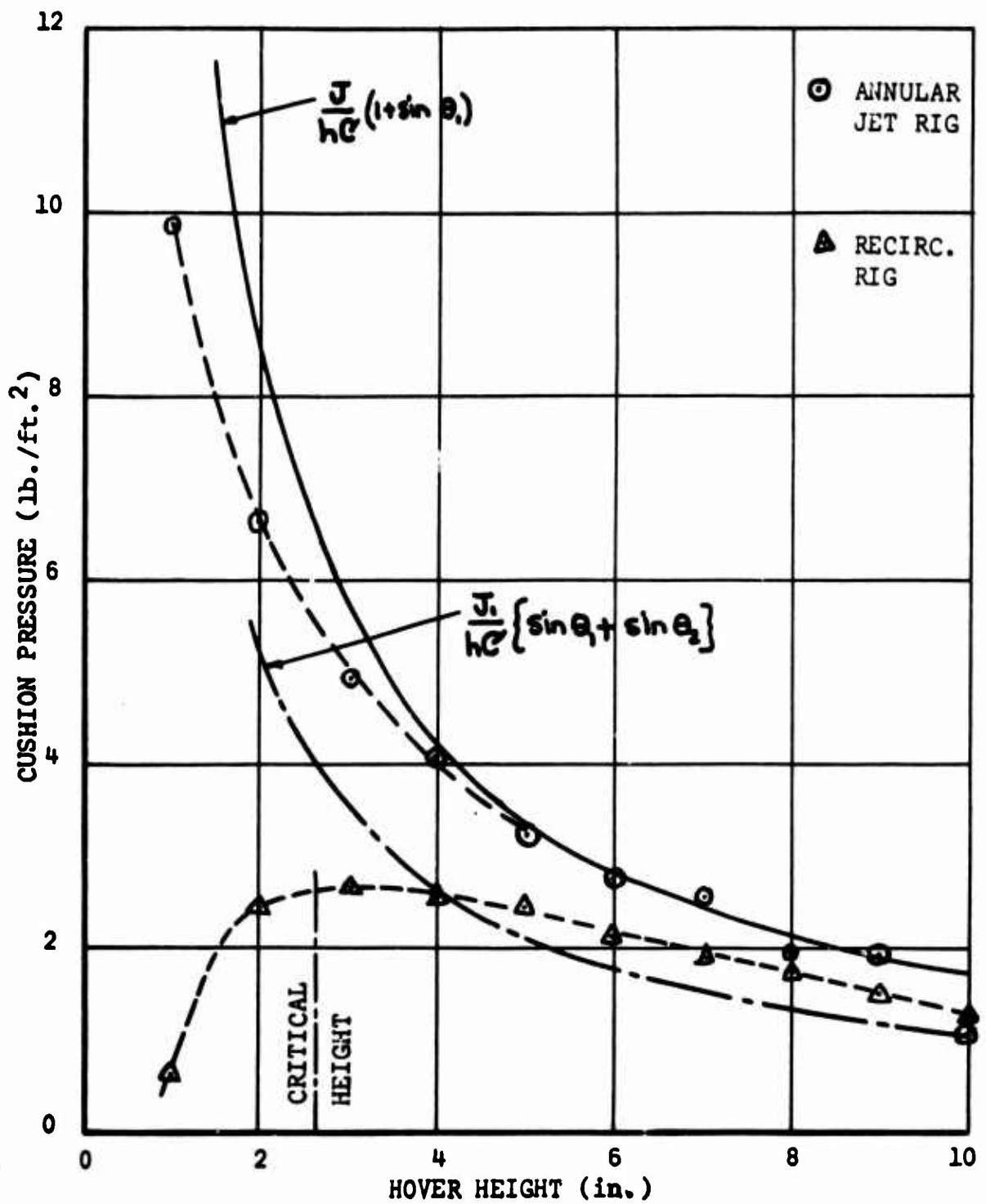
Figure 18.   Cushion Pressure Generated
By Annular Jet and Recirculation Systems.

28

We can only take refuge in the generalization that an energy conservation system has a better development potential than one which cannot conserve any energy at all.

Since the prospect of success is so tenuous, it would of course be highly imprudent to tie hardware development plans to the contingency of developing an efficient recirculation system.

AREAS WHERE FURTHER STUDY IS NEEDED

Apart from References 11 and 12, which are relatively trivial, little attempt has so far been made to develop the theory of recirculation. This is particularly unfortunate for the case of low height-to-thickness ratios, where marked static instability occurs, because, until we understand the physical causes, we can do little to alleviate the problem. Also, it is obviously impossible to optimize a configuration without a good understanding of the various causes of inefficiency.

Relative to other problems in subsonic aerodynamics, an adequate theoretical description of the recirculation phenomenon is quite a simple problem; relative to most other GEM problems of external airflow, it is complex, however, and the effort necessary to obtain adequate solutions should not be underestimated.

It is recommended that a high priority be assigned to a detailed study of the theory for low height-to-thickness ratios and to the calculation of the power required to sustain a vortex, using the alternative configuration assumptions of a constant displacement pump, a constant total pressure fan, and eductors. It is anticipated that each will result in quite different performance and stability characteristics and that the constant displacement system at least will have substantially better stability characteristics. It may also be possible (though not probable) to design an augmenter to give increased momentum flux as the working pressure drops (Reference 14) so that an augmenter driven system is also stable in heave. Also, when an accurate theoretical description of the flow field is available, we may find that fairly radical changes in geometry will improve both performance and stability.

Finally, a partial recirculation system (Figure 19), which is a hybrid combination of conventional recirculation and annular jet systems, should be considered as offering a fairly simple way of mitigating some of the disadvantages associated with either system by itself.

It is very strongly felt that extensive commitments to hardware would be most unwise without such a theoretical groundwork being laid.
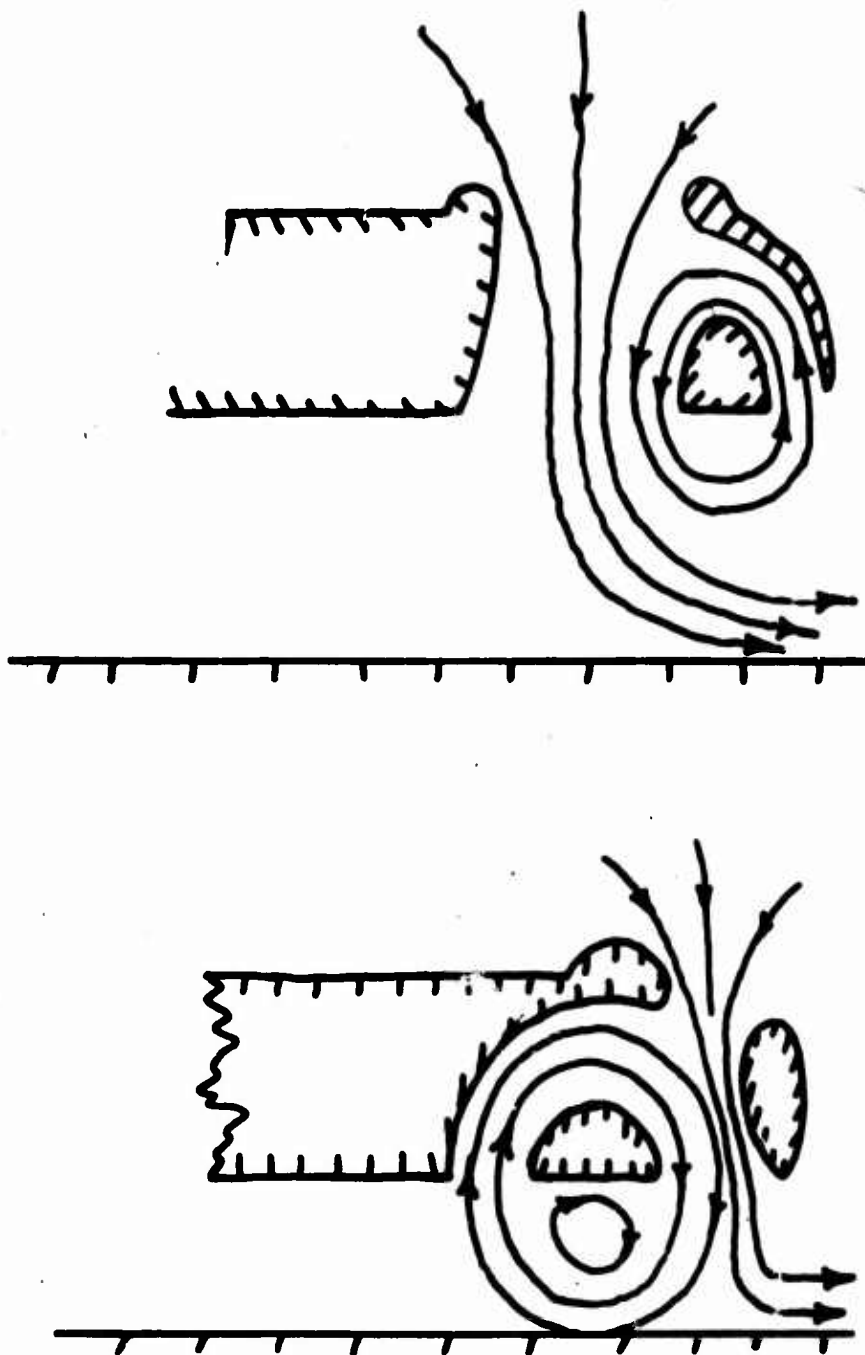
Figure 19. Two Possible Hybrid Systems.

DESCRIPTION OF TYPES OF AIRFLOW

Some broad generalizations about recirculating flow are given in Figure 20 for the ideal case of no viscous mixing. In practice, free air entrainment will always occur, leading to the flow picture postulates of Figure 21.
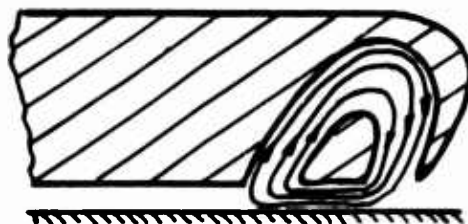
(a) Bernoulli Flow. $0 < \frac{h}{t} < 2$

Forcing the airflow through the cavity-zone bottleneck causes large pressure losses which increase with diminishing height, often causing static instability in heave. Intense suction occurs in the cavity region.

Transition begins at roughly h/t = 1.0 - 4.0; the actual value depends on the pressure distribution at the nozzle exit.

(c) Full Vortex Flow. $\frac{h_{CRIT}}{t} = \left(\frac{h_{CRIT}}{\ell_r}\right)\left(\frac{\ell_r}{t}\right)$

Critical height for full vortex flow is given by

$$\frac{\ell_r}{h_{CRIT}} = \frac{\cos\theta_1}{1 - \sin\theta_1} + \frac{\cos\theta_2}{1 + \sin\theta_2}$$

Vortex theoretically makes only line contact with ground plane.

AIR MOVING DEVICE

Cushion pressure equal to fan (suction) pressure

Diffusion and corner losses are very high at low values of h/t. Pressure drop can be high enough to cause negative cushion pressures.

(b) Constrained Vortex. $1 < \frac{h}{t} < \left(\frac{h}{t}\right)_{CRIT}$

Vehicle should be statically stable in this flow regime.
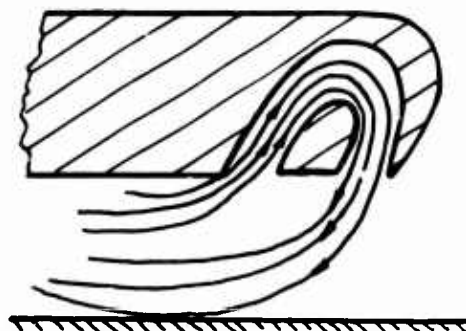
(d) Supercritical Flow $\frac{h}{t} > \left(\frac{h}{t}\right)_{CRIT}$

The vortex gradually collapses, giving a marked reduction of cushion lift with height. Static pressure measured at the center can still be quite high, however, due to local air flow.
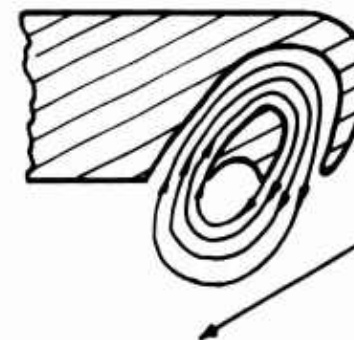
Intake suction is sufficient to prevent jet impinging on the ground. Zero cushion pressure for the inviscid flow case.

Alternative Supercritical Flow (Observed in Martin tests and reported in Reference 16)

31

Figure 20. Idealized Categories of Steady State Recirculation Flow, Neglecting Viscous Effects.

(a) CUSHION SEALED BY VORTEX

(b) FLOW OUT OF CUSHION
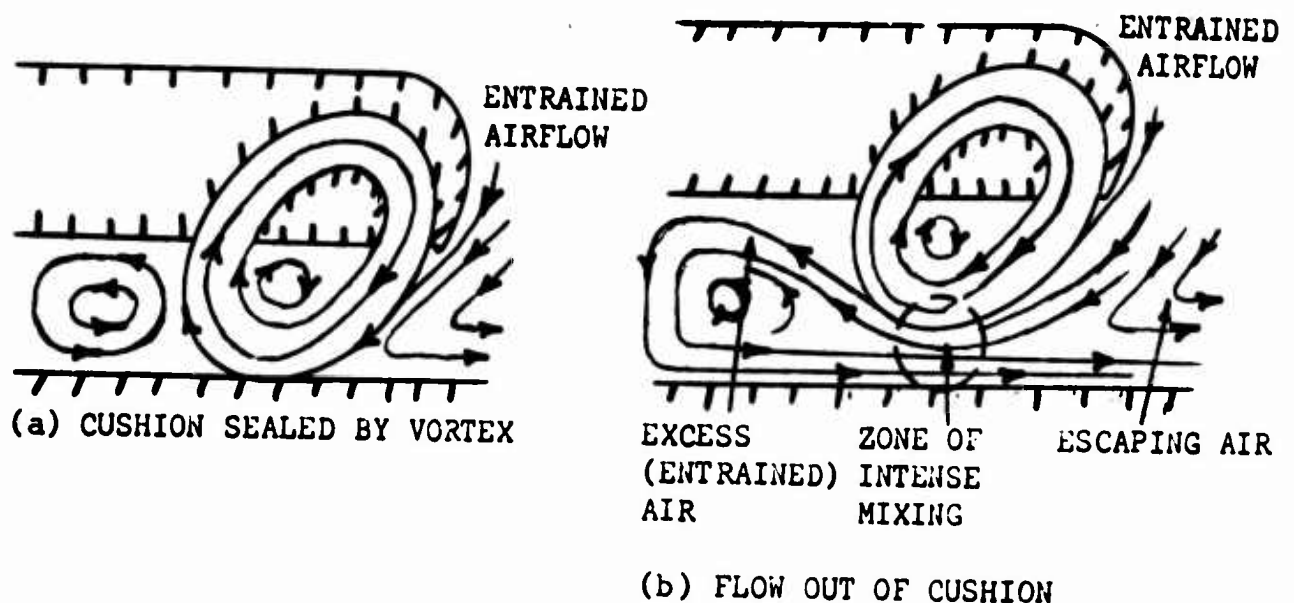
Figure 21. Two Alternative Flow Pictures
Possible With a Real (Viscous) Fluid.

It is obviously possible to measure the entrained airflow by measuring
the air mass flow out of a recirculation test rig. It is also possible
to calculate the power losses due to mixing, although the "zone of in-
tense mixing" in postulate (b) will present some problems in this re-
gard. It is also interesting to note that the losses incurred in this
zone will increase with decreasing hover height, in contrast to the
free-air entrainment losses.

At the present time, postulate (a) appears most likely to be correct.
In tufting surveys, no evidence could be found of an outflow from the
cushion, at any of the heights tested.

The Bernoulli-flow regime was first analyzed in Reference 11 on the ar-
bitrary assumption that the airflow velocity through the cavity varied
linearly with the operating height. This gave good agreement with ex-
periment, but it was impossible to justify the basic assumption. An
improved analysis is given in Appendices I and II of this report, al-
though no pretense to completeness is made, since only the salient
points of the theoretical treatment are sketched in. The physical ba-
sis is obviously much more satisfactory, and it appears safe to say
that the static instability in the Bernoulli-flow regime is a function
mainly of the pressure losses incurred in forcing the airflow through
the constriction made by the under surface of the center-body and the
ground plane. It is shown in Appendix I that, for incompressible flow,
static instability will still occur if the air-mover is of the constant
displacement (and hence constant momentum flux) type, such as the Frost
Fan, but that its magnitude is likely to be less.

When the momentum flux is constant, the only factor which contributes to instability is the loss coefficient, ϕ, which is due partly to corner losses and partly to expansion of the flow in the intake plane. The smaller the hover height, the greater is ϕ ($d\phi/dh < 0$), and since from Appendix I

$$\frac{d\Delta P_c}{dh} = -\frac{J_1}{2t_1 C}\frac{d\phi}{dh}$$

- it follows that $d\Delta P_c / dh > 0$, leading to divergence. Obviously, we can minimize this tendency by minimizing the loss coefficient, ϕ.

When the fan is not of the constant displacement type,

$$\frac{d\Delta P_c}{dh} = -\frac{J_1}{2t_1 C}\frac{d\phi}{dh} - \frac{\phi}{2t_1 C}\frac{dJ_1}{dh}$$

In this case the instability can be greater or less, depending on the sign of dJ_1/dh. Most generally, this term will be destabilizing.

The same observations are true, although with changed emphasis, in the transition region between Bernoüilli and constrained vortex flow. Substantial stability (and performance) improvements can obviously be expected from a program designed to reduce losses, since no recirculating system has (apparently) been designed so far with this aspect in mind. The only loss not susceptible to obvious improvement is that due to mixing of the entrained ambient air, and even this can be min nized by selection of a suitable configuration.

THE CRITICAL HEIGHT CONCEPT

The "critical height" concept advanced in Reference 11 indicates that a recirculation system will suffer a sudden loss in lift when

$$\frac{\ell_r}{h} \leq \frac{\cos\theta_1}{(1-\sin\theta_1)} + \frac{\cos\theta_2}{(1+\sin\theta_2)} \tag{8}$$

- the geometrical quantities being as defined in Figure 22.
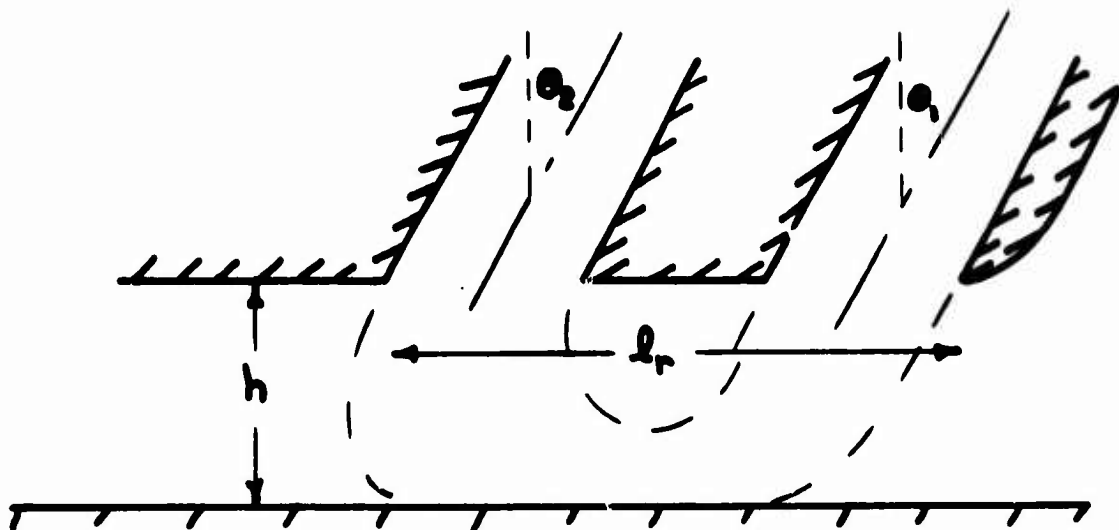
Figure 22. Recirculation Geometry.

Some results obtained with a model rig at Bristol University, England (Reference 15), are plotted in Figure 23. For this case,

$$\left(\frac{\ell_r}{h}\right)_{CRIT} = 4.144$$

or

$$\left(\frac{h}{t}\right)_{CRIT} = 0.241$$

For the test results plotted in Figure 23, Reference 15 gives a maximum value for ℓ_r/t of 8.0, resulting in the critical height shown. This is obviously in reasonable agreement with experiment, being at about 75 per cent of the height at which the rapid fall-off in cushion pressure begins. The same result was noted in Reference 11 when analyzing the Martin two-dimensional data, and the 25 per cent error was attributed to jet spread due to mixing and intake suction.

Actually, it is now possible to refine this estimate by including the effect of viscous mixing of the jet in the ambient zone. From equation (21) the mass flow will be increased by mixing in the ratio

$$\frac{\dot{m}}{\dot{m}_0} = 1 + \frac{0.04 \left(\frac{\pi}{2} - \theta_1\right)(h/t)}{(1 - \sin \theta_1)} \quad (9)$$

34
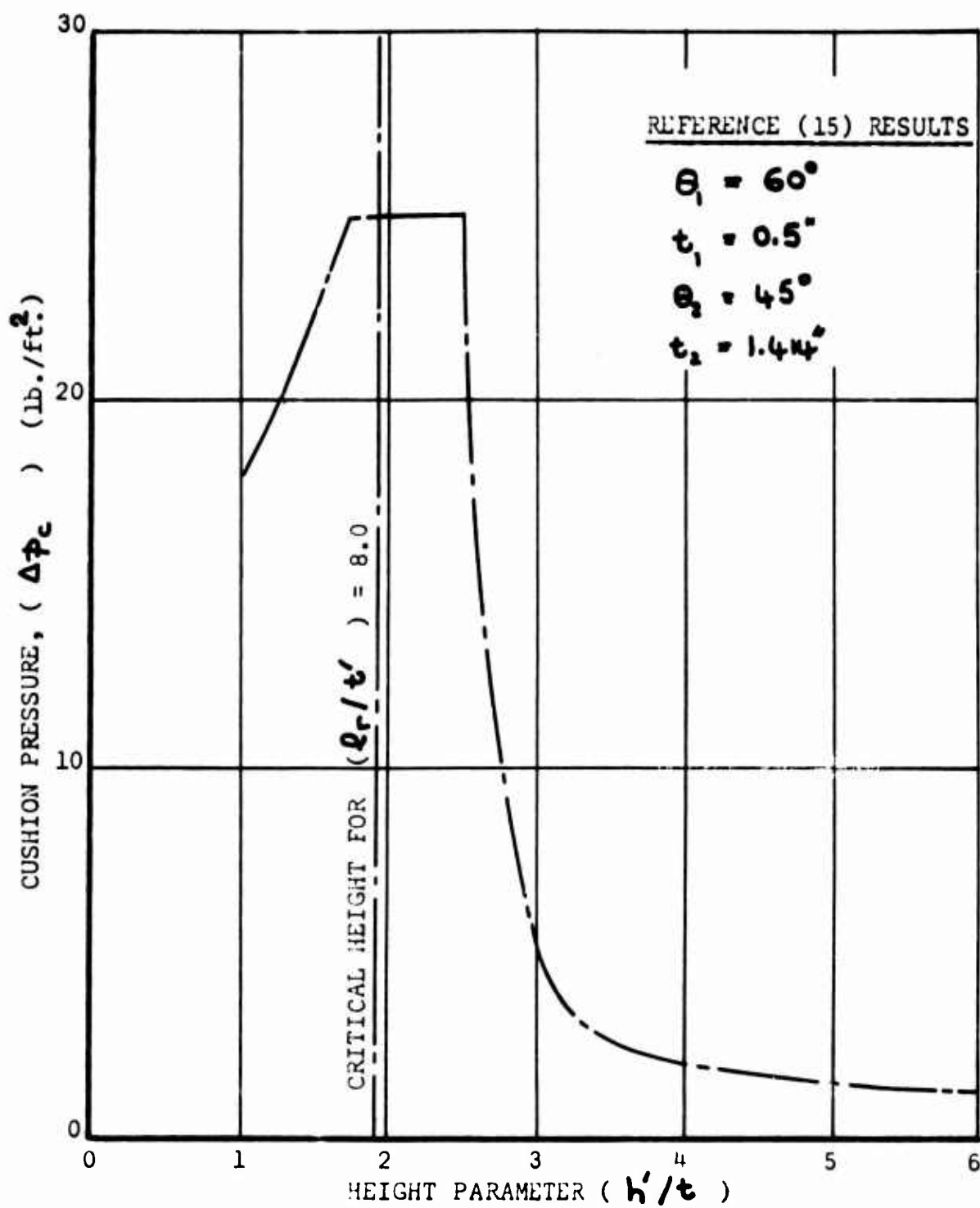
Figure 23. Cushion Pressure Variation With
Height for Reference (15) Model Tests.

Assuming that the jet thickness varies linearly with its mass flow, then from equations (8) and (9),

$$\frac{\Delta h_{CRIT}}{\ell_r} = \frac{0.04\left(\pi/2 - \theta_1\right)}{\left\{\frac{\cos\theta_1}{(1 - \sin\theta_1)} + \frac{\cos\theta_2}{(1 + \sin\theta_2)}\right\}(1 - \sin\theta_1)} \qquad (10)$$

This is quite a small increase in h_{CRIT}. Due to jet spread, however, the orientation of the jet with respect to the intake is now less critical. Thus, viscous mixing effects, all of which are susceptible to theoretical analysis, are expected to account for the 25 per cent difference between the measured and the theoretical (inviscid flow) critical height.

THE INFLUENCE OF INTAKE SUCTION
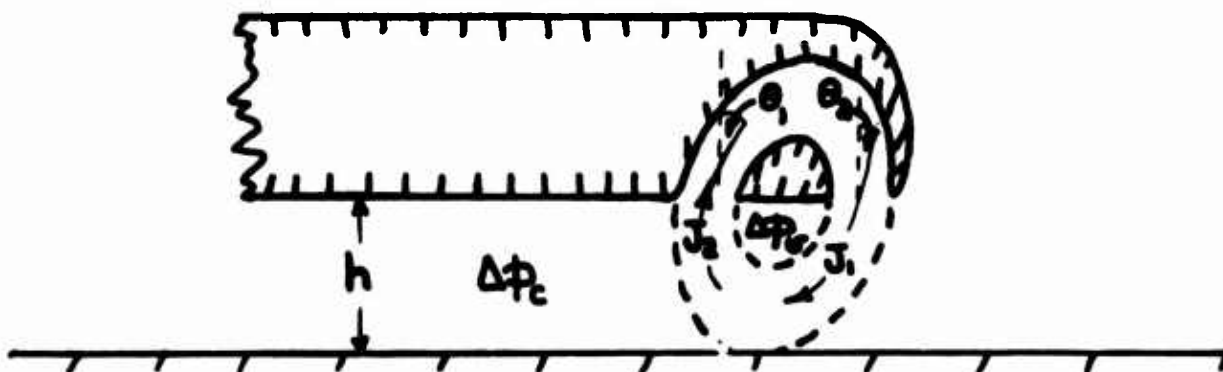
Figure 24. Conditions at Intake.

It is obvious from Figure 24 that the cavity pressure is given by

$$-\Delta p_U \, h\, C = J_1\, (1 - \sin\theta_1) \qquad (11)$$

Previously published investigations (References 11, 12, and 13) have then proceeded to calculate cushion pressure from the equality

$$\left(\Delta p_C - \Delta p_U\right)h\, C = J_2\,(1 + \sin\theta_2) + (J_1 - J_2)$$

$$= J_1 + J_2\, \sin\theta_2 \qquad (12)$$

36

whence $\qquad \Delta P_c = \dfrac{J_1}{hC}\left\{\sin\theta_1 + \dfrac{J_2}{J_1}\sin\theta_2\right\}$ (13)

- and both J_1 and J_2 can be calculated knowing the cushion and cavity pressures.

CALCULATION OF POWER REQUIRED

From Appendix IV, the power required is equal to

$$A_J U_J \Delta H = \frac{\dot{m}_J}{\rho}\,\Delta H$$ (14)

- where ΔH is the total pressure rise imposed upon the airflow. For an annular jet machine, of course, $\Delta H = \Delta P_J$. .

The total pressure losses thought to be involved in recirculation are sketched in Figure 25.
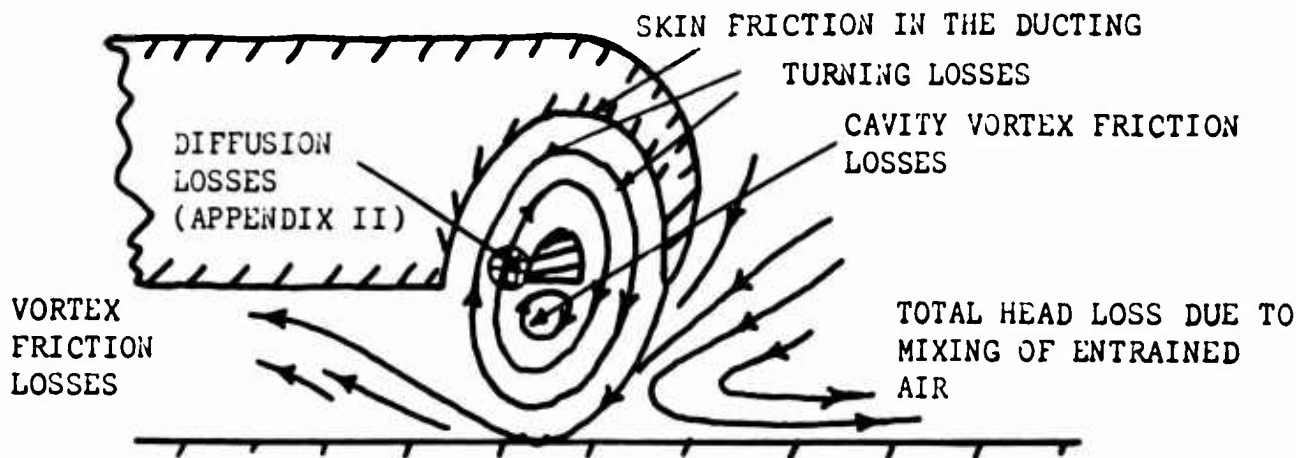
Figure 25.   Power Loss Incurred in Recirculation.

For the purposes of this report we shall consider only two of these power loss mechanisms, using a very approximate analysis.

Mixing Loss

Neglecting the cavity vortex loss, mixing losses can be considered to apply only to the outside of the recirculating flow field. In the full vortex condition the radius of the periphery subject to ambient pressure is, from Reference 11,

$$r_1 = \frac{h}{1 - \cos(90 - \theta_1)} = \frac{h}{1 - \sin\theta_1}$$
$$r_2 = \frac{h}{1 + \sin\theta_2}$$
$$\tag{15}$$

Thus, the peripheries are

$$x_1 = \left(\frac{\pi}{2} - \theta_1\right) r_1 = \frac{\left(\frac{\pi}{2} - \theta_1\right) h}{1 - \sin\theta_1}$$

and

$$x_2 = \left(\frac{\pi}{2} + \theta_2\right) r_2 = \frac{\left(\frac{\pi}{2} + \theta_2\right) h}{1 + \sin\theta_2}$$
$$\tag{16}$$

In the ambient mixing zone, the dynamic head at the nozzle is

$$q_o = \frac{1}{2}\rho v_j^2 = \Delta P_j$$

From Reference 10, and assuming mixing on one side only, the dynamic head loss in the ambient zone is given by

$$\Delta q_1 = q_o - q_{x_1} = q_o\left\{1 - \left(\frac{\delta\dot{m}_o}{\delta m}\right)^2\right\} \tag{17}$$

or

$$\frac{\Delta H_1}{\Delta P_j} = 1 - \left(\frac{\delta\dot{m}_o}{\delta m}\right)^2 \tag{18}$$

where

$$\frac{\delta m}{\delta\dot{m}_o} = 1 + 0.04\frac{x}{t}$$

$$= 1 + \frac{0.04\left(\frac{\pi}{2} - \theta_1\right)\left(h/t\right)}{1 - \sin\theta_1} \tag{19}$$

The dynamic head loss in the cushion zone can be calculated in the same way. However, the entrainment function is here much less certain, because of cushion vorticity, and its effect is less because of the higher static pressure.

38

The ambient zone pressure loss is plotted in Figure 26 for the two-dimensional Martin model No. 1, using both the half-entrainment function of equation (19) and the full entrainment function

$$\frac{\delta \dot{m}}{\delta \dot{m}_o} = 1 + 0.08 \frac{x}{t} \tag{20}$$

It is seen that the experimentally measured losses are significantly higher than the theoretical calculations. Thus, this comparison serves only to show that the theoretical treatment gives results of the right order of magnitude and tends to underestimate rather than overestimate the viscous mixing pressure loss. It is obvious that more detailed experimental studies are required in this area, in parallel with more detailed theoretical studies.

Turning Losses

Duct losses involved in turning a corner are usually expressed as a function of the local dynamic head. That is,

$$\Delta H_T = K_T \frac{1}{2} \rho v^2 = K_T \frac{1}{2} \rho \left(\frac{\dot{m}}{\rho A}\right)^2$$

$$= \frac{K_T}{2\rho} \left(\frac{\dot{m}}{A}\right)^2 \tag{21}$$

From Reference 11, the mass flow is

$$\frac{\dot{m}_J}{A_J} = \sqrt{2\rho \Delta P_J} \frac{(e^{x_1} - 1)}{x_1} \tag{22}$$

Thus

$$\frac{\Delta H_T}{\Delta P_J} = K_T \frac{(e^{x_1} - 1)}{x_1} \tag{23}$$

Note that: $\quad \dfrac{\Delta H_T}{\Delta P_J} \rightarrow K_T \quad \text{as} \quad x_1 \rightarrow 0$

This is plotted in Figure 27 for $K_T = 0.2$, a figure representing good practice for a 180° bend, together with the half-entrainment mixing loss. In comparison with the annular jet, which has a loss ratio of unity, it is evident that a good recirculation system could have about half the system losses at normal operating heights.

39
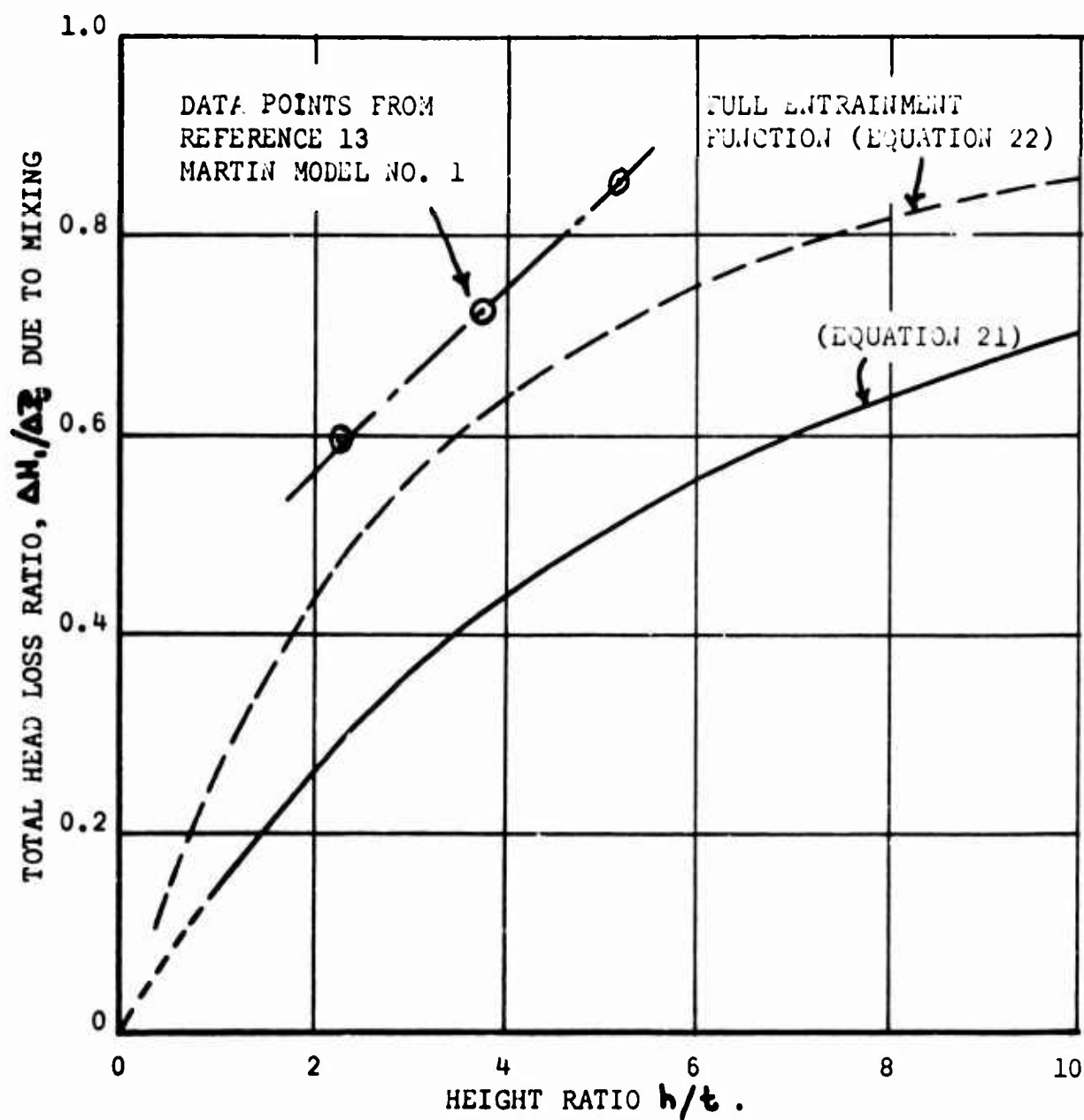
Figure 26. Comparison Between Theoretical and Experimental Entrainment Losses.

ANNULAR JET LOSS RATIO
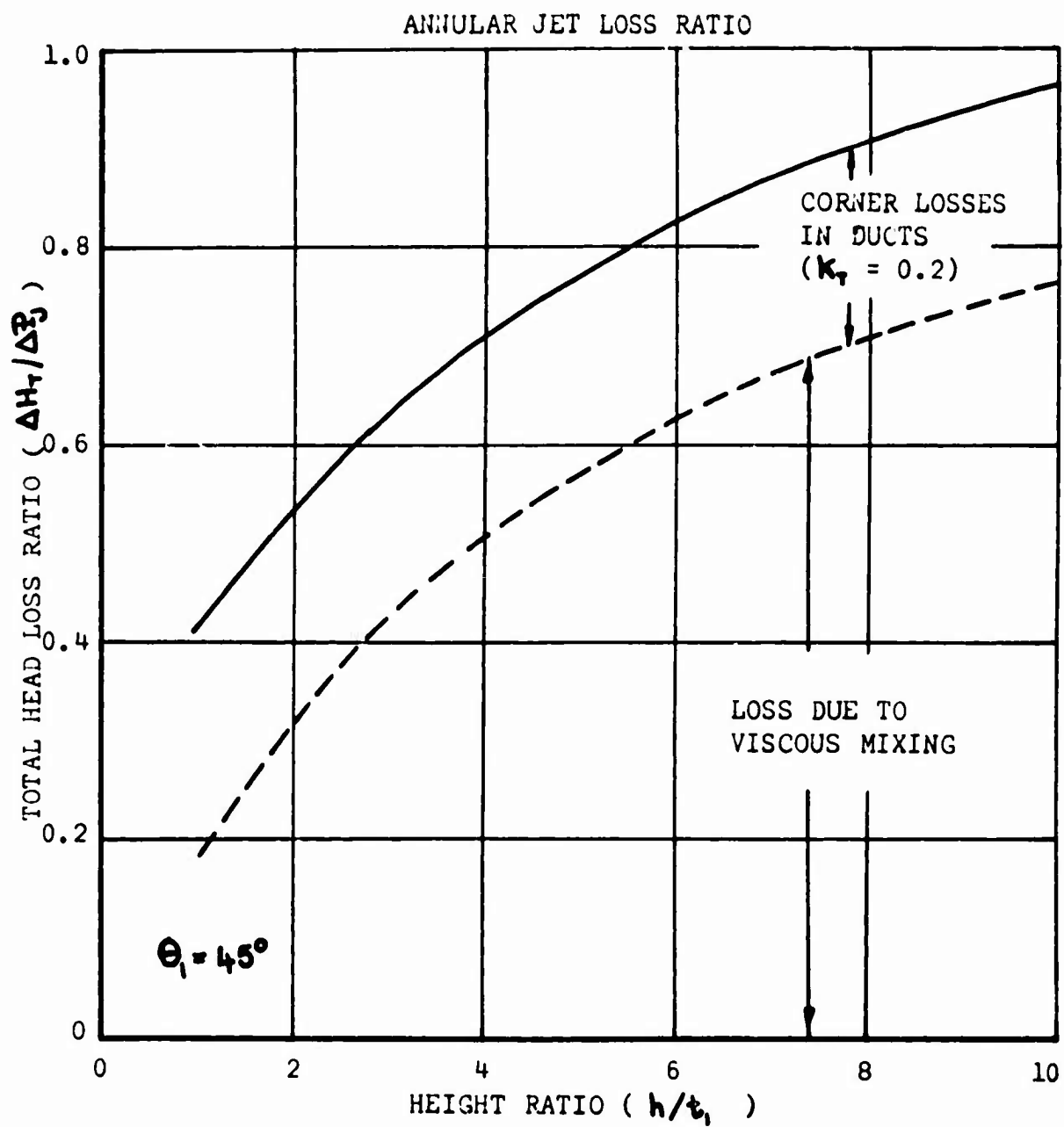
Figure 27. Losses Incurred In Recirculation Flow.
(Mixing and Turning Losses Only).

Expressing the ideal power required as a function of the cushion pressure,

$$\frac{E_j}{A_j \, \Delta P_c \sqrt{\frac{2\Delta P_c}{\rho}}} = \frac{(e^{x_1}-1)(\Delta H_1/\Delta P_j)}{x_1\left[\frac{\sin\theta}{1-\sin\theta_1}(e^{2x_1}-1)\right]^{3/2}} \qquad (24)$$

For a conventional annular jet, the relevant equation is

$$\frac{E_j}{A_j \, \Delta P_c \sqrt{\frac{2\Delta P_c}{\rho}}} = \frac{(1-e^{-x})}{x(1-e^{-2x})^{3/2}} \qquad (25)$$

Equations (24) and (25) are plotted in Figure 28, and it is evident that the power requirement for recirculation is substantially greater than for an annular jet at the same cushion pressure, and with the same jet exit area A_j , even with the low pressure loss estimates used. Since a recirculation machine requires a significantly higher cushion pressure in order to offset the negative lift forces acting in the cavity region, this simple analysis would seem to indicate that recirculation requires substantially more power than an annular jet.

CORNER EFFECTS

It has been postulated that a right-angled corner may cause a loss in performance because of a reduction in local jet velocity (a "hole") at the junction of the two jet sheets.

This possibility was investigated experimentally, using the corner test rig illustrated in Figures 29 and 30. The results are plotted in Figures 31 and 32 for annular jet and recirculation configurations respectively. It is obvious that for both cases the cushion pressure is substantially the same in the corner rig but that detailed variations do occur relative to the other test rigs; the reason for this is not hard to see.

In equating horizontal force to momentum, we write $\Delta P_c \, h \mathcal{C}$ for the cushion pressure force. In the two-dimensional case the periphery $\mathcal{C}$ is the length of the jet, and the possibility of ambiguity does not arise. In the three-dimensional case, however, the effective periphery is usually different to the geometric periphery of the nozzle $\mathcal{C}$; it might be represented by B - B in Figure 33, for example, while the geometric periphery is represented by A - A.

42
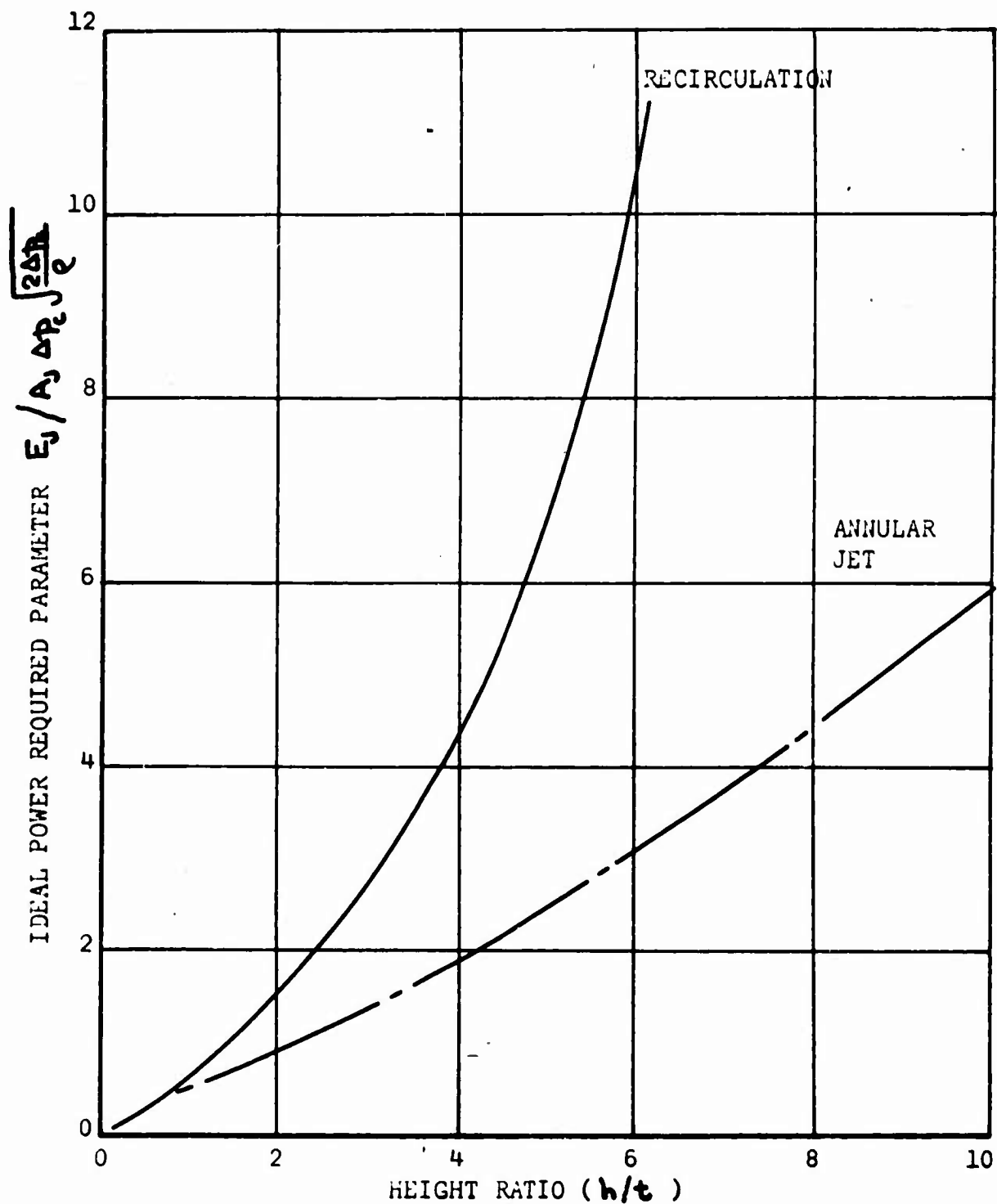
Figure 28.   Comparison of Power Requirements
For Annular Jet and Recirculation Systems.

43

FAN EXITS

RECIRCULATION

STATIC PRESSURE TUBE
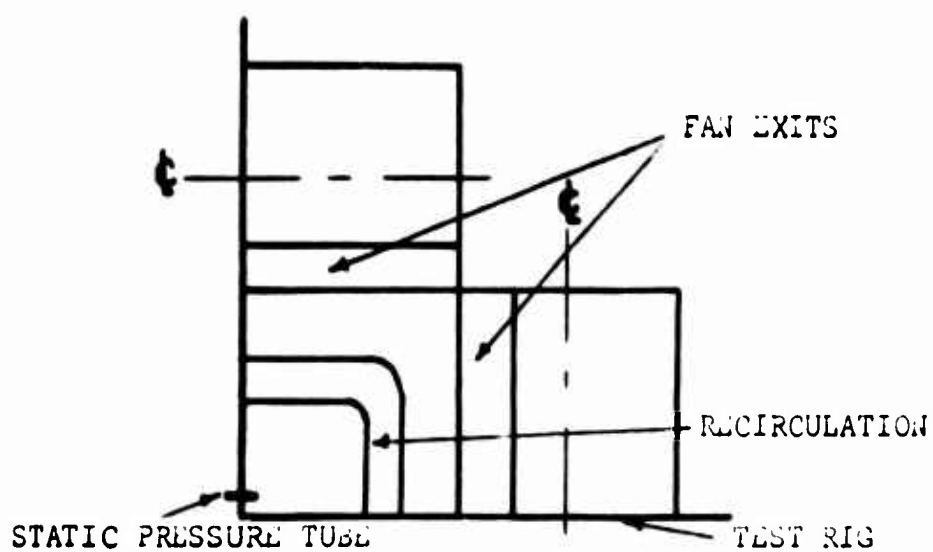
TEST RIG

Figure 29. Sketch of Corner Rig Test Setup - Plan View.
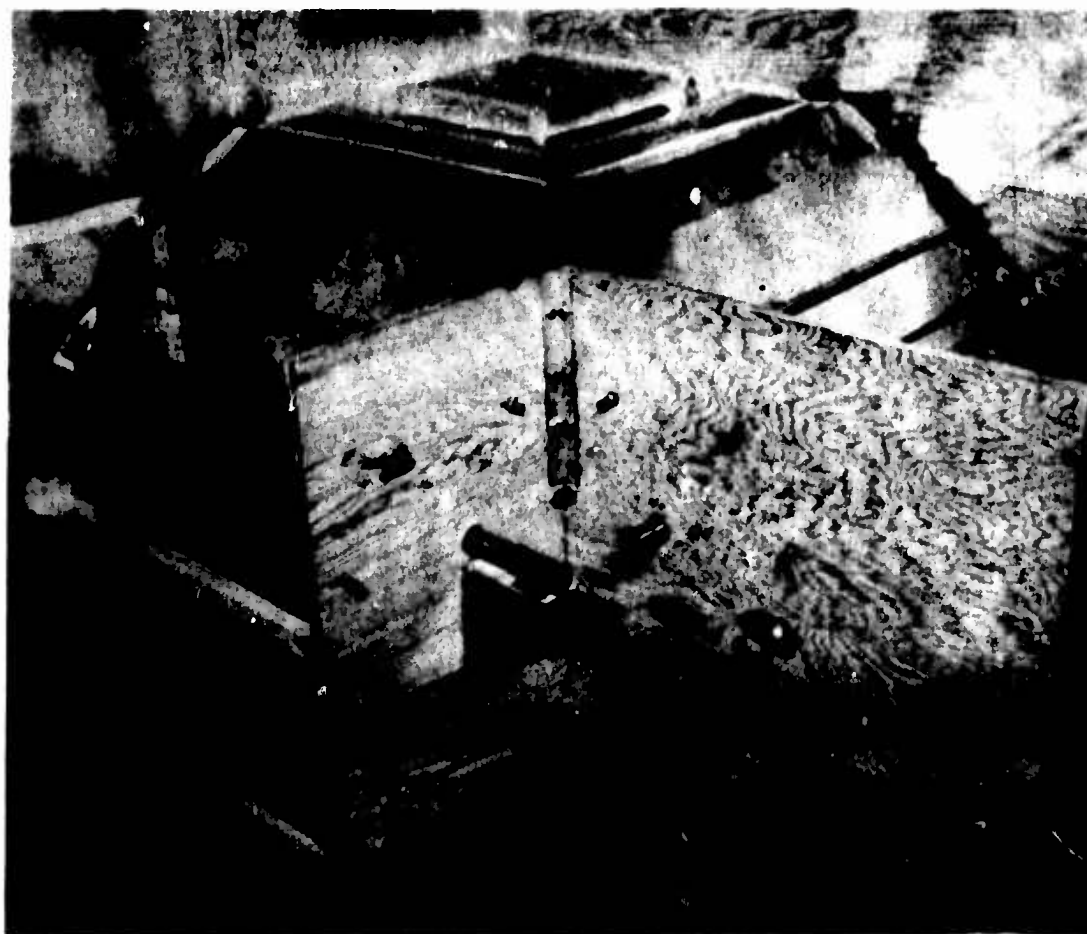
Figure 30. Two Frost Fans Mounted in the Corner
Test Rig (Recirculation); Ground Plane Removed.

44
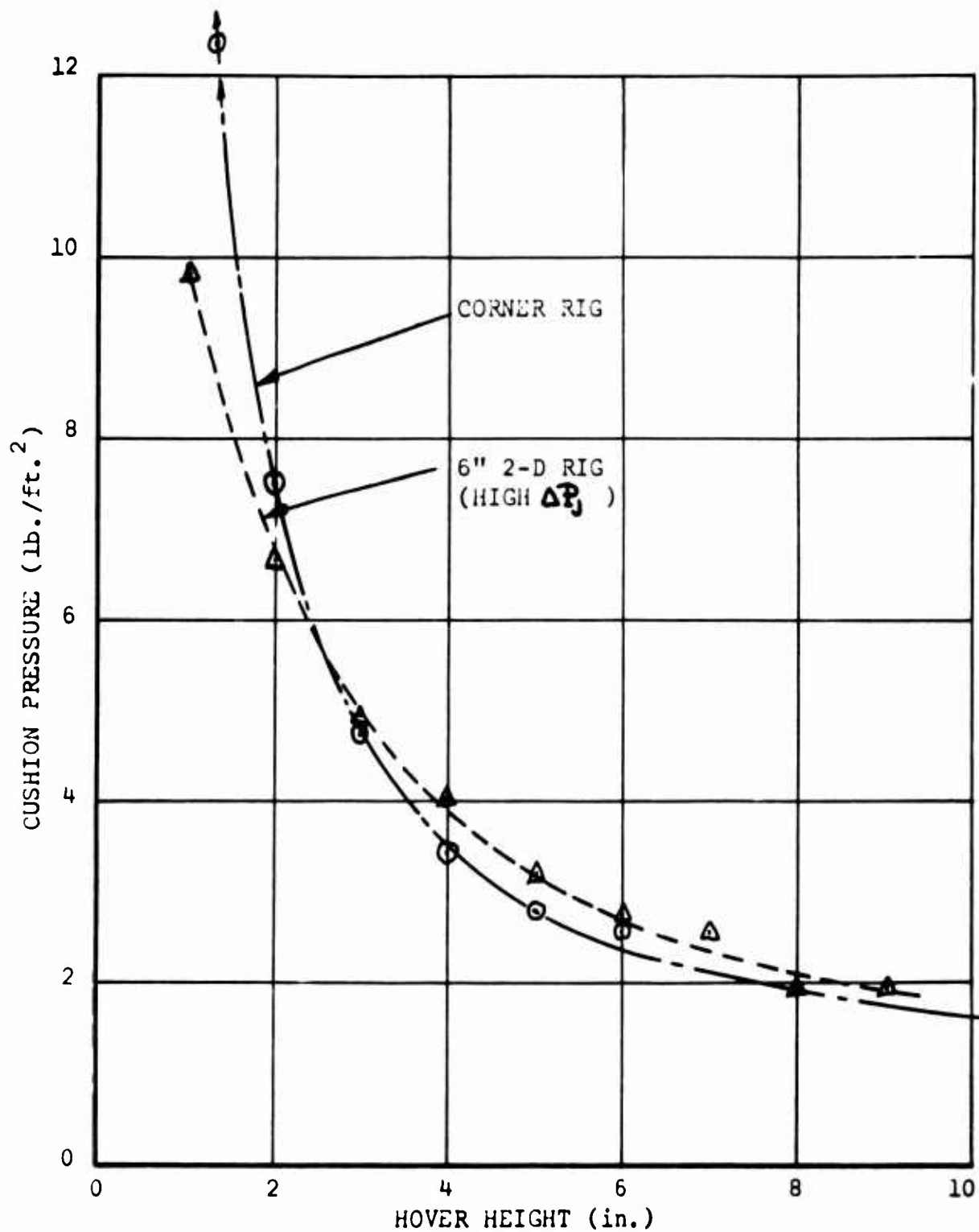
Figure 31. Cushion Pressure As A Function
Of Hover Height - Annular Jet (1000 R.P.M.).
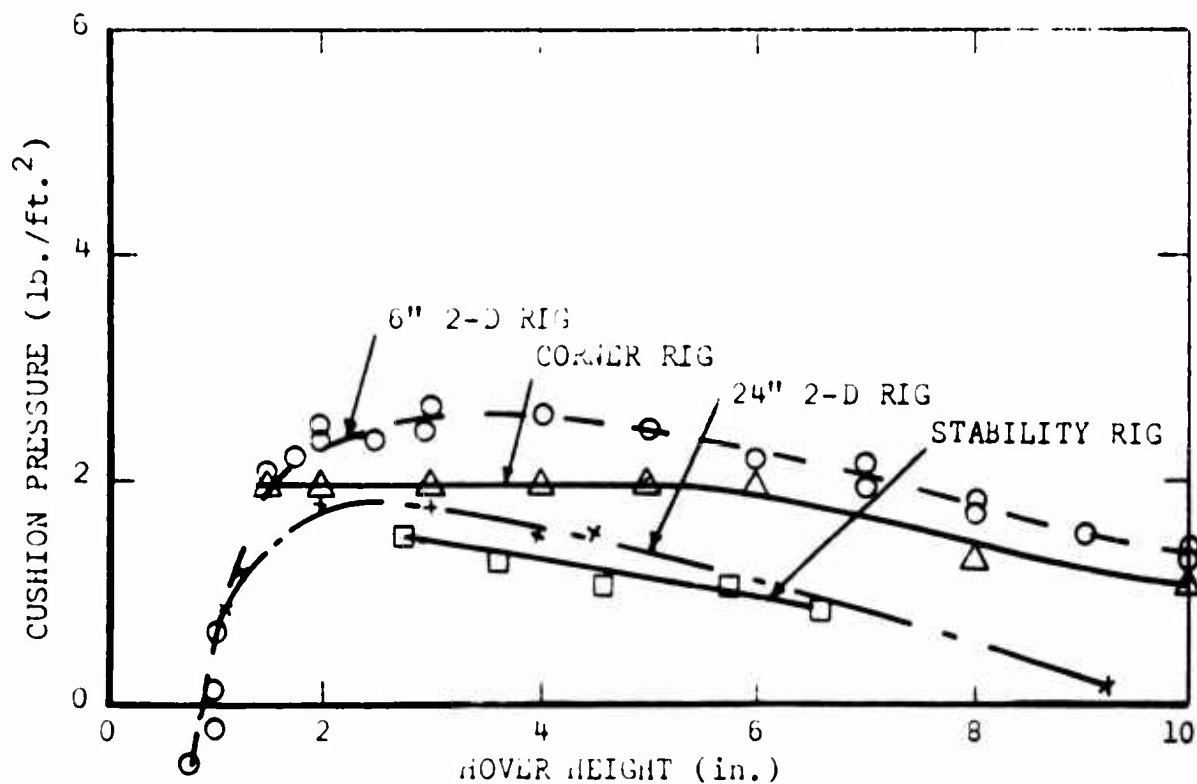
Figure 32.   Cushion Pressure As A Function of Hover Height.
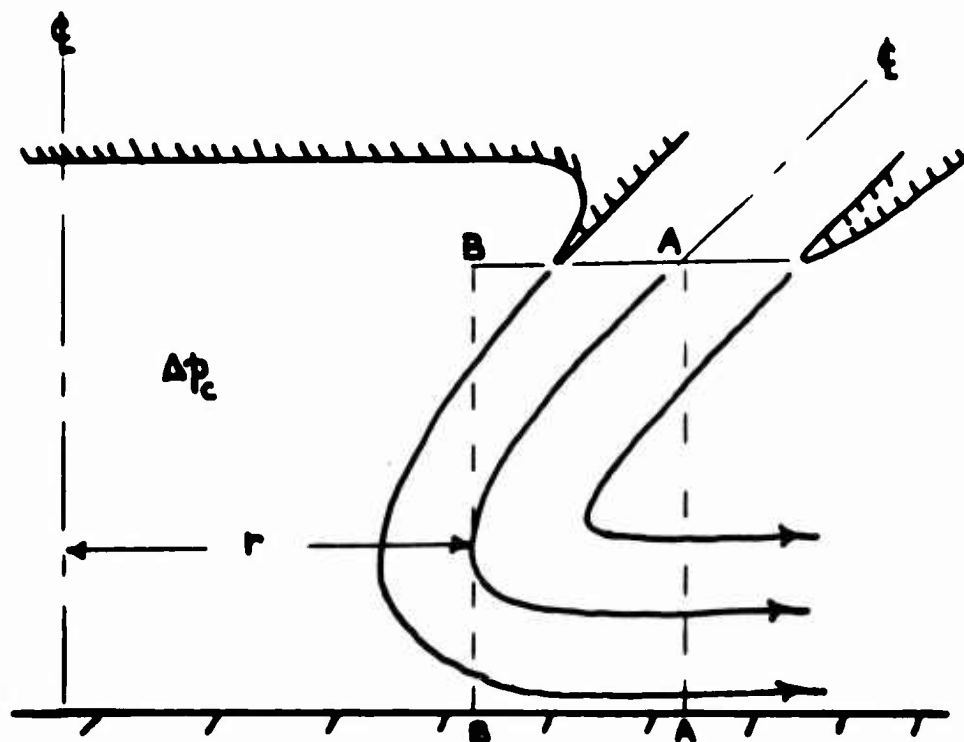
Figure 33.   Effective Periphery.

This problem is perhaps better illustrated by the three-dimensional jet sheet sketched in Figure 34. We can see quite clearly that although the cushion pressure force is $\Delta p_c h C$, our calculations can be considerably in error (depending upon the jet thickness and angle) if we take C to be the geometric periphery of the nozzle $\mathcal{L}$. They will be more accurate if we estimate a "mean" jet periphery for the particular configuration under consideration. Finally, maximum accuracy will be achieved if we develop and solve the exact layered-jet equations for a three-dimensional jet, since in this case the correct value is assigned to the incremental force acting upon each jet element.
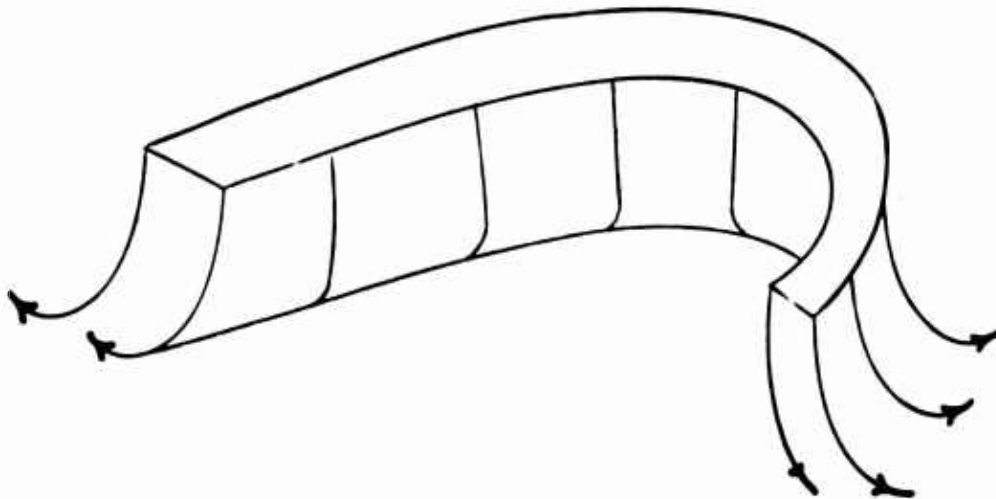
Figure 34.   Three-Dimensional Jet.

Without undertaking these calculations (which would be a major task requiring considerable funding in some future program), it is obvious that the effective periphery of two Frost Fans in a corner test rig must be less than for the equivalent two-dimensional case, resulting in higher cushion pressures. Needless to say, the arguments developed are equally applicable to the case of recirculating flow. These trends can be seen in Figures 31 and 32 when the characteristics of the various test rigs are known.

In Figure 31 the corner rig fans were each 24 inches long, and the total momentum flux fell off towards the ends, as has always been true with the prototype Frost Fan. The 6-inch two-dimensional rig utilizes only the center portion of the exhaust, so that to be directly comparable, these points should be multiplied by the flow factor of 0.85. When this is done the two-dimensional cushion pressure is always less than the corner rig pressure, the difference being greater at low values of height-to-thickness.

The same conclusions apply to the recirculation case, but we cannot use the same method of correcting the 6-inch rig data. Comparing the 24-inch corner rig data with the 24-inch two-dimensional measurements, we see that the latter gives a lower cushion pressure at all heights, although the difference is negligible at the critical height. The stability rig cushion pressure is less than the value obtained with the 24-inch two-dimensional rig (by a relatively small amount) because of leakage past the floating ground plane. We therefore conclude that there is no evidence for the so-called "corner loss" effect.

HEAVE STABILITY

From Reference 3, the equation of motion in heave, for an annular jet configuration, is

$$\ddot{h} - \sigma\, C_j\, \frac{d\,\Delta P_c}{d\dot{h}}\, \frac{dh}{dt} - \sigma\, C_j\, \frac{d\,\Delta P_c}{dh}\, \Delta h = 0 \qquad (26)$$

For the recirculation case we have no postulation for damping available. For an annular jet the concepts of "underfed" and "overfed" operation, introduced by Tulin, gave good agreement with the experimental results reported in Reference 3. Although these postulates might be extended to the case of recirculation, the absence of any experimental results achieved with the Frost Fan stability test rig (Figure 35) indicate that, in contrast to the annular jet case, the damping of heave motion is quite small.

Thus for constant momentum flux, and ignoring damping, equation (26) becomes

$$\ddot{h} - \sigma \left[\frac{d\,\Delta P}{dh}\right] \Delta h = 0 \qquad (27)$$

   - where the square brackets remind us that the cavity pressure must be included in the pressure lift term, and $\sigma = A/M$.

Now, from Appendix III,

$$\left. \begin{aligned} \Delta P_U &= -\frac{J_1}{hC}\left(1 - \sin\theta_1\right) \\[2mm] \Delta P_c &= \frac{J_1}{hC}\left(\sin\theta_1 + \frac{J_2}{J_1}\sin\theta_2\right) \end{aligned} \right\} \qquad (28)$$

48
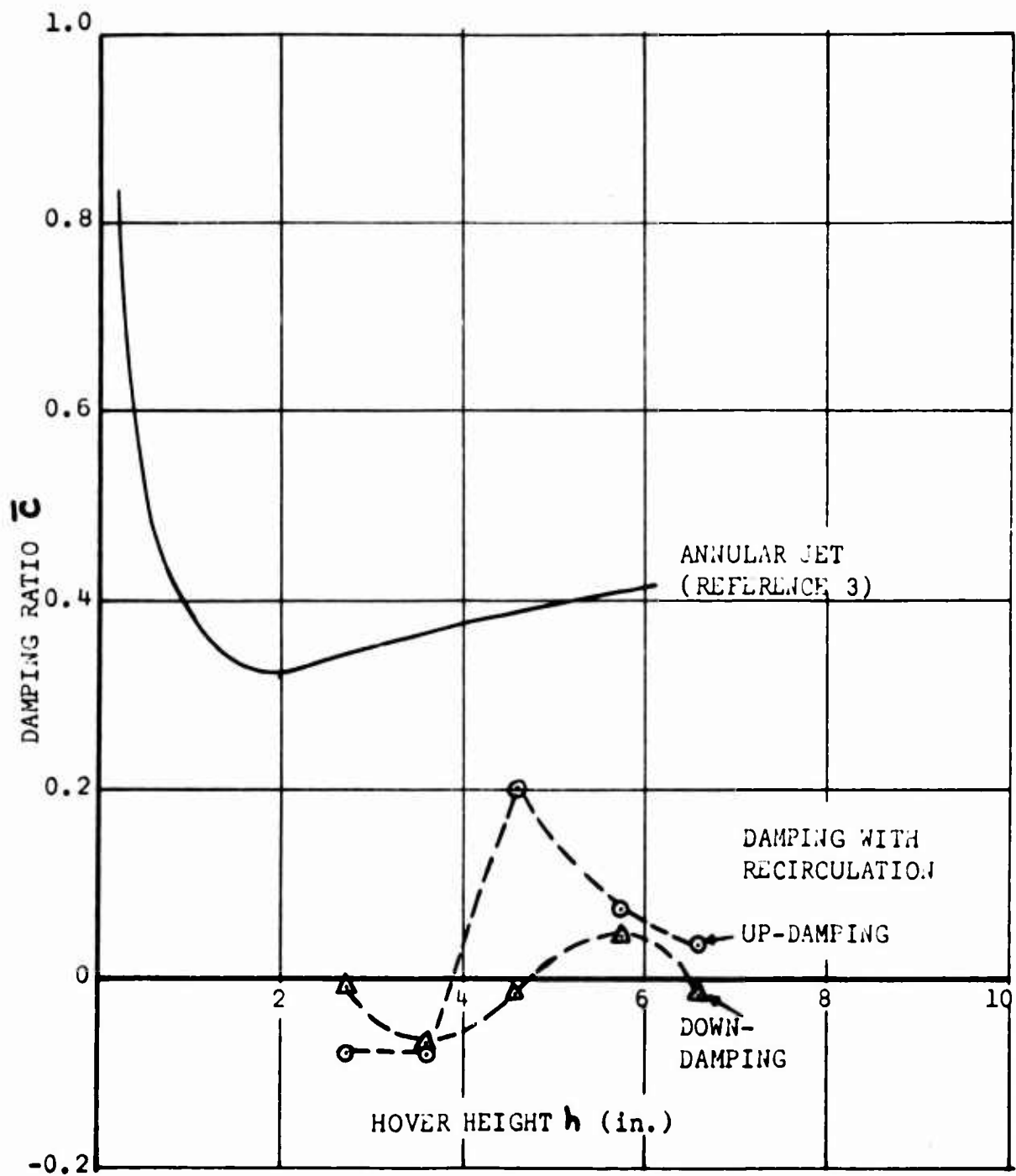
Figure 35. Heave Damping With Recirculation.

49

$$\frac{d\Delta P_r}{dh} = \frac{J_1}{h^2 C}\left(1 - \sin\theta_1\right)$$

$$\frac{d\Delta P_c}{dh} = -\frac{J_1}{h^2 C}\left(\sin\theta_1 + \frac{J_2}{J_1}\sin\theta_2\right)$$

(29)

(if J_2 is a constant)

Thus, equation (27) becomes

$$\ddot{h} + \frac{A_c}{M}\frac{J}{h^2 C}\left(\sin\theta_1 + \frac{J_2}{J_1}\sin\theta_2\right) - \frac{A_r}{M}\frac{J}{h^2 C}\left(1 - \sin\theta\right) = 0 \qquad (30)$$

The frequency of oscillation is therefore

$$\omega = \frac{1}{h}\sqrt{\frac{A_c}{M}\frac{J}{C}\left[\sin\theta_1 + \frac{J_2}{J_1}\sin\theta_2 - \frac{A_r}{A_c}\left(1 - \sin\theta_1\right)\right]} \qquad (31)$$

Note that $\omega > 0$ if

$$\sin\theta_1 > \frac{\frac{A_r}{A_c} - \frac{J_2}{J_1}\sin\theta_2}{\left(1 + \frac{A_r}{A_c}\right)} \qquad (32)$$

So long as equations (28) apply, then, we conclude that, with constant momentum flux, static stability at one hover height implies static stability at all hover heights. Static instability is restricted to heights below the critical value, where $d\Delta P_c/dh$ starts to increase above the value given by equation (29).

In the Frost Fan stability rig the cushion pressure is lower than the theoretical value, as shown in Figure 36, due to leakage and non-uniformity of the jet, and, at the lower heights, the onset of the Bernoulli flow regime effects. At the lower heights, the slope $d\Delta P_c/dh$ was significantly less than the theoretical value.

The heave frequencies measured are plotted in Figure 37, and it is seen that these are negative (static instability) below about 4-1/2-inch hover height.

50
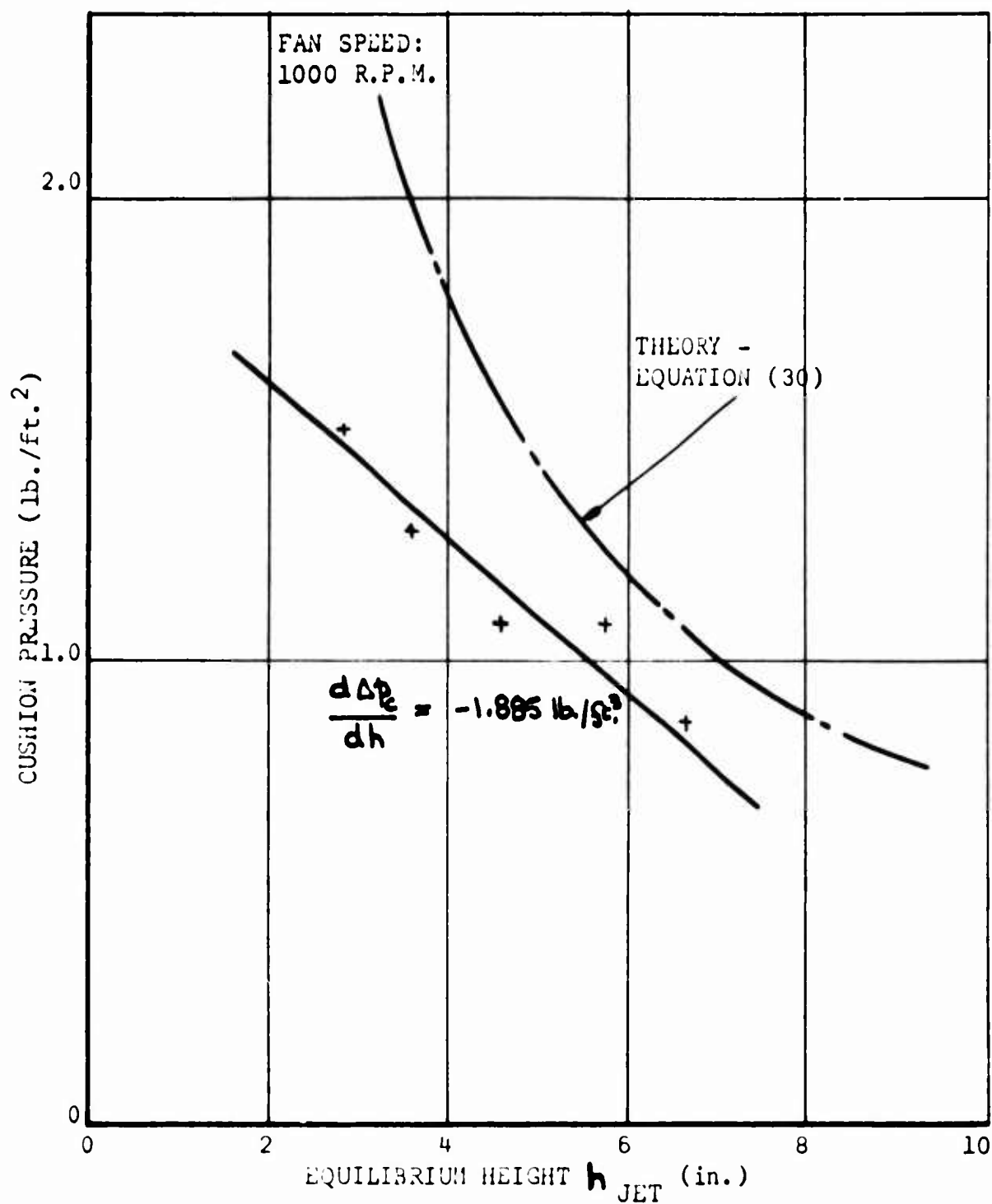
Figure 36. Variation of Cushion Pressure With
Height in Recirculation Stability Rig.
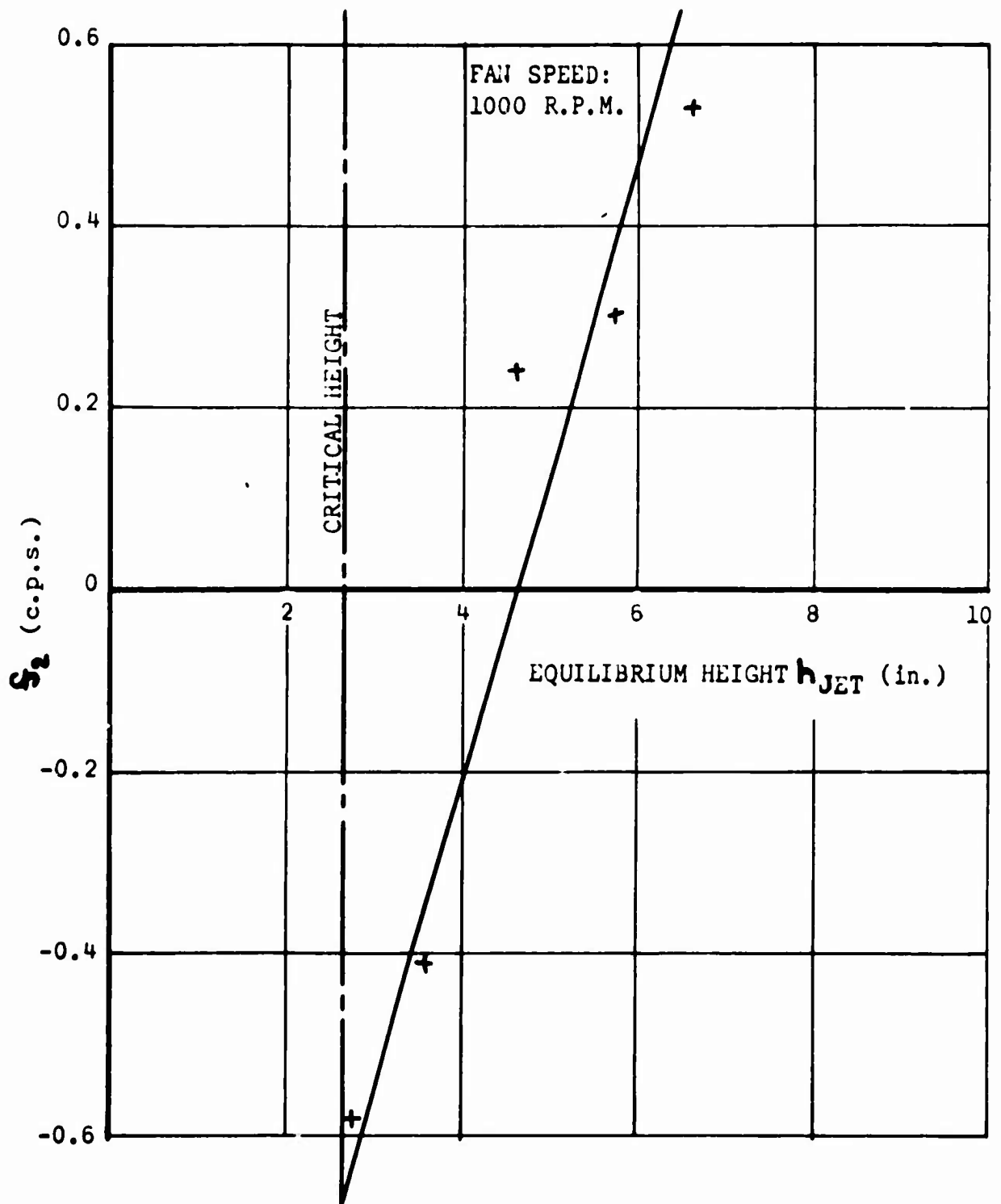
Figure 37. Heave Frequency Measured
With Recirculation Stability Rig.

THE INFLUENCE OF FLOW BLOCKAGE BY INSTRUMENTATION RAKES

A series of runs were made in the two-dimensional rig with and without
pitot-static rakes in the exhaust and inlet planes. As shown in Fig-
ures 38 and 39, as the true recirculation flow regime was entered, the
rakes caused sufficient change in the airflow patterns as to render
their readings of no value.
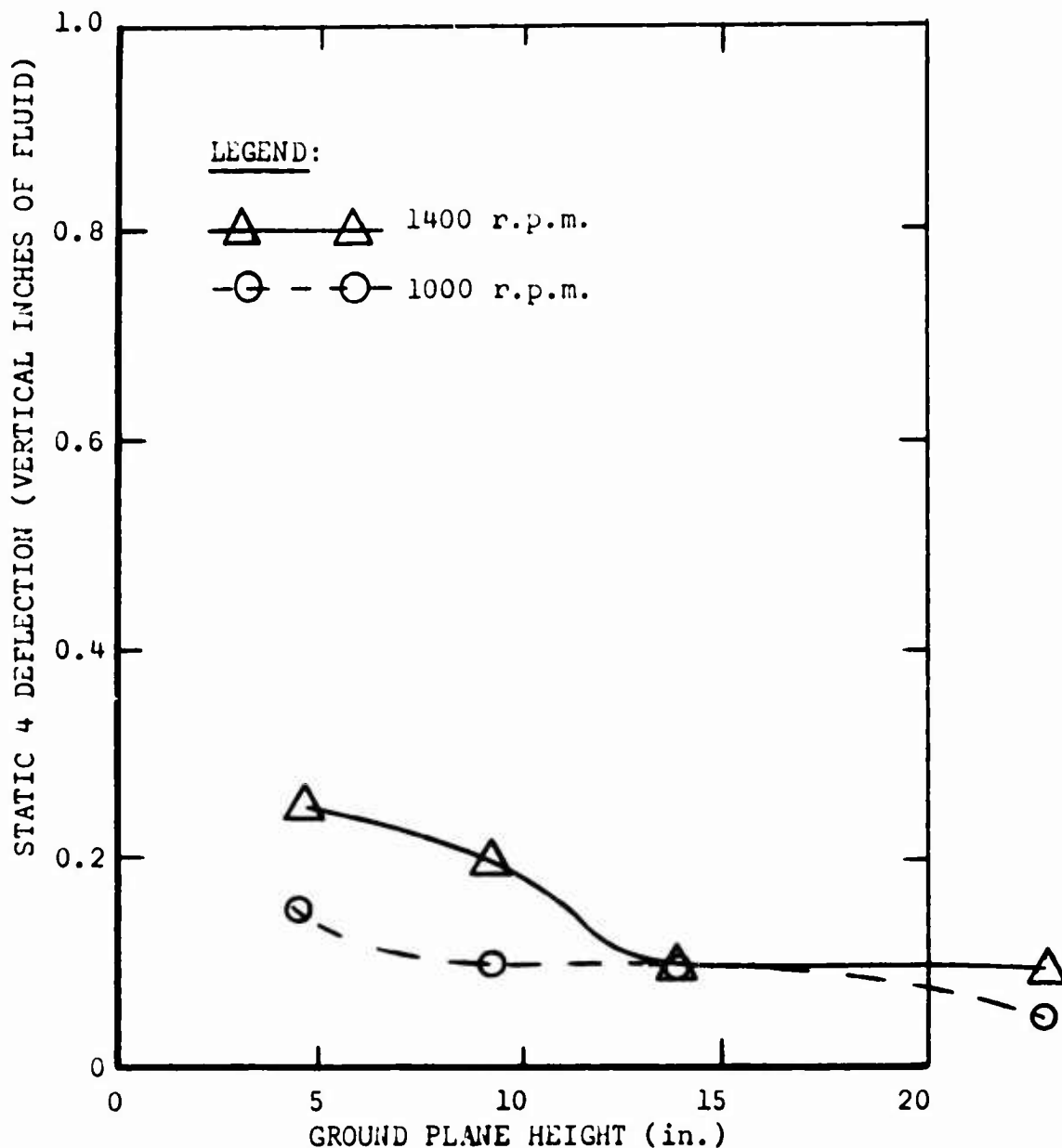
Figure 38. Recirculation Stability Rig; Two Rakes Installed.
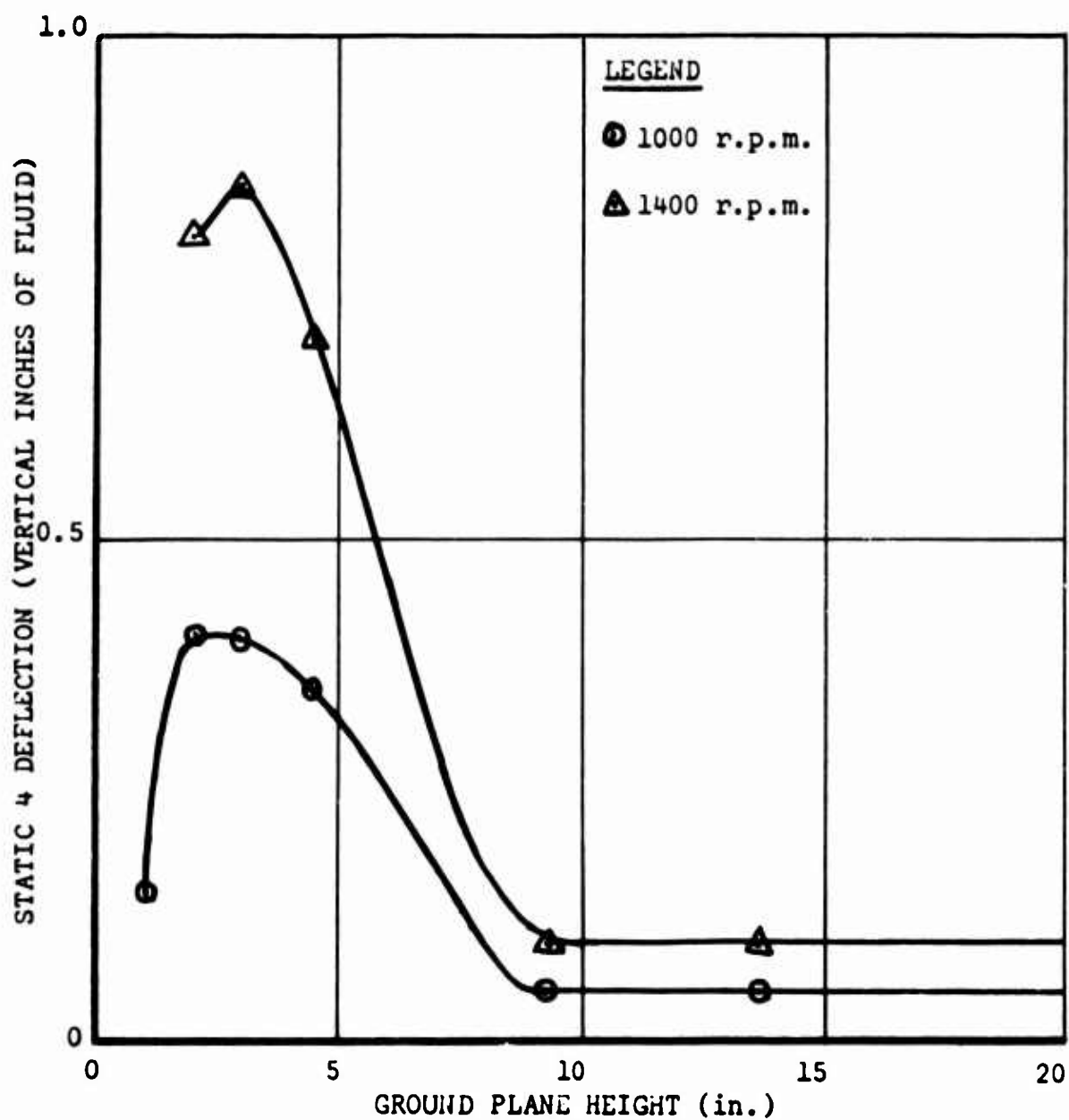
Figure 39. Recirculation Stability Rig; No Rakes Installed.

SECTION TWO

THE CROSSFLOW FAN

INTRODUCTION

The crossflow fan is a relatively unknown air moving device which, in common with other peripheral fan devices, offers hope of significant increases in overall system efficiency for GEM's by reason of the virtual elimination of duct losses, which in a conventional GEM may account for half the total power loss.

In this section, an elementary theory of the crossflow fan is developed. It is found that this theory gives an adequate description of observed fan performance, so far as air mass flow and its variation with back-pressure is concerned. However, the important details of fan exit losses and slip could not be resolved in the present program because no experimental observation of the internal flow field was possible. Although any one of a number of postulations could be made, it is felt that the analytical results of such a procedure would be of little value. Thus the shaft power required can only be calculated by assuming an overall efficiency.

The experimental results discussed in this section were made possible by the kindness of the Torrington Manufacturing Company in loaning one of its prototype crossflow fans, which was constructed under license from the European patent holder.

CROSSFLOW FAN GEOMETRY

A typical crossflow design and its essential geometry is shown schematically in Figure 40, and the airflow relative to the fan blades is shown in Figure 41. As shown in Figure 41, the intake airflow relative to the blade is similar to the picture for an axial flow fan, and air is accordingly forced into the center of the rotor, with a marked swirl velocity component.

At the exit the air passes out of the rotor with only a small angle of attack relative to the blades, so that they offer little impediment to it. Apart from the total head rise which occurs as the air passes through the blades by way of the intake, the vortex rotation induced in the center of the fan gives rise to a pressure gradient (as in a C.F. blower) which increases the total head of the exit airflow.
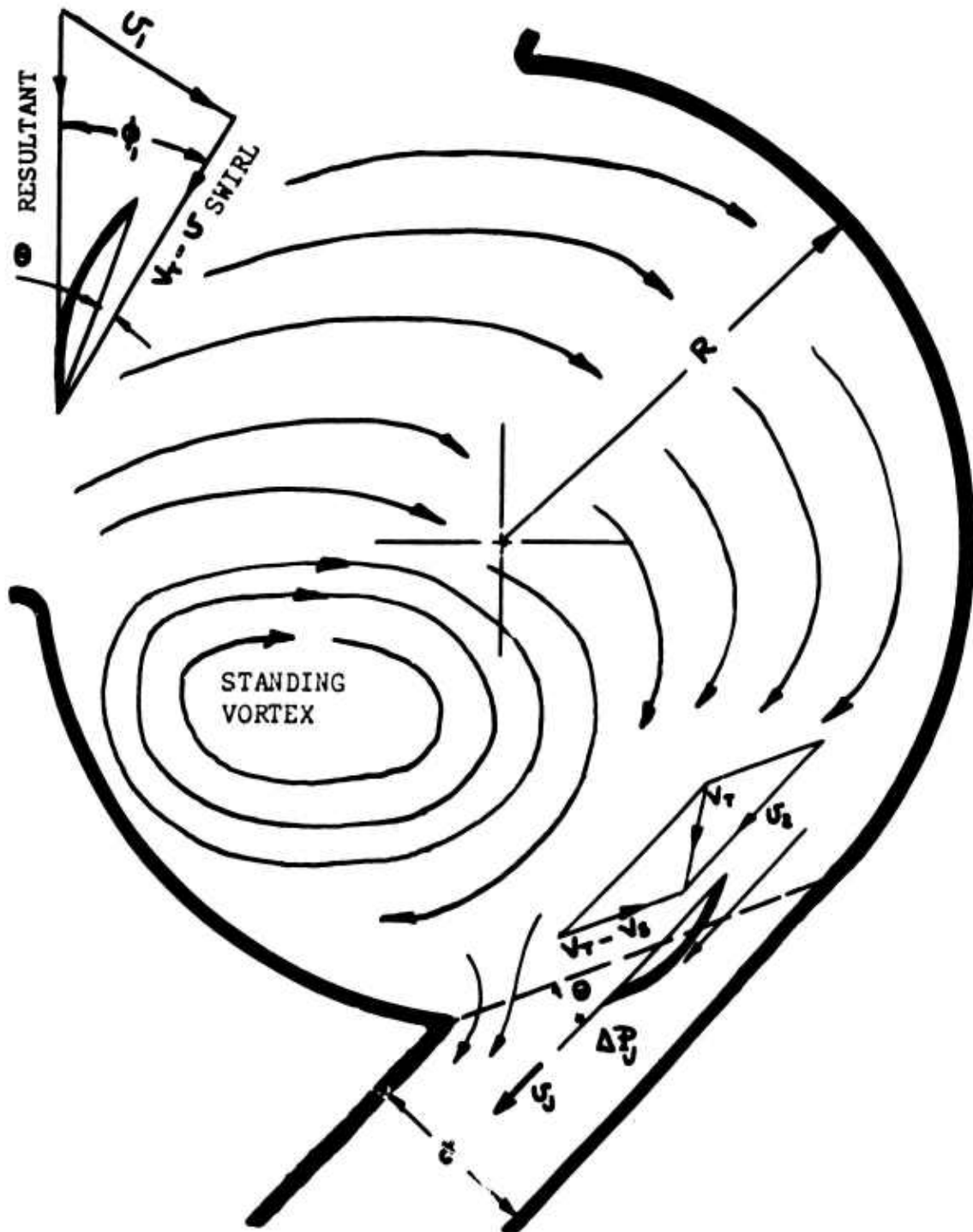
Figure 40. Crossflow Fan Geometry.
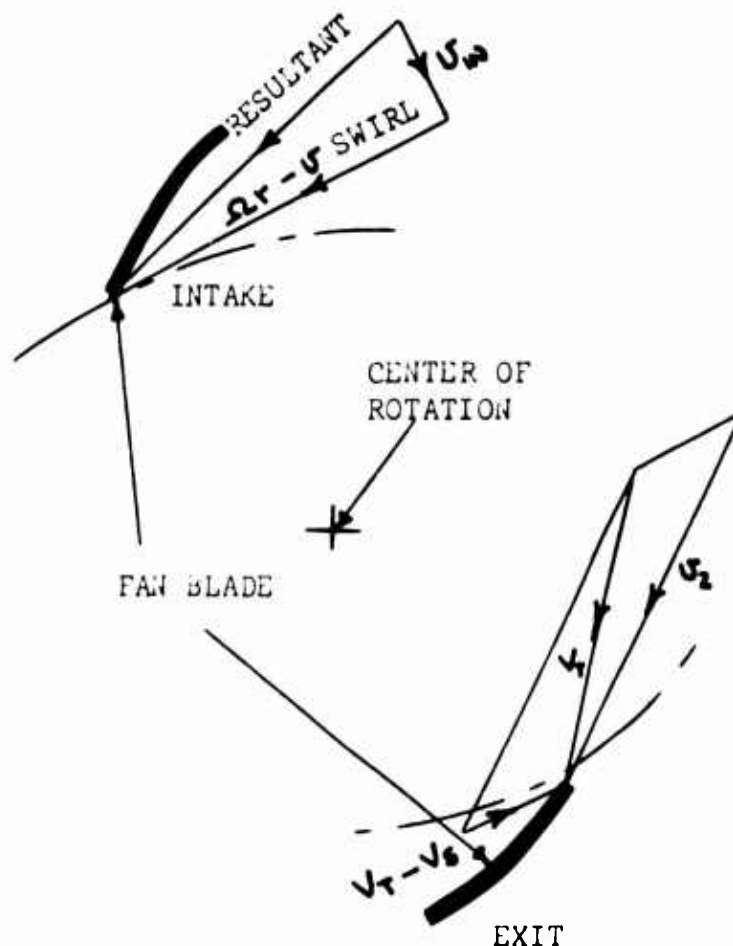
Figure 41.   Airflow Relative to
Transverse Flow Fan Blades.

A limitation of the crossflow fan is that its blade sections must be
double-ended since air flows over them in both directions. This means
that the section drag coefficient will be fairly high at full scale
Reynold's numbers, and that $C_{L_{MAX}}$ will be quite low.

A second problem is the bending moment induced in the blades by centri-
fugal force, which will prevent high tip speeds from being achieved.
To some extent this particular limitation is alleviated by the high
volumetric flow coefficients which can be achieved, however, these be-
ing as high as $\dot{m}_j / \rho A_j V_T$ = 1.4, which is almost as high as the
Frost Fan configuration.

At first sight, therefore, the crossflow fan seems to possess a number of limitations, but the concept is sufficiently novel to merit at least a preliminary theoretical and experimental investigation, if only to serve as the basis for comparison with the Frost Fan concept currently under development.

In the work which follows, therefore, we shall examine some basic theoretical considerations which influence the performance of a crossflow fan. The investigation will be carried out at a very elementary level because there is one important unknown - the flow pattern inside the fan cylinder - which cannot be accurately calculated at the present time. For this reason we must rely heavily on experimental observations.

In Figure 42 the nondimensional volume flow of a Torrington fan is plotted as a function of the jet static back-pressure parameter $\Delta P_J / q_T$. "Static efficiencies" as high as 60 per cent are reported in Reference 18 for this type of fan (although Reference 20 quotes a maximum of only 38 per cent) and from Appendix VI, the actual efficiency will be somewhat higher than these figures.

The values of the back-pressure parameter $\Delta P_J / q_T$ which can be handled by a crossflow fan are given in Reference 18 as 1.0 - 5.5, with a corresponding volumetric flow factor range of $\dot{m}_J / \rho A_J V_T = .05$ to 1.4.

THEORY

A crossflow fan has two distinct flow mechanisms for raising the pressure of the air passed through it, so that it may be regarded, technically, as a mixed flow device.

At the inlet the blades have a positive angle of attack with respect to the local airflow and, hence, pressurize the air in the same way as an axial fan.

As the air passes through the rotor exit, its already large rotational velocity is further increased, the fan blades having the same effect as the blades of a C.F. impeller. This further increases its total head.

TORRINGTON DATA

3100 r.p.m.

STD - 200-700
CROSSFLOW
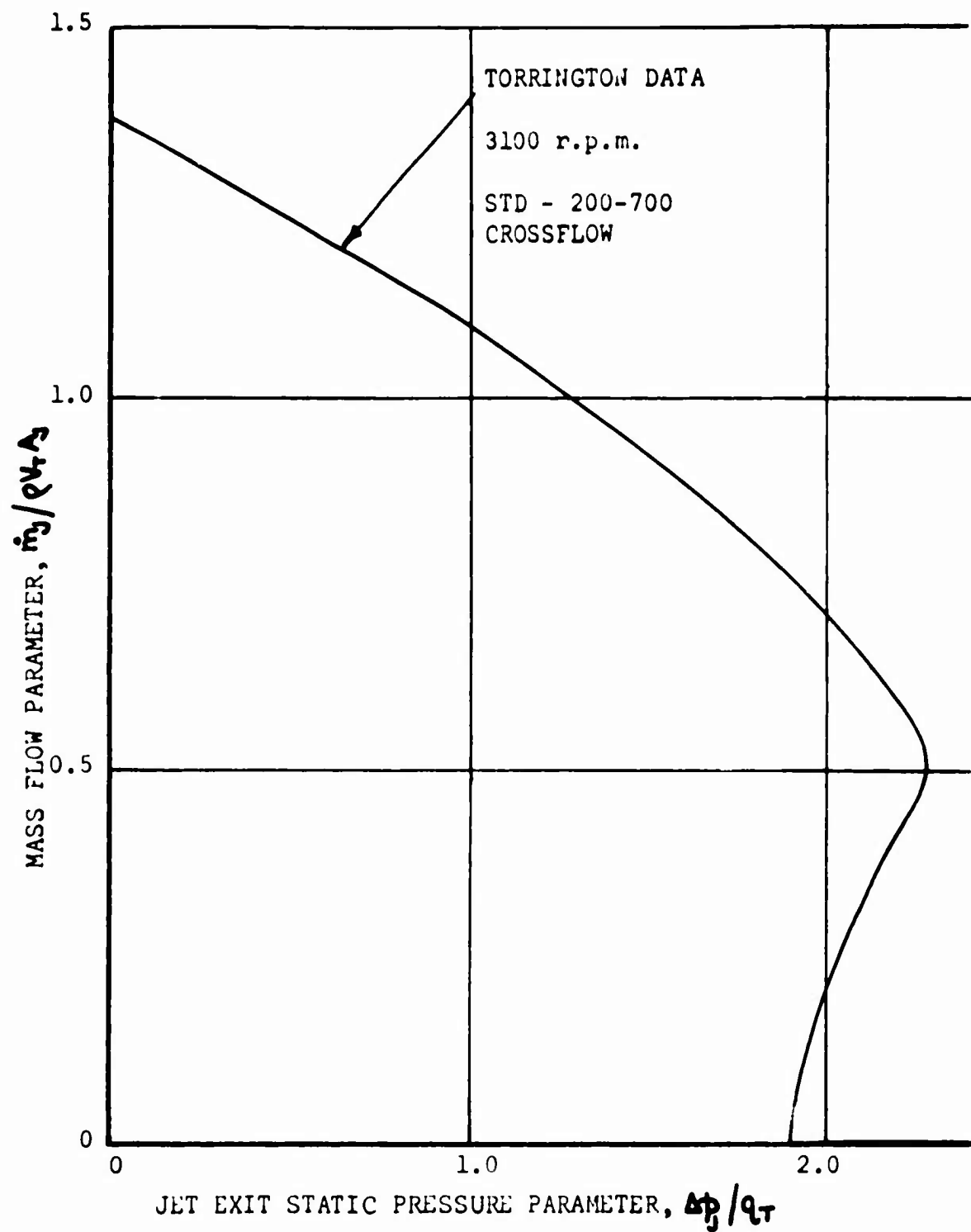
Figure 42. Variation of Mass Flow Parameter
With Jet Back-Pressure Parameter.

59

Inlet Flow Conditions

The reactive pressure rise follows from the geometry of Figure 43.
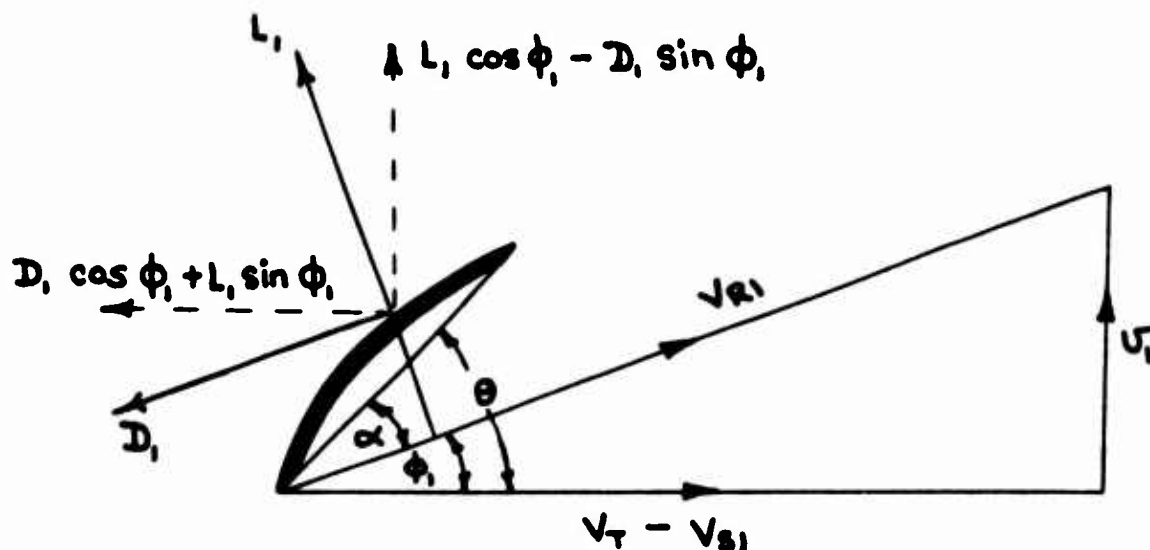
Figure 43. Inlet Flow Conditions.

If (bc) is the blade area, its lift and drag are given by

$$L_1 = C_L \frac{1}{2} \rho \, (bc) \left[(V_T - V_{S1})^2 + U_1^2 \right] \tag{33}$$

$$D_1 = C_D \frac{1}{2} \rho \, (bc) \left[(V_T - V_{S1})^2 + U_1^2 \right] \tag{34}$$

If we neglect the inlet swirl velocity component V_{S1} , we have the relationships

$$\left. \begin{array}{l} \sin \phi_1 = \dfrac{U_1}{\sqrt{V_T^2 + U_1^2}} \\[4mm] \cos \phi_1 = \dfrac{V_T}{\sqrt{V_T^2 + U_1^2}} \end{array} \right\} \tag{35}$$

If the blades are far apart, for small angles, $C_L = a \alpha = a(\theta - \phi)$.

60

If the angle α is large or if the blades are close enough for cascade effects to be important

$$C_L = \mathfrak{F}(\alpha) \tag{36}$$

$$L_1 \cos\phi_1 - D_1 \sin\phi_1 = \tfrac{1}{2}\rho V_T^2 (bc)\, c_i \sqrt{1+\left(\tfrac{V_J}{V_T}\right)^2}\left\{1-\tfrac{V_J}{V_T}\tfrac{C_D}{C_L}\right\} \tag{37}$$

We can generally regard C_D / C_L as being negligible in relation to unity, so that equation (37) may be simplified by removal of this term.

Now the lift component normal to the local surface of the fan blade datum is equal to the rise in total pressure multiplied by the reflective blade area. Specifically, if

$$\psi = \frac{\text{intake circumference}}{2\pi R} \tag{38}$$

$$n = \text{ total number of blades,}$$

then $\psi_1 n\left(L_1\cos\phi_1 - D_1\sin\phi_1\right) = \Delta P_1 A_1$

$$= \Delta P_1 \psi_1\, 2\pi R\, b \tag{39}$$

Substituting equation (37) and defining a blade solidity parameter,

$$\sigma = \frac{nC}{2\pi R} \tag{40}$$

$$\frac{\Delta P_1}{q_T} = \sigma\, C_L \sqrt{1+\left(\sqrt[V_J]{V_T}\right)^2} \tag{41}$$

A fundamental parameter is $\dfrac{V_J}{V_T} = \dfrac{\dot{m}_J}{\rho A_J V_T}$

61

For continuity of mass flow $\dfrac{u_5}{V_T} = \left(\dfrac{u_1}{V_T}\right)\left(\dfrac{A_2}{A_1}\right)$

$$\therefore \; \frac{\Delta P_i}{q_T} = \sigma \, C_L \sqrt{1+\left(\frac{A_2}{A_1}\right)^2\left(\frac{u_5}{V_T}\right)^2} \left.\begin{array}{c} \\ \\ \\ \\ \\ \\ \end{array}\right\} \qquad (42)$$

$$\text{where } C_L = a\left\{\theta - \cos^{-1}\frac{1}{\sqrt{1+\left(\frac{A_2}{A_1}\right)^2\left(\frac{u_5}{V_T}\right)^2}}\right\}$$

$$a = \text{ lift curve slope,}$$

or C_L is obtained from cascade data

Exit Flow Conditions

When the fan blades are at a large angle of incidence θ to the tangential chord, their operation is closely analogous to that of a centrifugal impeller. If $\mathcal{S}$ is the slip factor, the tangential velocity of the air leaving the exit blades will be $\mathcal{S}V_T$. If u_2 is the velocity component across the blade plane, over an effective fan exit area $\psi_2 \, 2\pi R$, then the mass flow is

$$\dot{m}_2 = \rho \, u_2 \, \psi_2 \, 2\pi R \qquad (43)$$

and the magnitude of the resultant velocity vector is

$$V_2 \, R = \sqrt{(\mathcal{S}V_T)^2 + u_2^2} \qquad (44)$$

Thus, the exit total head is

$$\Delta P_J = \Delta p_J + \tfrac{1}{2}\rho \, u_J^2$$

$$= \Delta p_J + \frac{1}{2\rho}\left(\frac{\dot{m}_2}{A_J}\right)^2$$
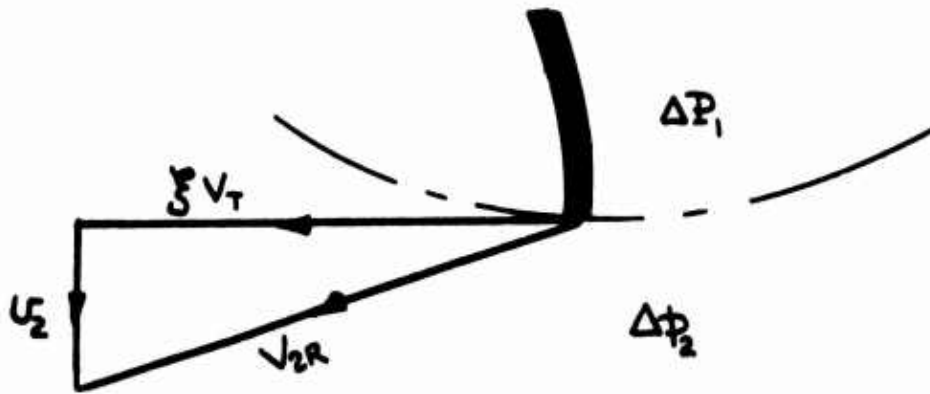
$$= \Delta p_2 + \tfrac{1}{2}\rho \, u_{2R}^2$$

Figure 44. Exit Flow Conditions.

If ΔP_1 is the total head upstream of the exit blade plane

$$\Delta P_J = \Delta P_1 + \tfrac{1}{2} \rho \, \xi^2 V_T^2 \tag{45}$$

$$= \Delta P_2 + \tfrac{1}{2} \rho \, V_{2R}^2$$

$$\therefore \Delta P_2 = \Delta P_1 - \tfrac{1}{2} \rho \, v_2^2$$

$$\Delta P_J + \tfrac{1}{2} \rho \, v_J^2 = \Delta P_1 + \tfrac{1}{2} \rho \, \xi^2 V_T^2$$

$$\therefore v_J = \sqrt{\frac{2}{\rho} \Delta P_1 + \xi^2 V_T^2 - \frac{2}{\rho} \Delta P_J}$$

$$\frac{v_J}{V_T} = \sqrt{\frac{\Delta P_1}{q_T} + \xi^2 - \frac{\Delta P_J}{q_T}} \tag{46}$$

$$= \frac{\dot{m}_J}{\rho \, V_T A_J}$$

Note that even with zero slip, neither the flow coefficient nor the back-pressure coefficient exceed unity unless $\Delta P_J > 0$. As Figure 45 shows, actual measurements give coefficients in excess of unity, so that the intake lift or pressurization effect must be an important factor.

63
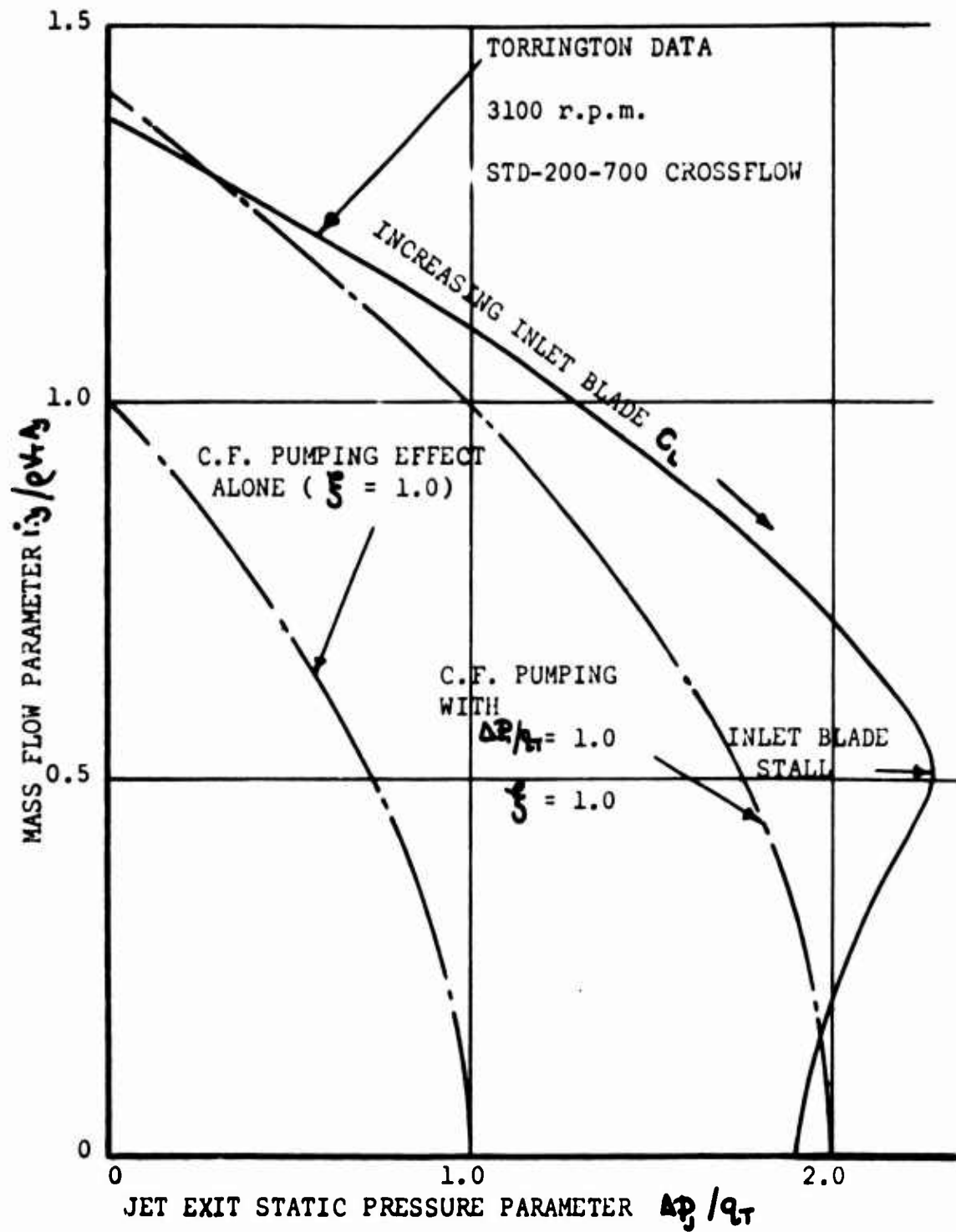
Figure 45. Variation of Mass Flow Parameter
With Jet Back-Pressure Parameter.

Total Pressure Rise and Mass Flow

It will be noted from the foregoing paragraphs that we have ascribed all of the "aerodynamic", or "reaction", pressure rise to the inlet station and all of the swirl to the exit station. In practice, both effects will be distributed between intake and exit of course, but in the absence of detailed experimental data, there is little point in refining the analysis to account for this.

Substituting equation (42) for ΔP_1 into equation (46)

$$\left(\frac{U_j}{V_T}\right)^2 = \sigma C_L \sqrt{1 + \left(\frac{A_2}{A_1}\right)^2 \left(\frac{U_j}{V_T}\right)^2} + \zeta^2 - \frac{\Delta P_2}{q_T} \tag{47}$$

Obviously the best way to obtain numerical results is to solve equation (47) in the form

$$\frac{\Delta P_J}{q_T} = \zeta^2 + \sigma C_L \sqrt{1 + \left(\frac{A_2}{A_1}\right)^2 \left(\frac{U_j}{V_T}\right)^2} - \left(\frac{U_j}{V_T}\right)^2 \tag{48}$$

Note that for $\left(\dfrac{U_j}{V_T}\right) = 0$

$$\frac{\Delta P_J}{q_T} = \zeta^2 + \sigma C_L \tag{49}$$

where $C_L \longrightarrow a\,\theta$ if θ is small

$\longrightarrow \mathcal{F}(\theta)$ if θ is large.

Also, if $\dfrac{\Delta P_J}{q_T} = 0$

$$(\sigma C_L)^2 \left[1 + \left(\frac{A_2}{A_1}\right)^2 \left(\frac{U_j}{V_T}\right)^2\right] = \left[\left(\frac{U_j}{V_T}\right)^2 - \zeta^2\right]^2$$

$$\left(\frac{U_j}{V_T}\right)^4 - \left[2\zeta^2 + \left(\frac{A_2}{A_1}\right)^2 (\sigma C_L)^2\right] \left(\frac{U_j}{V_T}\right)^2 + \zeta^4 - (\sigma C_L)^2 = 0$$

$$\left(\frac{U_j}{V_T}\right)^2 = \left[\zeta^2 + \frac{1}{2}\left(\frac{A_2}{A_1}\right)^2 (\sigma C_L)^2\right] \pm \sigma C_L \sqrt{1 + \zeta^2 \left(\frac{A_2}{A_1}\right)^2 + \frac{1}{4}\left(\frac{A_2}{A_1}\right)^4 (\sigma C_L)^4} \tag{50}$$

Approximate Cascade Relationships For Lift Coefficient

When blades are cascaded close together, their behavior is quite different to that measured with a single blade.
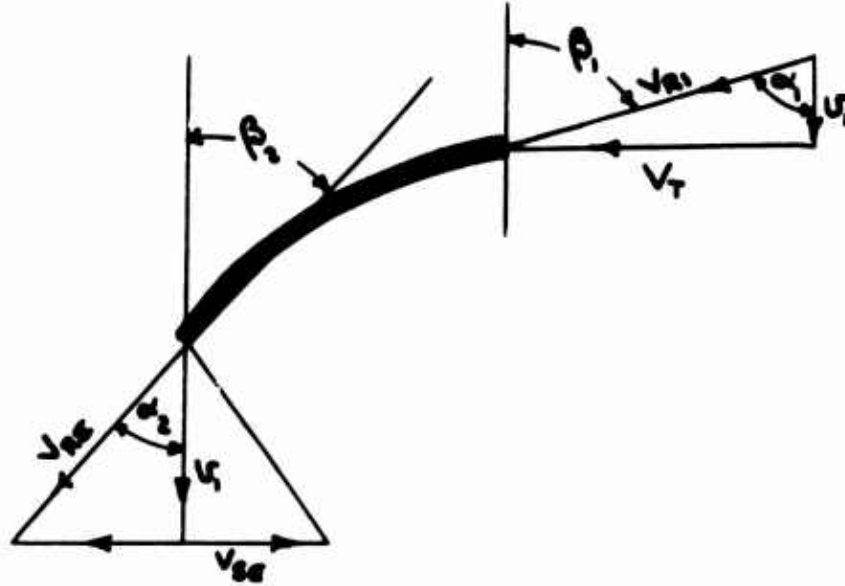
Figure 46. Cascade Flow.

If we define the flow vectors as in Figure 46, then, from Reference 23,

$$\sigma C_L = (\tan \alpha_1 - \tan \alpha_2) \sin \phi_r \tag{51}$$

where

$$\cot \phi_r = \frac{1}{2} (\tan \alpha_1 + \tan \alpha_2) \tag{52}$$

where

$$\sigma = \frac{\text{chord}}{\text{gap}} = \frac{C}{S}$$

and

$$S = \frac{2\pi R}{n} = \frac{\text{datum circumference}}{\text{number of blades}}$$

The solidity definition of the preceding section on Inlet Flow Conditions is unchanged.

66

Experimental cascade data are usually not available for a particular fan blade geometry, so that recourse must be made to empirical relationships which have been established in the course of developing gas turbine compressors.

Reference 23 gives

$$\alpha_2 = \beta_2 + \delta \tag{53}$$

$$\delta = \frac{(\beta_1 - \beta_2)}{\sqrt{\sigma C}} \left[0.23 \left(\frac{2a}{C} \right)^2 + 0.1 \left(\frac{\alpha_2}{50} \right) \right] \tag{54}$$

where the quantities are as defined in Figure 47 and are in degrees.
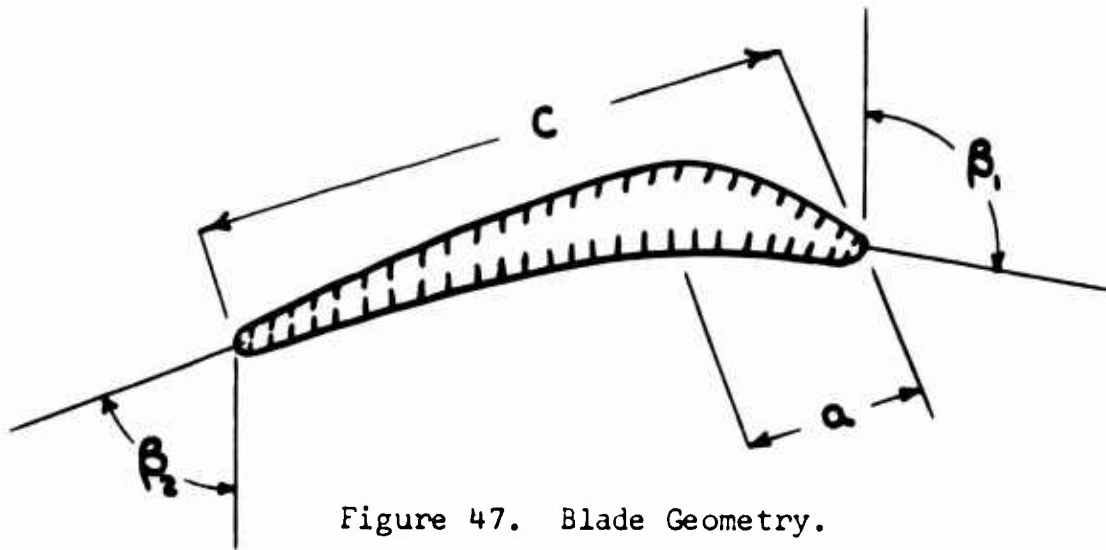
Figure 47. Blade Geometry.

Substituting for δ in equation (53)

$$\alpha_2 = \beta_2 + \frac{(\beta_1 - \beta_2)}{\sqrt{\sigma C}} 0.23 \left(\frac{2a}{C} \right)^2 + \frac{(\beta_1 - \beta_2)}{\sqrt{\sigma C}} 0.002 \alpha_2$$

$$\therefore \alpha_2 = \frac{\left[\beta_2 + \frac{0.23}{\sqrt{\sigma C}} (\beta_1 - \beta_2) \left(\frac{2a}{C} \right)^2 \right]}{\left[1 + \frac{0.002}{\sqrt{\sigma C}} (\beta_1 - \beta_2) \right]} \tag{55}$$

- a relationship which can be assumed to apply up to the stall, which occurs when the deflection angle ($\alpha_1 - \alpha_2$) becomes too large. Approximate values for the stall, taken from Reference 23, are given in Figure 48.
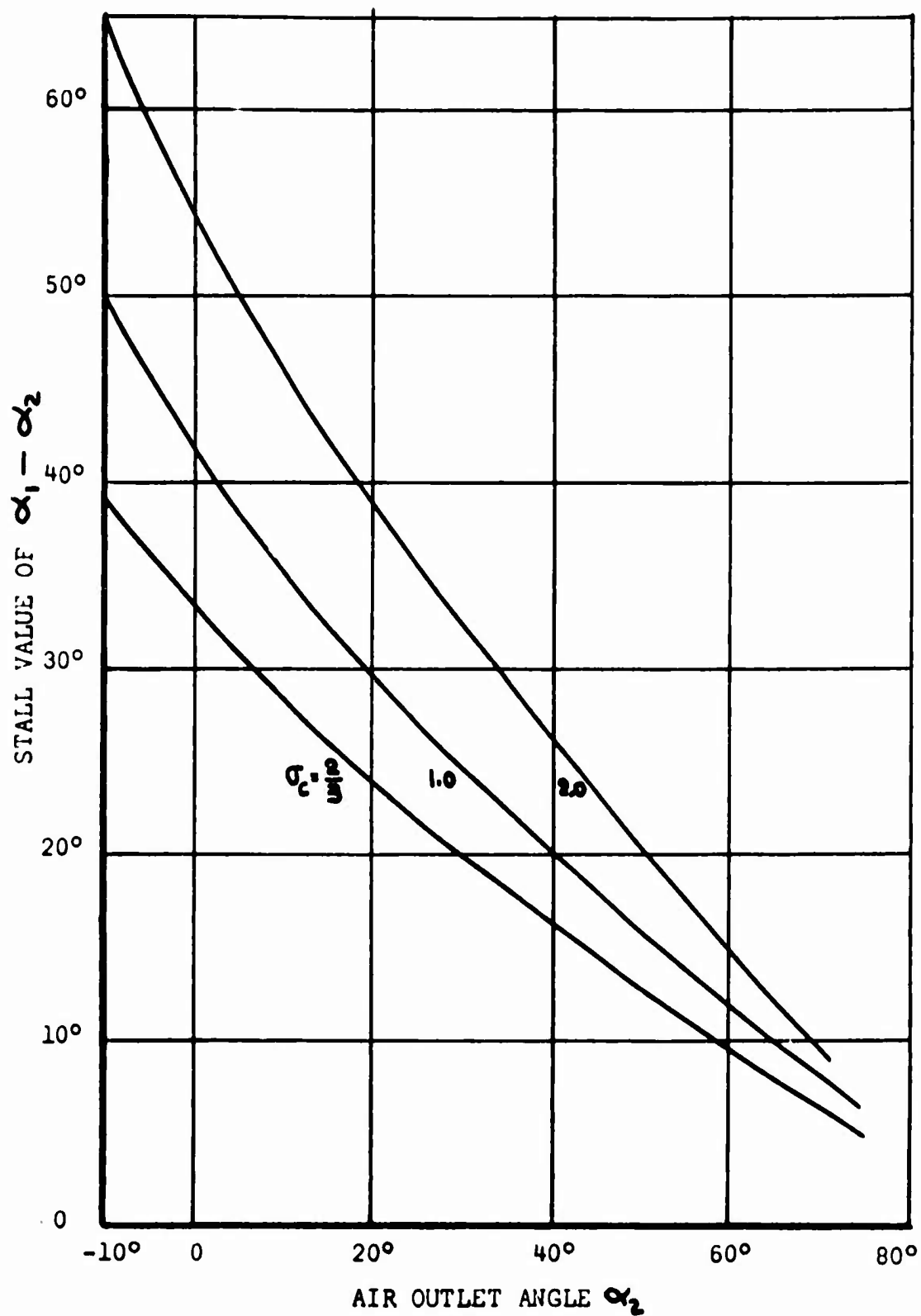
Figure 48.   Stalling Angles for Cascades (From Reference 23).

The variation of mass flow parameter with jet back-pressure parameter is plotted in Figure 49 for the Torrington model fan and two calculated examples. The actual performance calculations are presented in Appendix VIII, Tables 9 and 10.

EXPERIMENTAL OBSERVATIONS

The fan illustrated in Figure 50 was obtained on loan through the offices of the Torrington Manufacturing Company and was installed in the test rig illustrated in Figure 51. Rotational speed was measured with a Metron model 47M10G (#F4891) tachometer, calibrated to ± 1 per cent, and the shaft power input was measured by using the torque balance described in References 9 and 24. Aerodynamic instrumentation consisted of a specially manufactured total head rake and static pressure wall taps in the fan exit plane, used in conjunction with a Frost-designed and -manufactured manometer board.

The measured velocity distributions at the fan exit are given in Figures 52 - 63. The location of the pressure tubes is given in Table 1. A summary of these results is tabulated in Table 2, and the volume flow coefficient and observed total efficiencies are plotted in Figures 64 and 65. Because of the marked scatter in the results, no attempt has been made to fit curves to this data.

In Figure 66 the measured volume flow coefficients are compared with the Torrington data, and the agreement is seen to be quite poor, except in the low back-pressure range. Even here the scatter is much greater than we should expect from experimental measurements of this type.

The reasons for this poor agreement are not fully understood. Some of the horizontal velocity distributions are extremely irregular, as in the case of Figure 60 for example, indicating that local deviations in blade angle of attack may be in part responsible. The fan is placarded at 1600 r.p.m., since blade deflection under centrifugal force will cause them to foul the fan case at higher speeds. This flexure will logically also cause a change in blade incidence at the different test speeds used, and this factor could also cause scatter.

Finally, at the low rotational speeds employed, the maximum peripheral speed is only 22.3 feet per second. Thus the Reynold's number is

$$\textbf{Re} = \frac{22.3 \times 0.1875 \times 10^4}{12 \times 1.566} = 0.2225 \times 10^4$$

This is in the region where very random effects associated with flow break-away may be expected. For these reasons no attempt has been made to reduce scatter in the results by the use of more refined experimental techniques.

69
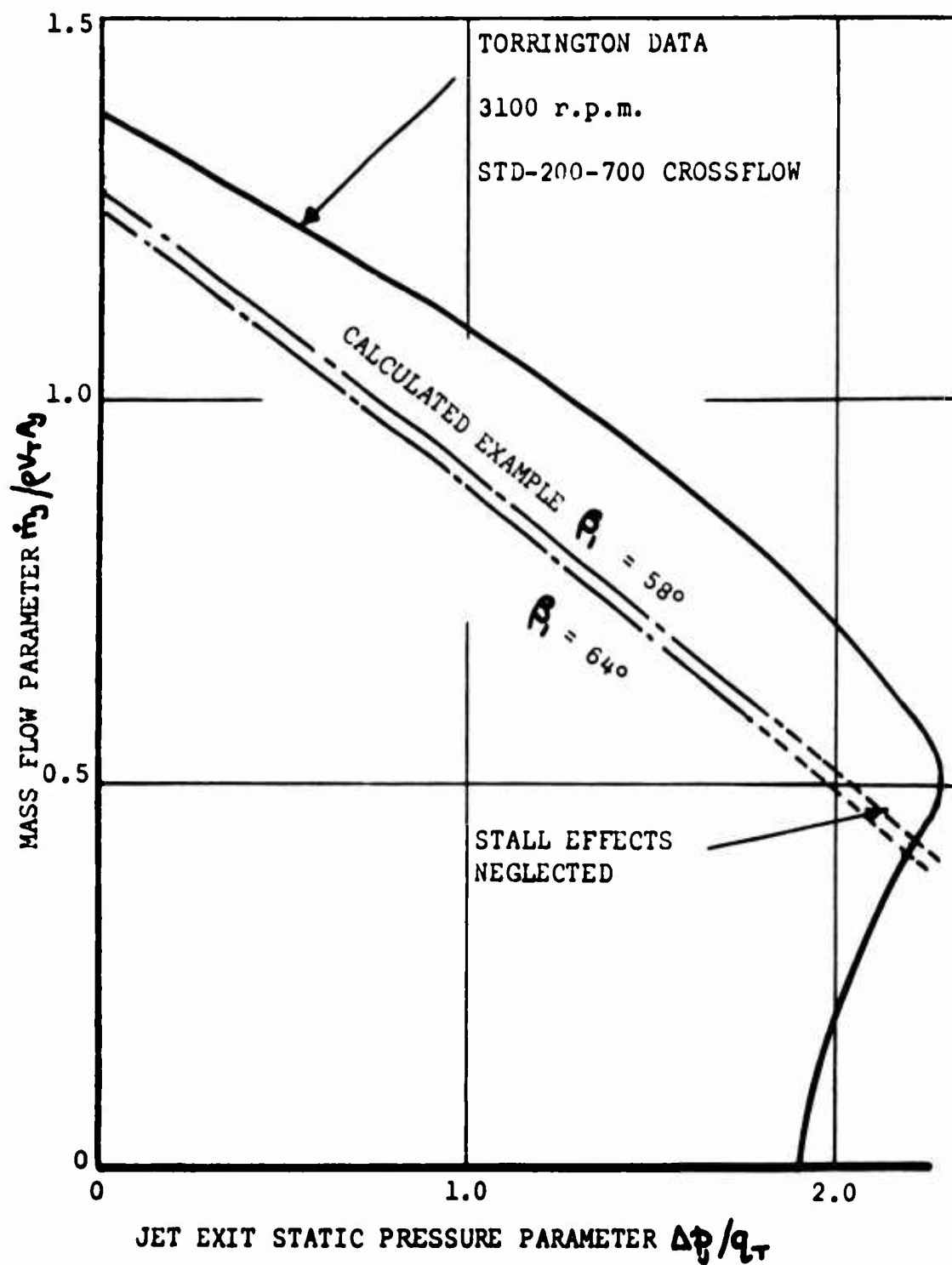
Figure 49. Variation of Mass Flow Parameter
With Jet Back-Pressure Parameter.

BLANK PAGE
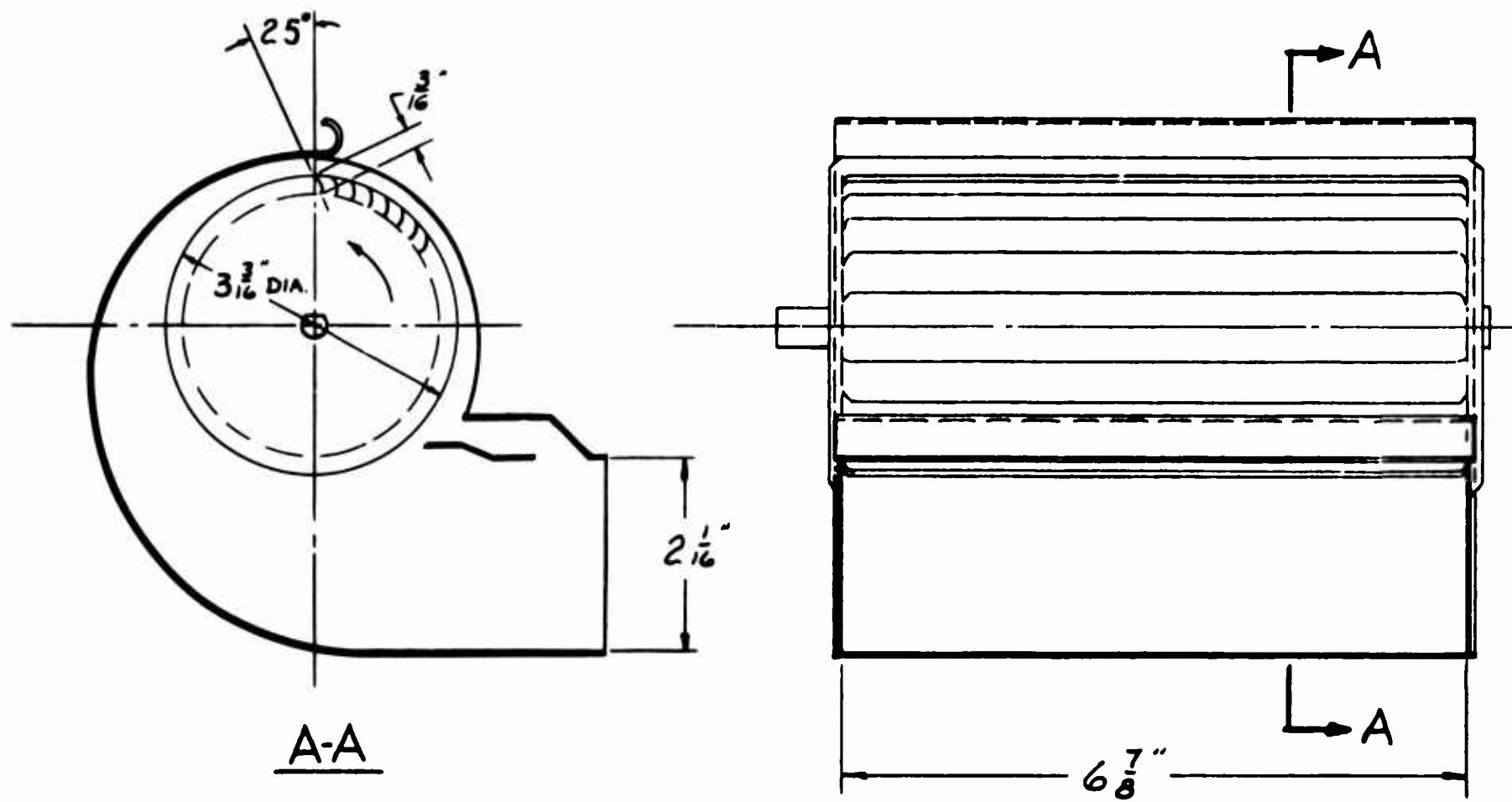
Figure 50. General Arrangement of Torrington Crossflow Fan.

72
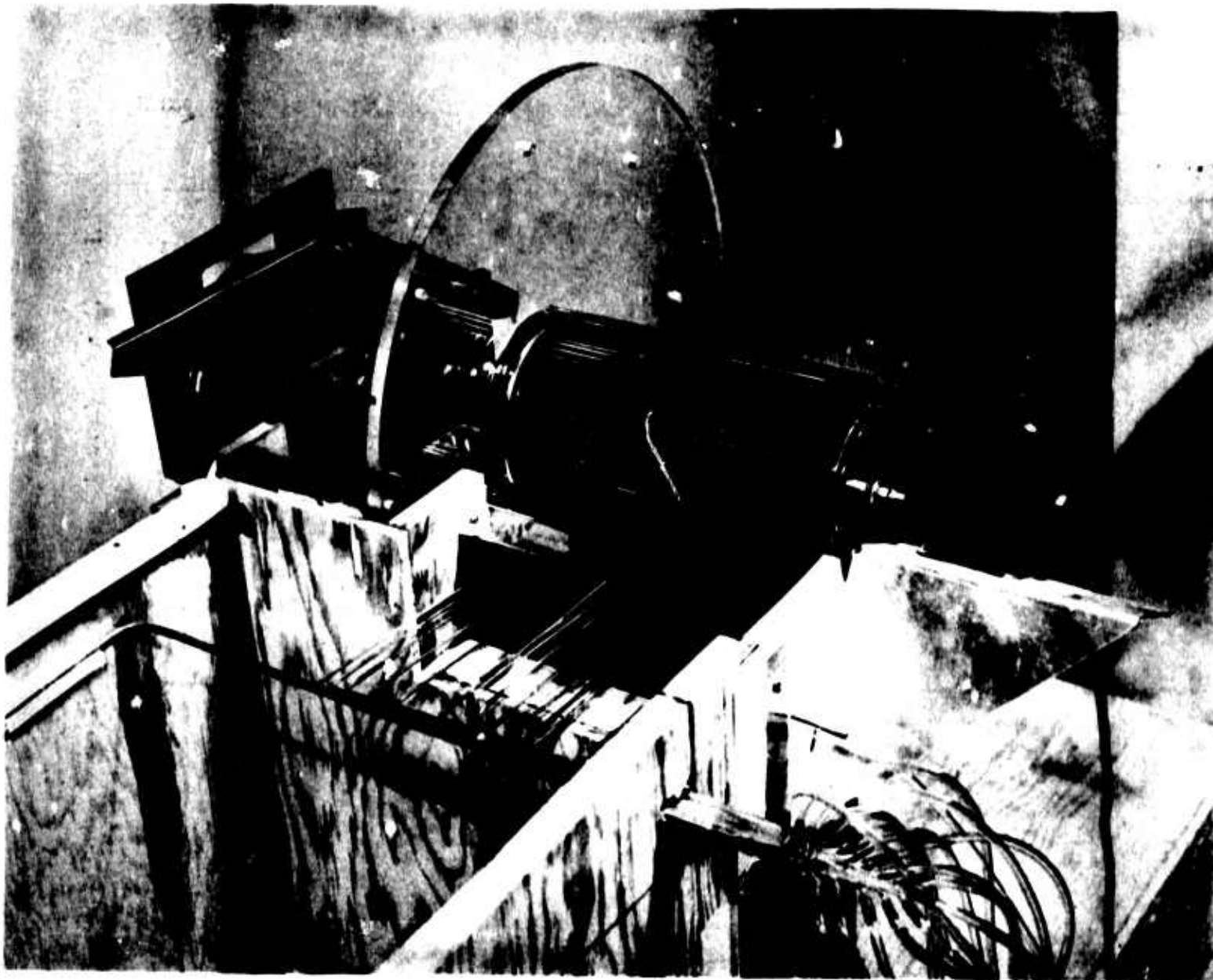
Figure 51. Crossflow Fan Test Rig.
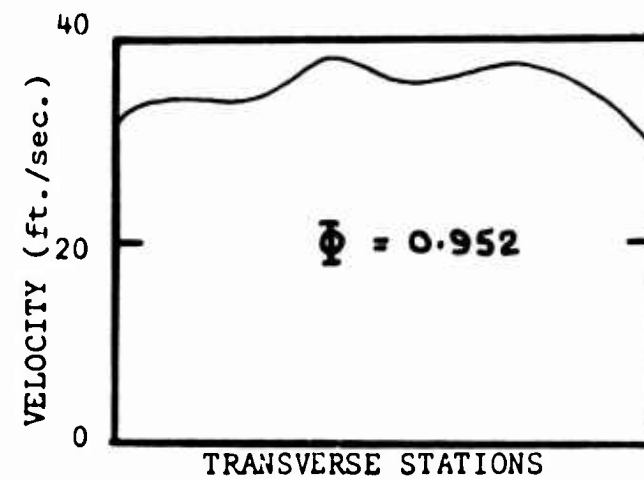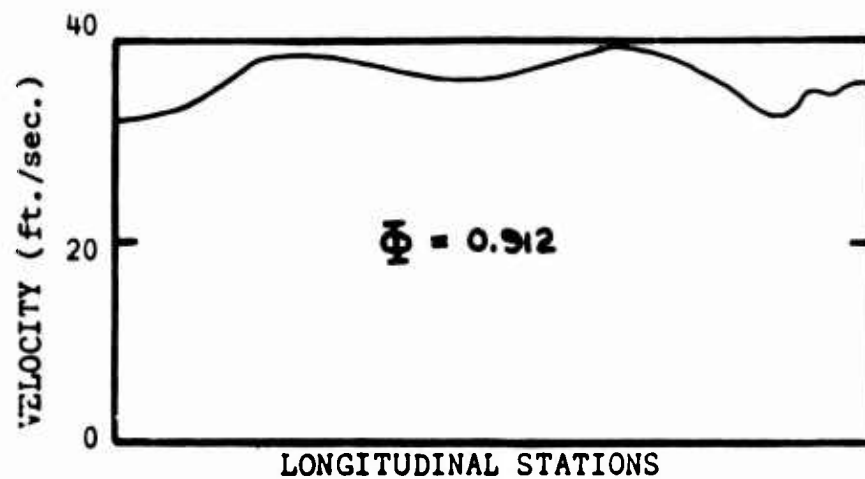
Figure 52. Velocity Profile Test No. 1. Configuration: Closed, Speed: 1600 r.p.m.
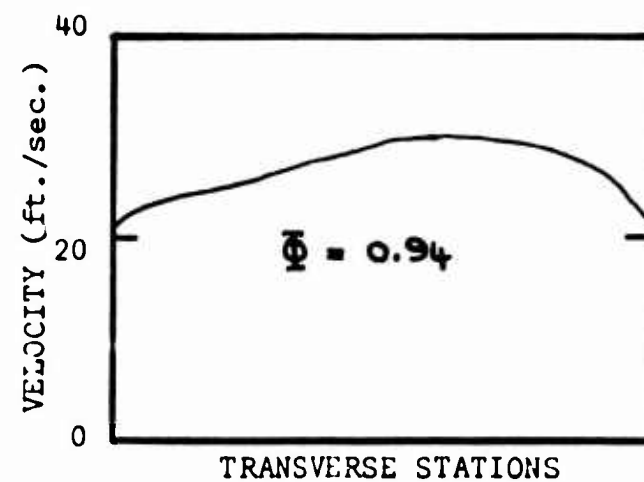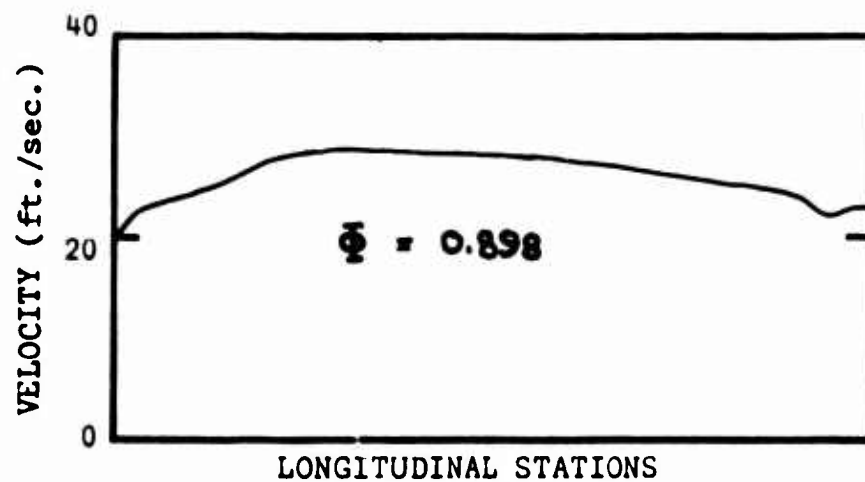
Figure 53. Velocity Profile Test No. 2. Configuration: Closed, Speed: 1200 r.p.m.
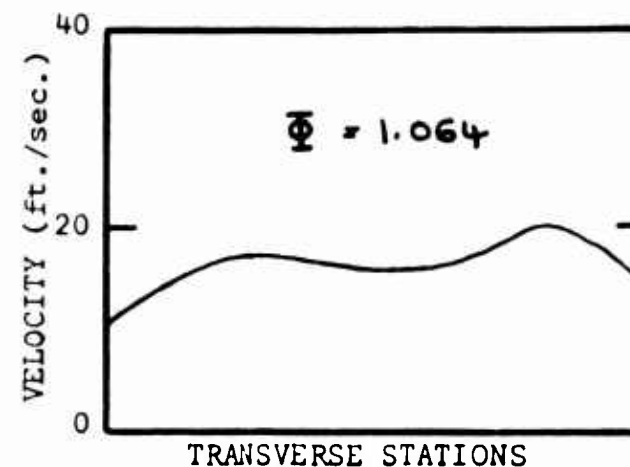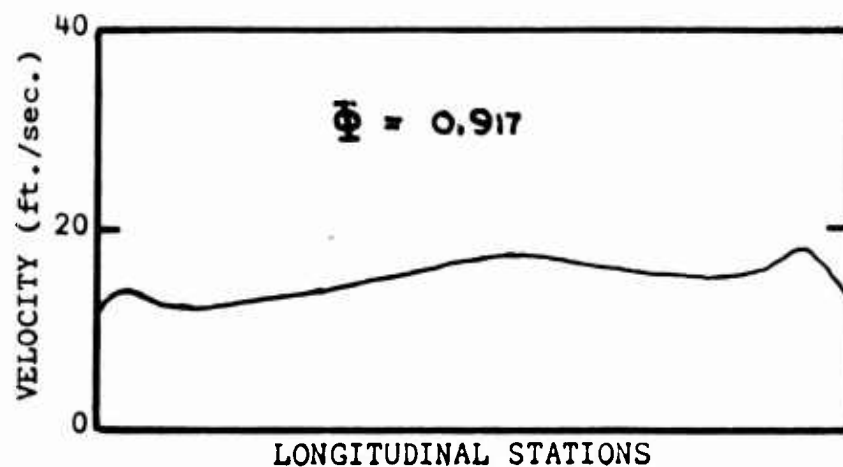
Figure 54. Velocity Profile Test No. 3. Configuration: Closed, Speed: 800 r.p.m.
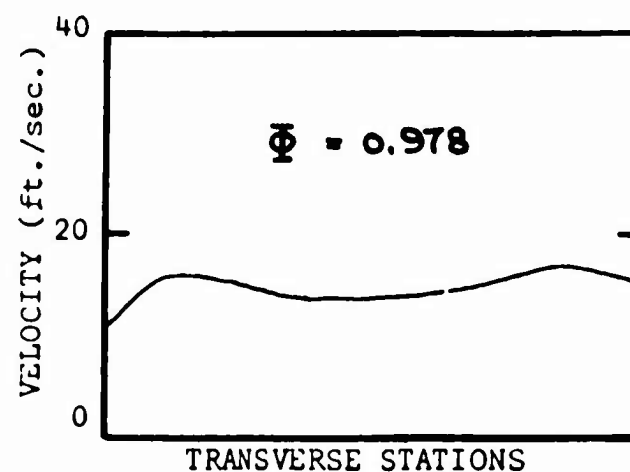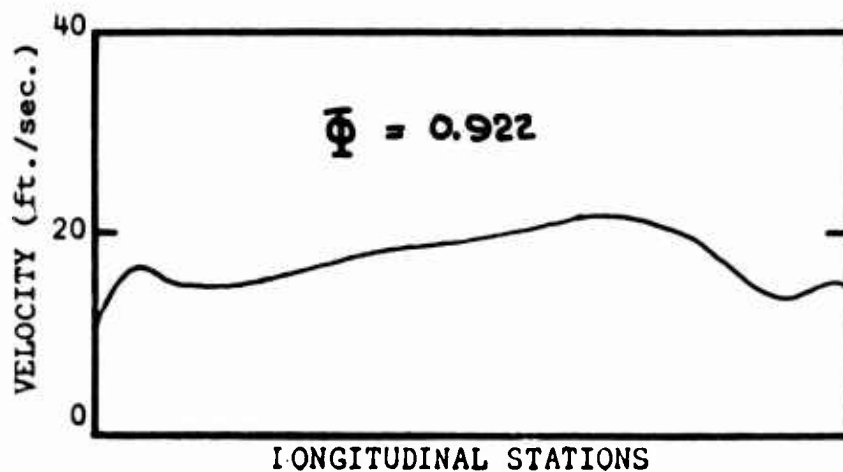
Figure 55. Velocity Profile Test No. 4. Configuration: Open 1/3, Speed: 800 r.p.m.
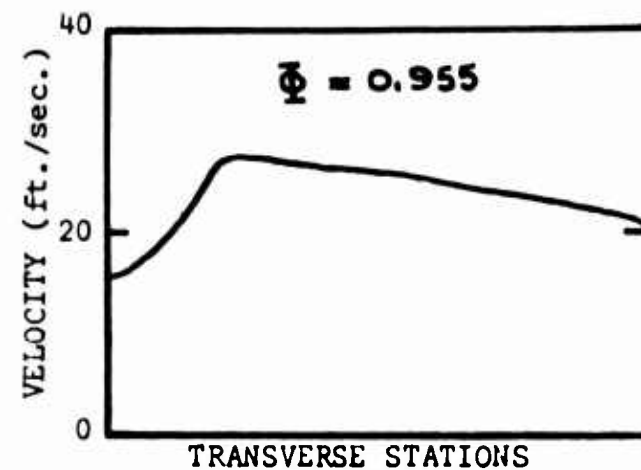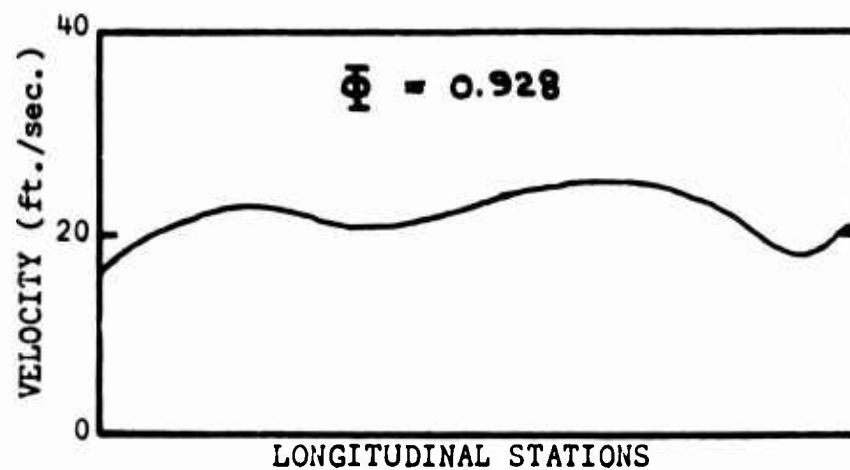
Figure 56.   Velocity Profile Test No. 5.   Configuration: Open 1/3, Speed: 1200 r.p.m.
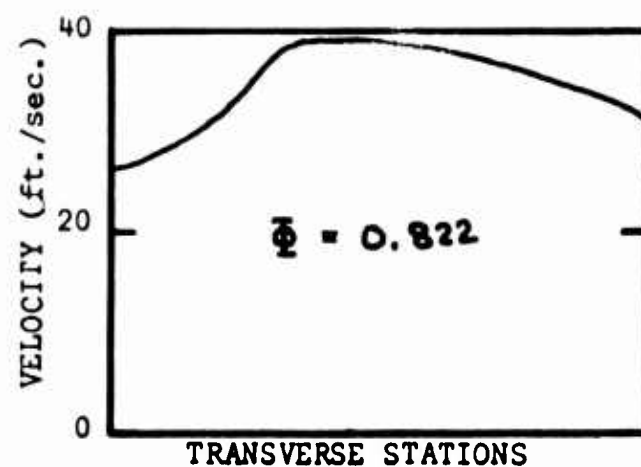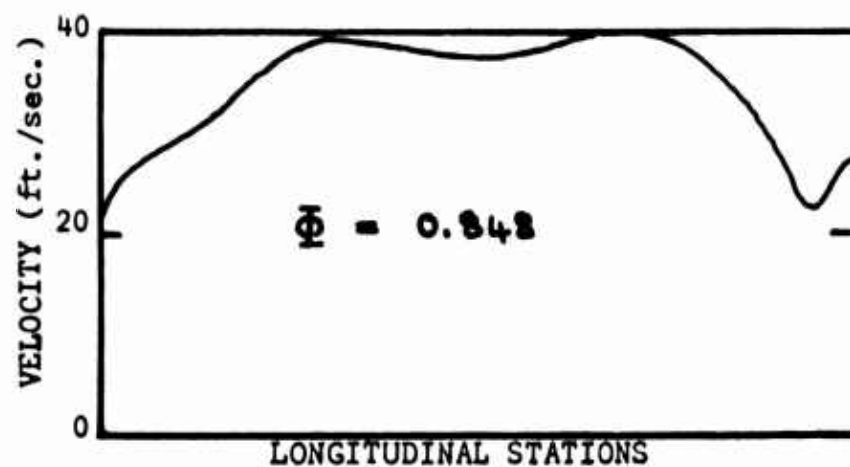
Figure 57.   Velocity Profile Test No. 6.   Configuration: Open 1/3, Speed: 1600 r.p.m.
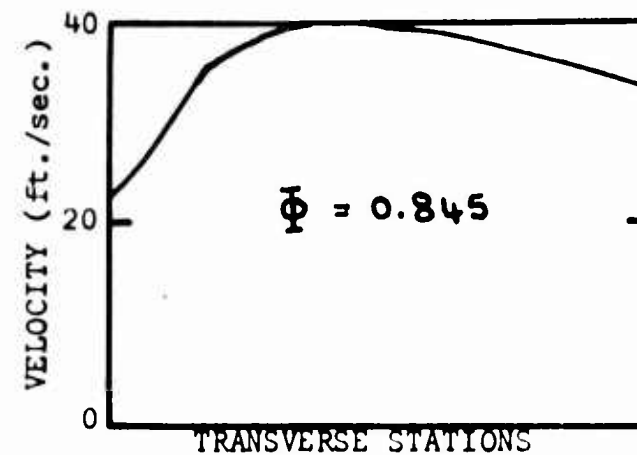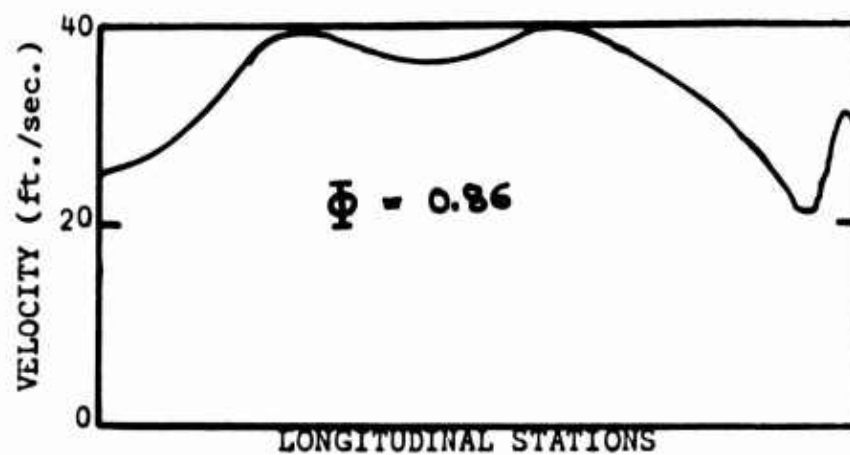
Figure 58.   Velocity Profile Test No. 7.   Configuration: Open 2/3, Speed: 1600 r.p.m.
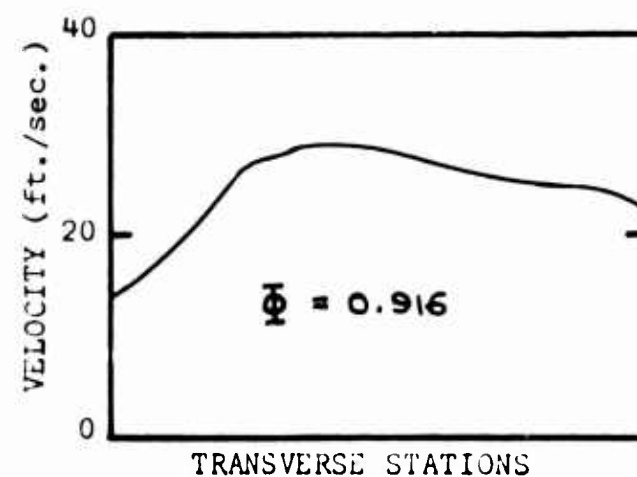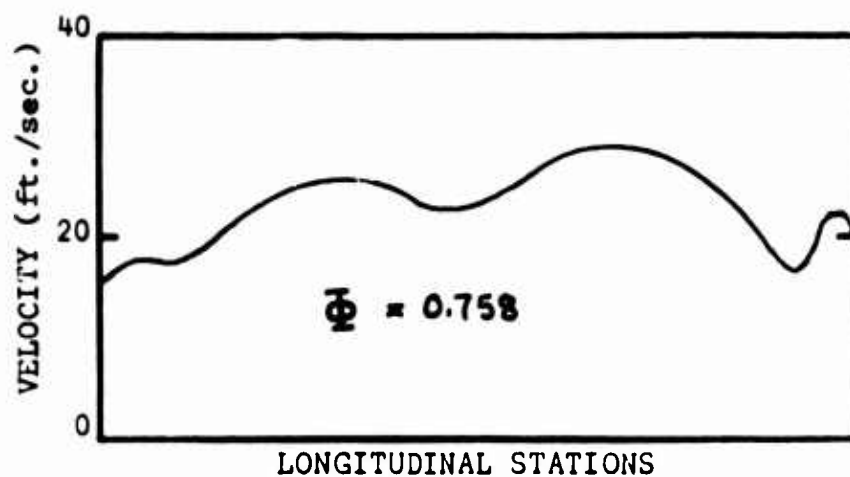
Figure 59.   Velocity Profile Test No. 8.   Configuration: Open 2/3, Speed: 1200 r.p.m.
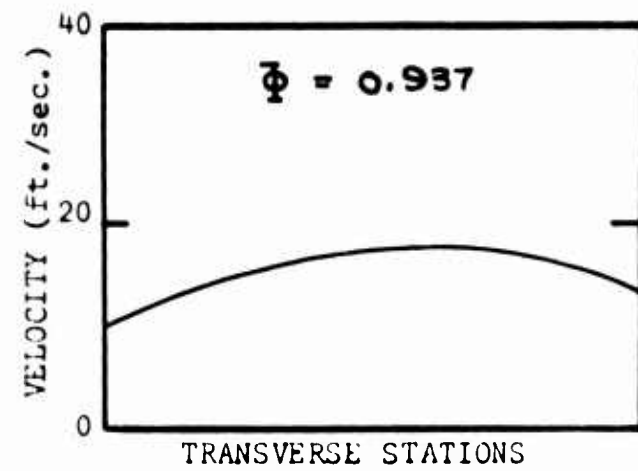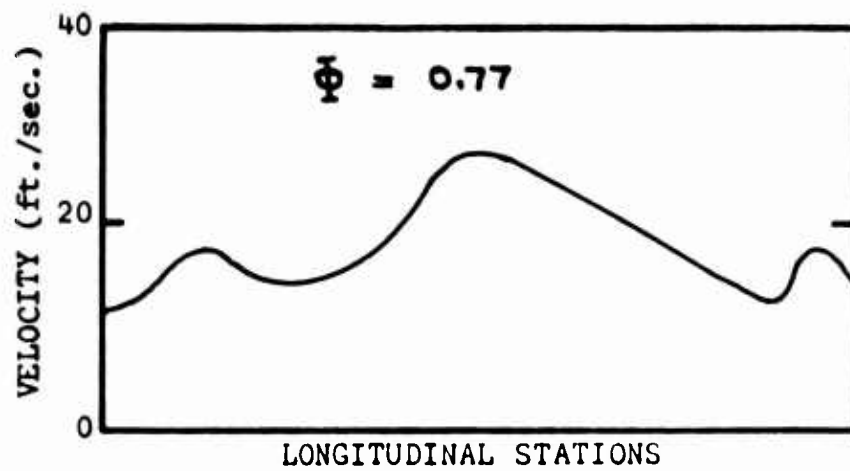
Figure 60. Velocity Profile Test No. 9. Configuration: Open 2/3, Speed: 800 r.p.m.
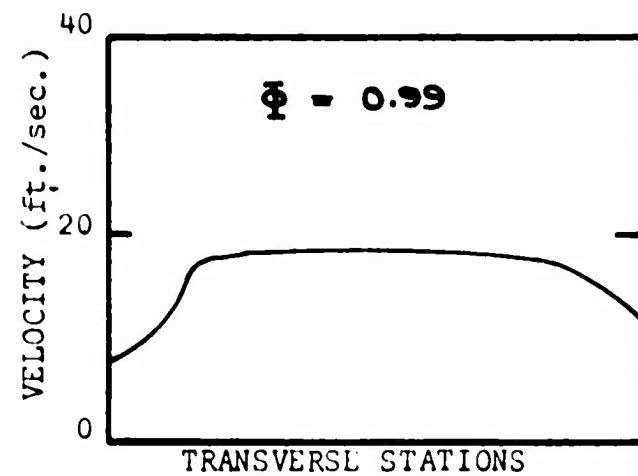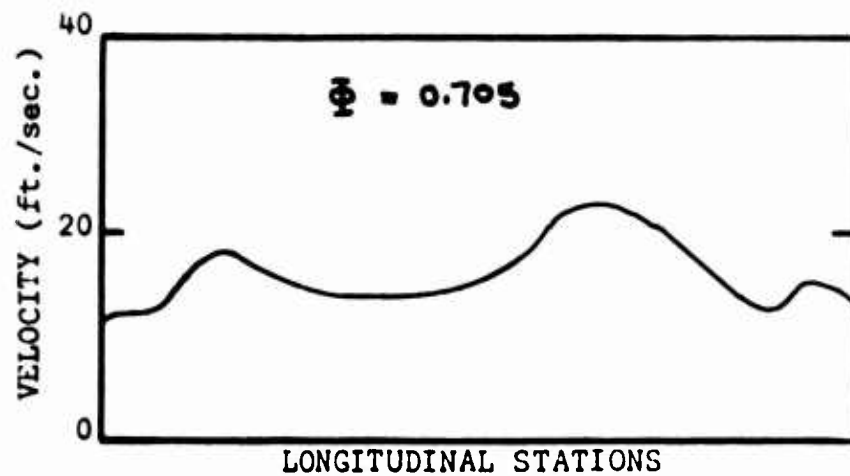
Figure 61. Velocity Profile Test No. 10. Configuration: Fully Open, Speed: 800 r.p.m.
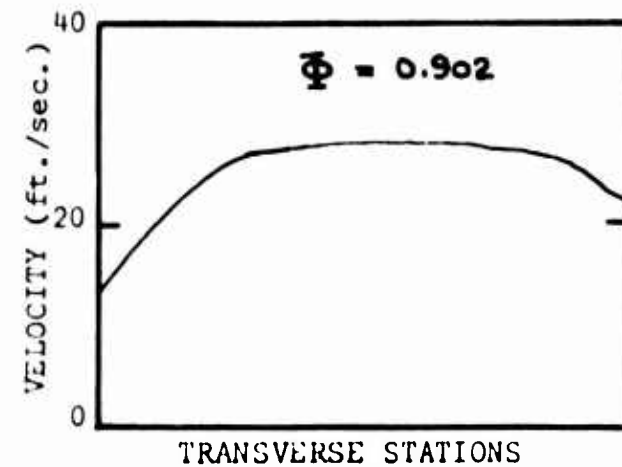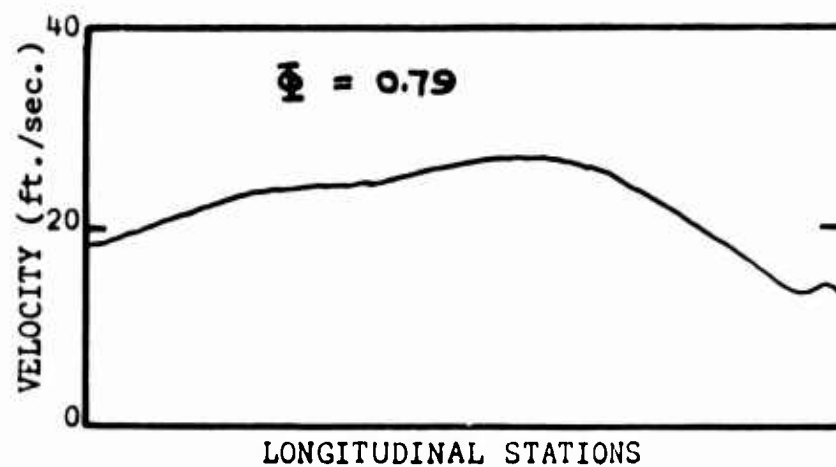
Figure 62. Velocity Profile Test No. 11. Configuration: Fully Open, Speed: 1200 r.p.m.
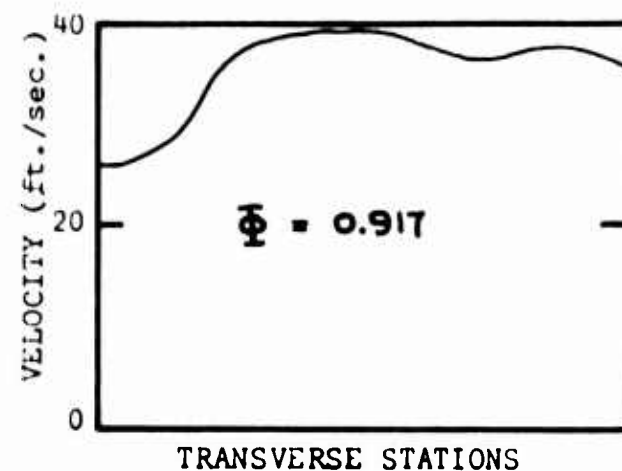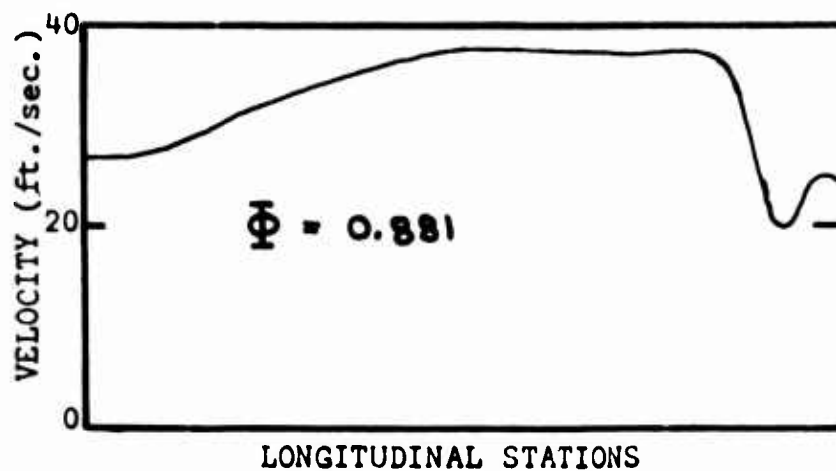
Figure 63. Velocity Profile Test No. 12. Configuration: Fully Open, Speed: 1600 r.p.m.

BLANK PAGE

TABLE 1

LOCATION OF PRESSURE TUBES

TUBE NUMBER	DISTANCE (INCH.)
1	0.13
2	0.34
3	0.67
4	1.09
5	1.66
6	2.47
7	3.50
8	4.47
9	5.31
10	5.88
11	6.25
12	6.53
13	6.78
14	-
15	0.03
16	0.25
17	0.56
18	1.56
19	1.84
20	2.03

NOTE: (1) Tubes 1 through 13 are longitudinal stations and the distances are measured from the left hand edge of the fan exit.

(2) Tube 14 is the manometer zero.

(3) Tubes 15 through 20 are transverse stations and the distances are measured from the front edge of the fan exit.

TABLE 2

SUMMARY OF RESULTS

RUN NO.	RPM	Φ	$\Delta\rho$ (lb/ft^3)	ξ_J (ft.lb/sec)	Shaft BHP	η Effi- ciency	$\frac{\Delta\rho}{q_T}$	$\dot{m}_J$ (slugs/sec)	V_T (ft/sec)	$\frac{\dot{m}_J}{A_J V_T \rho}$
1	1600	.868	.780	6.72	.02385	51.2	1.61	.00681	22.3	1.54
2	1200	.844	.520	2.62	.01430	33.3	1.84	.00474	16.73	1.43
3	800	.976	.204	.845	.00655	23.5	1.69	.00339	11.15	1.53
4	800	.900	.111	.520	.00655	14.5	0.92	.00302	11.15	1.36
5	1200	.885	.111	1.780	.01250	25.9	0.41	.00490	16.73	1.48
6	1600	.697	.149	2.570	.03100	15.1	0.31	.00553	22.3	1.25
7	1600	.727	.037	2.540	.03335	13.9	0.08	.00577	22.3	1.30
8	1200	.758	.037	1.200	.01610	13.6	0.14	.00444	16.73	1.34
9	800	.720	.111	.596	.00835	13.0	0.92	.00322	11.15	1.45
10	800	.698	0	.289	.00894	5.9	0	.00284	11.15	1.28
11	1200	.712	.074	.955	.01610	10.8	0.27	.00399	16.73	1.20
12	1600	.808	.074	3.460	.03335	18.9	0.15	.00633	22.3	1.43

80

BLANK PAGE
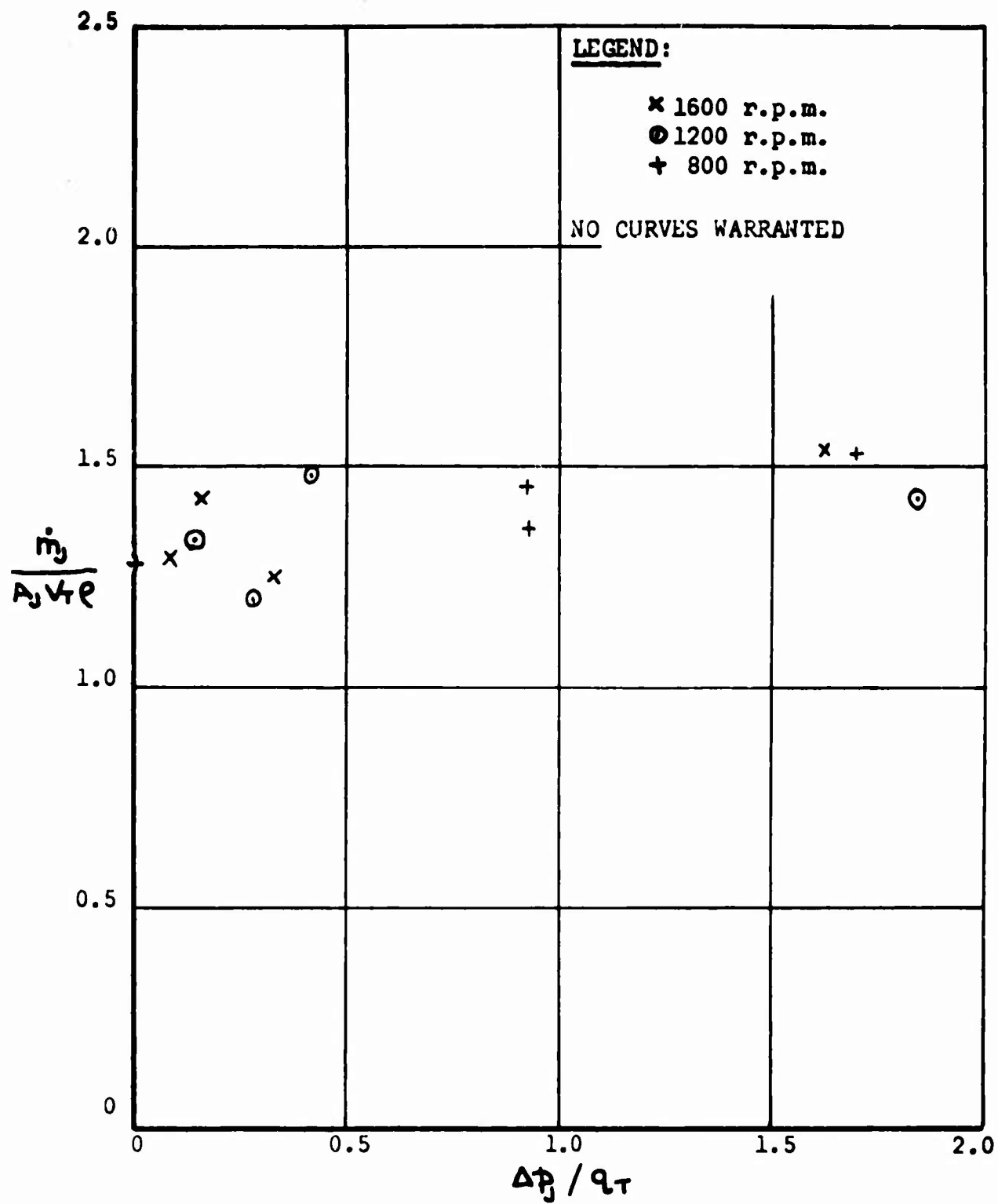
Figure 64. Summary of Measured Mass Flow.
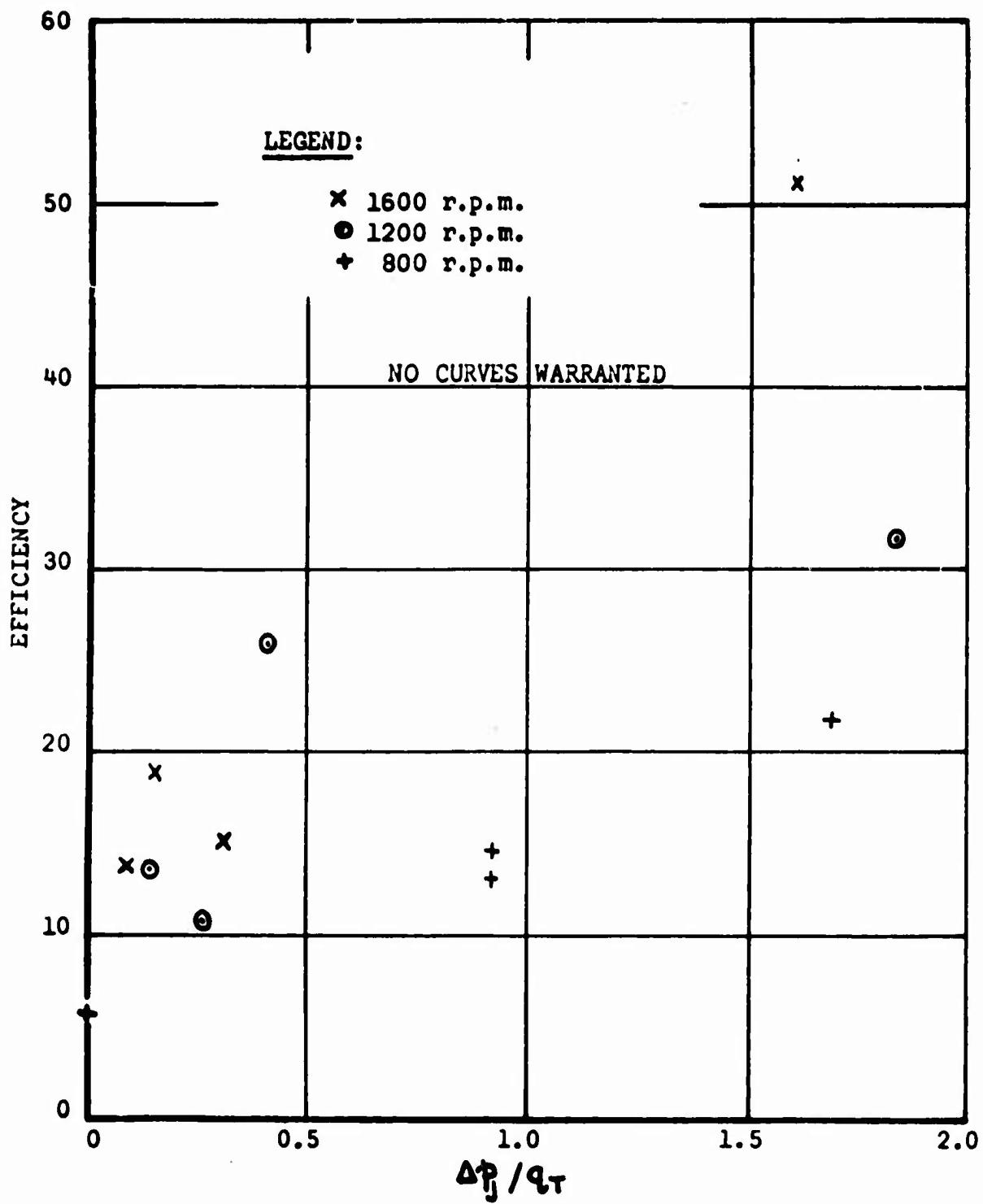
Figure 65. Summary of Measured Efficiency.
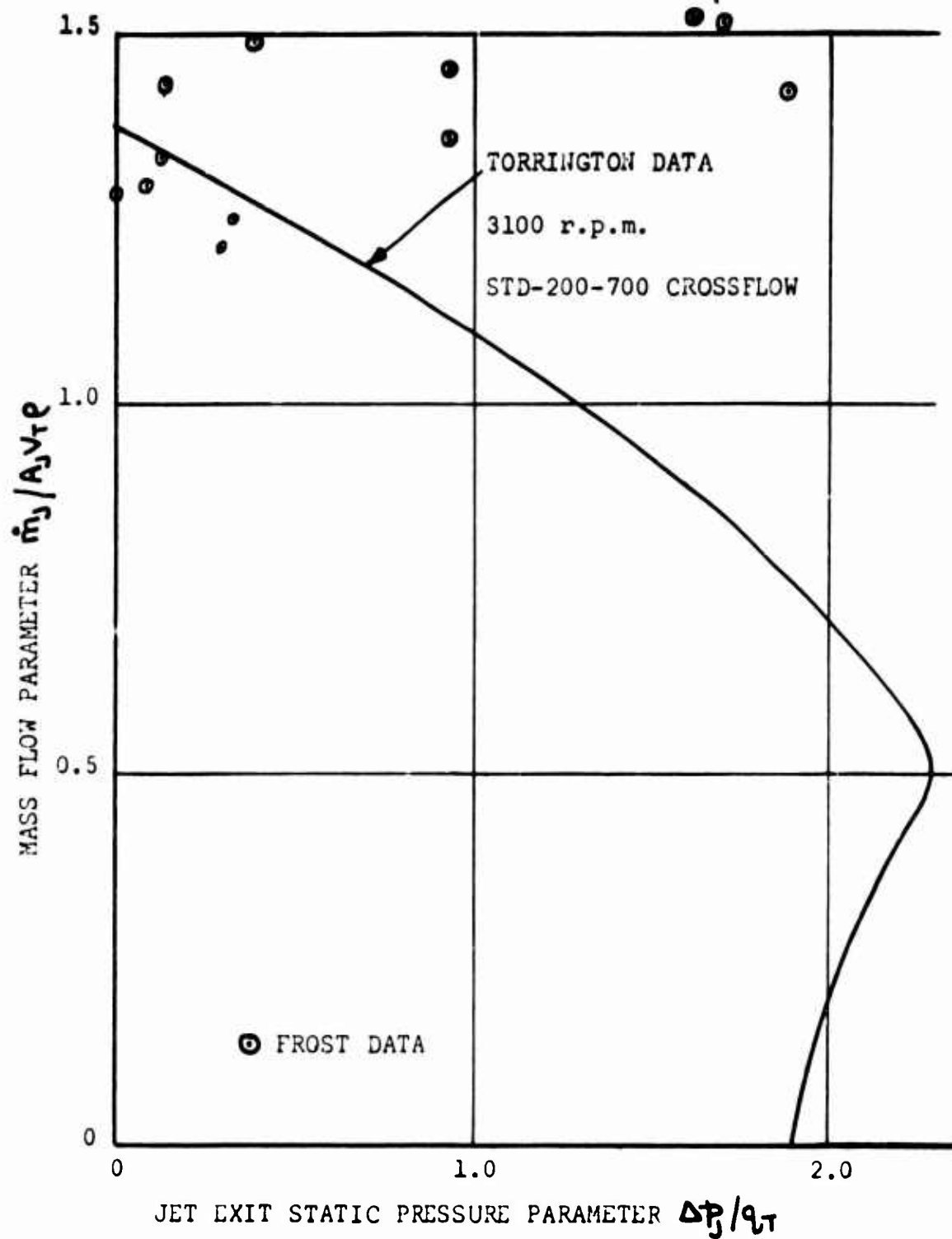
Figure 66. Variation of Mass Flow Parameter
With Jet Back-Pressure Parameter.

DISCUSSION AND RECOMMENDATIONS

The theoretical and experimental program originally envisioned in Reference 25 has been substantially exceeded in this present report. From an experimental point of view, the generous loan of the Torrington Blower, which was substantially larger than the German design already available in-house, enabled power input measurements to be made, and hence the efficiency to be determined. In view of the fact that an efficiency of 50 per cent was measured, it seems likely that a larger unit could be developed to the point of giving 80 per cent for GEM applications.

The theory given in Section One of this report represents a significant improvement in understanding the flow mechanisms involved, and, in view of the agreement obtained in Figure 49 there is no reason to suppose that it cannot be refined to the point where accurate performance prediction is possible. As a comparison, however, it should be realized that nearly a century elapsed between the first successful use of the axial flow propeller and the final formulation by Goldstein and Glauert of a satisfactory theoretical basis for predicting and optimizing its performance. It is therefore reasonable to expect that considerably more experimental and theoretical work will have to be carried out if the full potential of the crossflow fan is to be realized.

The first requirement is the availability of a full-scale crossflow fan, manufactured to close tolerances, the blades of which are both adjustable in pitch, and which can also be changed to permit the effect of varying blade solidity to be studied. A small cascade tunnel is also desirable in order that the cascade aerodynamics of the blades can be studied in detail before they are assembled in the fan. When this equipment is used, detailed performance measurements should be made and compared with the theory developed in this report, using at least three different blade solidities and three angles of attack for each solidity. At the same time, the principal characteristics of the flow inside the rotor should be mapped out in as much detail as possible.

When acceptable agreement between theory and experiment has been obtained, it is suggested that a crossflow fan assembly be designed for a specific GEM application and carried to the point where detailed stress and weight calculations have been completed. This will then enable a meaningful comparison to be made with the Frost Fan concept.

84

SECTION THREE

SMALL-SCALE MODEL TESTS OF THE FROST FAN CONFIGURATION

INTRODUCTION

Airflow and power measurements made on a simple model of the Frost Fan were reported previously in Reference 9 for a single exit area, with the fan exhausting to ambient. This section presents the results of another test program run with a 6-inch diameter Frost Fan made from plexiglass. The program was conducted in two parts during February 1963.

DESCRIPTION OF EQUIPMENT AND EXPERIMENTAL PROCEDURE

The investigation consisted of two main parts. In Part 1, a series of runs was performed in which the effect on the performance of the fan of varying exit area was investigated, with ambient jet back-pressure.

The fan model used for the tests is illustrated in Figures 67 and 68. Instrumentation was a Metron r.p.m. indicator, Model 47MI0G (Number F4891) calibrated to +1 per cent, and a Dwyer No. 25 manometer coupled to a 1/8-inch Dwyer Pitot Static Head. The total head orifice of the pitot static head was 1.40 inches downstream of the model exit plane. Its range of operating positions with respect to that plane is shown in Figure 69. The airflow from the nozzle exit was monitored on the Dwyer manometer, the r.p.m. being read directly from the Metron tachometer. A spring balance was used to measure the motor torque; this can be seen in Figure 68. The motor was free to swivel around its shaft on ball bearings. Thus, from knowledge of the motor torque and r.p.m., the motor shaft brake horsepower could be calculated. The manometer readings were used to estimate the mass flow rate for ambient conditions and the power in the jet. Finally, the efficiency of the model was calculated from the ratio of the jet power to shaft brake horsepower.

For Part 2, a plenum chamber was fitted over the fan exit, as shown in Figure 70. A simple flap valve in the wall of the plenum chamber was used to monitor the static pressure within the plenum chamber, this pressure being read by means of an inclined tube manometer. A series of torque and dynamic pressure readings was taken for a range of values of fan r.p.m. at a constant plenum chamber pressure. Five sets of runs were performed in this way.

REDUCTION OF EXPERIMENTAL DATA

The following relationships and conversion factors were used to reduce the experimental data:

1-inch head of water on the manometer

$$= 5.19 \text{ pounds per square foot} \quad (56)$$

Shaft brake horsepower $\quad = \text{Torque} \times \text{r.p.m.} \times \dfrac{2\pi}{60} \times \dfrac{1}{550}$

From the measured model geometry, this was equivalent to

Shaft brake horsepower $\quad = \text{Spring balance force (ounces)}$

$$\times \text{ r.p.m.} \times 2.59 \times 10^{-6} \quad (57)$$

Dynamic pressure $\quad q = \frac{1}{2}\rho U_j^2$

where U_j is the jet velocity and q is obtained from (56). Thus, if h is the manometer reading in inches of water, we have

$$U_j = 73.4 \sqrt{h} \quad \text{feet per second} \quad (58)$$

Due to friction at the walls of the jet nozzle, the velocity is not constant across the exit for a given motor speed. To find the variation of U_j with position in the nozzle, a series of flow measurements was taken along the vertical and horizontal centerlines of the jet exit plane. These data, plotted in Figures 71 and 72, were used to calculate a flow factor, Φ , which is needed when estimating the mass flow rate, $\dot{m}_j$. It was assumed that Φ does not vary with jet velocity, for a given exit area.

If $\qquad A_j$ = jet exit area, and

$\qquad U_{jc}$ = jet velocity measured at the center of the jet,

we have

$$\dot{m}_j = A_j \, U_{jc} \, \Phi \, \rho \quad (59)$$

The power in the jet, E_j , was calculated from the equation

$$E_j = \frac{1}{2} \dot{m}_j \, U_{jc}^2 \, \Phi^2 + \Delta p_j \, A_j \, U_{jc} \, \Phi \quad (60)$$

When the jet back-pressure is ambient, $\Delta p_j = 0$, and the second term of (60) vanishes.

The efficiency η was found from

$$\eta = \frac{\xi_u / 550}{\text{shaft BHP}} \tag{61}$$

A useful parameter for purposes of comparing the effects of changing jet exit area conditions is the momentum flux.

We define

$$M = \frac{\dot{m} \, u_{jc} \, \Phi}{\text{shaft b.h.p.}}$$

M is thus the momentum flux per shaft brake horsepower.

DISCUSSION OF RESULTS

Part 1

Tables of measured results and reduced data are given in Appendix VIII and are plotted in Figures 71 through 78.

Figure 71 shows a typical vertical velocity profile and illustrates the asymmetry in the airflow caused by the converging nozzle. Even when the nozzle is parallel (maximum area), some asymmetry was detected, due probably to the airflow entering the nozzle at an angle to the nozzle walls. The aerodynamic interference of the rollers, and of the circular track which supports the rollers across the exit, is clearly visible in the horizontal profile plotted in Figure 72. Plots of this type were used to estimate the flow factor, by which is multiplied the central velocity to give mean jet velocity at the fan exit.

Figures 73 through 78 relate the dynamic characteristics of the model to the speed of the motor driving the fan. Although the model was rather crude, the results in this group of figures are seen to conform surprisingly well to the "best-fit" curves.

Figure 75 shows that the shaft brake horsepower of the motor varies directly with $(\text{r.p.m.})^3$, as would be expected from simple energy considerations. Measurement of torque was found to be difficult to perform with accuracy, particularly at the higher speeds, when the spring balance vibrated considerably.

The variation of fan efficiency with motor speed and jet exit area is plotted in Figures 76 and 77. These figures indicate that, for this particular model exhausting to ambient, maximum efficiency is obtained at fan speeds of between 400 r.p.m. and 500 r.p.m. for the range of exit areas tested. Also, the exit area giving the best efficiency occurs in the range of 35 per cent to 45 per cent of the maximum area. The highest efficiency achieved, when these two optimum conditions coincided, was approximately 9 per cent.

It was observed during the experiment that the flexible coupling between the motor and the fan had a tendency to shorten while the motor was operating, pulling the fan rotor towards the case and causing rubbing and excessive friction. This condition was corrected periodically but undoubtedly did cause some of the torque readings to be uncharacteristically high. In this connection, it is pointed out that the test runs performed at 57 per cent exit area were a repetition of the tests reported in Reference 9. A comparison of the results, however, shows an increase in efficiency from a maximum of 2.6 per cent to a maximum of 6.2 per cent. The aerodynamic results (mass flow and jet power) are virtually unchanged, the improved efficiency deriving entirely from the reduction in friction caused by adjus￼ ￼ the fan rotor at frequent intervals during the later test series.

The conditions leading to optimum efficiency (400 - 500 r.p.m., 35 - 45 per cent of maximum area) are seen in Figure 78 to give also the maximum value for the ratio Momentum flux/Shaft b.h.p. This parameter is useful as a performance criterion of an actual vehicle, since momentum flux is closely related to the cushion pressure.

Part 2

The tables of measured and calculated results for Part 2 of the experiment are also given in Appendix VIII and are plotted in Figures 79 through 84.

As in Part 1, vertical and horizontal traverses were made across the jet exit to establish whether the flow factor was a function of back-pressure. It was found that the flow factor was not very sensitive to changes in back-pressure but did decrease linearly as the pressure increased, due probably to increased leakage at the blade edges.

In Figure 82, the effect of back-pressure on shaft brake horsepower required to maintain a particular fan speed is plotted. The close grouping of the curves indicates that the power required is not very sensitive to back-pressure.

The variation of efficiency with r.p.m. and back-pressure is plotted in Figures 83 and 84. The curve of efficiency versus r.p.m. for the ambient back-pressure case is also superimposed on Figure 83 for comparison. Probably the most reliable portion of this plot is that lying in the speed range 500 to 800 r.p.m. In this range, it is seen that the efficiency increases approximately monotonically with increase of back-pressure. This effect also shows up clearly in the cross plot, Figure 84. This behavior is predicted by the theory of the Frost Fan, detailed in Reference 26.

It should be pointed out that the back-pressures used in these tests are considerably smaller in magnitude than those which will exist in an operating GEM, and the efficiency is degraded accordingly in our unsophisticated model.
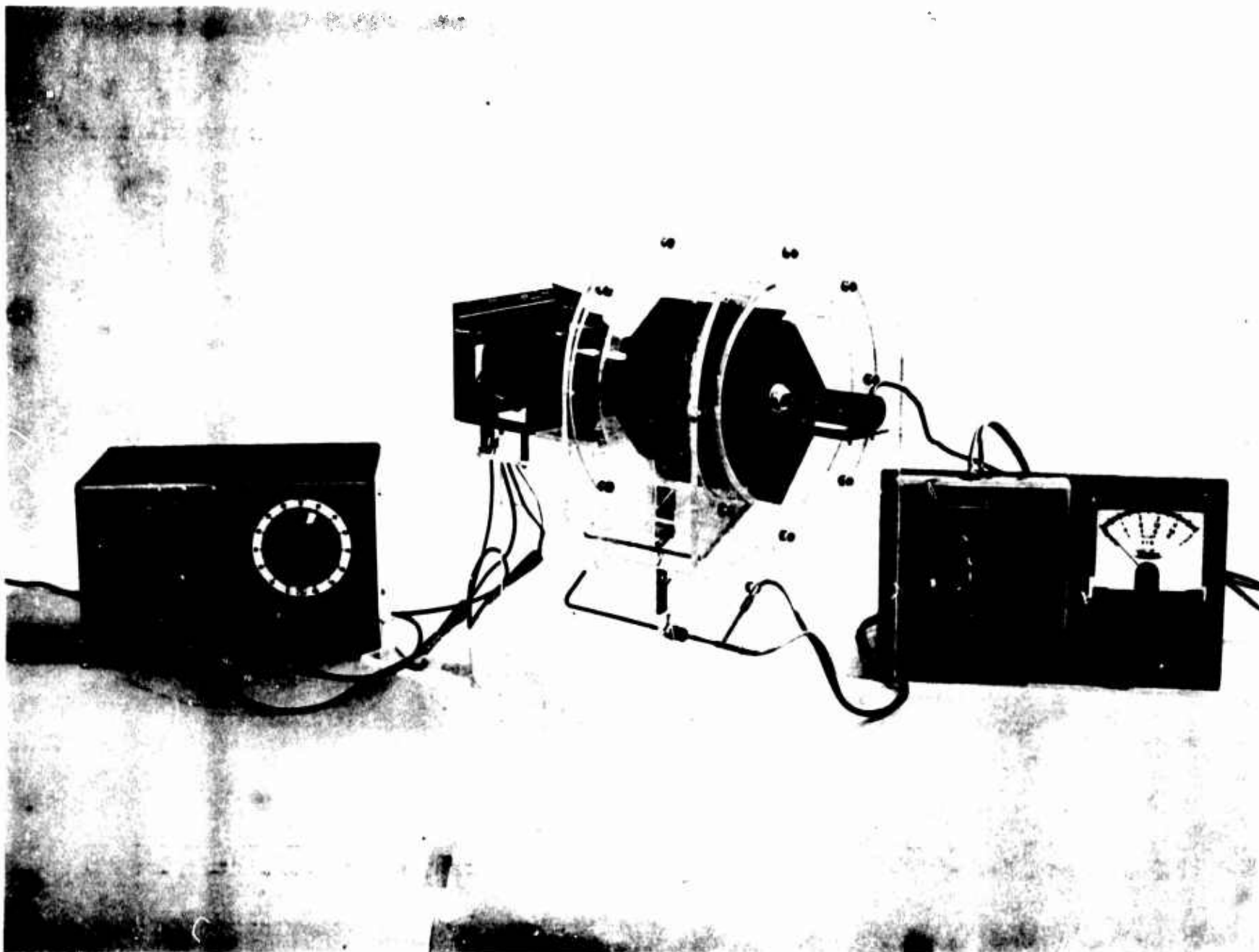
Figure 67. Front View of Model Test Rig.
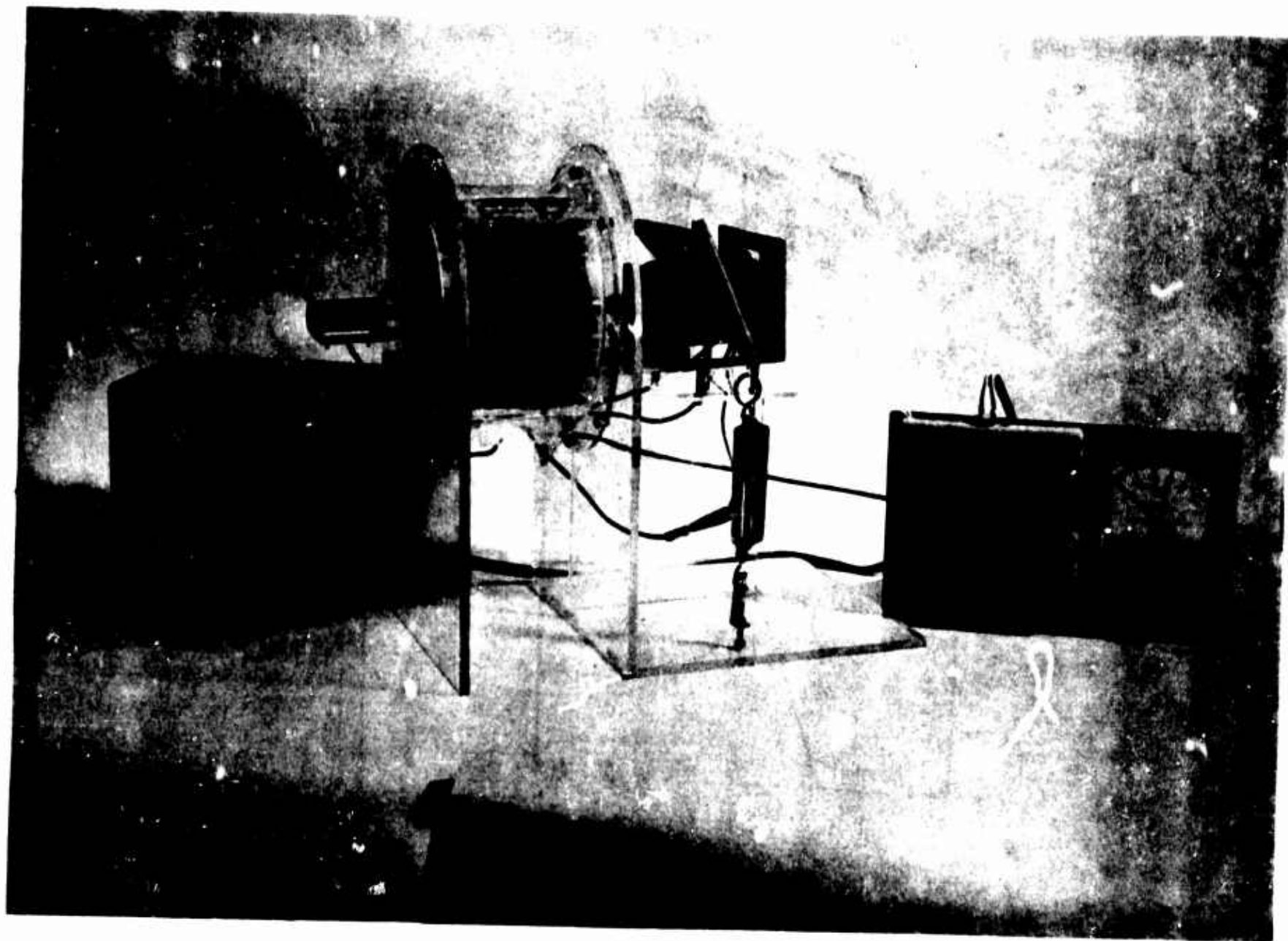
Figure 68. Rear View of Model Test Rig.

FAN CENTER

CENTER OF FAN CASE

VIEW "A"

1.53" (max.)

60°

90°
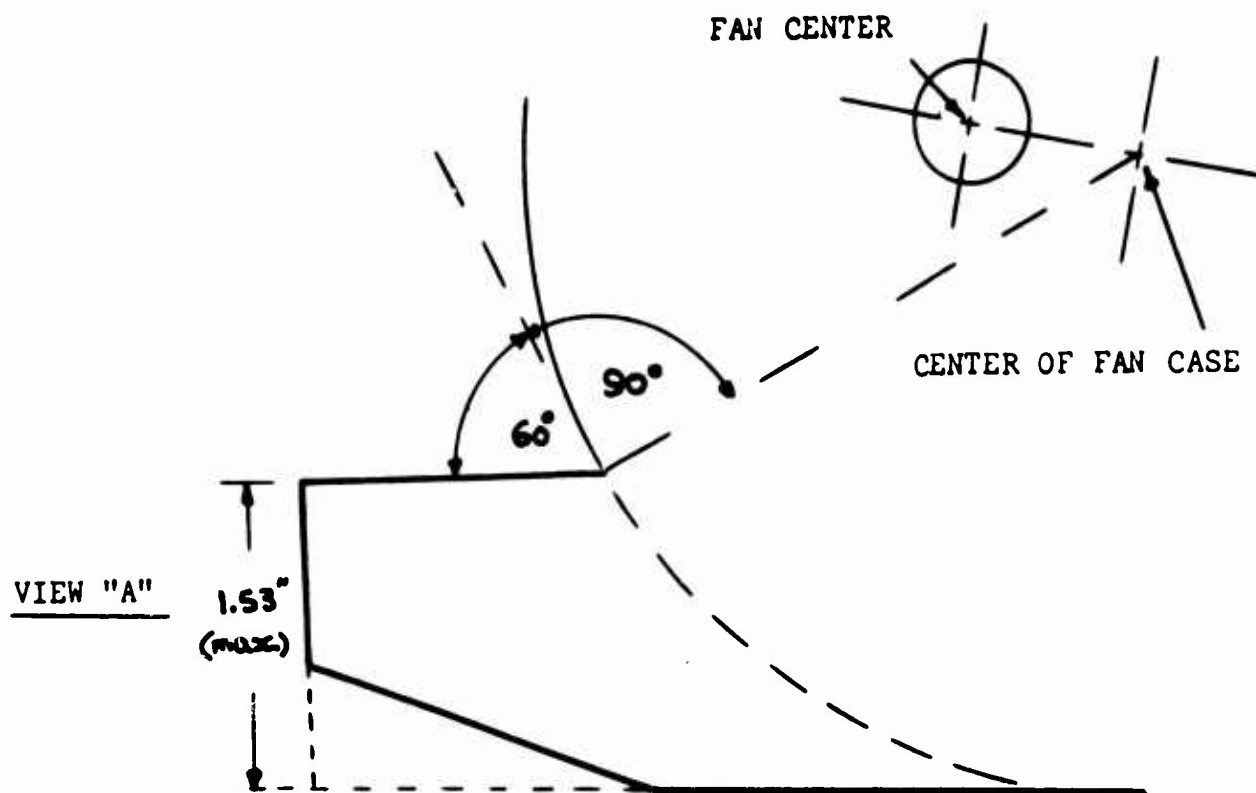
PITOT HEAD POSITIONS FOR
VERTICAL TRAVERSE (TYPICAL)

VIEW "A"

5.5"

PITOT HEAD POSITIONS FOR
HORIZONTAL TRAVERSE
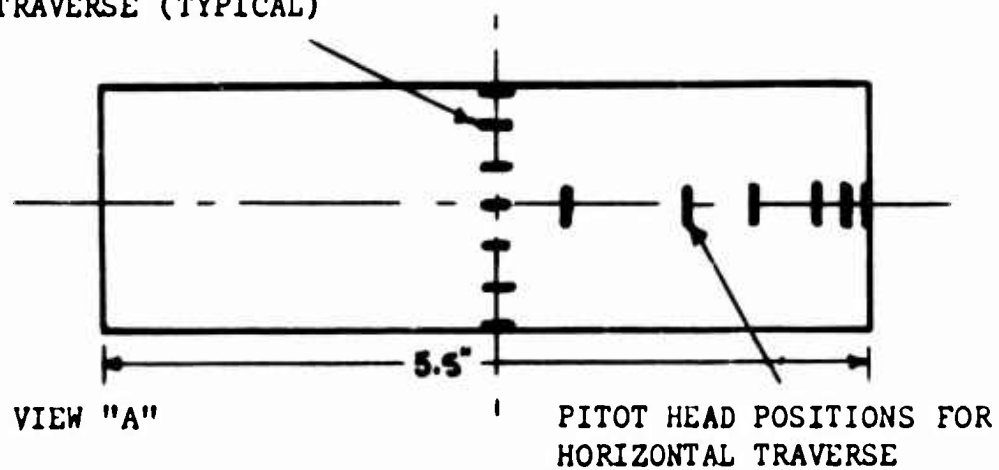
Figure 69. Geometry of Model Fan.

TO MANOMETER

HINGED SEALING
FLAPS

3"

5.5"

8.5"

12"

8.5" Diam.

24"

12"

TO PITOT HEAD
(ADJUSTABLE)

PLENUM CHAMBER ASSEMBLED WITH MODEL
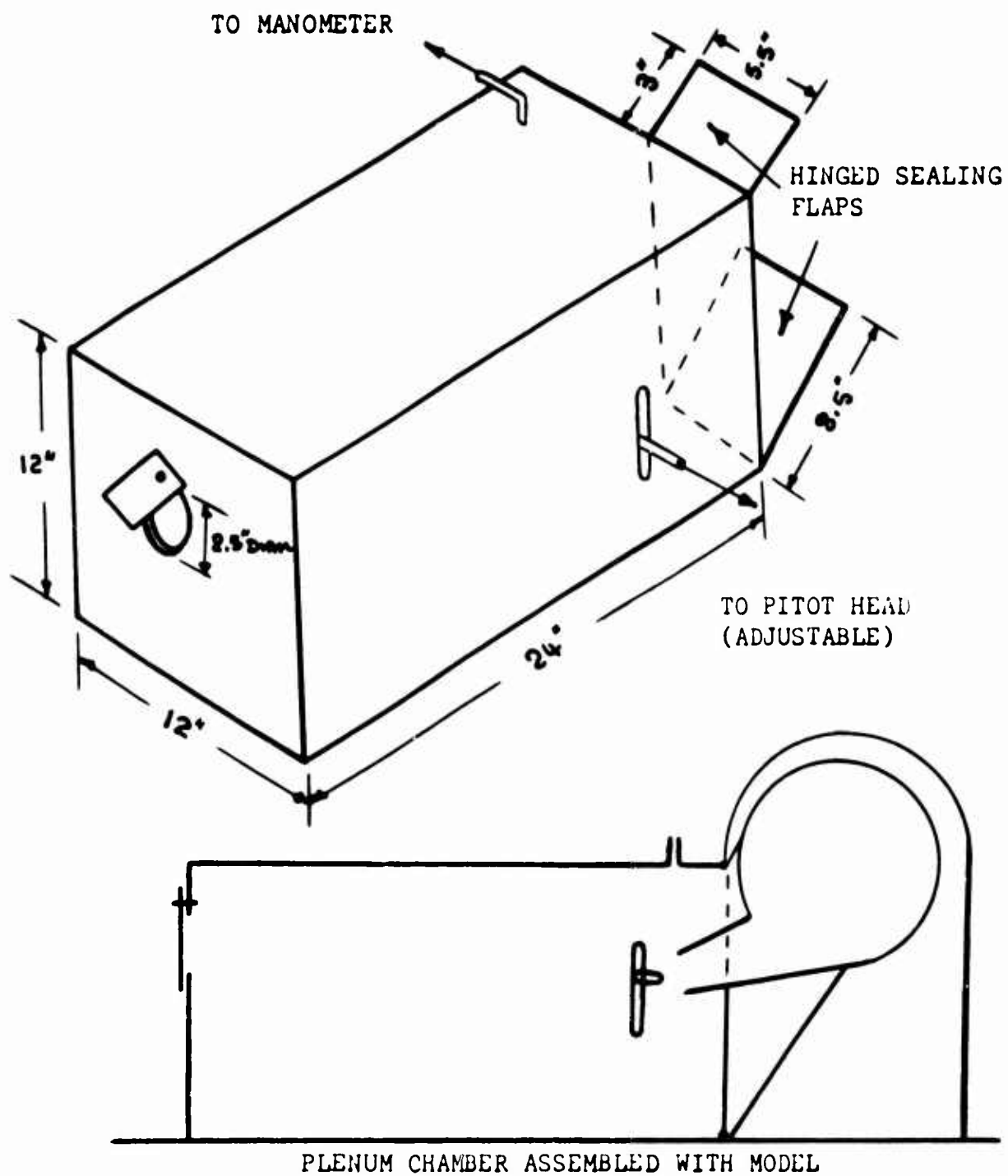
Figure 70.   Plenum Chamber.

93

DEPTH OF JET EXIT = 0.5",
AREA = 33 PER CENT OF MAXIMUM
AREA OF RECTANGLE = 153.72
AREA UNDER CURVE = 137.16

$$\Phi = \frac{137.16}{153.72} = 0.893$$
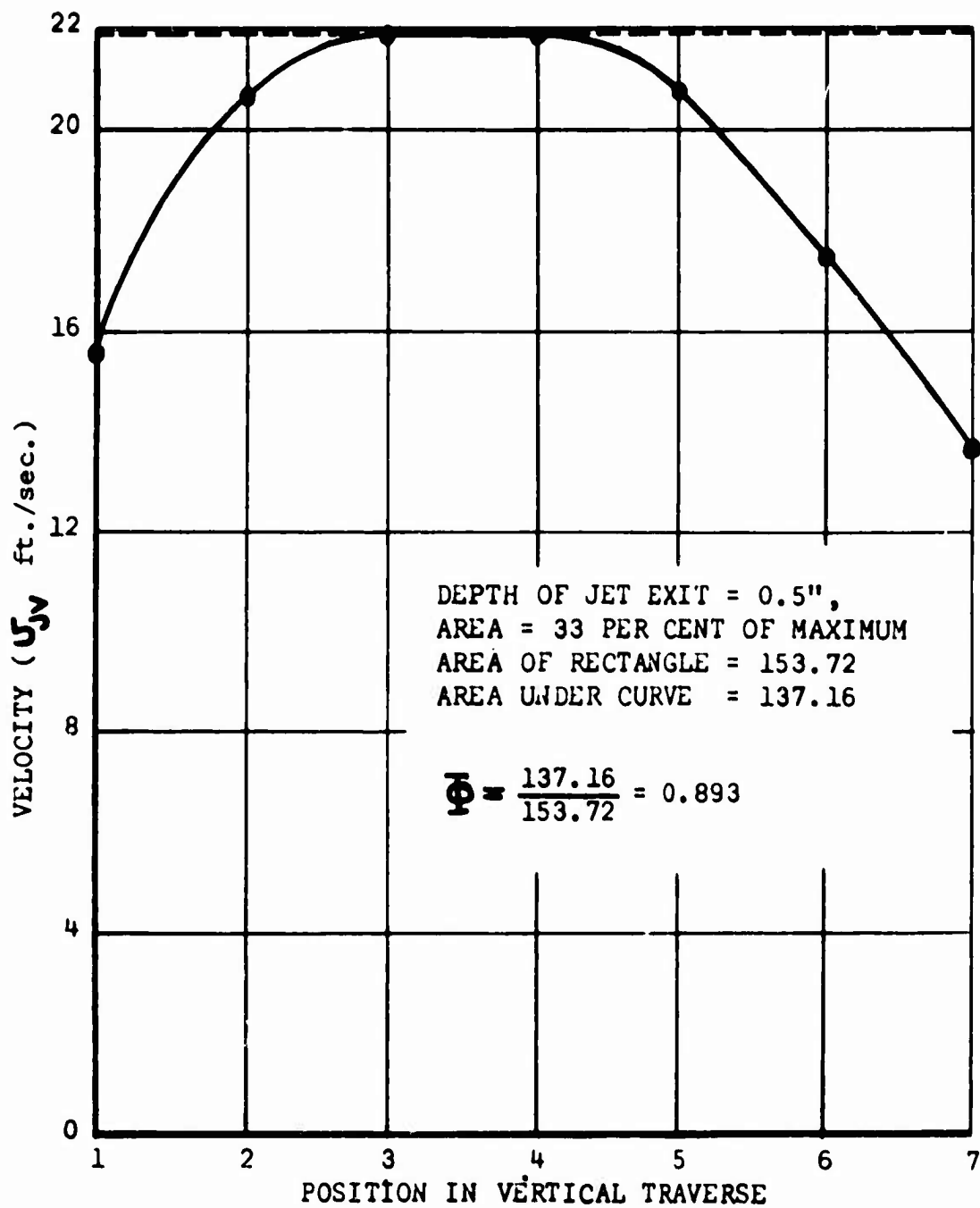
Figure 71. Vertical Velocity Profile
Across Jet Centerline At 400 RPM.

DEPTH OF JET EXIT = 0.5",
AREA = 33 PER CENT OF MAXIMUM
AREA UNDER RECTANGLE = 60.4
AREA UNDER CURVE = 56.8

$$\Phi = \frac{58.8}{60.4} = 0.975$$
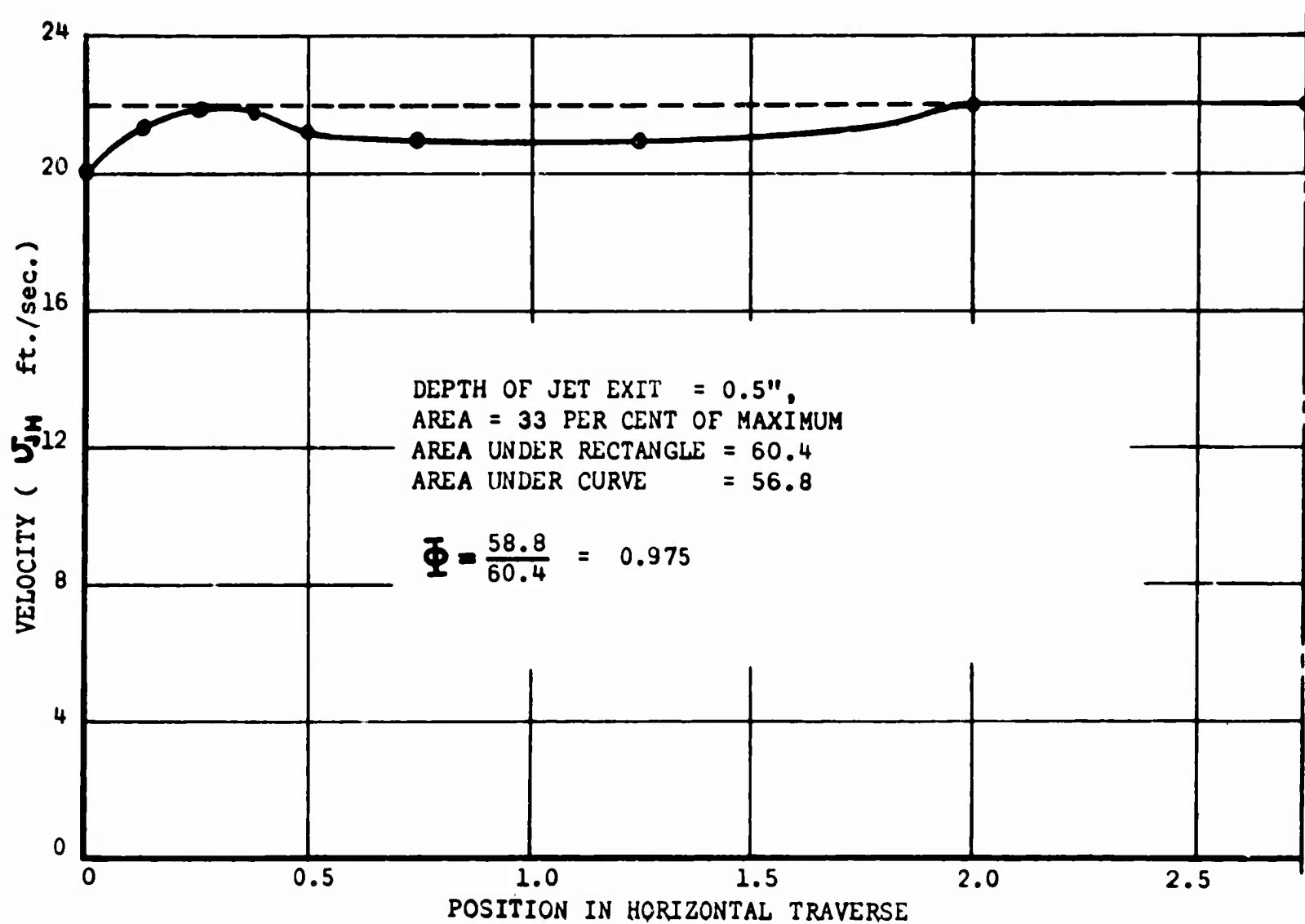
Figure 72. Horizontal Velocity Profile Across Jet Centerline at 400 RPM.
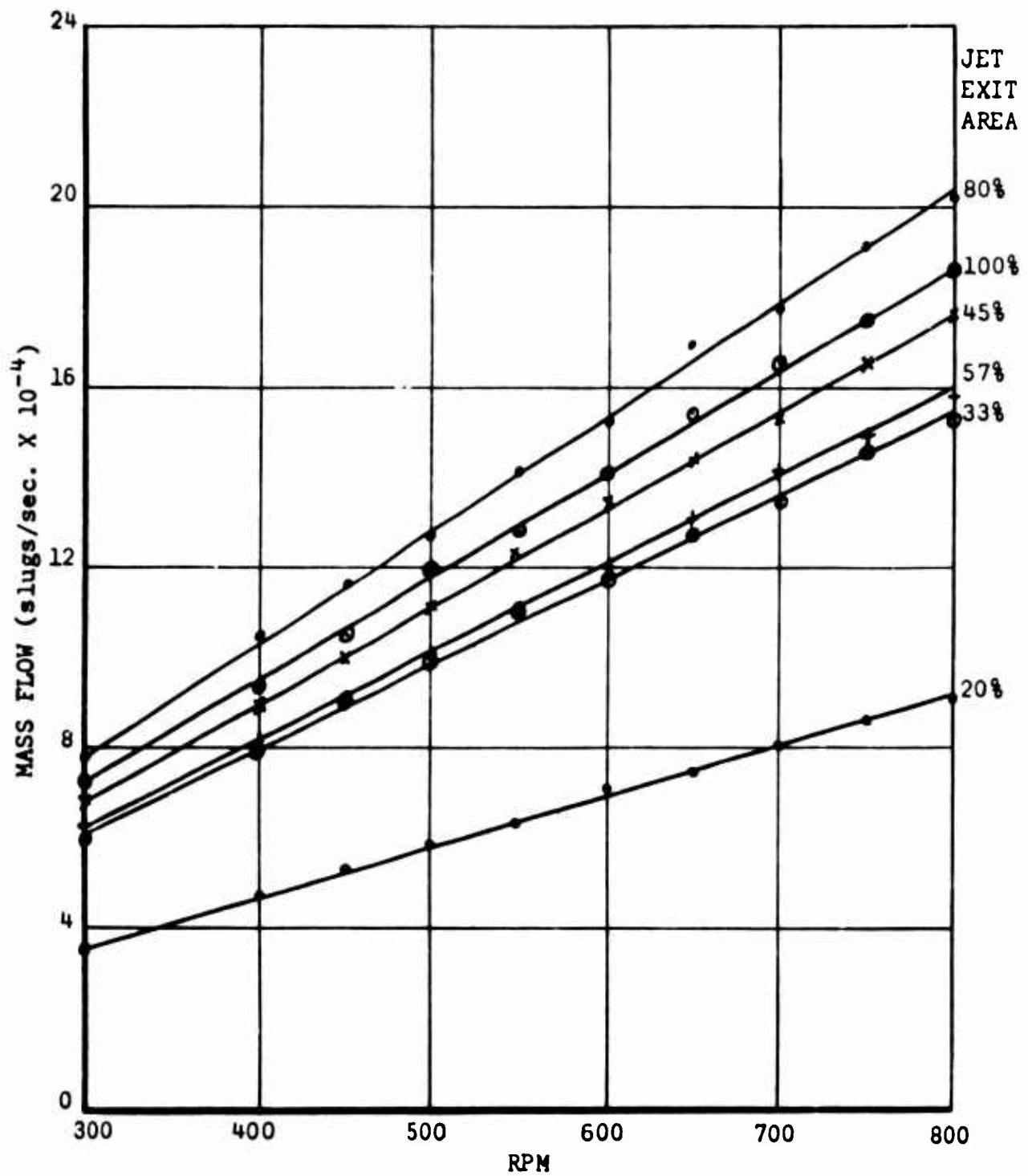
Figure 73. Variation of Mass Flow Rate With RPM
For Various Exit Areas, Exhausting to Ambient.

BLANK PAGE
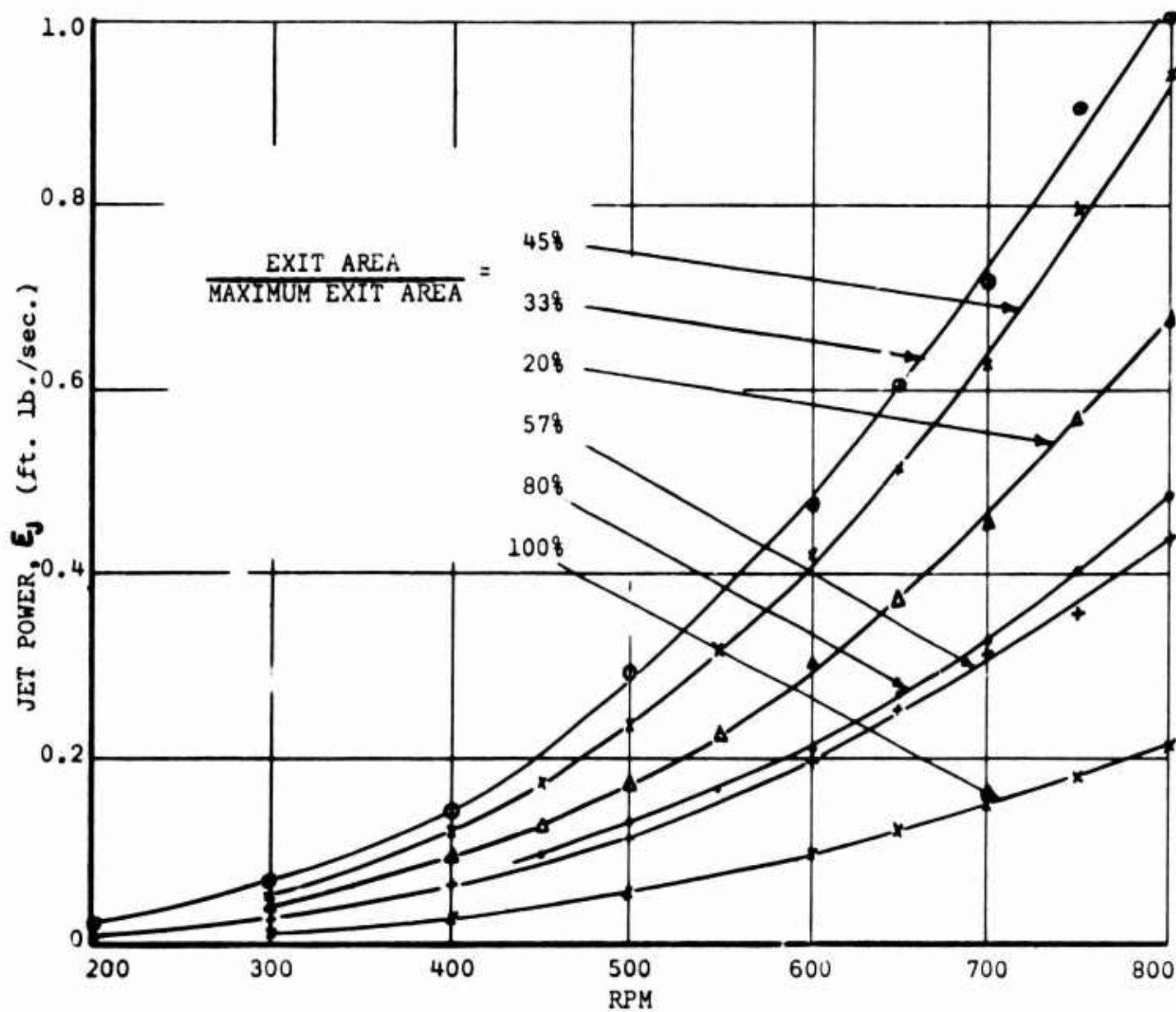
Figure 74. Variation of Jet Power With RPM For Various Exit Areas, Exhausting To Ambient.

97
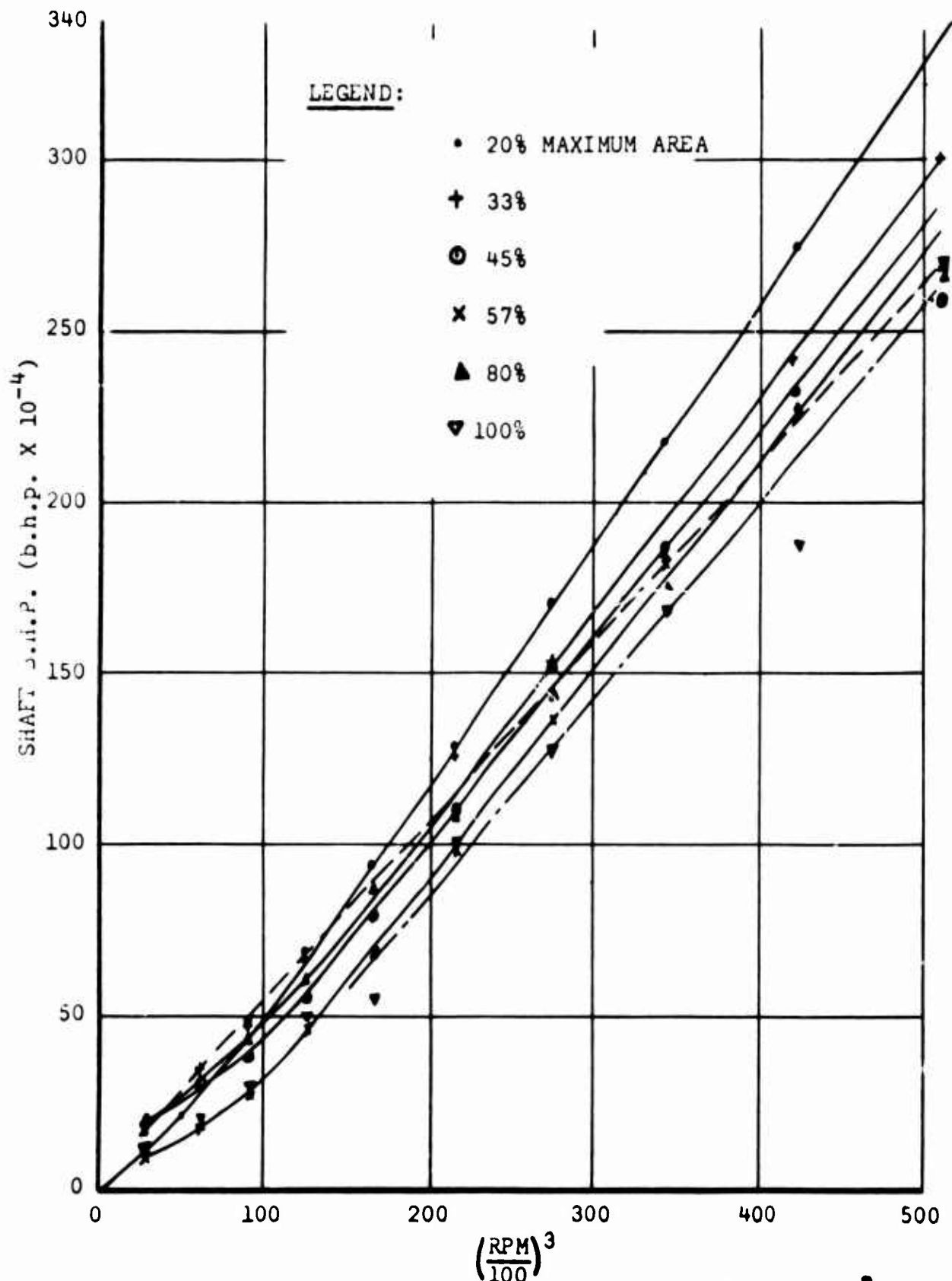
Figure 75. Variation of Shaft B.H.P. With $\left(\frac{RPM}{100}\right)^3$ For Various Exit Areas Exhausting to Ambient.
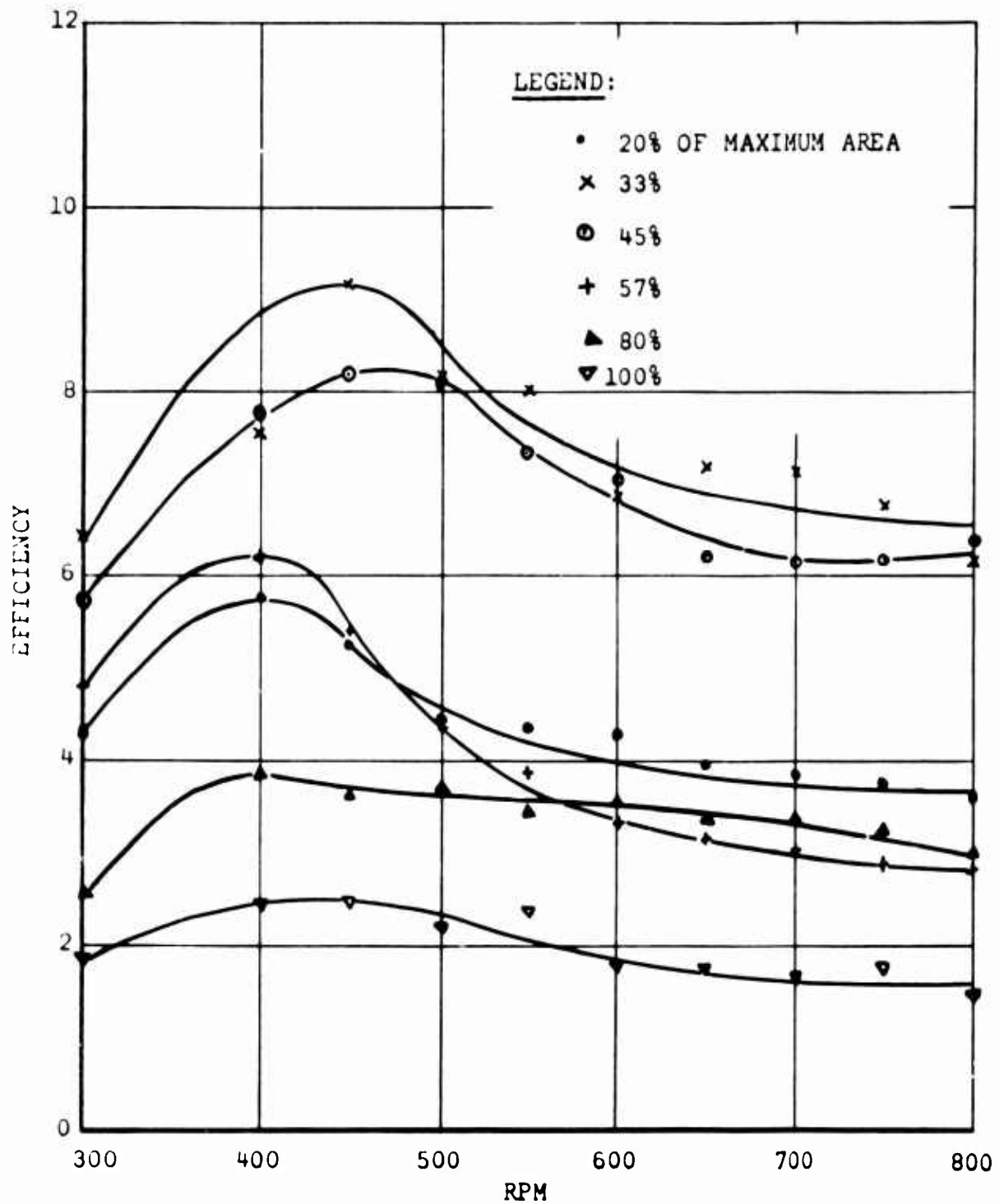
Figure 76. Variation of Efficiency With RPM
For Various Exit Areas, Exhausting to Ambient.

99
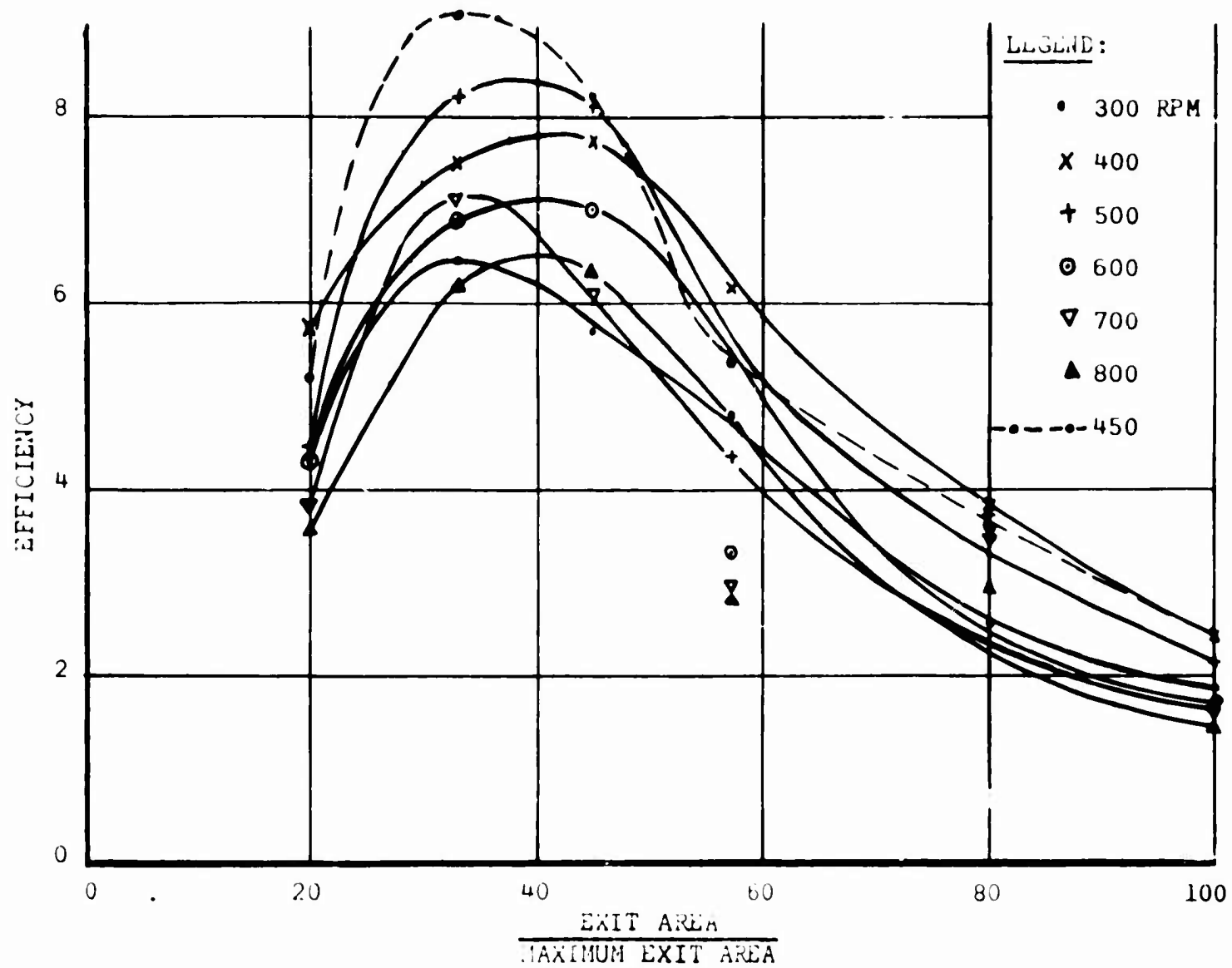
Figure 77. Variation of Efficiency with Exit Area, Exhausting to Ambient. (Cross Plot of Figure 76).

BLANK PAGE
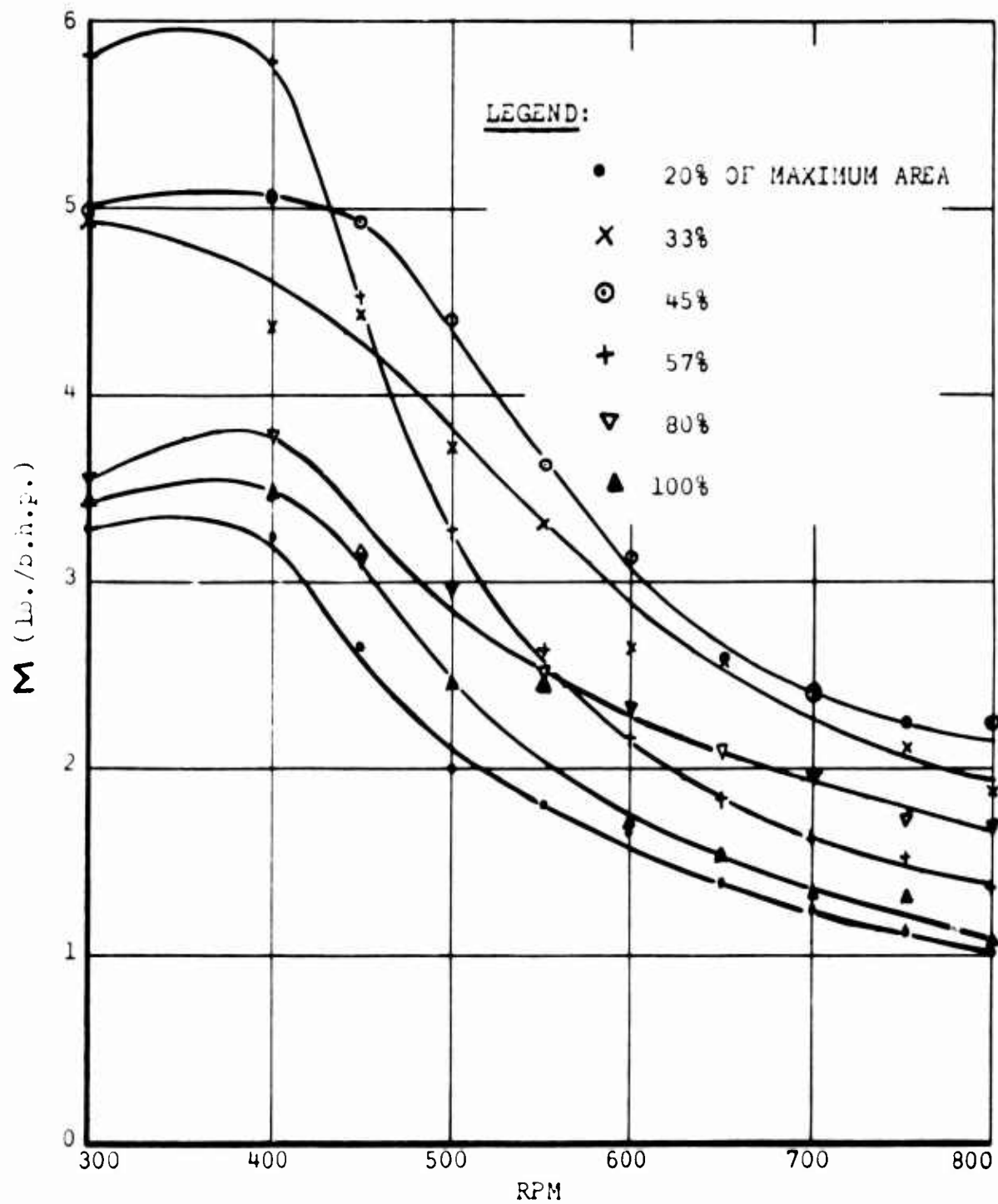
Figure 78. Variation of Momentum Flux Per Shaft BHP With RPM, For A Range of Exit Areas, Exhausting to Ambient.
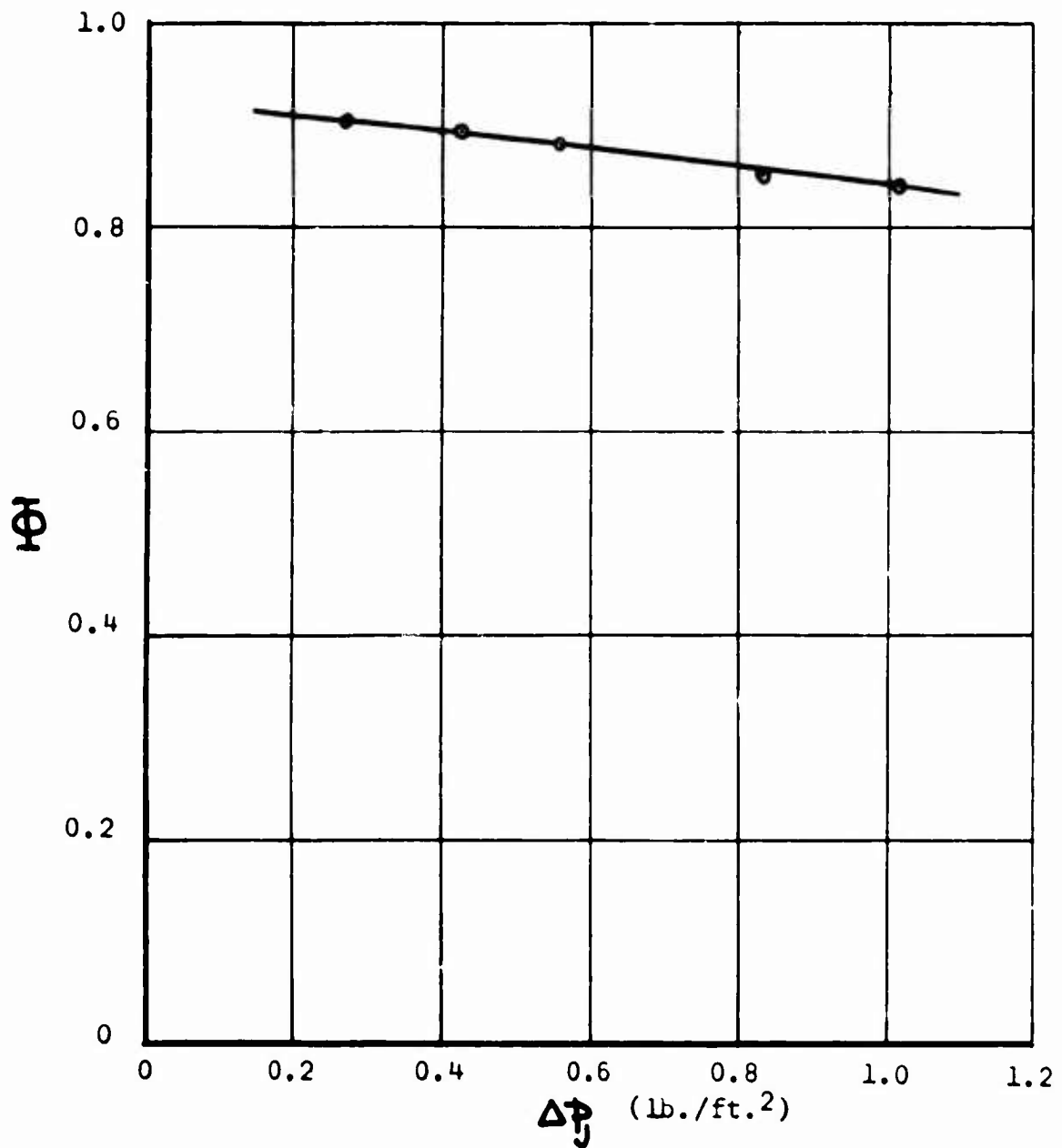
Figure 79. Effect of Plenum Chamber
Pressure ΔP_j On Flow Factor Φ .
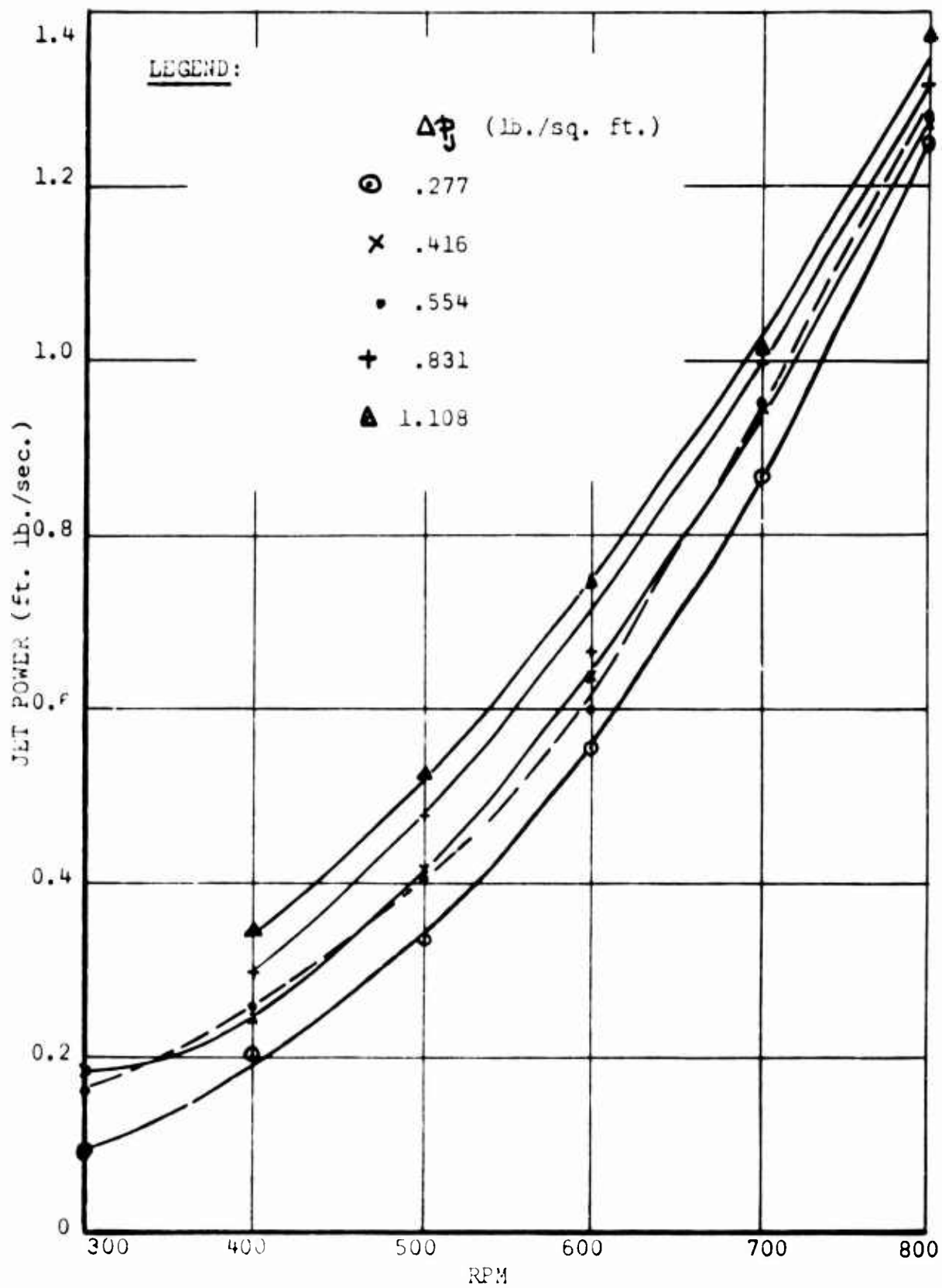
Figure 80. Variation of Jet Power With RPM,
For Various Back-Pressures.
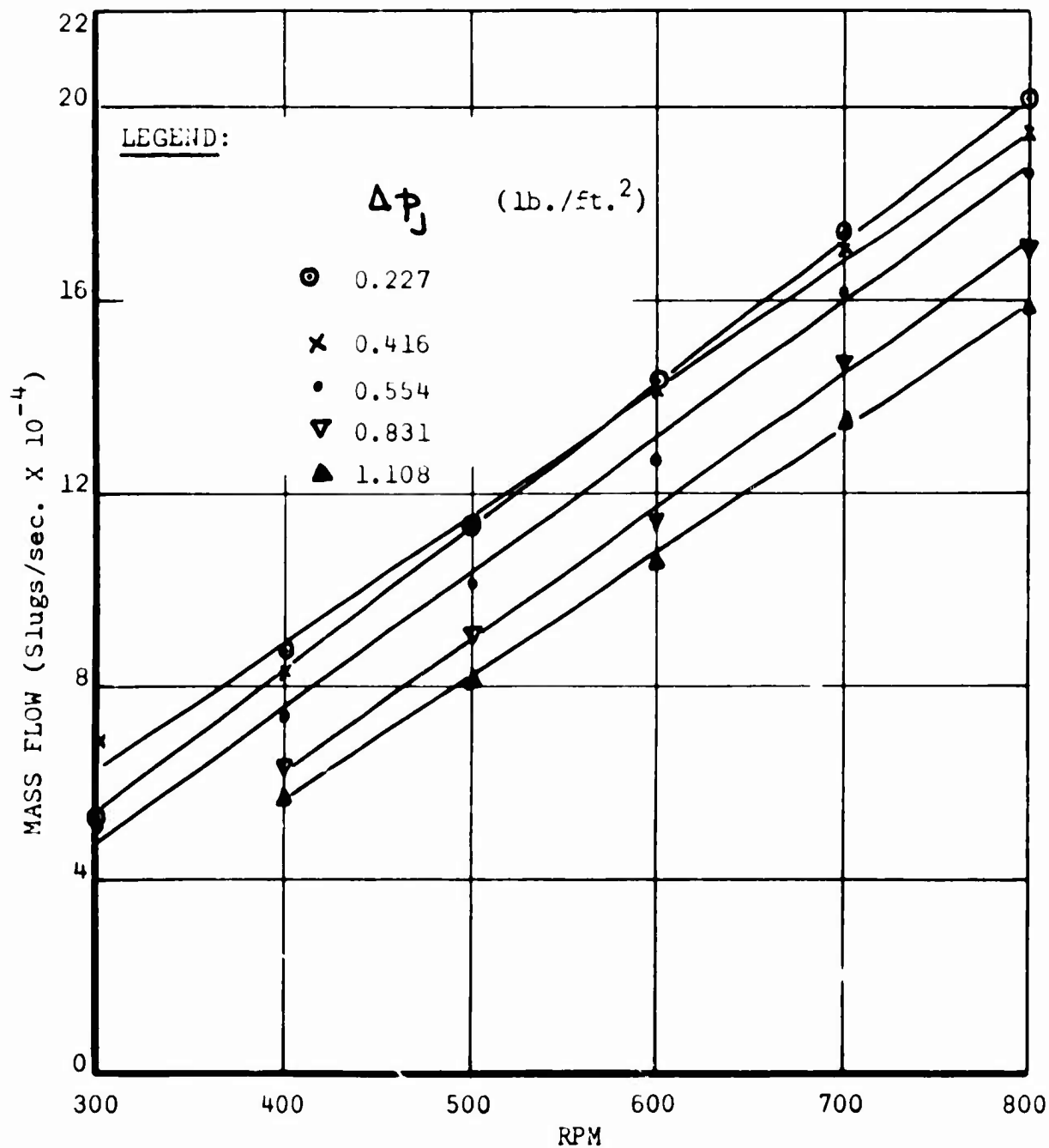
Figure 81. Variation of Mass Flow Rate With RPM,
For A Range of Back-Pressures.
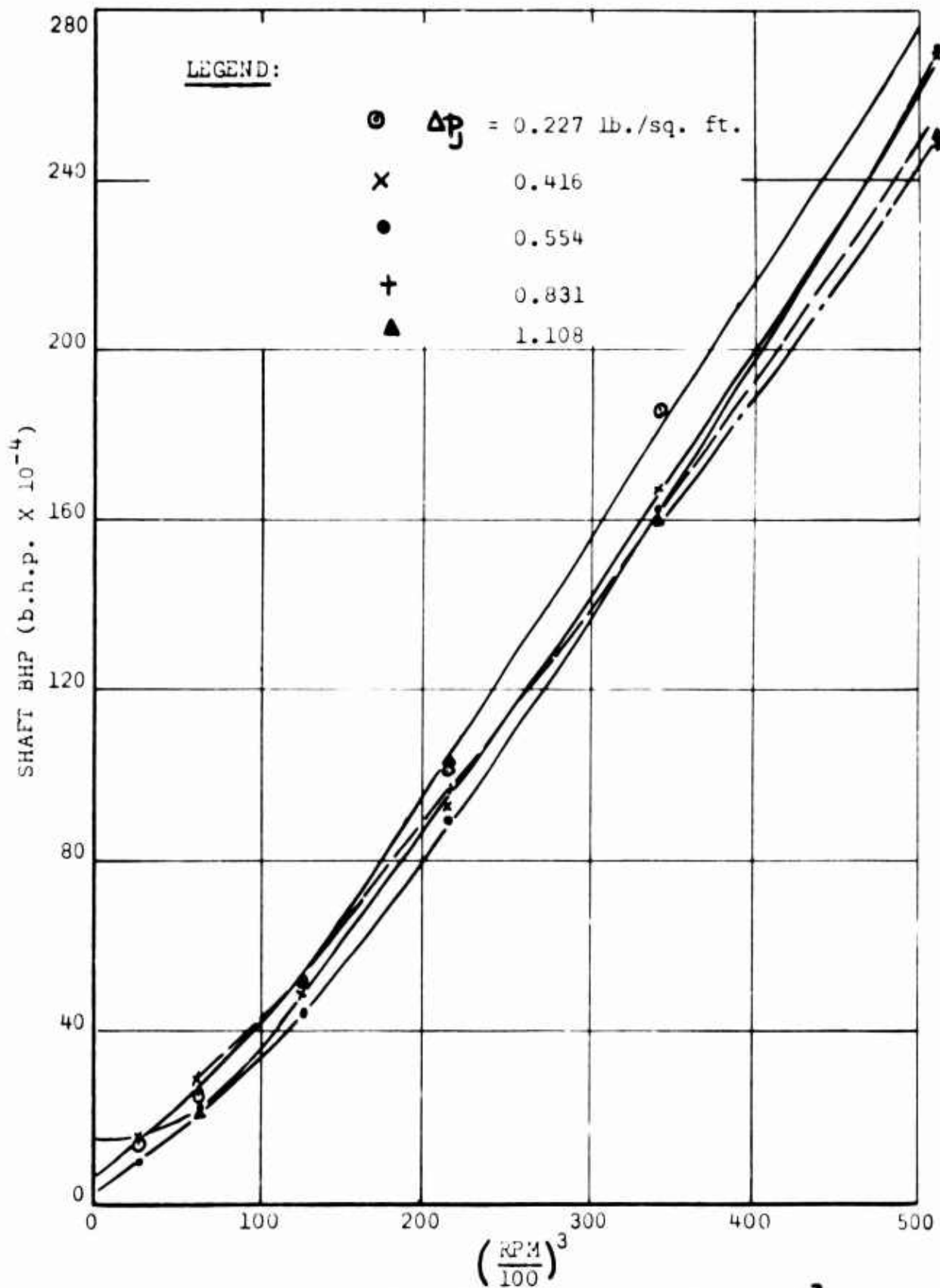
Figure 82. Variation of Shaft BHP With $\left(\frac{RPM}{100}\right)^3$ For A Range of Back-Pressures.

105
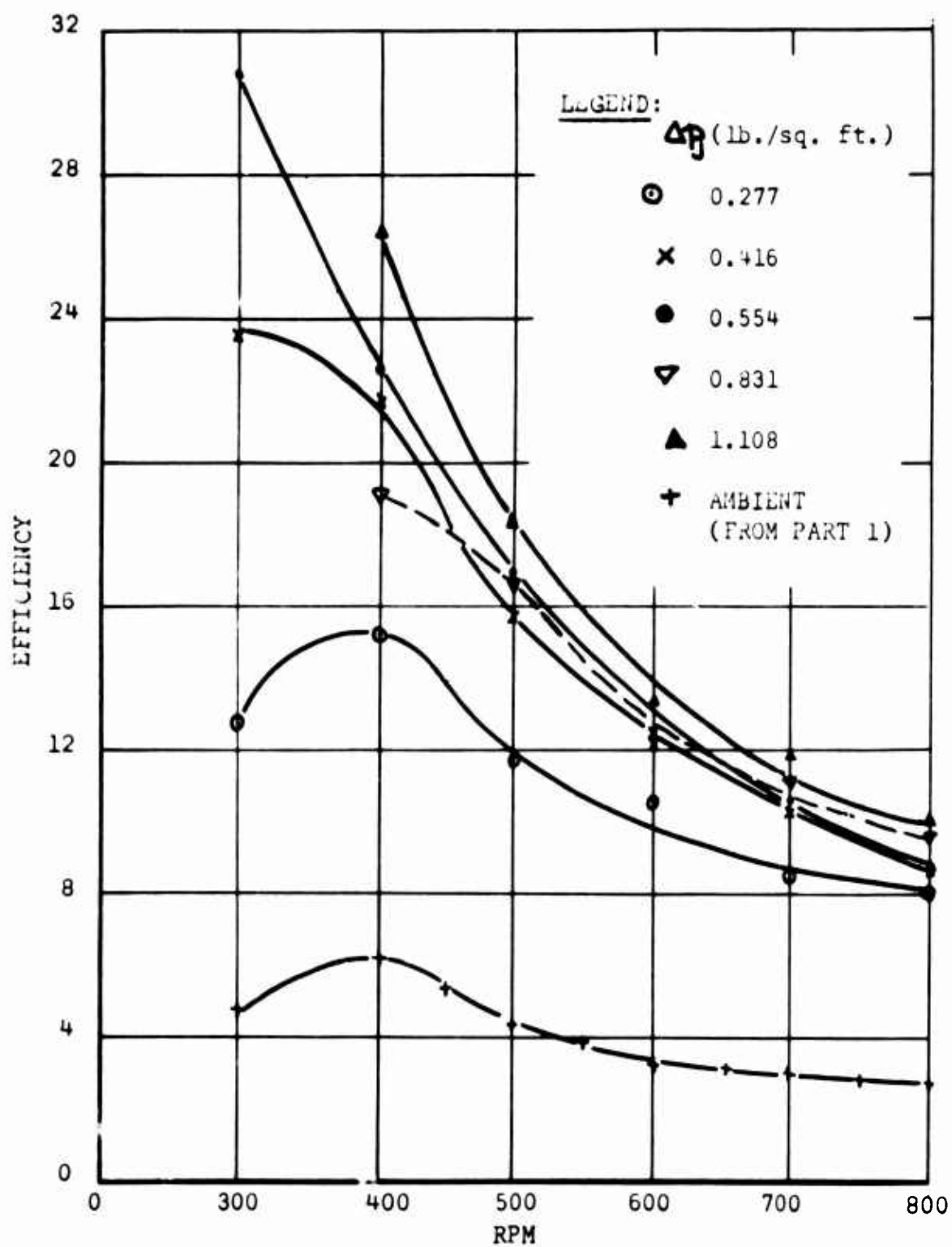
Figure 83. Variation of Efficiency With
RPM, For A Range of Back-Pressures.
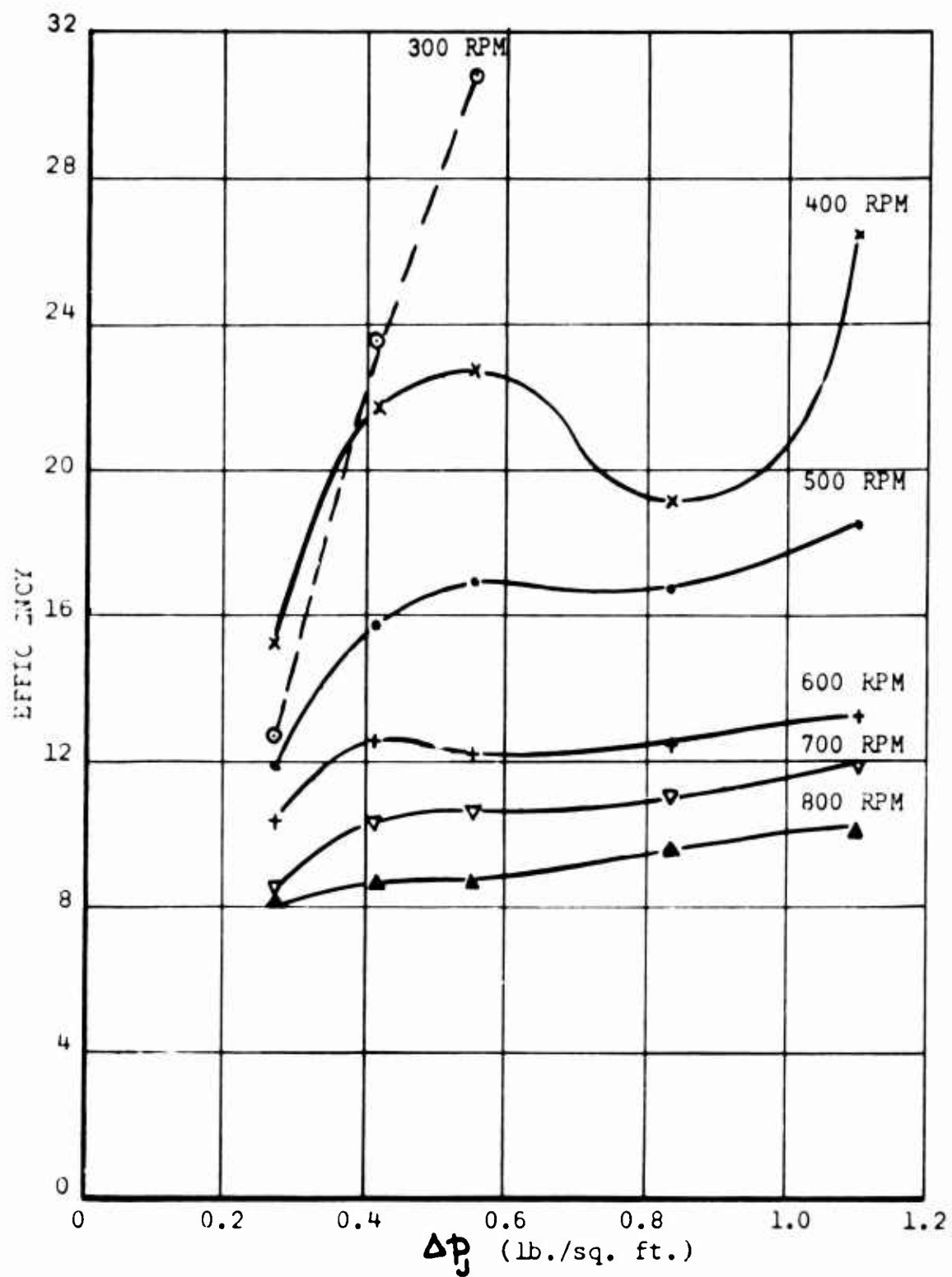
Figure 84. Variation of Efficiency With Back-Pressure, For A Range of Values of **RPM** (Cross Plot of Figure 83).

107

FROST FAN THEORY

INTRODUCTION

A detailed analysis of the theoretical advantages of a peripheral fan installation for Ground Effect Machines would be inappropriate in this report, which is concerned with the aerodynamic theory of one particular configuration, the Frost Fan. For a discussion of some of the system advantages implicit in the use of peripheral installations, the reader is referred to the introduction of Reference 25 and to the more detailed discussion in Reference 26.

Figure 85.   Ideal Peripheral Fan.

In principle, a peripheral fan is an attempt to approximate to the ideal air mover illustrated in Figure 85 in order to obtain near-zero duct losses together with maximum static stability in pitch and roll, and improved heave stiffness.

One way of achieving this type of peripheral flow is by use of the idealized rotary displacement pump illustrated in Figure 86, where the vanes are assumed to have zero mass and are infinite in number. We shall find that this idealization in the Frost Fan theory is analogous to the Froude actuator disc in propeller and helicopter rotor theory.

Figure 86.   Ideal Vane Pump.

A practical interpretation of Figure 86 - by no means the only one possible - is shown in Figure 87. In this application, the blades are hinged so that they can conform to the eccentric case, to which the tips are constrained on both sides by ball-bearing rollers turning in tracks. The blades are mass balanced about their inboard hinges so that the radial load on the tip rollers - and hence their frictional drag - can be reduced to a minimum. Another version, described and illustrated in Reference 26, utilizes only partially balanced blades and one degree of tip restraint, the blades being held against the case by the out-of-balance centrifugal force. As more knowledge is gained we can obviously hope to develop substantially cheaper constructional methods, possibly with the entire rotor and blade assembly as a single plastic extrusion. At the present time, however, it is more important to gain a thorough understanding of the principles involved and to develop theoretical treatments which reliably anticipate experimental results.

FAN BLADE

ROTOR ASSEMBLY

FAN CASE

DIRECTION OF
ROTATION
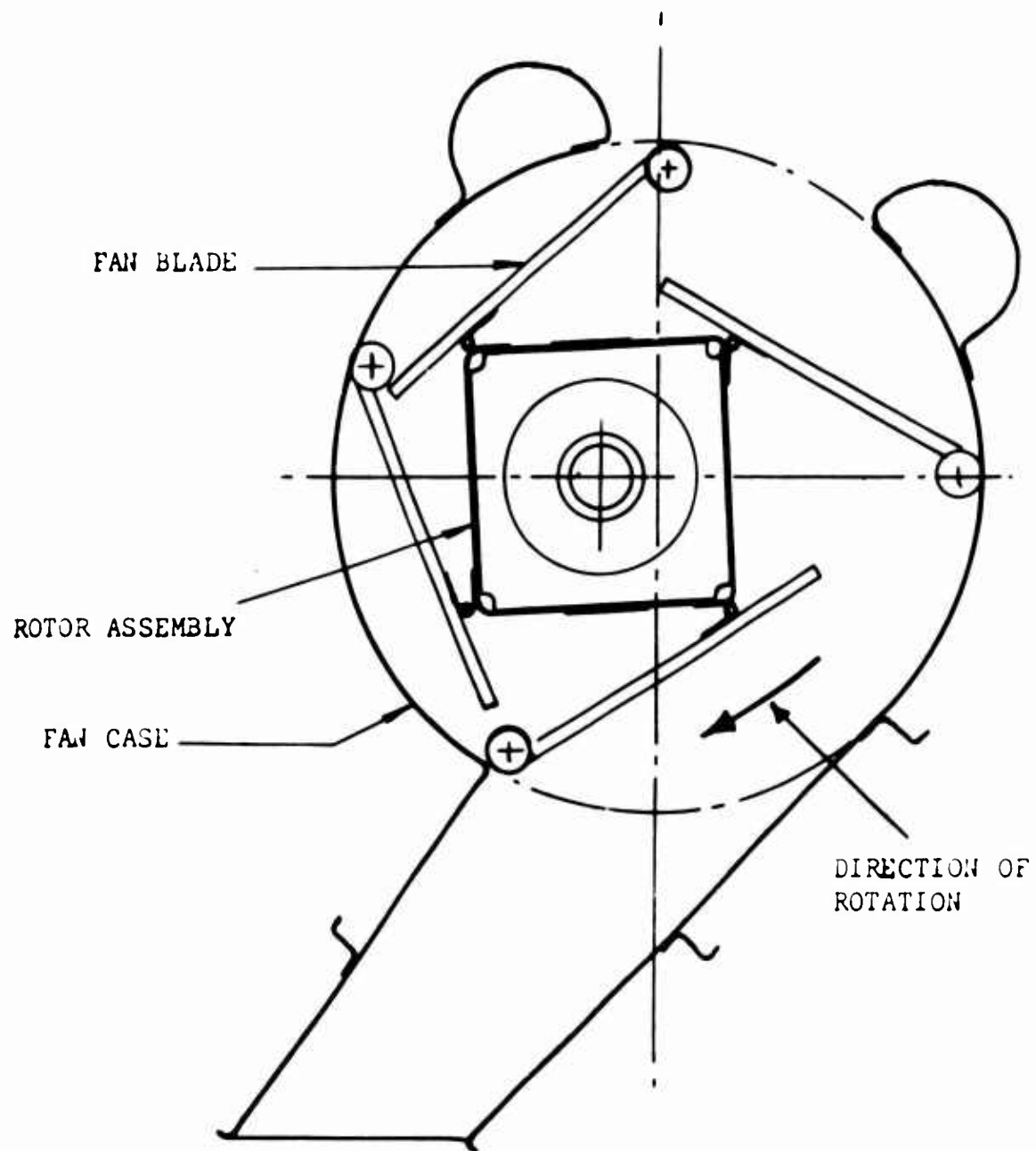
Figure 87. Frost Fan Assembly.

110

Figure 88. Simple Actuator Theory Model.

Considering the elemental fluid element in Figure 88(b) which is trapped between adjacent actuator vanes (of which there is assumed to be an infinite number), we see that its mass is, for incompressible flow and zero slip

$$\delta_{Mo} = \rho \left[\tfrac{1}{2} b R^2 \delta\theta - \tfrac{1}{2} b r_D^2 \delta\theta \right]$$

$$= \tfrac{1}{2} \rho b R^2 \delta\theta \left[1 - (r_D/R)^2 \right] \tag{62}$$

111

Since the rotational speed is Ω radians per second, this mass will pass through a given plane in $\delta\theta/\Omega$ seconds. Thus, the mass flow rate is

$$\frac{\dot{m}_o}{b} = \frac{\delta m_o}{t b} = \frac{1}{2}\rho\,\Omega R^2\left[1 - \left(\frac{r_b}{R}\right)^2\right] \tag{63}$$

or

$$\frac{\dot{m}_o}{bR} = \frac{1}{2}\rho\mu V_T = \frac{\mu q_T}{V_T} \tag{64}$$

where

$$\mu = \left[1 - \left(\frac{r_b}{R}\right)^2\right] \;,\quad V_T = \Omega R \tag{64a}$$

The ideal jet velocity is given by the equation for continuity,

$$\text{that is,}\quad \dot{m}_o = \rho A_J \upsilon_J \tag{65}$$

so that

$$\upsilon_{Jo} = \frac{\dot{m}_o}{\rho A_J} = \frac{1}{2}\mu\frac{V_T}{\hat{t}_J} \tag{65}$$

where

$$\hat{t}_J = \frac{t_J}{R}$$

The ideal jet momentum flux is

$$\frac{J_o}{bR} = \frac{\dot{m}_o \upsilon_{Jo}}{bR} = \mu^2\frac{q_T}{2\hat{t}_J} \tag{66}$$

where

$$q_T = \frac{1}{2}\rho V_T^2 = \frac{1}{2}\rho\,\Omega^2 R^2 \tag{67}$$

Note that J varies inversely with the jet exit dimension t_J . Thus, this provides a convenient means of imposing control moments on the vehicle. The jet power, when exhausting to ambient, is

$$\frac{E_{Ja}}{bR} = \frac{\dot{m}_o \upsilon_J^2}{2bR} = \frac{\mu^3}{8}\frac{q_T V_T}{\hat{t}_J^2} \tag{68}$$

When exhausting to a static overpressure Δp_J , the equivalent jet power is greater, because additional work is being done against the backpressure. The additional power is obviously $\Delta p_J A_J \upsilon_J$, so that the

general equation for jet power when exhausting to a static overpressure is

$$\frac{E_{JO}}{bR} = \frac{1}{8}\mu^3\frac{q_T V_T}{\hat{E}_J^2} + \frac{1}{2}\mu V_T \Delta P_J$$

$$= \frac{1}{2}\mu q_T V_T\left[\frac{1}{4}\left(\frac{\mu}{\hat{E}_J}\right)^2 + \frac{\Delta P_J}{q_T}\right] \qquad (69)$$

The ratio of the ideal momentum flux to the jet power from equations (66) and (69) is

$$V_T\frac{J_O}{E_{JO}} = \frac{\mu/\hat{E}_J}{\frac{1}{4}\left(\mu/\hat{E}_J\right)^2 + \Delta P_J/q_T} \qquad (70)$$

Finally, the total pressure at the jet exit for zero leakage is

$$\Delta P_{JO} = \Delta P_J + \frac{1}{2}\rho U_J^2$$

$$\frac{\Delta P_{JO}}{q_T} = \frac{1}{4}\left(\frac{\mu}{\hat{E}_J}\right)^2 + \frac{\Delta P_J}{q_T} \qquad (71)$$

Skin Friction Losses

Although it would be relatively simple to calculate the wetted area for a particular Frost Fan design, the value to be assigned to the skin friction coefficient C_f is uncertain enough for little value to be gained from such a calculation. Thus, we shall represent the fan by the simple idealization of a rotating cylinder of air and shall add to this the duct losses incurred in the exit nozzle. The peripheral velocity of this air cylinder will obviously vary between the extremes of Ωr_b and ΩR, and it is convenient to assume some equivalent mean velocity $\phi\Omega R$. Then, since the wetted area of the periphery of this cylinder is $2\pi\phi Rb$, the skin friction torque associated with it is

$$\phi R \cdot C_f \phi^2 q_T \cdot 2\pi\phi Rb \qquad (72)$$

The ends of the cylinder can be treated in a similar manner, using the construction sketched in Figure 89.
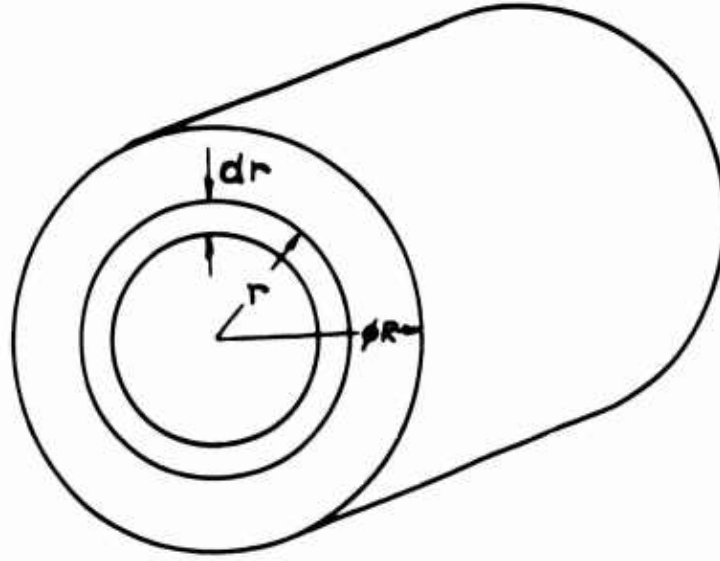
Figure 89. Geometry for Calculating End Losses.

Here the elemental torque due to the elemental annulus is

$$r. \quad C_f \tfrac{1}{2} \rho \, \Omega^2 \, r \, 2\pi r \, dr$$

Thus, the total torque for each end is

$$2\pi C_f \tfrac{1}{2} \rho \, \Omega^2 \int_0^{\phi R} r^3 \, dr \;=\; 2\pi C_f \tfrac{1}{2} \rho \Omega^2 \frac{\phi^4 R^4}{4}$$

$$= \frac{\pi}{2} C_f \, q_T \, \phi^4 R^2 \qquad\qquad (73)$$

Adding equation (72) to twice the value given by equation (73) (for two ends) and multiplying by Ω , the total power dissipated is

$$E_{SF} \;=\; 2\pi R^2 C_f q_T \phi^4 V_T \left[\frac{b}{R} + \frac{1}{2R} \right] \qquad (74)$$

In calculating efficiency, we require the ratio

$$\frac{E_{SF}}{E_{JO}} \;=\; \frac{4\pi \phi^4 C_f}{\mu} \; \frac{\left[1 + \tfrac{1}{2}b \right]}{\left[\frac{1}{4}\left(\frac{\mu}{E_J}\right)^2 + \frac{\Delta P_J}{q_T} \right]} \qquad (75)$$

114

The Influence of Slip

The calculation of slip due to air leakage through the gap between blades and case is very complicated if a full account is taken of all the factors involved. In this simple analysis we shall consider that there is a mean effective gap, of area A_L, and that the pressure differential across it is ΔP_J. Thus the velocity through this gap will be

$$U_L = \sqrt{\frac{2}{\rho} \Delta P_J} \qquad (76)$$

and the leakage mass flow will be

$$\dot{m}_L = \rho A_L U_L = A_L \sqrt{2\rho \, \Delta P_J} \qquad (77)$$

Now

$$\Delta P_J = \Delta P_J + \frac{1}{2}\rho U_J^2$$

$$= \Delta P_J + \frac{\dot{m}_J^2}{2\rho A_J^2} \qquad (78)$$

Also, utilizing equation (64) the actual mass flow ($\dot{m}_J$) is

$$\dot{m}_J = \dot{m}_o - \dot{m}_L = \mu \frac{q_T}{V_T} bR - \dot{m}_L \qquad (79)$$

Substituting for $\dot{m}_J$ in (78)

$$\Delta P_J = \Delta P_J + \frac{1}{2\rho A_J^2}\left[\mu \frac{q_T}{V_T} bR - \dot{m}_L\right] \qquad (80)$$

Substituting for ΔP_J in equation (77)

$$\frac{\dot{m}_L}{A_L} = \overline{m}_L = \sqrt{2\rho \, \Delta P_J + \left[\mu \frac{q_T}{V_T \, \hat{t}_J} - a_L \overline{m}_L\right]}$$

Squaring both sides

$$(1 - a_L^2)\overline{m}_L^2 + 2\frac{\mu q_T}{V_T \, \hat{t}_J} a_L \overline{m}_L - \left(\frac{\mu q_T}{V_T \, \hat{t}_J}\right)^2 - 2\rho \, \Delta P_J = 0 \qquad (81)$$

115

$$\therefore \ \overline{m}_L = \frac{-2a_L\left(\frac{\mu q_T}{V_T \hat{\epsilon}_J}\right) + \sqrt{4a_L^2\left(\frac{\mu q_T}{V_T \hat{\epsilon}_J}\right)^2 + 4(1-a_L^2)\left[\left(\frac{\mu q_T}{V_T \hat{\epsilon}_J}\right)^2 + 2\rho \Delta P_J\right]}}{2 - 2a_L^2}$$

$$= \frac{-a_L\left(\frac{\mu q_T}{V_T \hat{\epsilon}_J}\right) + \sqrt{\left(\frac{\mu q_T}{V_T \hat{\epsilon}_J}\right)^2 + 2\rho \Delta P_J(1-a_L^2)}}{1 - a_L^2} \tag{82}$$

Note that for $\Delta P_J \longrightarrow 0$

$$\overline{m}_L \longrightarrow \frac{\mu q_T}{V_T \hat{\epsilon}_J} \Big/ 1 + a_L \tag{83}$$

$$\frac{\dot{m}_J}{A_J} \longrightarrow \frac{\mu q_T}{V_T \hat{\epsilon}_J} - \overline{m}_L a_L \longrightarrow \frac{\mu q_T}{V_T \hat{\epsilon}_J} \Big/ 1 + a_L \tag{84}$$

$$\therefore \ \dot{m}_J / A_J \longrightarrow \overline{m}_L$$

Equation (84) is the same as equation (64) except for the addition of the term $(1 + a_L)$ to the numerator. It follows from equation (65) that

$$\frac{U_J}{V_T} = \frac{\dot{m}_J}{A_J} \Big/ \rho V_T = \frac{\mu}{2\hat{t}_J(1+a_L)} = \frac{\mu}{2(\hat{\epsilon}_J + \hat{\epsilon}_L)} \tag{85}$$

where $\hat{t}_J = \frac{A_L}{bR} = \frac{A_L}{A_J}\hat{\epsilon}_J = a_L \hat{\epsilon}_J$

When the back-pressure ΔP_J is finite, equation (82) gives

$$\overline{m}_L = \frac{\mu q_T}{V_T \hat{\epsilon}_J} \Big/ 1 - a_L^2 \left\{ \sqrt{1 + \frac{4}{\mu^2}\left(\hat{t}_J^2 - \hat{t}_L^2\right)\left(\frac{\Delta P_J}{q_T}\right)} - a_L \right\} \tag{86}$$

Therefore, from equation (84)

$$\frac{\dot{m}_J}{A_J} = \frac{\mu q_T}{V_T \hat{\epsilon}_J} \left\{ 1 + \frac{a_L^2}{1 - a_L^2} - \frac{a_L\sqrt{1 + \frac{4}{\mu^2}\left(\hat{t}_J^2 - \hat{t}_L^2\right)\left(\frac{\Delta P_J}{q_T}\right)}}{1 - a_L^2} \right\}$$

116

$$= \frac{\mu q_T}{V_T \hat{t}_J} \frac{}{1-a_L^2} \left\{ 1 - a_L \sqrt{1 + \frac{4}{\mu^2}(\hat{t}_J^2 - \hat{t}_L^2)\left(\frac{\Delta P_J}{q_T}\right)} \right\} \tag{87}$$

and

$$\frac{\dot{m}_J}{\dot{m}_o} = \left\{ 1 - a_L \sqrt{1 + \frac{4}{\mu^2}(\hat{t}_J^2 - \hat{t}_L^2)\left(\frac{\Delta P_J}{q_T}\right)} \right\} \frac{1}{1-a_L^2} \tag{88}$$

The effect of slip on efficiency is obtained by accounting for the reduction in the kinetic energy E_J which is occasioned by the leakage. From equation (68)

$$E_J = \frac{1}{2} \dot{m}_J U_J^2 + \Delta P_J A_J U_J$$

$$= \frac{\dot{m}_J^3}{2\rho^2 A_J^2} + \frac{\Delta P_J \dot{m}_J}{\rho} \tag{89}$$

$$\frac{E_J \text{ without slip}}{E_J \text{ with slip}} = 1 + \frac{E_L}{E_J} = \frac{\dfrac{\dot{m}_o^3}{2\rho A_J^2} + \Delta P_J \dot{m}_o}{\dfrac{\dot{m}_J^3}{2\rho A_J^2} + \Delta P_J \dot{m}_J}$$

$$= \frac{1 + 2\rho \dfrac{A_J^2 \Delta P_J}{\dot{m}_o^2}}{\dfrac{\dot{m}_J}{\dot{m}_o}\left[\left(\dfrac{\dot{m}_J}{\dot{m}_o}\right)^2 + \dfrac{2\rho A_J^2 \Delta P_J}{\dot{m}_o^2} \right]} \tag{90}$$

and since $\dfrac{\dot{m}_o}{A_J} = \dfrac{\mu q_T}{V_T \hat{t}_J}$ from equation (64)

$$1 + \frac{E_L}{E_S} = \frac{1 + \dfrac{4}{\mu^2} \hat{t}_J^2 \left(\dfrac{\Delta P_J}{q_T}\right)}{\left(\dfrac{\dot{m}_J}{\dot{m}_o}\right)\left[\left(\dfrac{\dot{m}_J}{\dot{m}_o}\right)^2 + \dfrac{4}{\mu^2} \hat{t}_J^2 \left(\dfrac{\Delta P_J}{q_T}\right) \right]} \tag{91}$$

where ($\dot{m}_J / \dot{m}_o$) is given by equation (88).

117

Note that as $\Delta P_J \rightarrow 0$

$$1 + \frac{E_L}{E_J} \longrightarrow \left(\frac{\dot{m}_o}{\dot{m}_J}\right)^3$$

$$\longrightarrow (1 + a_L)^3 \qquad\qquad (92)$$

The Calculation of Efficiency

The total power requirement given by simple actuator disc theory, and neglecting friction effects, is

$$E_T = E_J + E_{SF} + E_L = E_J\left[1 + \frac{E_L}{E_J} + \frac{E_{SF}}{E_J}\right] \qquad (93)$$

$$\therefore \quad \frac{1}{\eta_F} = \frac{E_T}{E_J} = 1 + \frac{E_L}{E_J} + \frac{E_{SF}}{E_J} \qquad (94)$$

- where the two terms of equation (94) are given by equations (91) and (76).

Comparison of Simple Theory with Experiment

Before proceeding to refine the simple theory described in the previous sections, we shall compare its results with the experimental measurements reported in Reference 24. It should be remembered that this test rig, illustrated in Figure 90, was extremely crude, by normal experimental standards, and that its blades were not balanced. Thus, its absolute efficiency is very low (due to friction and large leakage losses) while its small size makes appreciable experimental scatter inevitable.

Considering first the measurements made when the fan was exhausting to ambient, the variation of the jet velocity at the center of the jet is plotted in Figure 91. The linearity with speed, as predicted by theory, is obviously excellent.

The flow factor (Φ) associated with this velocity is plotted in Figure 92, as a function of jet exit area. The considerable scatter is probably due to the rather complex shape of the nozzle and the fact that the measuring plane was some distance downstream of the nozzle exit plane.

118

Since the jet velocity varies linearly with r.p.m., we can conveniently use the parameters $\dfrac{V_J}{V_T}$ and $\dfrac{\dot{m}_J}{V_T}$

Since r_b = .2655, R = 0.3645 ft., bR = 0.167 ft.^{2} A_L = .00481, $\hat{t}_L$ = .0288

$$V_T = .03815 \text{ (r.p.m.)}, \quad 100\% \, A_J = .05845 \text{ ft.}^2 \quad \mu = 0.47$$

$$100\% \, \hat{t}_J = 0.35 \qquad\qquad \text{mean } \rho = 20.5 \times 10^{-4} \text{ slugs/ft.}^2$$

$$\dot{m}_J = V_{Jc} \rho A_J \Phi = 0.81 \times .05845 \times 20.5 \times 10^{-4} \times \left(\% A_J\right)$$

$$= 0.97 \times 10^{-4} \, V_J \left(\% A_J\right)$$

Thus, from Figure 91 we have

A_J/A_{JN} =	20%	33%	45%	57%	80%	100%
V_{Jc} =	46.2	43.1	37.9	32.2	26.0	20.8 (ft./ sec. at 800 r.p.m.)
V_{Jc}/V_T =	1.515	1.415	1.242	1.055	.852	.681
$\left(\dot{m}_J/V_T\right) \times 10^4$ =	.294	.454	.543	.5845	.661	.661

These results are plotted in Figures 94 and 95.

From equation (85)

$$\frac{V_T}{V_J} = \frac{2\left(\hat{t}_J + \hat{t}_L\right)}{\mu} \tag{95}$$

$$\frac{d\left(V_T/V_J\right)}{d\hat{t}_J} = \frac{2}{\mu} \tag{96}$$

Thus, we can determine the equivalent values of both $\hat{t}_L$ and μ from a plot of the type shown in Figure 93, since

$$\hat{t}_J = \frac{t_J}{R} = \frac{A_J}{bR} = \frac{A_J}{A_{JN}} \frac{A_{JN}}{bR} = \frac{A_J}{A_{JN}} \hat{t}_{JN}$$

Now $\dfrac{d\left(V_T/V_J\right)}{d\hat{t}_J} = \dfrac{d\left(V_T/V_J\right)}{d\left(A_J/A_{JN}\right)} \dfrac{d\left(A_J/A_{JN}\right)}{d\hat{t}_J}$

119

It is evident from Figure 93 that the best line drawn through the experimental dat has the slope which we should expect from equation (96), and we assume that the two points for the smallest exit areas are diverging from this because of blade stall at the intake, caused by the high blade angle of attack associated with the low mass flows.

The effective leakage area of the model is evidently greater than the measured geometric values, however, and we can determine this effective value from equation (95), since

$$\left(\frac{V_T}{U_J}\right)_{\hat{E}_J \to 0} = \frac{2\hat{E}_L}{\mu} \tag{97}$$

For the values in Figure 93

$$\hat{E}_L = \frac{1}{2}\mu\left(\frac{V_T}{U_J}\right)_{\hat{E}_J \to 0} = 0.5 \times 0.47 \times 0.3 = .0706$$

$$a_{LN} = \frac{\hat{E}_L}{\hat{E}_{JN}} = \frac{.0706}{.35} = 0.2015$$

The measured $\hat{E}_L$ value is large, compared with the geometric leakage area of one blade ($\hat{E}_L$ = .0288), indicating that other gaps and flow mechanisms are of considerable importance or   at the blades are deflecting to cause larger gaps under the influence of centrifugal force.

From equation (84) we can now calculate the mass flow $\dot{m}_J$ and compare it with the model results using the values μ = 0.47, $\hat{E}_L$ = .0706.

For A_J / A_{JN} =

	5%	10%	20%	40%	60%	80%	100%
a_L =	4.03	2.015	1.008	.504	.336	.252	.2015
$1 + a_L$ =	5.03	3.015	2.008	1.504	1.336	1.252	1.2015
$\hat{E}_J(1+a_L)$ =	.088	.1055	.1407	.2105	.29	.3505	.421
U_J / V_T =	2.67	2.225	1.67	1.115	.84	.67	.559
$(\dot{m}_J / V_T) \times 10^4$ =	.16	.2665	.400	.534	.604	.642	.67

This is plotted in Figures 94 and 95 where the agreement with experiment is seen to be very good, except for very low mass flows. In summary then, it appears that the theory gives the correct result when the geometrically measured value is used for the parameter μ and when the leakage parameter $\hat{t}_L$ is about 145 per cent in excess of its geometric value. This latter is obtained by measuring the lateral blade clearance at both ends of a blade, multiplying by R, and adding the result to the tip clearance area. For maximum accuracy the average value for all the blades should be computed.

We now proceed to check the effect of jet back-pressure ΔP_J on jet velocity, using the experimental data in Reference 24, which is tabulated in Table 3.

Since $U_J = \dfrac{\dot{m}_J}{\rho A_J}$, we have from equation (97)

$$\frac{U_J}{V_T} = \frac{\mu}{2\hat{t}_J(1-a_L^2)}\left\{ 1 - a_L\sqrt{1+\frac{4}{\mu^2}\left(\hat{t}_J^2 - t_L^2\right)\left(\frac{\Delta P_J}{q_T}\right)} \right\} \qquad (98)$$

from which it follows that $U_J = 0$ when

$$\frac{\Delta P_J}{q_T} = \left(\frac{\mu}{2\hat{t}_J a_L}\right)^2 = \left(\frac{\mu}{2\hat{t}_L}\right)^2 \qquad (99)$$

In the limit, as $\dfrac{\Delta P_J}{q_T} \longrightarrow 0$,

$$\frac{U_J}{V_T} \longrightarrow \frac{\mu}{2\hat{t}_J(1-a_L^2)}\left\{ 1 - a_L\left[1 + \frac{2}{\mu^2}\left(\hat{t}_J^2 - \hat{t}_L^2\right)\left(\frac{\Delta P_J}{q_T}\right)\right] \right\} \qquad (100)$$

Differentiating equation (100) with respect to $\dfrac{\Delta P_J}{q_T}$

$$\frac{d\left(U_J/V_T\right)}{d\left(\Delta P_J/q_T\right)} \longrightarrow -\frac{\hat{t}_L}{\mu} \text{ as } \frac{\Delta P_J}{q_T} \longrightarrow 0 \qquad (101)$$

For the test fan this is seen from Figure 96 to be in reasonable agreement with the theoretical slope at this point, when the geometrical value of $\mu = 0.47$ is used in conjunction with $\hat{t}_L = .0706$.

121

TABLE 3

REDUCTION OF REFERENCE 24 DATA FOR
POSITIVE BACK-PRESSURE ΔP_J IN JET

RPM	V_T	$\frac{1}{2}\rho V_T^2$	ΔP_J =	.277	.416	.554	.831	1.108
						v_{JC}/v_T		
300	11.42	.134		.796	1.03	.796	-	-
400	15.24	.239		.975	.935	.844	.75	.677
500	19.05	.373		1.013	1.02	.926	.86	.771
600	22.85	.538		1.07	1.06	.964	.904	.843
700	26.7	.733		1.105	1.087	1.05	.987	.915
800	30.5	.958		1.122	1.083	1.062	1.01	.9425

RPM				$\Delta P_J/q_T$				
300				2.065	3.105	4.14	-	-
400				1.16	1.742	2.32	3.48	4.64
500				.743	1.117	1.485	2.23	2.97
600				.515	.774	1.029	1.545	2.06
700				.378	.568	.755	1.133	1.51
800				.289	.435	.578	.868	1.157

$$\Phi = 0.81$$

Returning to equation (98) we see that it can be written as

$$\frac{U_J}{V_T} = \left(\frac{U_J}{V_T}\right)_{CONST} - \Delta\left(\frac{U_J}{V_T}\right)$$

where

$$\left(\frac{U_J}{V_T}\right)_{CONST.} = \frac{\mu}{2\hat{E}_J(1-a_L^2)} = \left[\left(\frac{U_J}{V_T}\right)_0 + a_L\right]$$

$$\Delta\left(\frac{U_J}{V_T}\right) = a_L^2 + \left(\frac{2\hat{E}_L}{\mu}\right)^2(1-a_L^2)\left(\frac{\Delta P_J}{q_T}\right)$$

(102)

In other words, $\Delta\left(\frac{U_J}{V_T}\right)$ should be a linear function of $\frac{\Delta P_J}{q_T}$.

That is,

$$\frac{d\,\Delta(U_J/V_T)^2}{d\left(\Delta P_J/q_T\right)} = \frac{2\hat{E}_L}{\mu}(1-a_L^2) = K$$

so that

$$\hat{E}_L^2(1-a_L^2) = \frac{\mu^2 K}{4}$$

$$\left(\hat{E}_L^2\right)^2 - \hat{E}_J^2\left(\hat{E}_L^2\right) + K\left(\frac{\mu\hat{E}_J}{2}\right)^2 = 0$$

$$\therefore \hat{E}_L^2 = \frac{1}{2}\left[\hat{E}_J^2 - \sqrt{\hat{E}_J^4 - \mu^2\hat{E}_J^2 K}\right]$$

or

$$a_L^2 = \frac{1}{2}\left[1 - \sqrt{1 - \left(\frac{\mu}{\hat{E}_J}\right)^2 K}\right]$$

(103)

This analysis gives us an alternative method of determining $\hat{E}_L$ from experimental data. However, it is doubtful whether it would be of value to apply it to the available data, because of the degree of experimental scatter present in it.

It will be noted from Figure 96 that, with the plenum chamber in position to create a back-pressure, the value of $U_J/V_T \rightarrow 0.95$ (approximately) as $\Delta P_J \rightarrow 0$, whereas a value of 0.87 is obtained when exhausting to ambient ($\Delta P_J = 0$). The reasons for this 9 per cent displacement are not clear, but are probably connected with vortex flow or some similar constraint which is introduced by the plenum chamber. Thus, this inconsistency is not regarded as important for present

123

purposes. The slope of the data, on the other hand, is exceedingly important, and the good agreement with equation (101) is regarded as adequate justification for the basic leakage flow postulate, at low values of $\Delta P_J / q_T$.

It also appears (from Figure 96) that the experimental data follow the theoretical prediction [equation (98)] as $\Delta P_J / q_T$ increases, when allowance is made for the 9 per cent displacement in reading apparently caused by the presence of the plenum chamber.
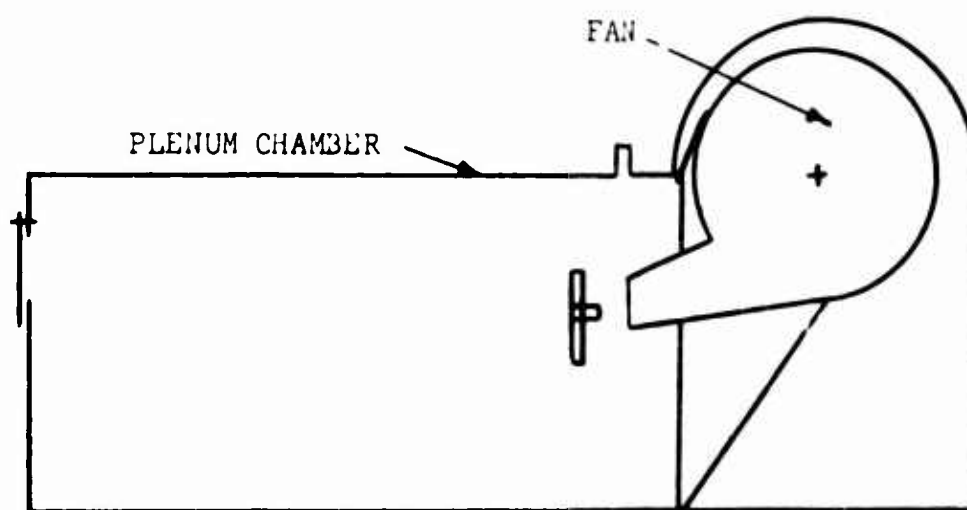
Figure 90.   Sketch of Model Fan Installed in Plenum Chamber.

BLANK PAGE
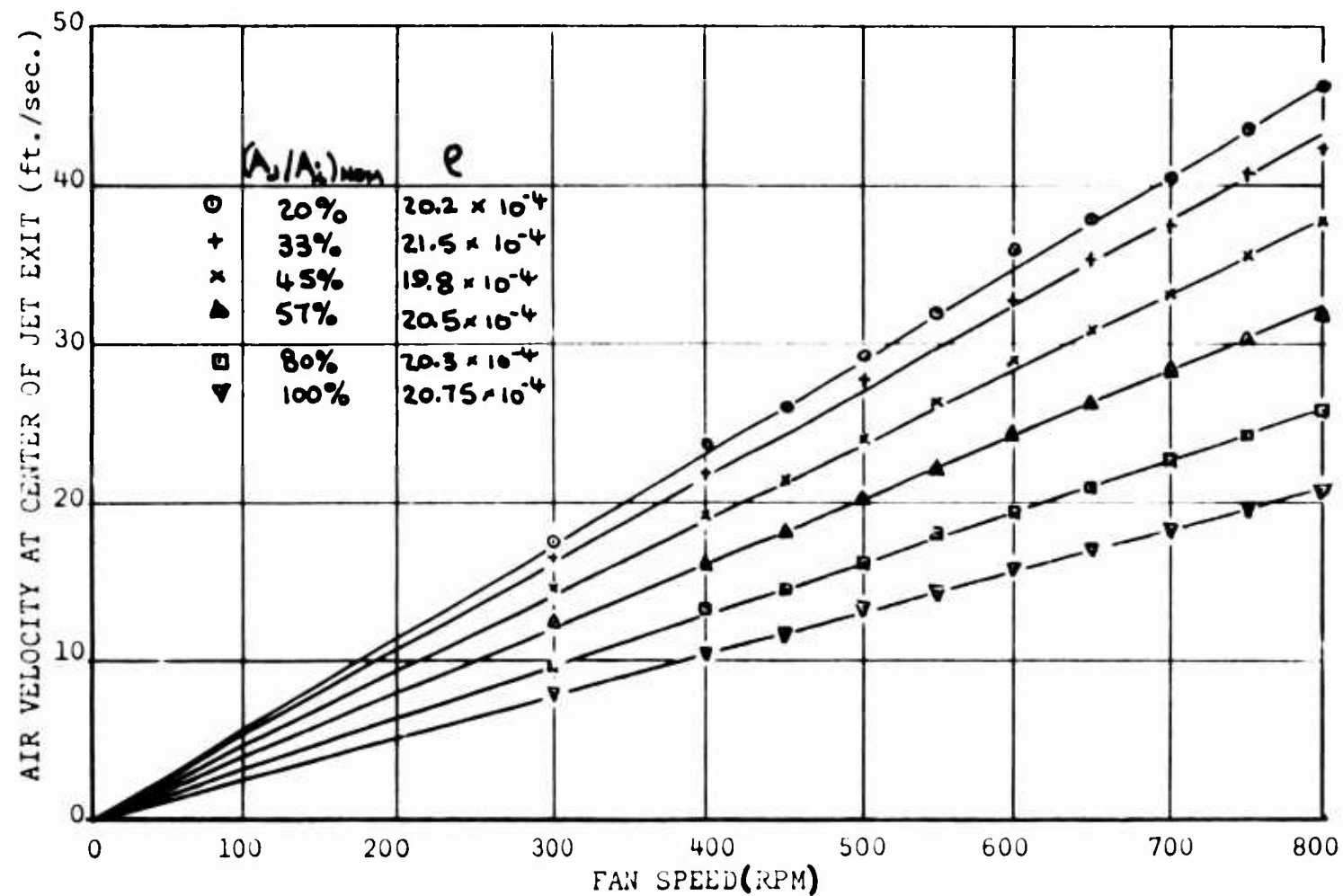
Figure 91.   Variation of Jet Velocity With Exit Area and Rotational Speed.
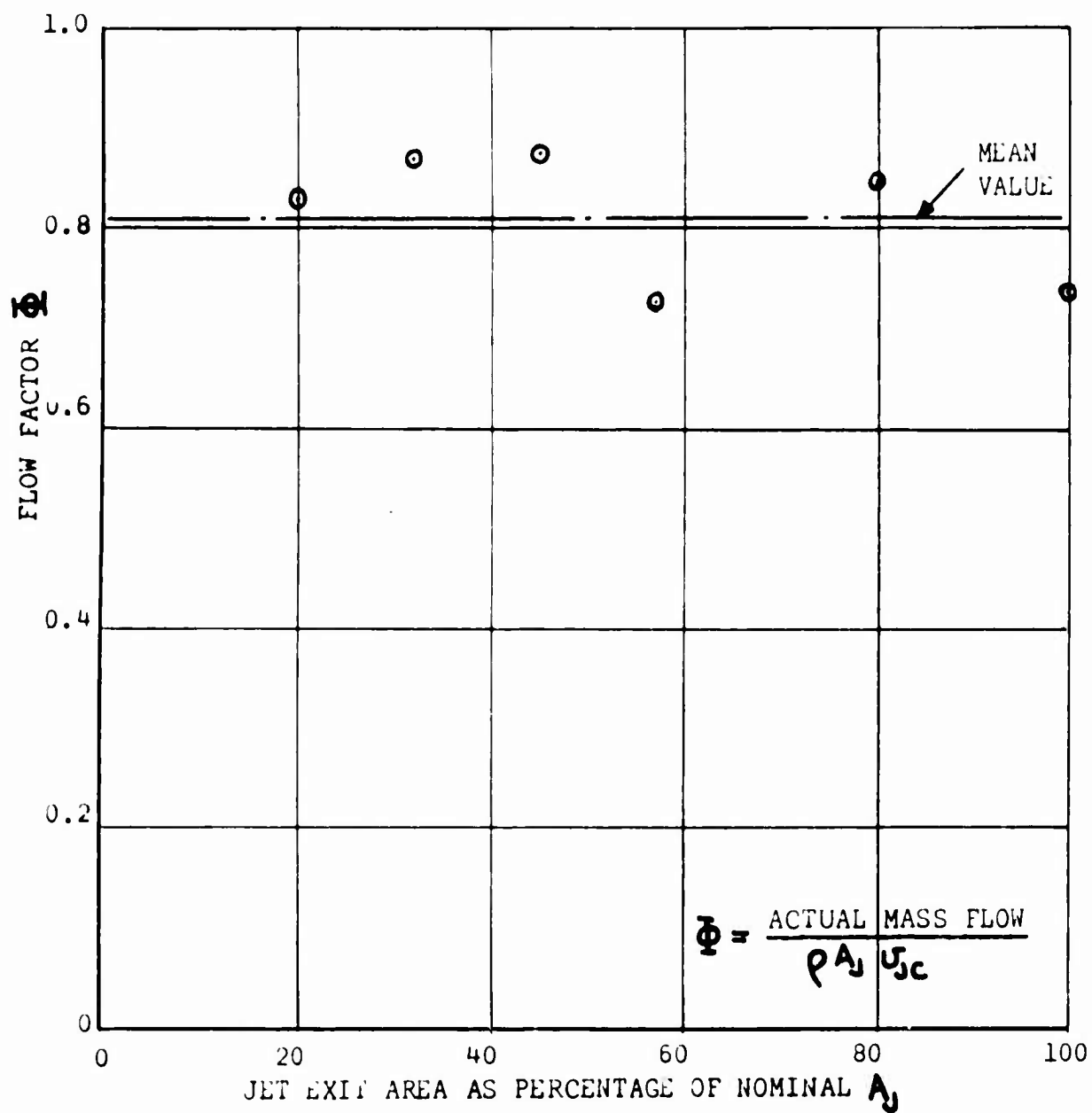
Figure 92.   Flow Factor Measurements At Various
Exit Area Ratios (Fan Exhausting to Ambient).

126
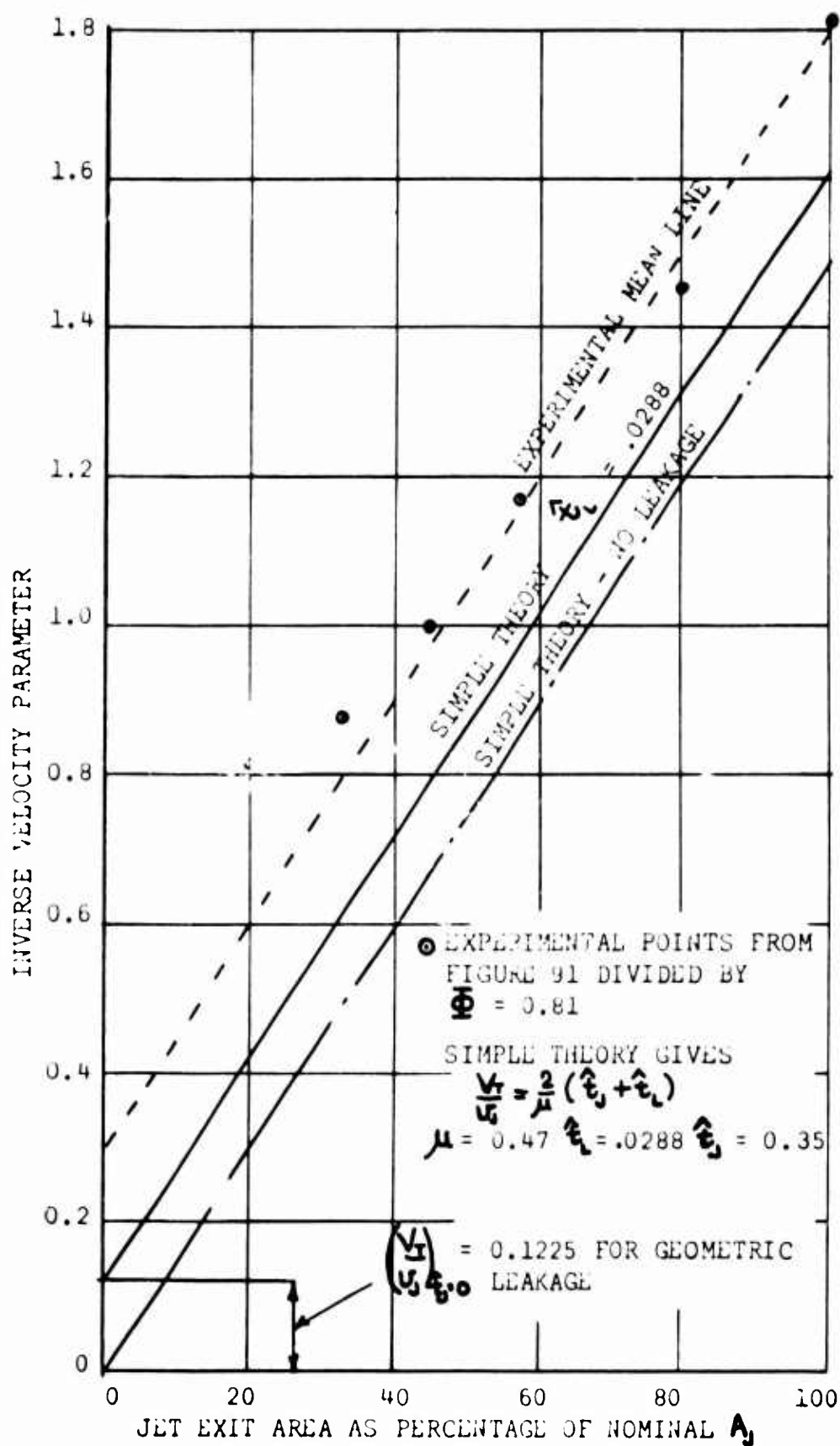
Figure 93. Inverse of the Velocity Parameter U_J/V_T As A Function of Exit Area Ratio (Exhausting to Ambient).
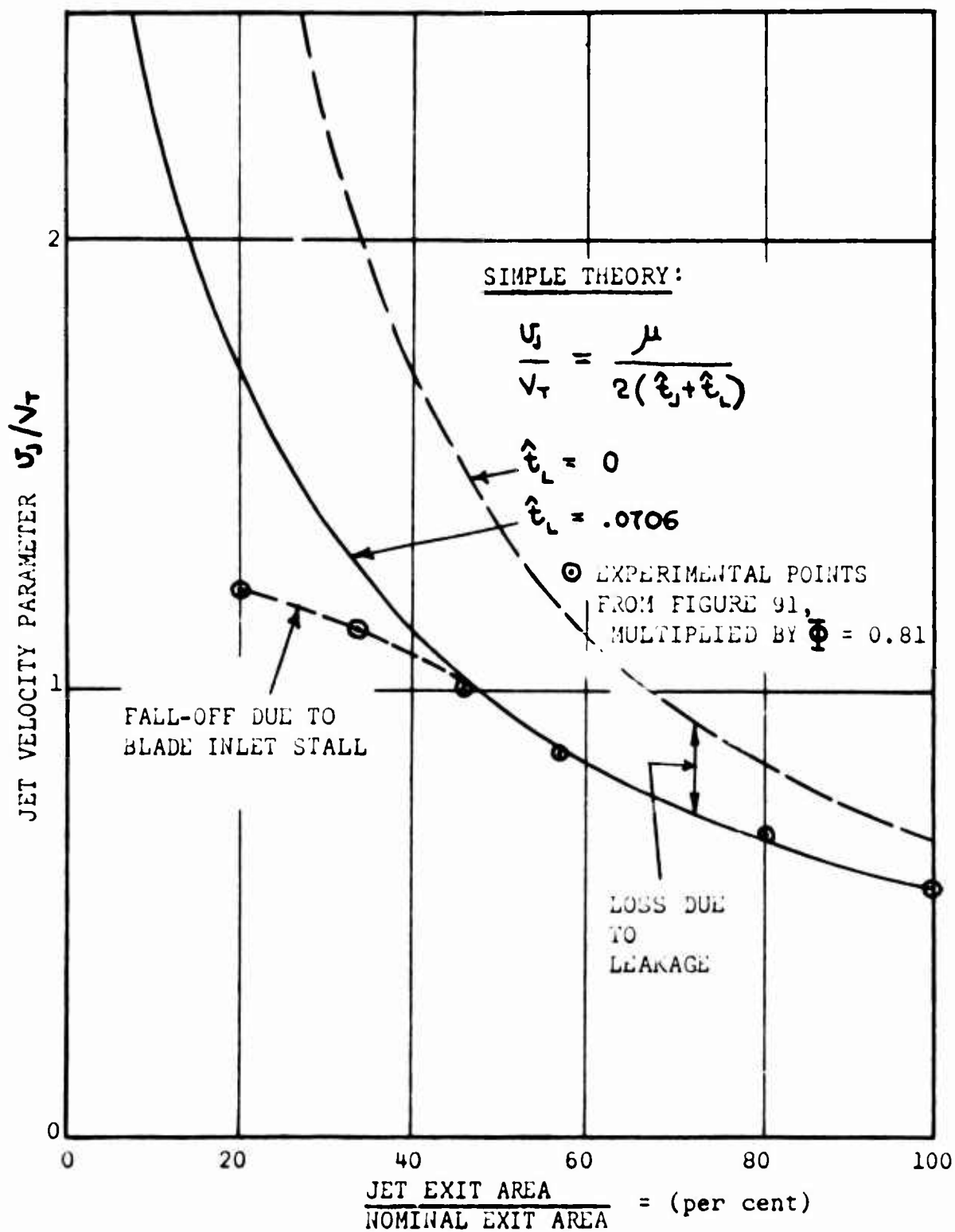
Figure 94. Jet Velocity Parameter U_J/V_T As A Function of Exit Area Ratio (Exhausting to Ambient).
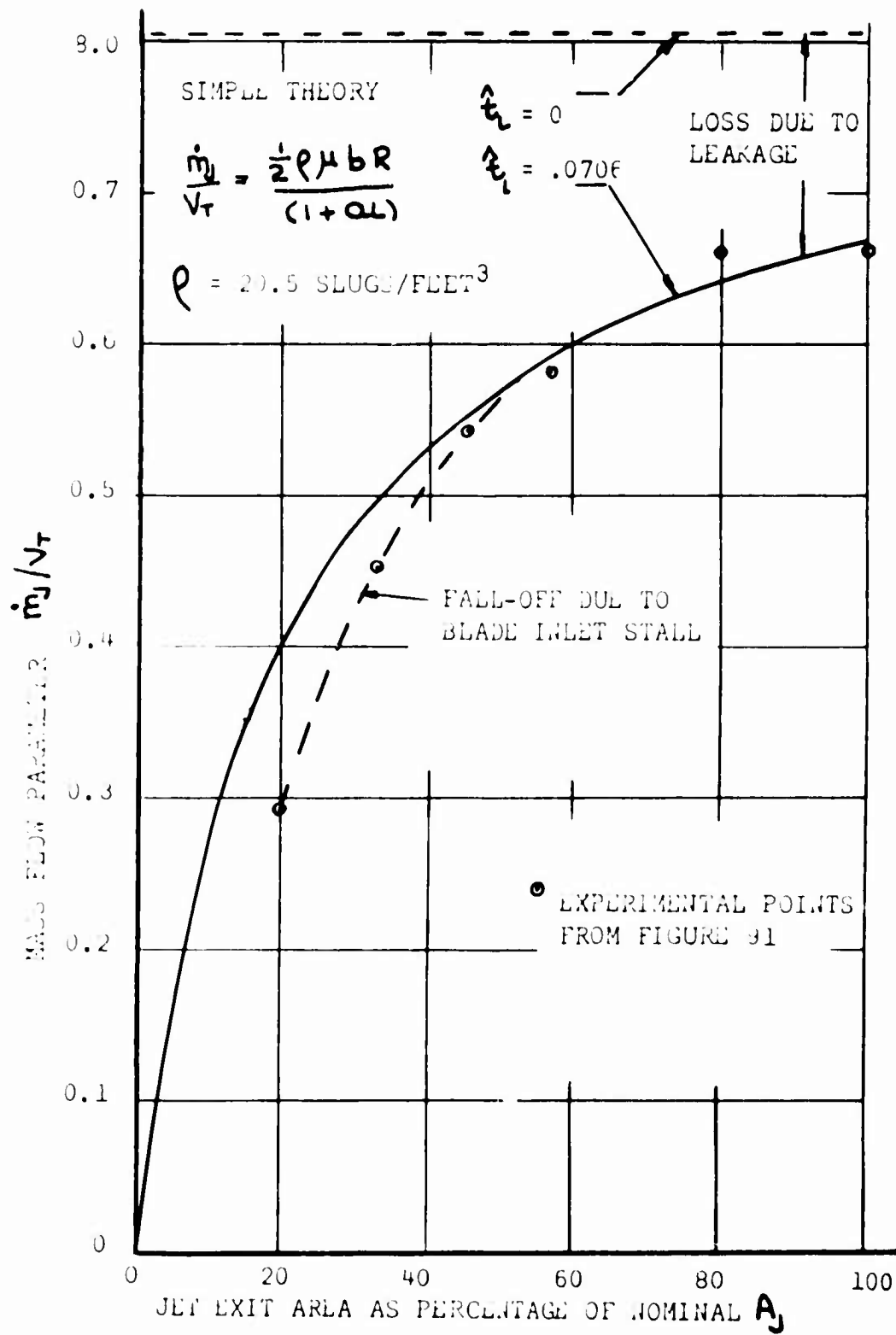
Figure 95. Mass Flow Parameter $\dot{m}_J/V_T$ As A Function of Exit Area Ratio (Exhausting to Ambient).
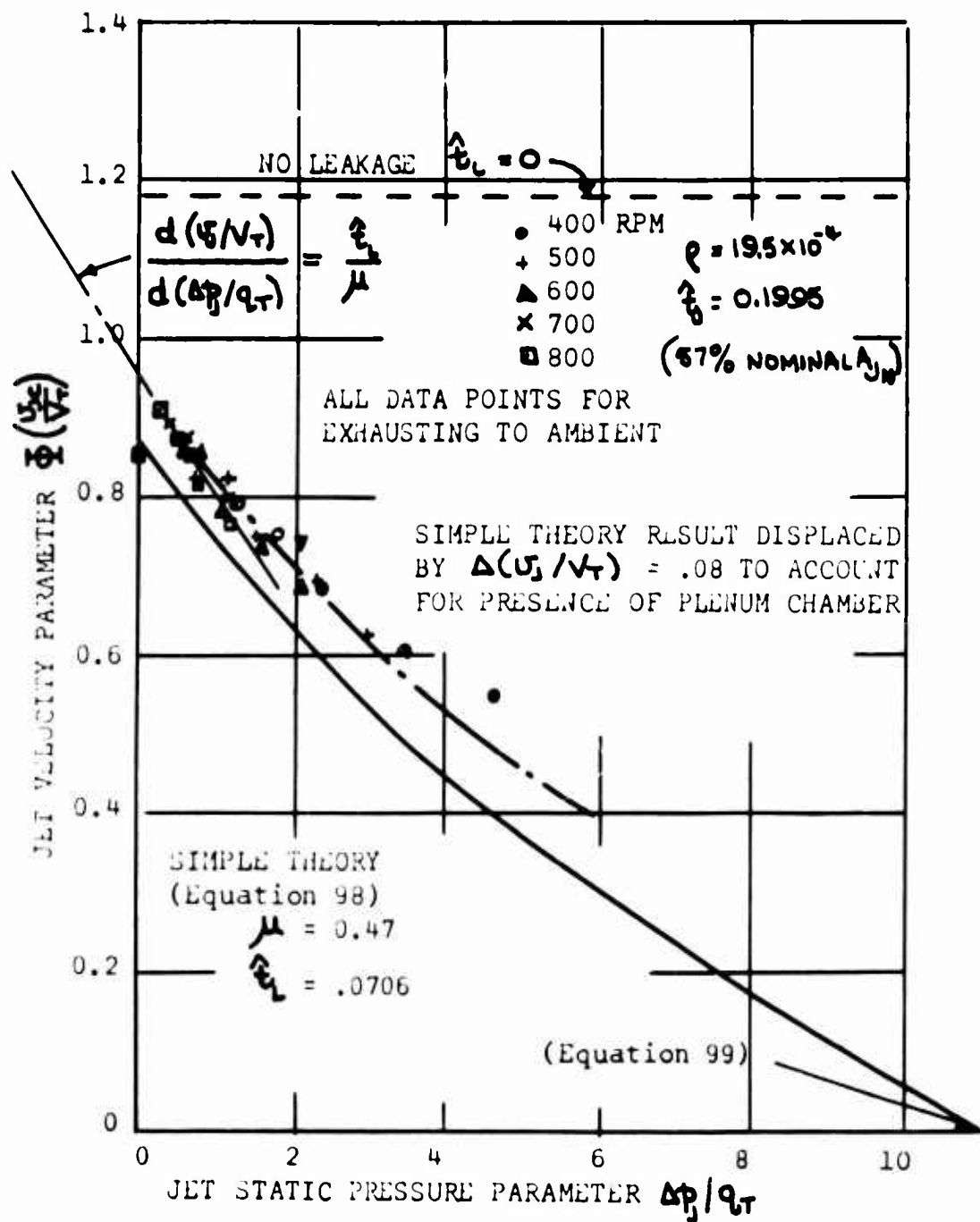
Figure 96. Variation of the Jet Velocity Parameter U_J/V_T With Jet Exit Static Pressure Parameter $\Delta p_J/q_T$

130

Blade Angle of Attack And Slip Factor

The analysis entitled "The Influence of Slip" is adequate, in the present state of knowledge, for calculating rotor slip due to leakage past the blades, as is shown by the good agreement between theory and experiment in Figure 96, for low back-pressure ratios.

A further factor which enters into slip calculations is the angle of attack of the blade in way of the inlet, however, since this can influence the apparent slip. From Figure 97 the angle of attack of the blade is
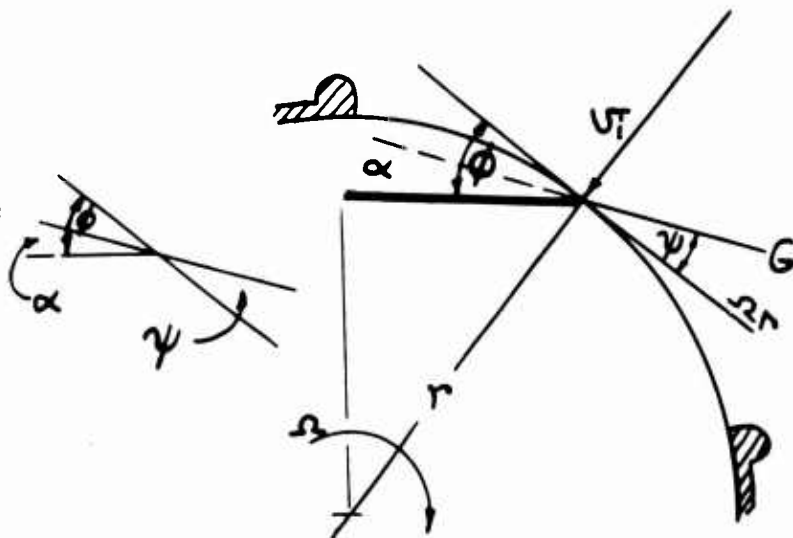
Figure 97. Blade Angle of Attack at Inlet Station.

$$\alpha = \phi - \psi \tag{104}$$

where $\psi = \tan^{-1}\left(\dfrac{v_i}{\Omega r}\right)$ $\qquad$ (105)

From continuity, the inlet mass flow must equal that at the jet exit.

That is, $\qquad \rho A_i v_i = \dot{m}_J$

$$\therefore \; v_i / v_T = m_J / \rho A_i = \frac{v_J}{v_T}\frac{A_J}{A_i} \tag{106}$$

and $\qquad \psi = \tan^{-1}\left(\frac{v_J}{v_T}\right)\left(\frac{A_J}{A_{JN}}\right)\left(\frac{A_{JN}}{A_i}\right)\left(\frac{v_T}{\Omega r}\right)$

$$= \tan^{-1}\left(\frac{v_J}{v_T}\right)\left(\frac{A_J}{A_{JN}}\right)\left(\frac{A_{JN}}{A_i}\right)\left(\frac{R}{r}\right) \tag{107}$$

131
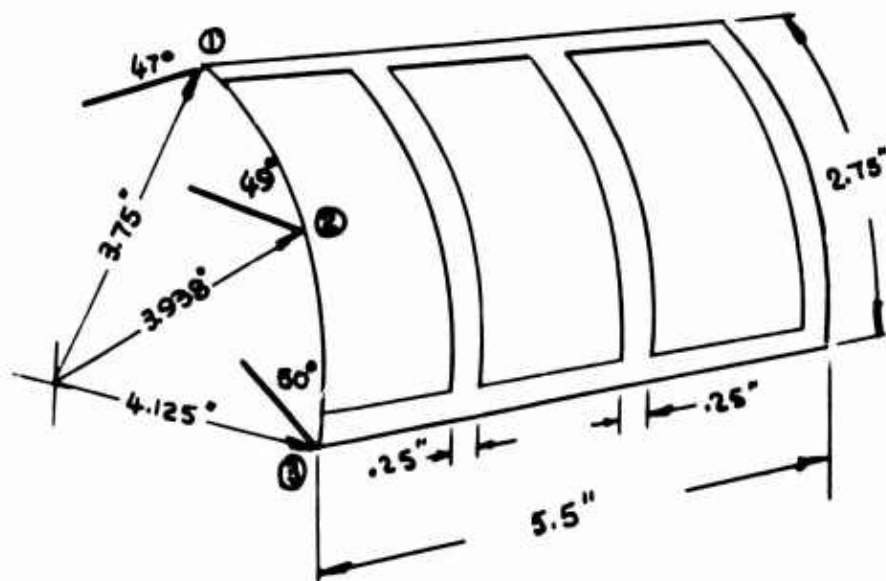
Figure 98. Geometry of Model Fan Intake.

Equations (104) and (107) have been used in Table 4 to calculate the
mean inlet blade angle of attack of the Frost Fan model (the geometry
of which is shown in Figure 98), and the result is plotted in Figure
99. This is then used, in conjunction with Figure 94, to assess the
reduction in theoretical mass flow which is attributable to blade in-
cidence, and the result of this calculation is plotted in Figure 100.
Because pre-swirl effects have been neglected, the apparent stall in-
cidence is higher than would be anticipated for a flat plate. The pre-
swirl velocity will be a function of V_i and Ωr , however, so that its
neglect is justifiable at the present stage of theoretical development.

It should be emphasized that the foregoing postulation of the influence
of blade angle of attack is no more than that at the present time. I+
is quite possible that an entirely different flow mechanism causes the
divergence shown in Figure 100. Needless to say, the fact that we ob-
tain good correlation with angle of attack, in Figure 100, can in no
way be construed as proof that angle of attack is indeed the signifi-
cant parameter.

TABLE 4

BLADE ANGLE OF ATTACK AT THE INLET

Intake station			(1)		(2)		(3)
r			3.75		3.938		4.125
r/R			.857		.90		.943
$(A_{JN}/A_i)(r/R)$			.713		.679		.648
A_J/A_{JN}	5%	10%	20%	40%	60%	80%	100%
$(U_J/V_T)_{THEORY}$	2.67	2.225	1.67	1.115	.84	.67	.559
$(A_J/A_{JN})(U_J/V_T)_{THEORY}$	.1335	.2225	.334	.446	.504	.536	.559
$\tan \psi_{STN(2)}$	.0906	.151	.227	.303	.342	.364	.3795
$\psi_{STN(2)}$	5.18	8.59	12.79	16.72	18.88	20.0	20.78
$\alpha_{STN(2)}$	43.82	40.41	36.21	32.28	30.12	29.0	28.22
A_J/A_{JN}		20%	33%	45%	57%	80%	100%
$(U_J/V_T)_{EXPT.}$		1.227	1.147	1.006	.855	.69	.552
$(U_J/V_T)_{THEORY}$		1.67	1.27	1.03	.87	.67	.559
$\dfrac{(U_J/V_T)_{EXPT.}}{(U_J/V_T)_{THEORY}}$		.735	.902	.976	.982	1.029	.988
α		36.2	33.4	31.7	30.4	29.0	28.22

$A_i = 0.0955$ ft.^{2} $\qquad A_{JN}/A_i = 0.611$
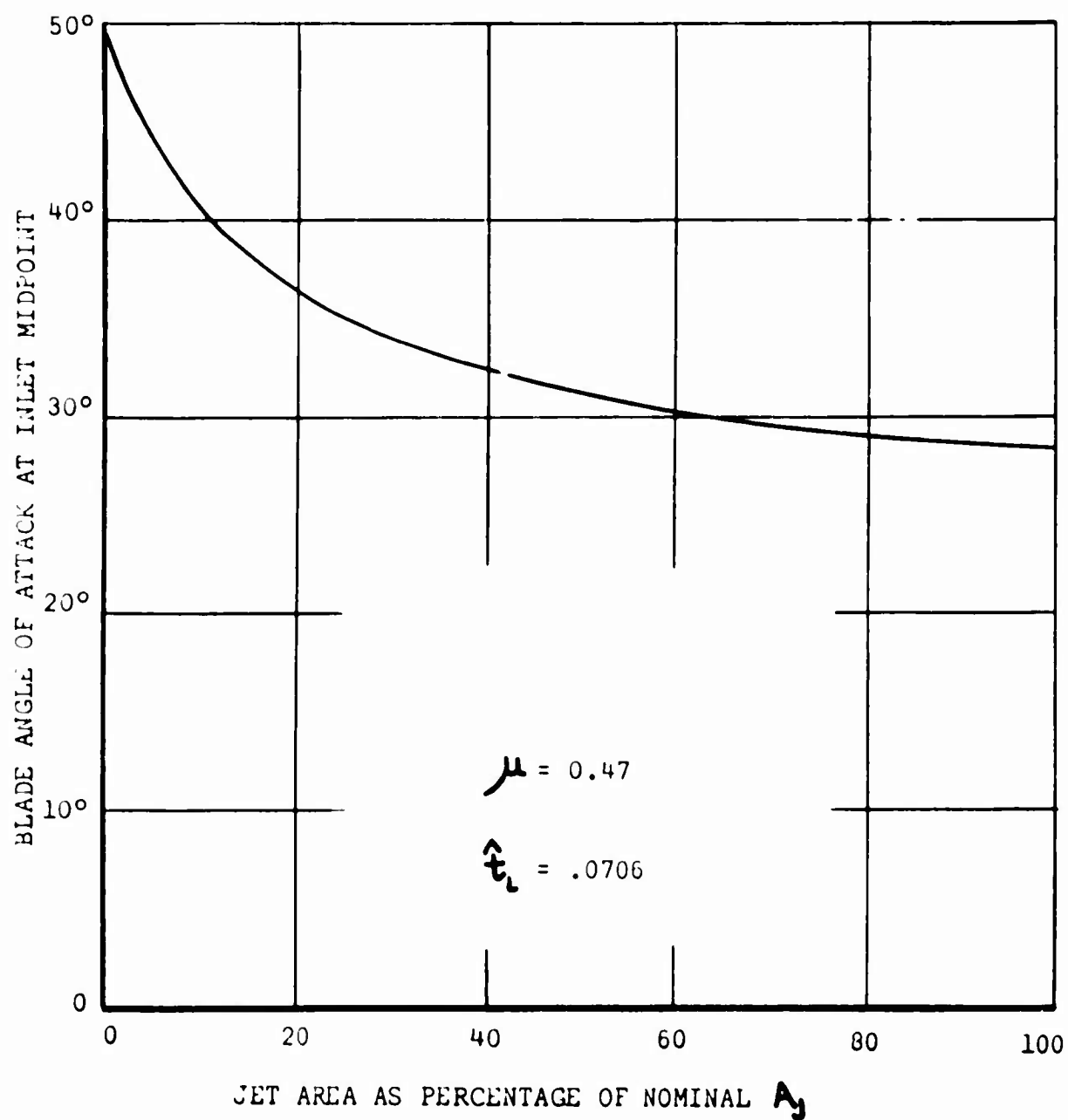
Figure 99. Theoretical Variation of Mean Blade Angle
of Attack at Intake Midpoint (Geometry of Figure 98).

BLANK PAGE
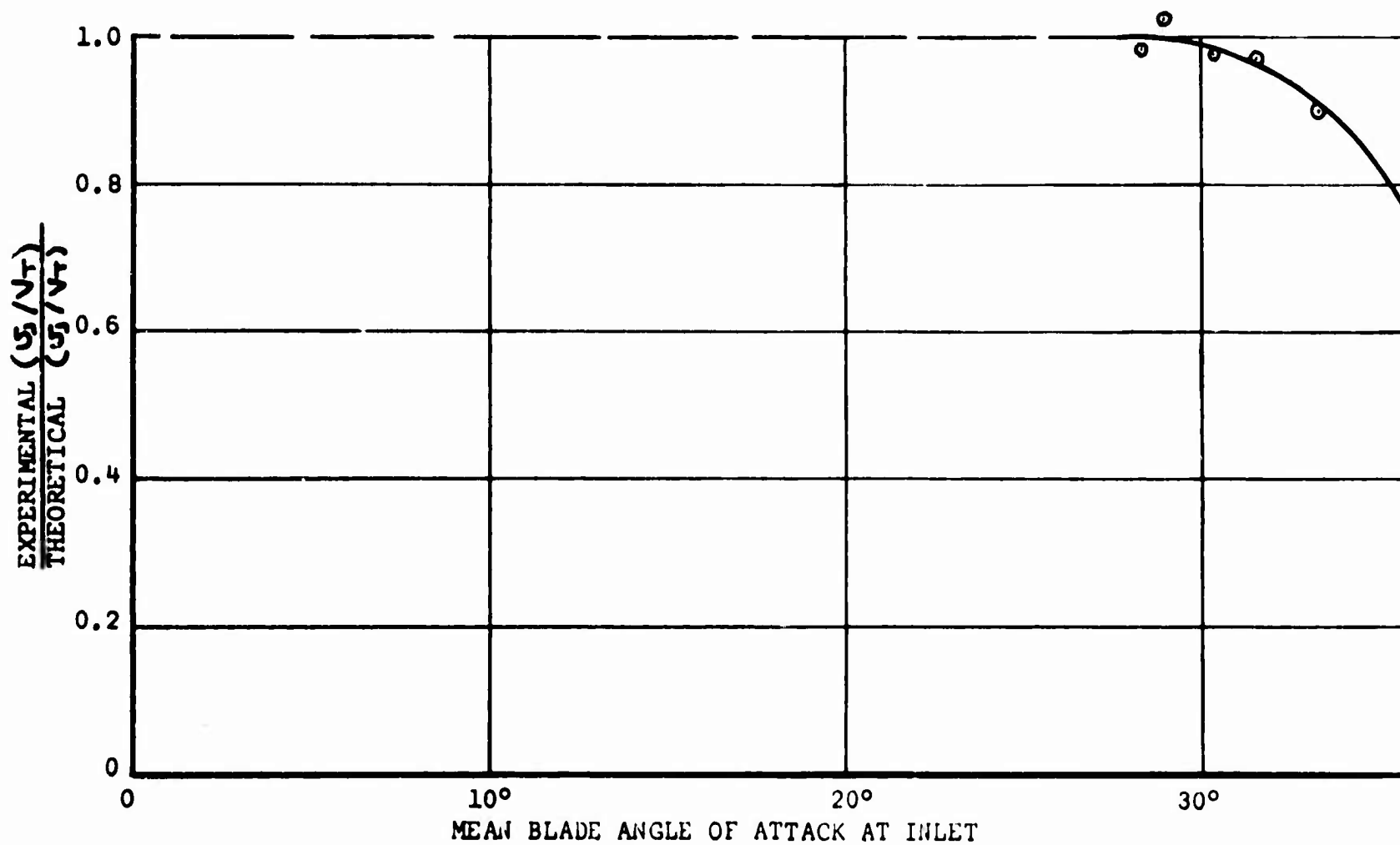
Figure 100. Effect of Blade Angle of Attack on Jet Velocity.

135

We define three areas $A_{①}, A_{②}, A_{③}$, as shown in Figure 101, each of which will be a function of a particular fan's geometry. The induction volume change will be

$$\Delta A_i b \quad = \quad b\left(A_{②} - A_{①} \right) \tag{108}$$

- where b is the fan case width.

The exhaust volume change will be

$$\Delta A_J b \quad = \quad b\left(A_{④} - A_{③} \right) \tag{109}$$

When the exhaust volume change is less than the figure obtained for the intake, the air remaining in each sector will be pressurized after the trailing blade has passed the exhaust port. This will cause the leading blade to lift off the case and permit air to flow underneath it until the pressure in the sector ahead of it is nearly equalized. Following this around the fan, it is obvious that the volume of air taken in during induction will be reduced and that the mass flow will now be defined by the volume change during exhaust.

Thus, the effective induction volume $\Delta A b$ is the least value given by equations (108) and (110).

If there are (n) blades, the (ideal) air mass discharged per revolution will be

$$nb\rho\, \Delta A$$

Thus, the ideal air mass flow will be

$$\dot{m}_o = nb\rho \Delta A \frac{\Omega}{2\pi} \qquad \text{slugs/second} \tag{110}$$

Comparing this with equation (63)

$$nb\, \Delta A\, \frac{\rho V_T}{2\pi R} = \frac{1}{2}\rho V_T \mu b R$$

$$\therefore \quad \mu = \frac{n\, \Delta A}{\pi R^2} \tag{111}$$
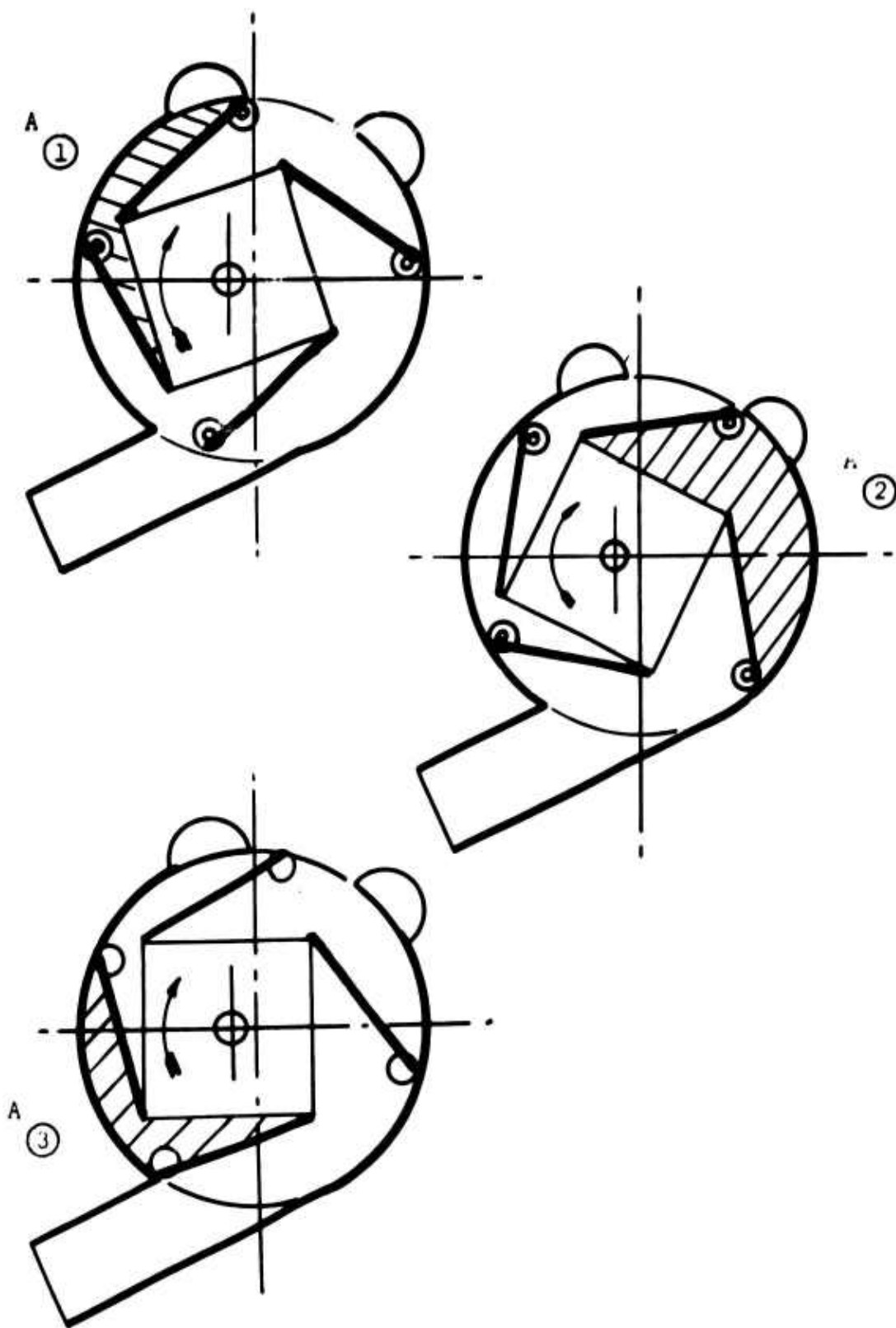
Figure 101. Definition of Areas A ① A ② A ③

For the model Frost Fan described in Reference 24,

$$A_{\text{①}}/\pi R^2 = .0686$$

$$A_{\text{②}}/\pi R^2 = .176$$

$$A_{\text{③}}/\pi R^2 = .0866$$

$$\therefore A_i/\pi R^2 = .1074$$

and $\quad A_J/\pi R^2 = .0894$

$$\therefore \mu = 4 \times .0894 = \underline{0.3576}$$

For the test model of Reference 24 it is obvious, from Figure 93, that this value for μ will not give such good agreement with experiment as the simple theory value of equation (64a). Since the model test data can not be regarded as definitive, the question of which way to calculate μ must be left open at the present time.

Blade Tip Reaction Due to Dynamic Loads
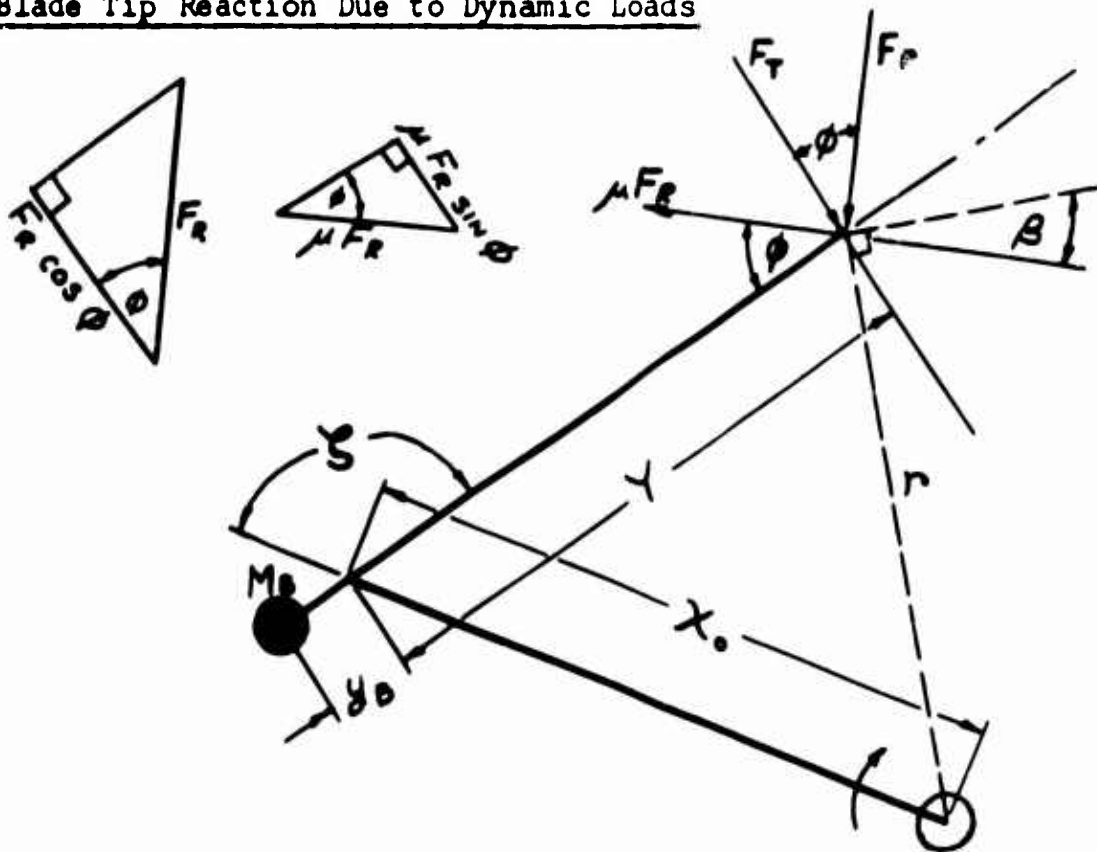
Figure 102. Blade Geometry.

We consider the blade geometry shown in Figure 102. The centrifugal (CF) torque about the hinge is

$$Q_{\gamma} = M_{mD} \, \Omega^2 \, x_o \sin \gamma \qquad (112)$$

- where M_{mD} = first mass moment of blade about its hinge

Ω = fan shaft rotational speed

x_o = hinge offset

γ = blade lead angle

The inertia torque is

$$Q_I = I_D \ddot{\gamma} \quad = \quad \frac{d^2\gamma}{d\theta^2} \, \Omega^2 \, I_D \qquad (113)$$

where I_D = second moment of mass of blade about its hinge.

These two torques are reacted by the tip force F_T which gives a moment

$$-F_T Y = -F_R Y \cos \phi + \mu_F Y F_R \sin \phi \qquad (114)$$

where μ_F is the friction coefficient.

Equating moments,

$$\frac{F_R Y}{\Omega^2} \left[\cos \phi - \mu_F \sin \phi \right] = I_D \frac{d^2\gamma}{d\theta^2} + x_o M_{mD} \sin \gamma$$

or
$$\frac{d^2\gamma}{d\theta^2} + \frac{x_o M_{mD}}{I_D} \sin \gamma = \frac{F_R Y}{\Omega^2 I_D} \left[\cos \phi - \mu_F \sin \phi \right] \qquad (115)$$

The frequency parameter is

$$\frac{\omega}{\Omega} = \frac{x_o M_{mD}}{I_D} \qquad (116)$$

-and for small blade angles ($\gamma \to 0$) is the same as the undamped natural frequency for simple harmonic motion. For the large values of γ characteristic of a practical fan, there is no true natural frequency, since the equation is now non-linear. Thus there is little benefit to be obtained by "tuning" the blade for $\frac{\omega}{\Omega} = 1.0$.

139

Since equation (115) is similar to the equation of pendular motion, there will of course be a natural period for zero forcing input, but since the oscillation is not about $\zeta = 0$, its significance is difficult to evaluate.

It is evident, however, that there are a number of ways in which a blade can be designed in order to minimize the tip reaction loads.

One solution is to balance the blade statically about the hinge line, so that $M_{m\zeta} = 0$.

Then

$$F_R = \frac{d^2\zeta}{d\theta^2}\frac{\Omega^2 I_\zeta}{\gamma} \Bigg/ \cos\phi - \mu_F \sin\phi \tag{117}$$

A useful approximate solution to equation (67) is obtained by assuming that the friction coefficient $\mu_F \ll 1.0$.

Then

$$F_R = \frac{d^2\zeta}{d\theta^2}\frac{\Omega^2 I_\zeta}{\gamma} \Bigg/ \cos\phi \tag{118}$$

Equation (117) has been used to calculate the instantaneous value of F_R in Figures 104 to 108 for the fan geometry depicted in Figure 103 and Table 5, using numerical differentiation techniques, and assuming that μ_F is negligible.

Of immediate interest is the marked divergence from a sinusoidal variation of the instantaneous value of the F_R parameter plotted in Figure 108. If we had assumed a constant value of ϕ and a sinusoidal variation of amplitude $\Delta\zeta$:

That is,

$$\zeta = \zeta_o + \Delta\zeta \sin(\theta + \varphi)$$

then

$$\frac{d\zeta}{d\theta} = \Delta\zeta \cos(\theta + \varphi)$$

$$\frac{d^2\zeta}{d\theta} = -\Delta\zeta \sin(\theta + \varphi)$$

$$\left(\frac{1}{\cos\phi}\frac{d^2\zeta}{d\theta^2}\right)_{max} = \pm 0.38 \text{ from the values in Figures}$$
105 and 106

We can see from Figure 107 that the correct values are +0.948 and -0.464.

VIEW B-B   VIEW A-A
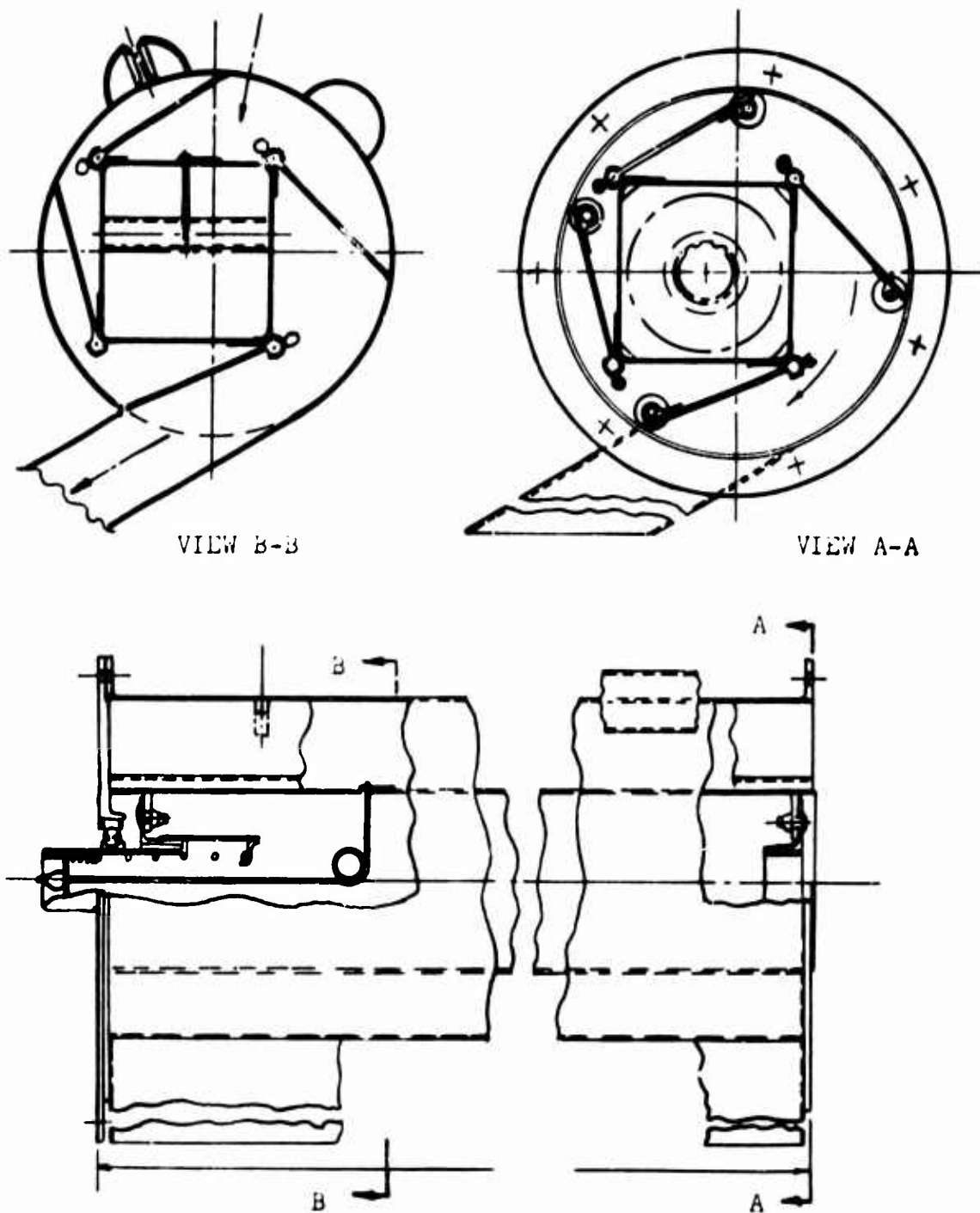
Figure 103.   Frost Fan Assembly.

141

TABLE 5

FAN GEOMETRY

θ	ζ	ϕ	ψ	ζ	STATION	$\cos\phi$
15	92.0	47	43	43	0	.672
45	89.5	53	37	45.5	1	.5918
75	94.0	56	34	41	2	.5592
105	104.0	56	34	31	3	.5592
135	113.0	52.5	37.5	22	4	.6088
165	119.0	48	42	16	5	.6691
195	120.0	42	48	15	6	.7431
225	119.0	37	53	16	7	.7986
255	116.0	34	56	19	8	.829
285	109.0	35	55	26	9	.8192
315	103.0	37.5	52.5	32	10	.7934
345	96.0	40	50	39	11	.766
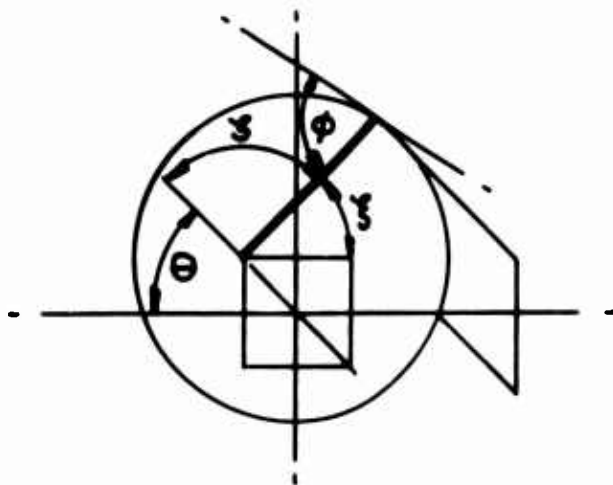
BLANK PAGE
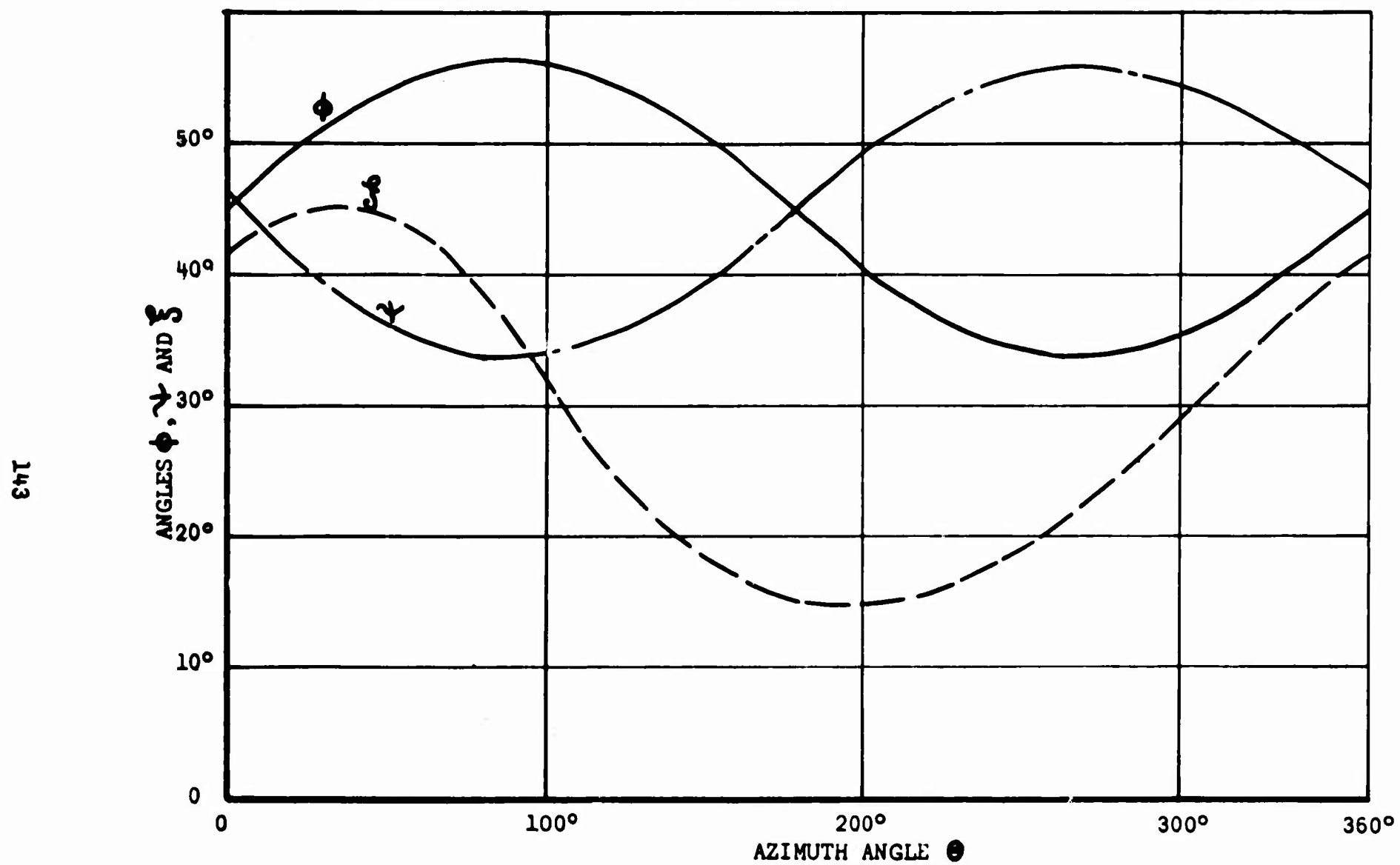
Figure 104. Angular Variations in Frost Fan Geometry.
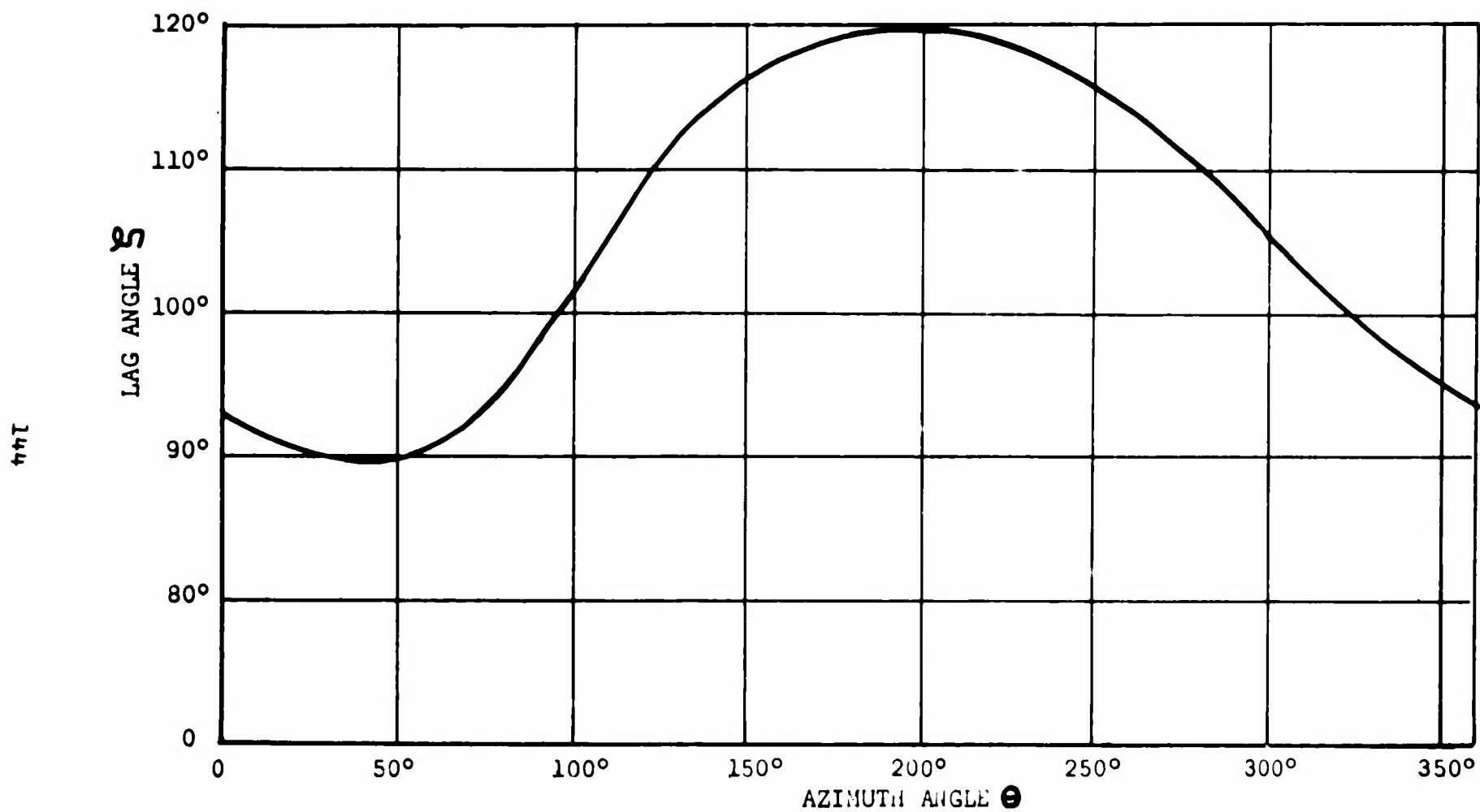
Figure 105. Variation of Lag Angle ζ With Azimuth Angle θ .

144
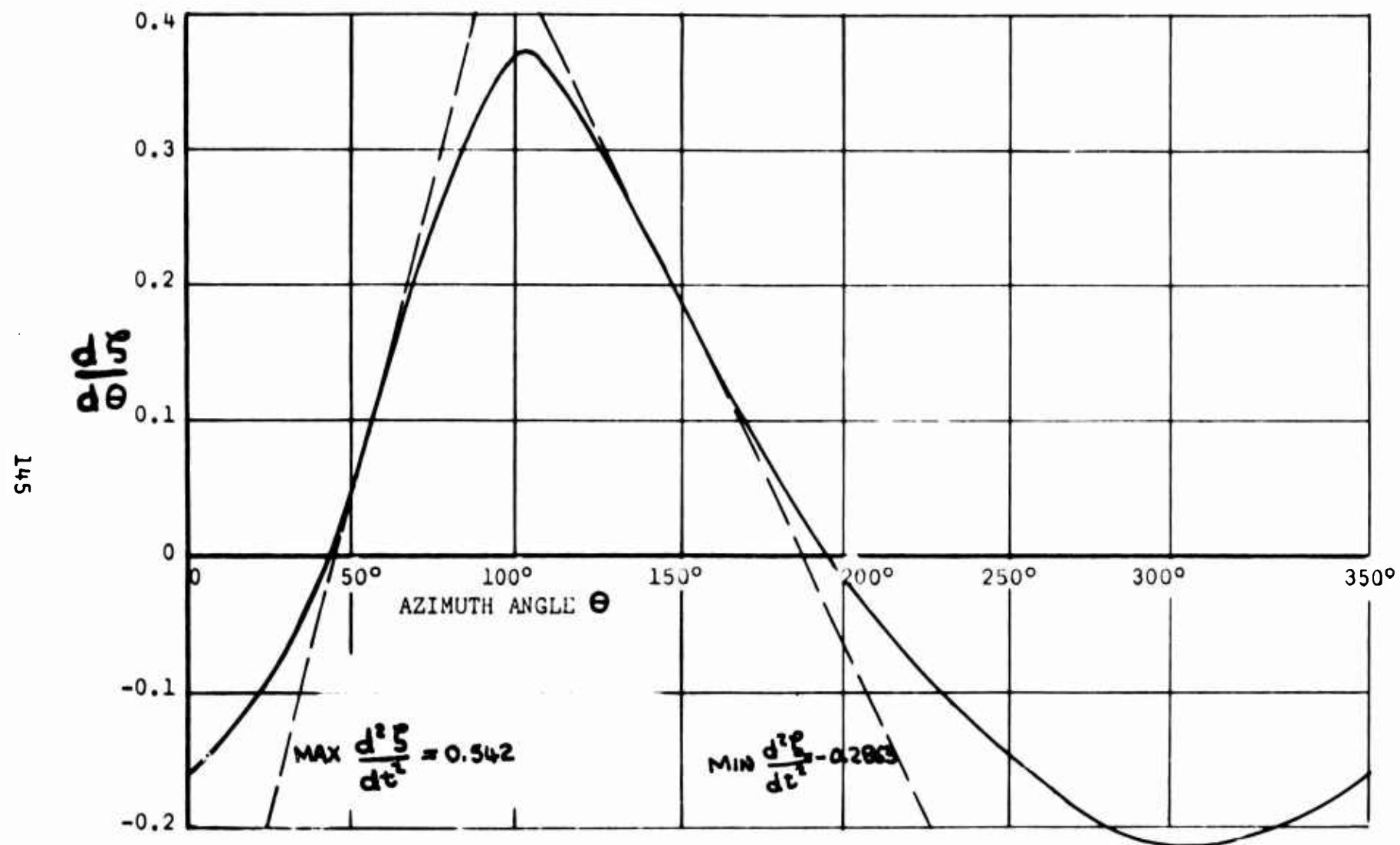
Figure 106.   First Derivative of Lag Angle ς .
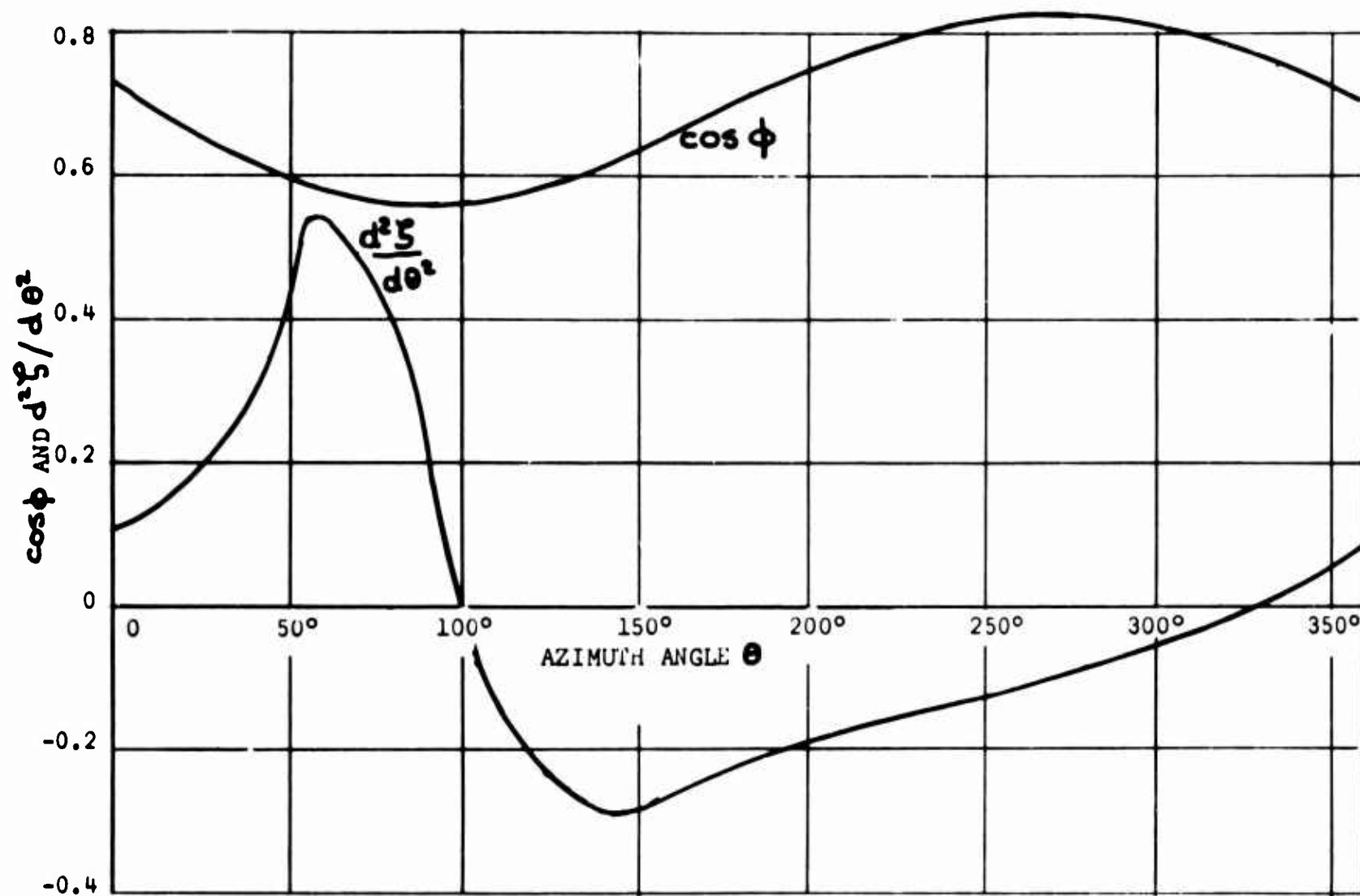
Figure 107. Second Derivative of Lag Angle ζ.
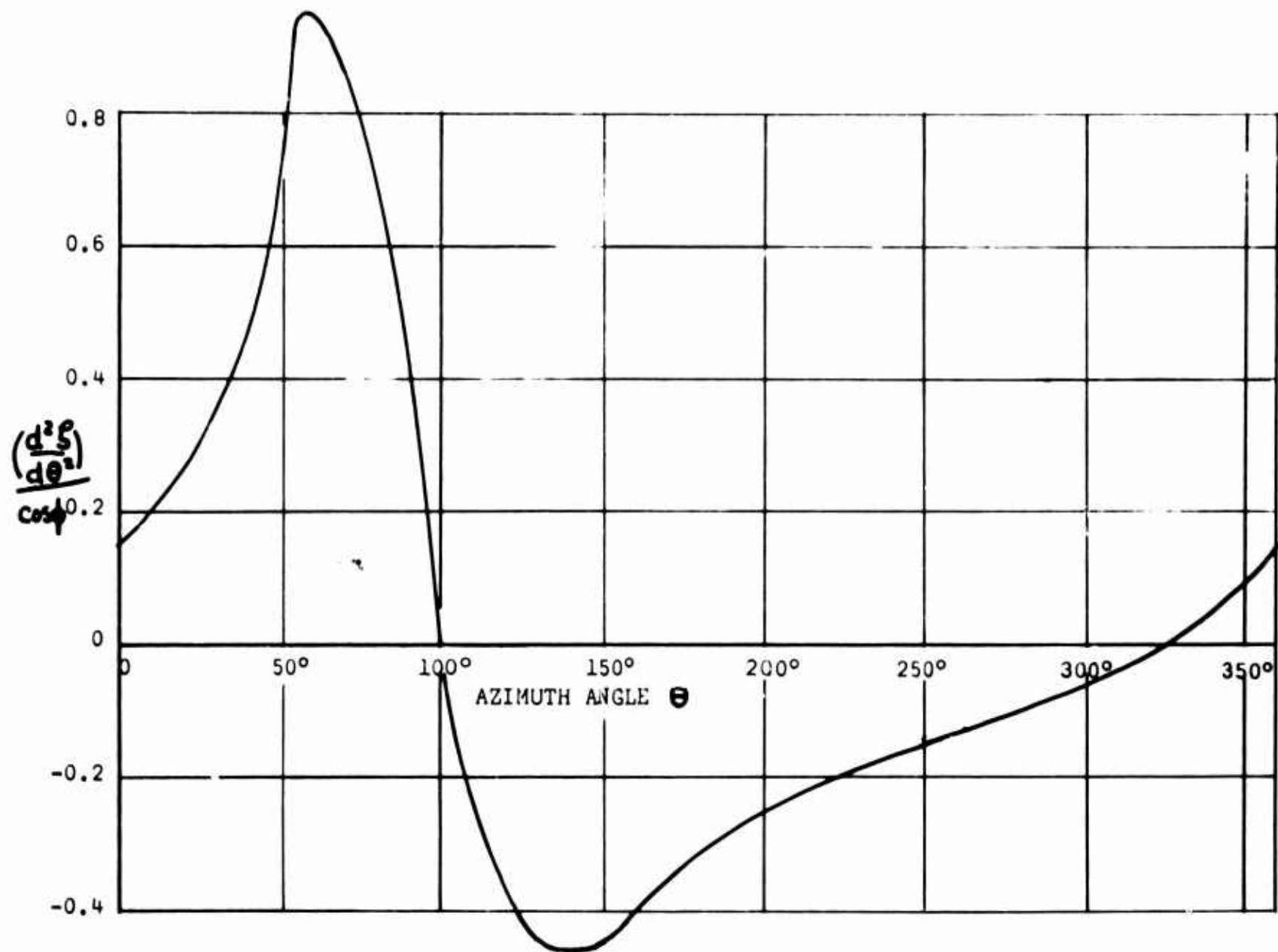
Figure 108. Approximate Normal Force Parameter $\gamma F_R / I_D \Omega^2$

Friction Power Loss Due to Dynamic Loads

The frictional force at the blade tip, tangential to the local radius vector, is obtained from equation (115). If we assume that the friction coefficient μ_F is negligibly small compared with unity, then

$$\frac{\mu_F F_R}{\Omega^2} = \mu_F \left[\frac{I_D}{Y \cos \phi} \frac{d^2 \zeta}{d\theta^2} + \frac{x_0 M_{mD}}{Y \cos \phi} \sin \zeta \right] \tag{119}$$

The total power loss associated with this is

$$E_F = \mu_F F_R \Omega r n \tag{120}$$

so that

$$\frac{E_F}{n \mu_F \Omega^3} = \frac{I_D r}{Y \cos \phi} \frac{d^2 \zeta}{d\theta^2} + \frac{x_0 M_{mD} r}{Y \cos \phi} \sin \zeta \tag{121}$$

If we evaluate this expression between $\theta = 0$ and 2π, then the mean value will be the effective power loss. Since for a given fan geometry we may wish to vary the first and second mass moments, it is convenient to divide equation (121) into two instantaneous power components.

$$\frac{E_F}{\mu_F n \Omega^3} = \left| \frac{\Delta E_\zeta}{Y} + \frac{\Delta E_\zeta}{Y} \right| \tag{122}$$

where

$$\frac{\Delta E_\zeta}{I_D} = \frac{r}{\cos \phi} \frac{d^2 \zeta}{d\theta^2} \tag{123}$$

$$\frac{\Delta E_\zeta}{x_0 M_{mD}} = \frac{r}{\cos \phi} \sin \zeta \tag{124}$$

The modulus in equation (122) implies tip restraint in both blade flapping directions, of course.

Equations (123) and (124) are plotted in Figure 109 for the geometry of the model fan of Reference 24, based on the calculations of Table 6. As we should expect, the angular acceleration term in particular is very non-linear.

For the actual first and second moments of blade mass about its hinge as measured and reported in Reference 24, the total frictional power parameter is plotted in Figure 110. Evidently the mean frictional power loss is given by

148

$$E_F = 0.076 \, n \frac{\mu_F \, \Omega^3}{Y} \times 10^{-3}$$

$$= 1.038 \, \mu_F \, \Omega^3 \times 10^{-3} \tag{125}$$

An appropriate expression for the mean frictional power loss of blades which are not mass-balanced can be obtained from equation (121)

that is, $E_F = n \mu_F \Omega^3 \dfrac{x_o \, M_{mD} \, R}{Y}$ (126)

$$= 0.8 \, \mu_F \, \Omega^3 \times 10^{-3} \text{ for the model fan} \tag{126a}$$

This approximation obviously is not too bad for the model fan, being low by 20 per cent, relative to equation (125). We can account for this by a factor ζ so that

$$E_F = \mu_F \, \zeta \, n \, \Omega^3 \, x_o \, M_{mD} \left(\frac{R}{Y} \right) \tag{127}$$

- where $\qquad \zeta = \dfrac{1.038}{0.8} = 1.3$ for the model fan.

Then from equation (69)

$$\frac{E_F}{E_J} = \frac{4 \mu_F n \, \zeta \left(\frac{x_o \, M_{mD}}{b \, Y R^3 \rho} \right)}{\mu \left[\frac{1}{4} \left(\frac{\mu}{\xi_J} \right)^2 + \frac{\Delta P_L}{q_T} \right]} \tag{128}$$

149

TABLE 6

CALCULATION OF INSTANTANEOUS FRICTION POWER COMPONENTS ΔE_y AND ΔE_g FOR MODEL FAN

θ	15°	45°	75°	105°	135°	165°	195°	225°	255°	285°	315°	345°
r	.3595	.362	.348	.322	.2925	.274	.2685	.2725	.286	.305	.326	.346
$\cos\phi$	.672	.5918	.5592	.5592	.6088	.6691	.7431	.7986	.8290	.8192	.7934	.7660
$r/\cos\phi$	.5345	.611	.623	.576	.481	.41	.3615	.3415	.345	.3725	.411	.451
$d^2\zeta/d\theta^2$	.152	.365	.44	-.08	-.278	-.252	-.195	-.155	-.118	-.075	-.022	+.048
$\Delta E_y/I_D$	.0812	.2235	.2743	-.0461	-.1338	-.1032	-.0705	-.0529	-.0407	-.02795	-.00905	.02165
ζ	92.0	89.5	94.0	104.0	113.0	119.0	120.0	119.0	116.0	109.0	103.0	96.0
$\sin\zeta$	.9994	1.0	.9976	.9703	.9205	.8746	.866	.8746	.8988	.9455	.9744	.9945
$\Delta E_g/x_0 M_{mD}$	.5345	.611	.621	.56	.443	.3585	.313	.2985	.31	.352	.4005	.449

TABLE 7

FRICTION POWER LOSS CALCULATION FOR MODEL FAN

θ	15°	45°	75°	105°	135°	165°
$\Delta E_{\ddot{\xi}} \times 10^8$	.01868	.0514	.0631	-.0106	-.03075	-.01622
$\Delta E_{\zeta} \times 10^8$	.0858	.0982	.0998	.09	.0711	.0576
$\Sigma \times 10^8$	.10448	.1496	.1629	.0794	.04035	.03385
θ	195°	225°	255°	285°	315°	345°
$\Delta E_{\ddot{\xi}} \times 10^8$	-.01622	-.01217	-.00937	-.00643	-.002085	+.00499
$\Delta E_{\zeta} \times 10^8$	.0503	.0479	.0498	.0565	.0643	.072
$\Sigma \times 10^8$	.03408	.03572	.04043	.05007	.062215	.07699

From Ref. 24, $X_o = 0.225$ ft. $Y = 0.293$ ft.

$M_{mD} = 0.713 \times 10^{-3}$ slugs/ft. $n = 4$

$I_D = 0.23 \times 10^{-3}$ slugs/ft.^{2} $\Sigma = \dfrac{E_F}{\mu_F \, n \, \Omega^3 Y}$
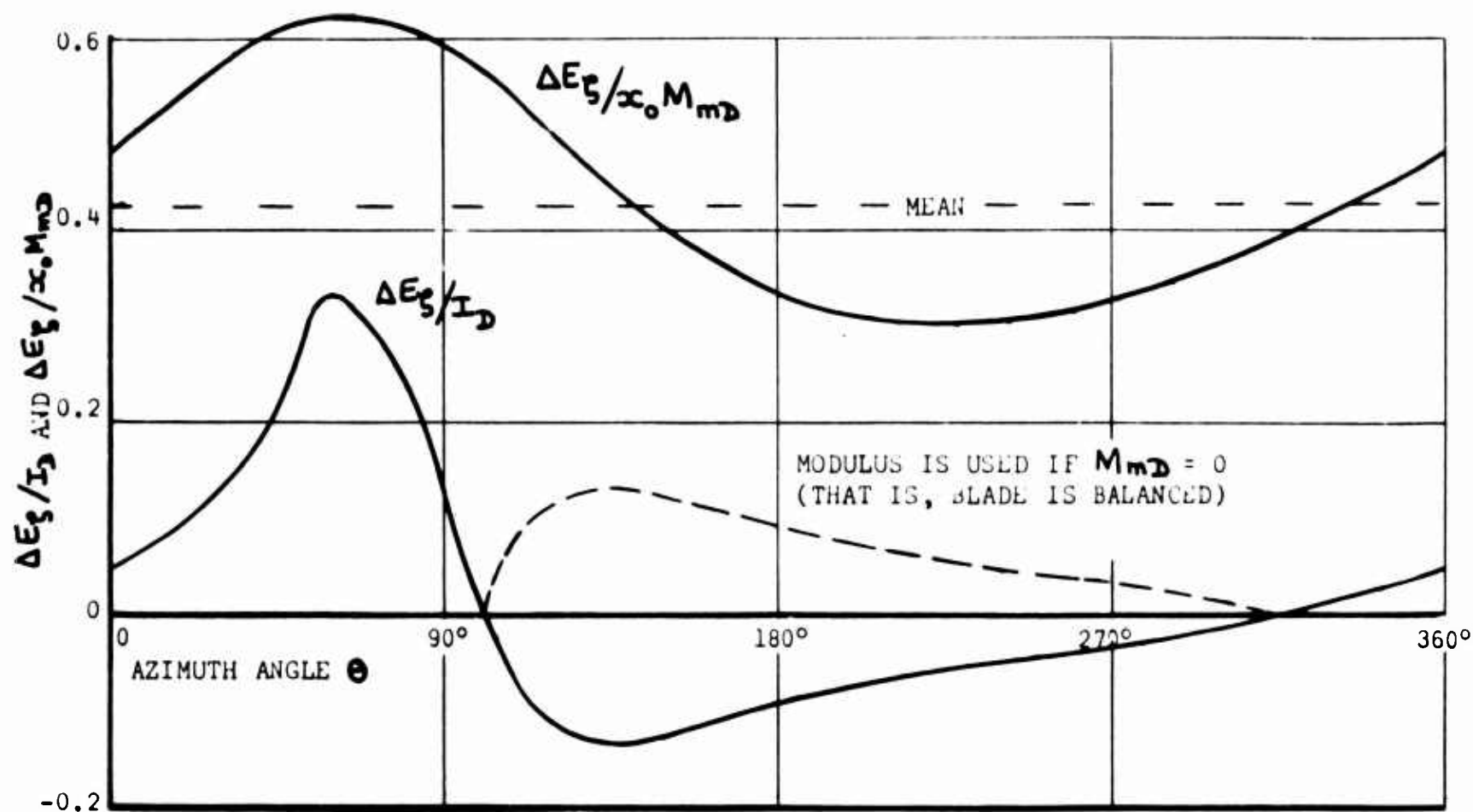
Figure 109. Instantaneous Power Absorption Parameters For One Blade (Model Fan Geometry).
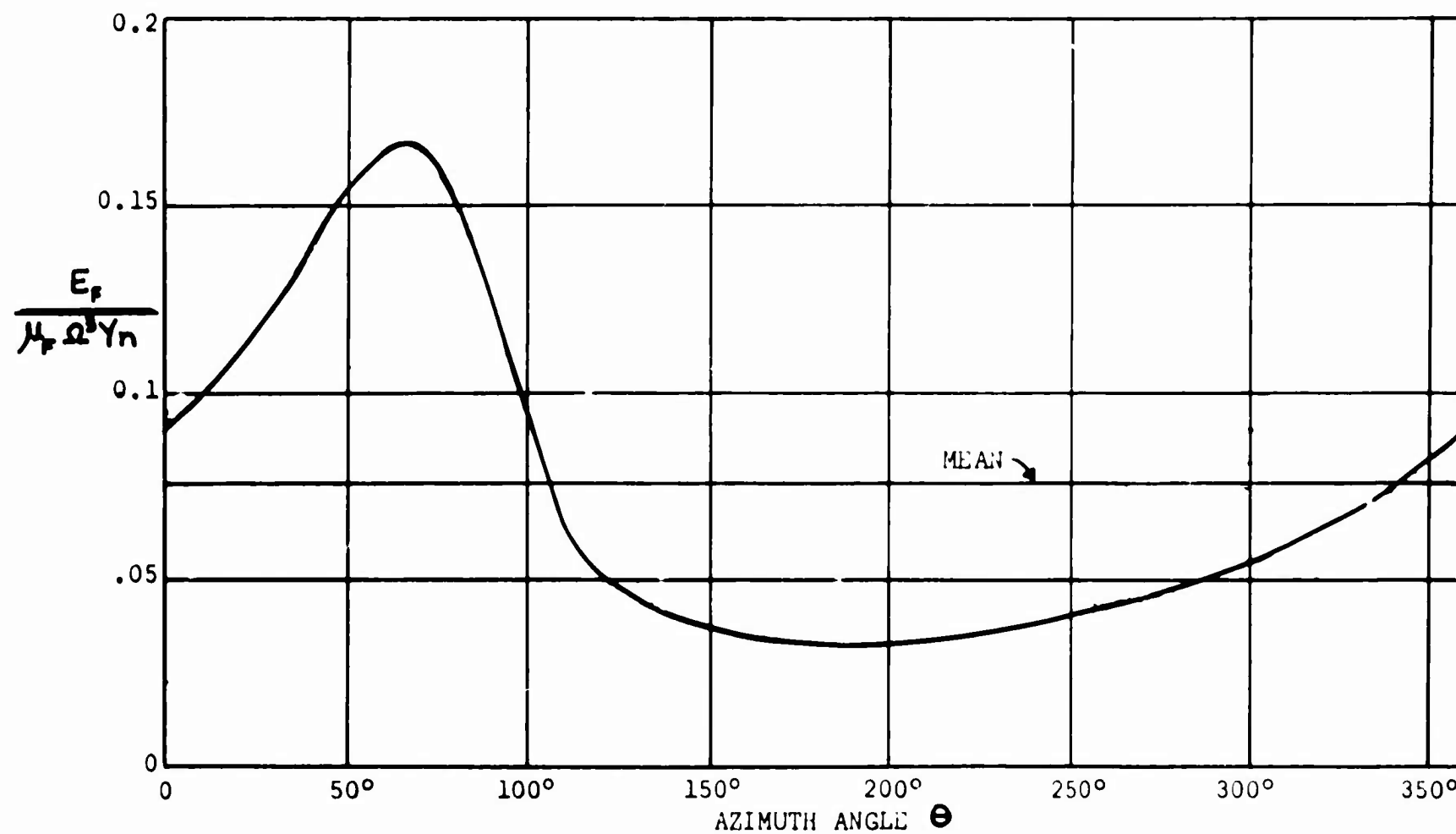
Figure 110. Instantaneous Friction Power Parameter $E_F/\mu_F \Omega^3 \gamma_n$ for Model Fan.

Friction Power Loss Due to Air Loads

The force necessary to generate the momentum flux observed in the fan jet efflux is reacted partly by the fan blades and partly on the intake lip.

For the purpose of obtaining an estimate of the mean tip reaction force F_R due to air loads, we assume that a static pressure equal to the jet exit total pressure acts uniformly over each blade when it is in the "pumping" position. Thus, the total force acting on the blade is $\Delta P_j bY$, and the resultant moment about the hinge is just half this. Thus, from equation (114)

$$F_T = F_R \cos\phi - \mu_F F_R \sin\phi = \frac{1}{2}\Delta P_j bY$$

$$F_R = \frac{\frac{1}{2} bY \Delta P_j}{\cos\phi - \mu_F \sin\phi} \tag{129}$$

The energy dissipated in friction is therefore

$$E_{AL} = \mu_F F_R V_T = \frac{\frac{1}{2}\mu_F bY . \Delta P_j V_T}{\cos\phi (1 - \mu_F \tan\phi)} \tag{130}$$

Assuming μ_F is small compared with unity and that E_j is given by equation (69) and ΔP_j by equation (71)

$$\frac{E_{AL}}{E_J} = \frac{\mu_F}{\cos\phi} \frac{Y}{R} \frac{1}{\mu} \tag{131}$$

For the model fan

$$\frac{E_{AL}}{E_J} = \frac{0.804 \mu_F}{0.7 \times 0.47} = 2.44 \mu_F$$

Diffusion Power Loss

There will, of course, be some skin friction loss associated with the exhaust duct, particularly if this is lengthy. When the exit area of this duct is larger than the effective working area of the fan, then additional losses will occur, which can be quite important.

The diffusion ratio τ_D is

$$\tau_D = \frac{\text{jet exit area}}{\text{fan working area}}$$

$$= \frac{b t_J}{(R - r_D) b} = \frac{\hat{t}_J}{1 - r_D/R} \tag{132}$$

This ratio is plotted in Figure 111 for the model fan and is seen to exceed unity for jet areas above about 80 per cent of nominal.

There is no simple analytical relationship governing total head loss due to diffusion, so that allowance for this effect will have to be made on a semi-empirical basis. For the model of Reference 24, this effect can probably be neglected entirely because of the relatively small diffusion involved even at the full nominal jet exit area position.

Power Required and Efficiency

Extending equation (93), the total power required by the fan is

$$E_T = E_J + E_{SF} + E_L + E_F + E_{AL} \tag{133}$$

or

$$\frac{E_T}{E_J} = \frac{1}{\eta_F} = \left(1 + \frac{E_L}{E_J}\right) + \frac{E_{SF}}{E_J} + \frac{E_F}{E_J} + \frac{E_{AL}}{E_J} \tag{134}$$

- where the individual components are, from the previous sections,

$$\frac{E_{SF}}{E_J} = \frac{4\pi \phi^4 C_f}{\mu} \frac{1 + \frac{2}{5}\phi \frac{R}{b}}{\frac{1}{4}\left(\frac{\mu}{\hat{t}_J}\right)^2 + \frac{\Delta P_J}{q_T}} \tag{75}$$

$$\left(1 + \frac{E_L}{E_J}\right) = \frac{1 + \left(\frac{2\hat{t}_J}{\mu}\right)^2 \frac{\Delta P_J}{q_T}}{\frac{\dot{m}_J}{\dot{m}_o}\left[\left(\frac{\dot{m}_J}{m_o}\right)^2 + \left(\frac{2\hat{t}_J}{\mu}\right)^2 \left(\frac{\Delta P_J}{q_T}\right)\right]} \tag{91}$$

$$\frac{\dot{m}_J}{\dot{m}_o} = \frac{1}{1 - a_L^2}\left\{1 - a_L \sqrt{1 + \frac{4}{\mu^2}\left(\hat{t}_J^2 - \hat{t}_L^2\right)\left(\frac{\Delta P_J}{q_T}\right)}\right\} \tag{88}$$

155

$$\frac{E_F}{E_J} = \frac{4\mu_F n \xi \left[\frac{x_0 M_{mD}}{\rho b Y R^3}\right]}{\mu\left[\frac{1}{4}\left(\frac{\mu}{\xi_J}\right)^2 + \frac{\Delta P_J}{q_T}\right]} \qquad (128)$$

$$\frac{E_{AL}}{E_J} = \frac{\mu_F}{\mu \cos\phi_0} \frac{Y}{R} \qquad (131)$$

Substituting these equations into equation (133) for the case of zero back pressure ($\Delta P_J = 0$)

$$E_T = E_J\left\{(1+a_L)^3 + \frac{16\pi\phi^4 C_f \hat{\xi}_J^2}{\mu^3}\left[1 + \frac{2}{5}\phi\frac{R}{b}\right]\right.$$

$$+ \frac{16\mu_F n \xi \hat{\xi}_J^2}{\mu^3}\left(\frac{x_0 M_{mD}}{bY\rho R^3}\right) + \left.\frac{\mu_F}{\mu \cos\phi}\left(\frac{Y}{R}\right)\right\}$$

$$= \frac{\mu^3 \rho V_T^3 b R}{16\hat{\xi}_J^2}\left\{\left[(1+a_L)^3 + \frac{16\pi\phi^4 C_f \hat{\xi}_J^2}{\mu^3}\left(1 + \frac{2}{5}\phi\frac{R}{b}\right)\right]\right.$$

$$+ \mu_F\left[\frac{16n\hat{\xi}_J^2 \xi}{\mu^3}\frac{x_0 M_{mD}}{bY\rho R^3} + \frac{Y/R}{\mu \cos\phi}\right]\right\} \quad (135)$$

When exhausting to ambient, the blade air load loss E_{AL} is negligibly small for an unbalanced blade. Thus, we may write equation (134) as

$$\frac{E_T}{\rho V_T^3 bR} = \frac{\mu^3(1+a_L)^3}{16\hat{\xi}_J^2} + \pi\phi^4 C_f\left[1 + \frac{2}{5}\phi\frac{R}{b}\right] + n\mu_F\xi\left(\frac{x_0 M_{mD}}{bY\rho R^3}\right) \quad (136)$$

Only the first term varies with the jet exit area.

Comparison of Theory With Experiment

We have already seen that simple theory gives excellent agreement with experiment so far as mass flow is concerned. Thus, our main concern in this section is with the estimation of power required, and from this the fan efficiency. In order to provide a basis for comparison, the model fan power required measurements of Reference 24 are reduced in Figure 112 and plotted as slopes in Figure 113. Justification for linear smoothing as a function of $(RPM)^3$ is given by equation (136).

In order to compare the theoretical power required to exhaust to ambient with experimental results, we make use of equation (136). The only unknown is the rolling friction coefficient μ_F. In Reference 27 the rolling friction coefficient is defined as

$$\mu_F = \frac{k}{r''} \tag{137}$$

- where r'' is the radius of the roller in inches. For the model fan, $r'' = 0.3125$ inches. The following values are given for in Reference 27.

Mating surfaces	k
Steel on steel	.002
Hard, polished steel on same	.0002-.0004
Hardwood on hardwood	.02

The model fan has steel on plastic mating surfaces, for which no data exists. By taking an arbitrary value of $k = .00625$, $\mu_F = .02$, the value used in Reference 26, this then gives the theoretical power variation calculated in Table 8 and plotted in Figure 114, where the agreement with experiment is seen to be very good at the higher exit area ratios.

From equations (89) and (92) the leakage plus exhaust power is, for exhausting to ambient,

$$E_J \left(1 + \frac{E_L}{E_J} \right) = \frac{\dot{m}_o^3}{2\rho^2 A_J^2} \left(\frac{\dot{m}_o}{\dot{m}_J} \right)^3 \tag{138}$$

At low jet exit areas we have seen that the air mass flow is lower than simple theory would indicate, possibly because of inlet blade stall. In other words, $\dot{m}_o$ is reduced. If we use Figure 95 to correct for this, by multiplying ($E_J + E_L$) by

$$\left(\frac{\dot{m}_J \text{ theory}}{\dot{m}_J \text{ experiment}} \right)^6$$

- we should get a power required curve of the correct order. Naturally, the fact that we are raising the experimental errors of Figure 95 to the power of six would make this a very dubious calculation for the present model fan results.

157

TABLE 8

CALCULATION OF POWER REQUIRED BY MODEL FAN EXHAUSTING TO AMBIENT

$\dfrac{A_J}{A_{JN}}$	10%	20%	40%	60%	80%	100%
$1 + a_L$	3.015	2.008	1.504	1.336	1.252	1.2015
$(1 + a_L)^3$	27.4	8.11	3.41	2.38	1.965	1.74
$\hat{\xi}_J^2$	.001225	.0049	.0196	.0441	.0784	.1225
$\dfrac{\mu^3}{16} \dfrac{(1+a_L)^3}{\hat{\xi}_J^2}$	145.2	10.73	1.128	.35	.1627	.0922

$\dfrac{A_J}{A_{JN}}$	20%	33%	45%	57%	80%	100%
$\dfrac{BHP}{\left(\frac{RPM}{100}\right)^3}$	.656	.546	.56	.518	.522	.47 $\times 10^{-4}$
$\dfrac{E_T}{\rho V_T^3 bR}$	1.905	1.586	1.625	1.50	1.515	1.363

$\rho = 20.5 \times 10^{-4}$ $\hat{\xi}_{JN} = 0.35$ $a_{LN} = 0.2015$

$\mu^3/16 = 0.00649$ $\phi = 0.864$ $R/b = 0.795$

$C_f = 0.004$ $2/5\,\phi\,(R/b) = 0.275$ $x_0 M_{mD}/bY\rho R^3 = 12.02$

$\pi \phi^4 C_f \left[1 + \frac{2}{5}\phi\left(\frac{R}{b}\right)\right] = 0.01383$ $\dfrac{n\hat{\xi}\,x_0 M_{mD}}{bY\rho R^3} = 62.6$

For $\mu_F = 0.02,$ $\mathcal{F}(\mu_F) = 1.252$

$V_T = 3.815\left(\frac{RPM}{100}\right)$ $BHP\left/\left(\frac{RPM}{100}\right)^3\right. = 0.1008\,\dfrac{E_T}{V_T^3}$

$\dfrac{E_T}{\rho V_T^3 bR} = 2.9 \times 10^4 \left(\frac{RPM}{100}\right)^3$

If we had employed a balanced blade for the model fan, so that $M_{m\theta} = 0$, then the friction power required would have been, from equation (123)

$$E_F = \frac{\Delta E_{\ddot{\vartheta}}}{\gamma} \, \eta \mu_r \, \Omega^3$$

From Figure 109 the mean value of $E_{\ddot{\vartheta}}$ would have been

$$.09 \times .23 \times 10^{-3} = 0.207 \times 10^{-4}$$

This gives a friction power loss which is

$$\frac{.0207}{.076} = 27.2 \text{ per cent of the unbalanced blade power loss.}$$

Applying this correction gives the broken line in Figure 114.

The maximum efficiency measured in Reference 24, when exhausting to ambient, is 9.1 per cent at $\hat{t}_J = 0.33$. Applying the balanced blade correction we get

$$\eta_r = 9.1 \text{ per cent} \times \frac{1.71}{0.8} = 19.5 \text{ per cent}$$

As shown in Figure 115, this is in good agreement with the predictions of Reference 26 when we remember that the leakage area of the Reference 24 model is very large.
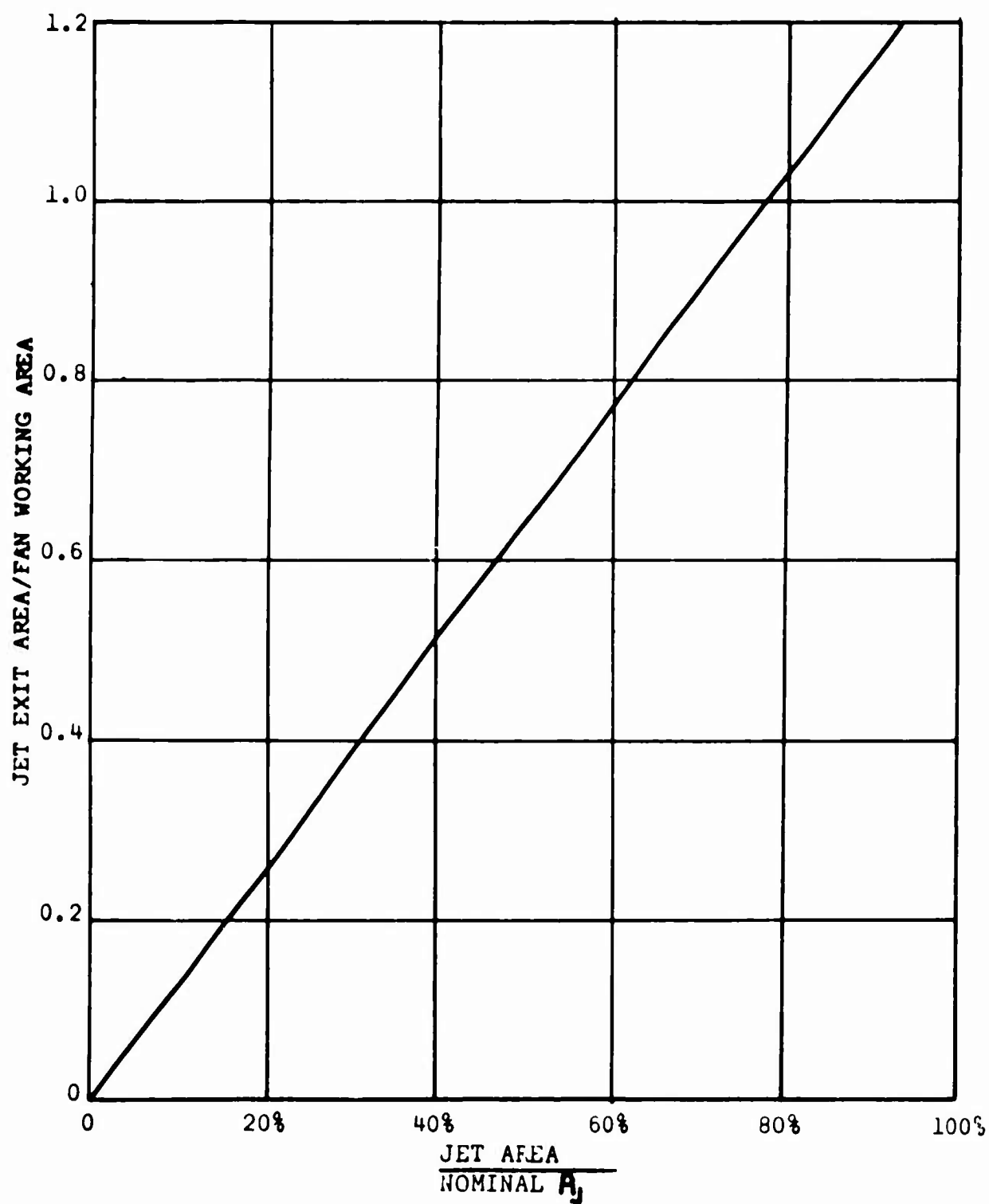
Figure 111.   Diffusion Ratio For Model Fan (μ = 0.47)

160
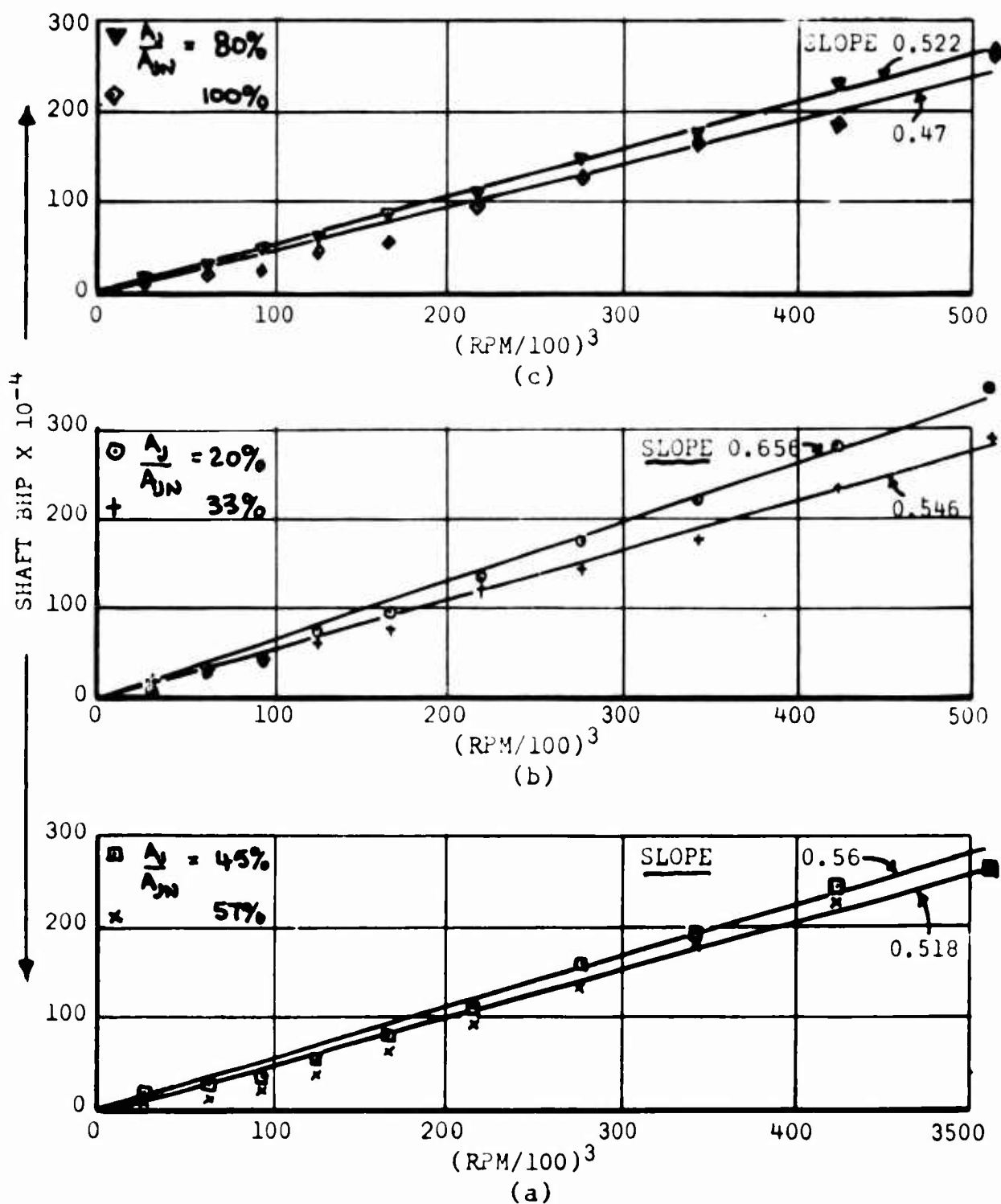
Figure 112. Experimental Power Measurements Reduced
To ρ = 20.5 X 10^{-4} Slugs/Feet^3.

161
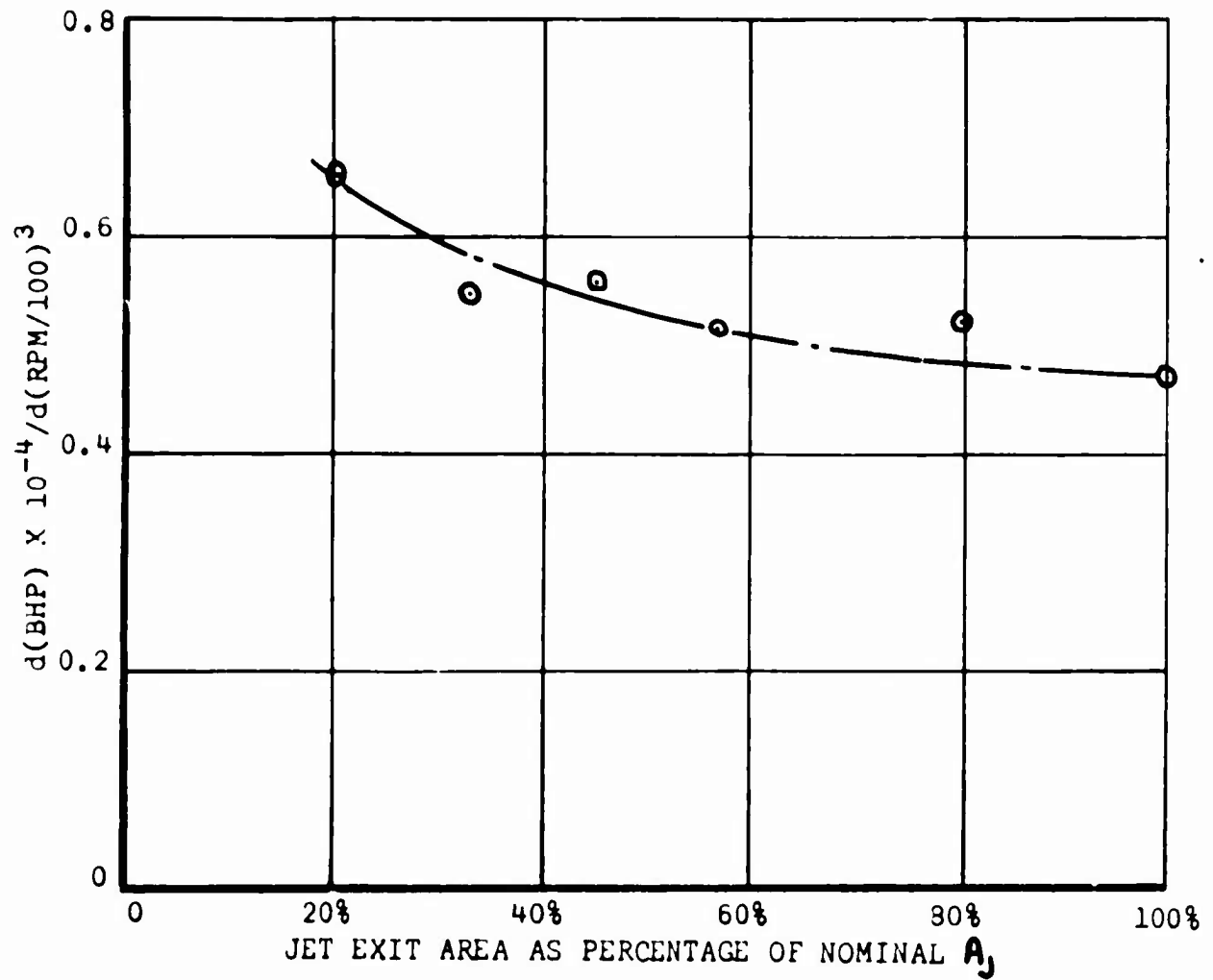
Figure 113. Variation of Power Parameter With
Exit Area (ρ = 20.5 X 10^{-4} Slugs/Feet^3).
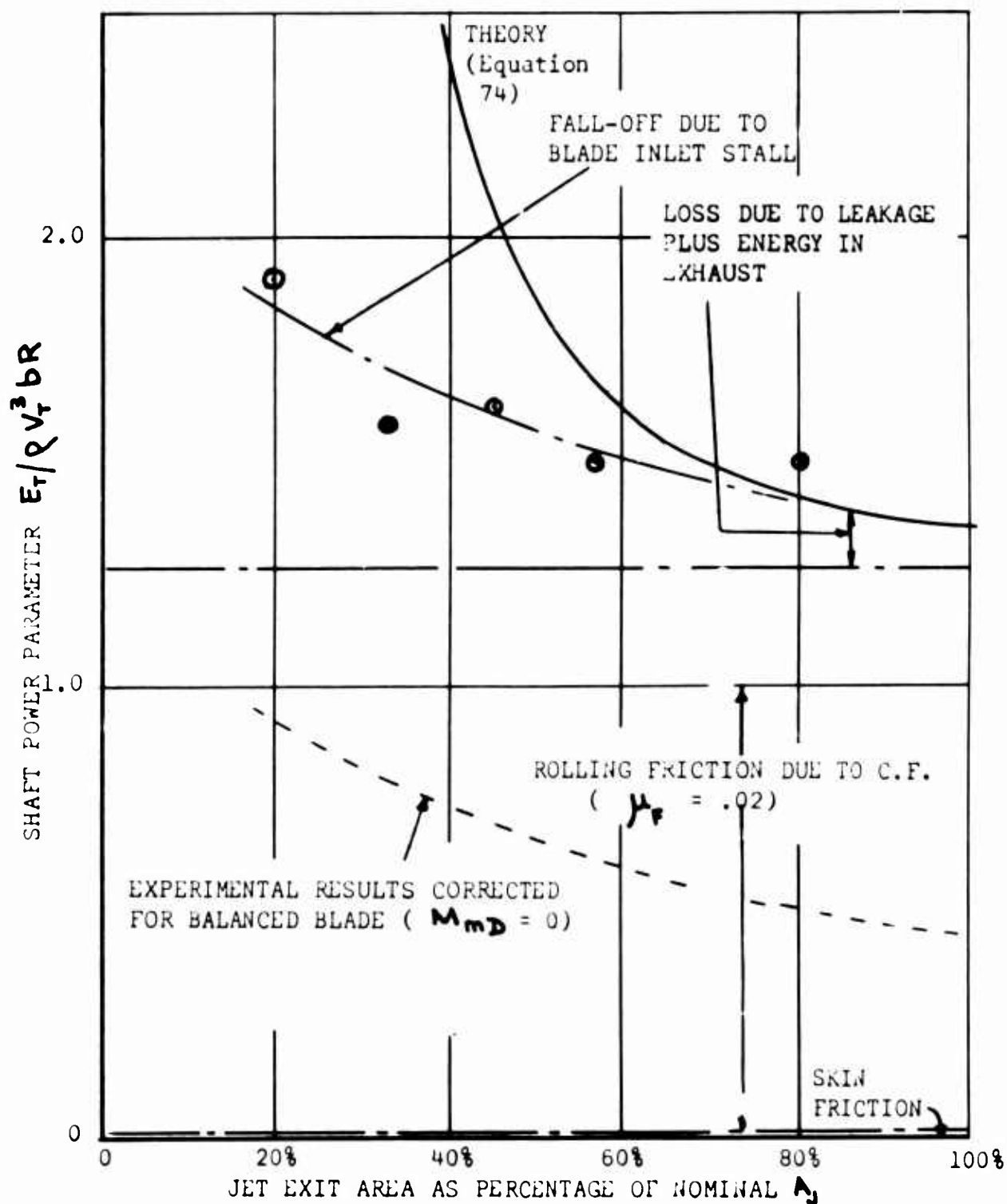
Figure 114. Comparison of Theory With
Experimental Points From Figure 113.

163
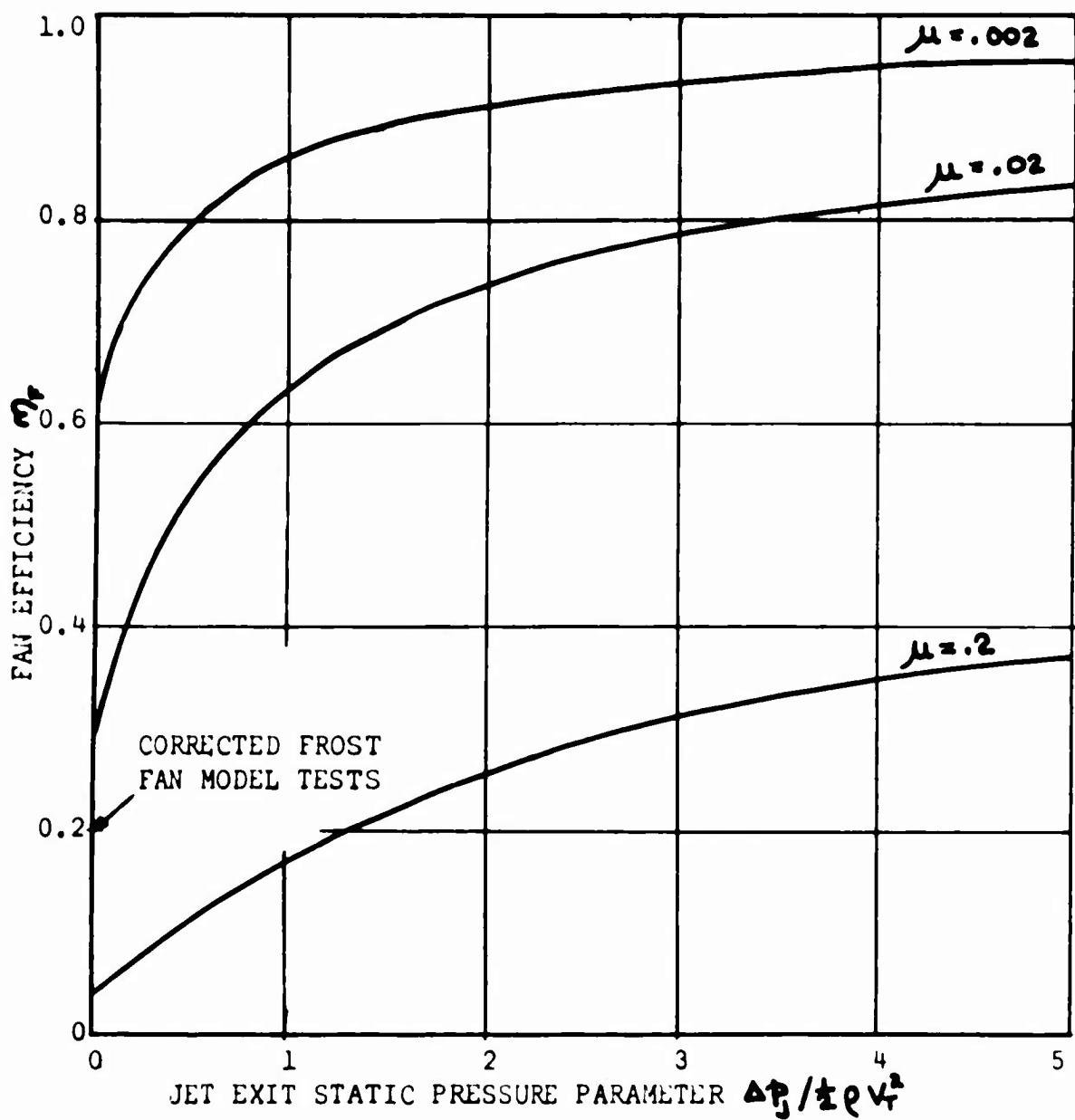
Figure 115. Effect of Blade Tip Rolling Friction
Coefficient Upon Efficiency of Frost Fan.

PROBLEMS OF BLADE STABILITY

Tests For Flapping Stability When Only Case Constraint is Employed

When only the case is used to restrain a blade and C.F. forces are re-
lied upon to hold the blade in contact with it, "flapping instability"
is defined as the inability of the blade to follow the case contour.
Obviously, this condition will be associated with the tip reaction
force F_R falling to zero, so that, from equation (115) the applicable
equation of motion is

$$\frac{d^2\zeta}{d\theta^2} + \left(\frac{\omega}{\Omega}\right)^2 \sin\zeta = 0 \tag{139}$$

For special (and unlikely) cases where $\zeta \rightarrow 0$ this can be linearized to
give the equation for undamped harmonic motion. More importantly,
is often close to the value $\pi/2$ so that we can assume the approxima-
tion $\sin\zeta = 1.0$.

$$\therefore \frac{d^2\zeta}{d\theta^2} = -\left(\frac{\omega}{\pi}\right)^2 \tag{140}$$

$$\frac{d\zeta}{d\theta} = -\left(\frac{\omega}{\Omega}\right)^2 \theta + C_1 \tag{141}$$

At some arbitrary angle θ_o, $\frac{d\zeta}{d\theta} = \left(\frac{d\zeta}{d\theta}\right)_o$

Thus

$$\left(\frac{d\zeta}{d\theta}\right)_o = C_1 - \left(\frac{\omega}{\Omega}\right)^2 \theta_o$$

or

$$C_1 = \left(\frac{d\zeta}{d\theta}\right)_o + \left(\frac{\omega}{\Omega}\right)^2 \theta_o$$

$$\therefore \frac{d\zeta}{d\theta} = \left(\frac{d\zeta}{d\theta}\right)_o + \left(\frac{\omega}{\Omega}\right)^2 (\theta_o - \theta) \tag{142}$$

Integrating again with respect to θ

$$\zeta = \left(\frac{d\zeta}{d\theta}\right)_o \theta + \left(\frac{\omega}{\Omega}\right)^2 \left(\theta_o\theta - \tfrac{1}{2}\theta^2\right) + C_2 \tag{143}$$

165

At the same arbitrary angle θ_0, $\gamma = \gamma_0$

$$\therefore \gamma_0 = \left(\frac{d\gamma}{d\theta}\right)_0 \theta_0 + \frac{1}{2}\left(\frac{\omega}{\Omega}\right)^2 \theta_0^2 + c_2$$

$$\therefore c_2 = \gamma_0 - \left(\frac{d\gamma}{d\theta}\right)_0 \theta_0 - \frac{1}{2}\left(\frac{\omega}{\Omega}\right)^2 \theta_0^2$$

$$\therefore \gamma = \gamma_0 - \left(\frac{d\gamma}{d\theta}\right)_0 (\theta_0 - \theta) - \frac{1}{2}\left(\frac{\omega}{\Omega}\right)^2 (\theta_0 - \theta)^2 \qquad (144)$$

Any one of equations (140), (142), or (144) can be used as a test of blade stability.

As an illustration of the use of equation (142) we note that for the model fan blade

$$\left(\frac{\omega}{\Omega}\right)^2 = \frac{x_0 M_{mD}}{I_D} = \frac{0.225 \times 0.713}{0.23} = 0.697$$

From Figure 107 the maximum negative value of $\frac{d^2\gamma}{d\theta^2}$ is -0.29, so that the blade will be stable. Alternatively, equations (142) or (144) could have been superimposed upon Figures 105 or 106 to reach the same conclusion.

An exact test can be applied when γ diverges appreciably from the value of $\pi/2$ necessary to render valid the foregoing approximations.

By writing $\quad p = \dfrac{d\gamma}{d\theta}$

so that $\dfrac{d^2\gamma}{d\theta^2} = p \dfrac{dp}{d\gamma}$

- equation (139) can be written as

$$\int_{p_0}^{p} p\, dp = -\left(\frac{\omega}{\Omega}\right)^2 \int_{\gamma_0}^{\gamma} \sin \gamma\, d\gamma \qquad (145)$$

$$p^2 - p_0^2 = -2\left(\frac{\omega}{\Omega}\right)^2 \left[\cos \gamma - \cos \gamma_0\right]$$

$$\therefore \frac{d\gamma}{d\theta} = \sqrt{\left(\frac{d\gamma}{d\theta}\right)_0^2 + 2\left(\frac{\omega}{\Omega}\right)^2 (\cos \gamma_0 - \cos \gamma)} \qquad (146)$$

This maximum flapping velocity can be superimposed upon a graph of required $d\zeta/d\theta$, such as Figure 107, in order to determine whether the blade will follow the case contour.

Bending Stability

In order to minimize friction losses, present Frost Fan designs incorporate ball-bearing rollers at the blade tips, which react the dynamic loads. This means that the blade acts as a rather complex beam, with pinned or fixed ends, depending upon the precise geometry employed. Under the influence of CF the blade will deflect towards the case, while the oscillatory inertia loading caused by blade flapping will cause it to vibrate in a translational mode.

This leads to two design requirements. The blade must be stiff enough to avoid rubbing against the case under maximum r.p.m. conditions, and its natural frequencies should not be in resonance with a flapping, forcing frequency. The calculations necessary to ensure that these requirements are met are well understood, of course, and will not be detailed in this report.

Determination of the Blade Frequency Parameter (ω/Ω) For a Uniform Blade

Consider a uniform blade, of mass distribution Δm per unit length, and with a point mass m_p situated at a distance y_p from the hinge.

Then
$$M_{mD} = m_p y_p + \Delta m \int_0^Y y \, dy$$

$$= m_p y_p + \tfrac{1}{2} m_b y \qquad (147)$$

where $m_b = \Delta m Y$, the total blade weight.

Similarly
$$I_D = m_p y_p^2 + \Delta m \int_0^Y y^2 \, dy$$

$$= m_p y_p^2 + \tfrac{1}{3} m_b Y^2 \qquad (148)$$

$$\therefore \left(\frac{\omega}{\Omega}\right)^2 = \frac{m_p y_p + \tfrac{1}{2} m_b Y}{m_p y_p^2 + \tfrac{1}{3} m_b Y} \, X_o \qquad (149)$$

Let $\quad \overline{m}_p = \dfrac{m_p}{m_b}, \quad \overline{y}_p = \dfrac{y_p}{Y}$

Then
$$\left(\frac{\omega}{\Omega}\right)^2 = \left(\frac{x_0}{Y}\right)\frac{\frac{1}{2} + \overline{m}_p \overline{y}_p}{\frac{1}{3} + \overline{m}_p \overline{y}_p^{\,2}} \tag{150}$$

Thus
$$\left(\frac{\omega}{\Omega}\right)^2 = \frac{3}{2}\frac{x_0}{Y} \qquad \text{for } m_p = 0 \text{ or } y_p = 0 \tag{150a}$$

and the larger the hinge offset distance x_0 is in relation to the blade length Y, the greater will be the frequency.

When $\overline{m}_p > 0$, there is obviously an optimum position for the point mass. From equation (150)

$$\frac{\partial}{\partial \overline{y}_p}\left[\frac{Y}{x_0}\left(\frac{\omega}{\Omega}\right)^2\right] = \frac{\overline{m}_p}{\frac{1}{3} + \overline{m}_p \overline{y}_p^{\,2}} - 2\overline{y}_p \overline{m}_p \frac{\left(\frac{1}{2} + \overline{m}_p \overline{y}_p\right)}{\left(\frac{1}{3} + \overline{m}_p \overline{y}_p^{\,2}\right)^2}$$

Equating to zero, $\quad \left(\overline{y}_p\right)_{opt.} = \dfrac{-1 + \sqrt{1 + \frac{4}{3}\overline{m}_p}}{2\overline{m}_p} \tag{151}$

As $\quad \overline{m}_p \to 0, \quad \left(\overline{y}_p\right)_{opt.} \to \dfrac{1}{3}$

As $\quad \overline{m}_p \to \infty, \quad \left(\overline{y}_p\right)_{opt} \to 0$

The variation of $\left(\overline{y}_p\right)_{opt}$ and $\frac{Y}{x_0}\left(\frac{\omega}{\Omega}\right)^2$ with mass ratio $\overline{m}_p$ is plotted in Figures 116 and 117 for practically attainable values, and it is evident that the use of a point mass enables relatively significant increases in frequency to be obtained.

When the point mass is not situated in the optimum position, its effect on the frequency parameter depends on whether it is situated inboard or outboard of the "center of percussion" which lies at the station $\overline{y}_p = 2.3$. This is illustrated in Figure 118.
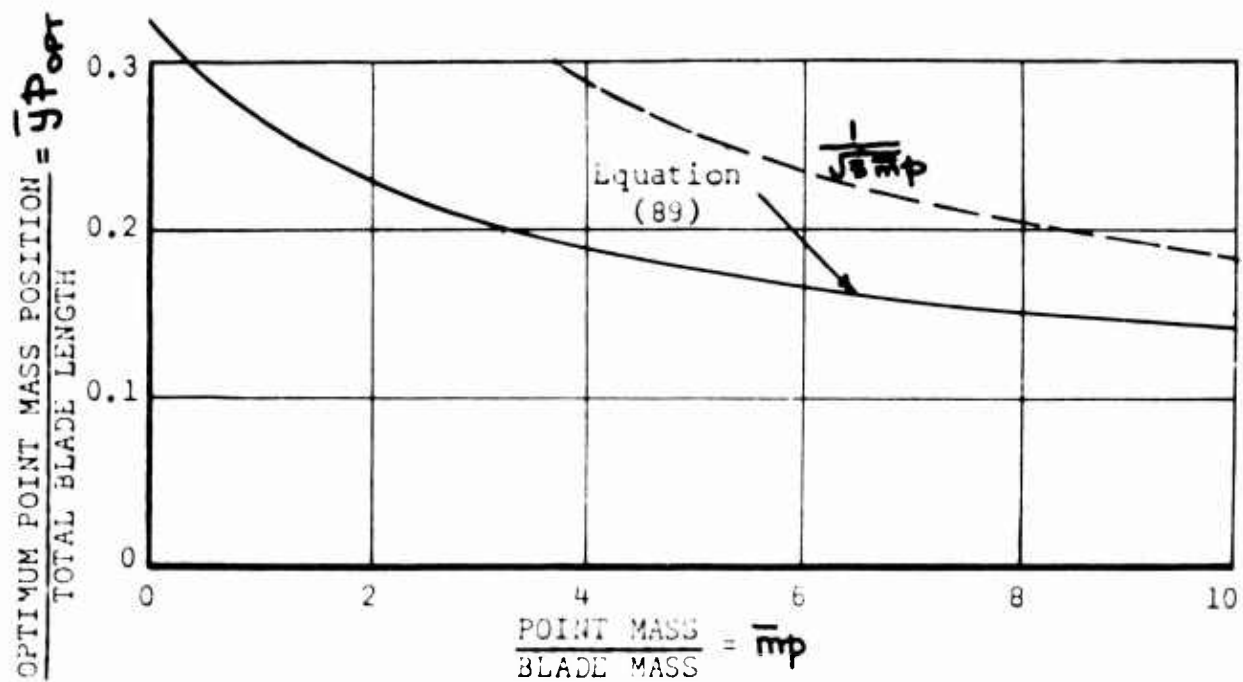
Figure 116. Optimum Position for a Point Mass on a Uniform Blade.
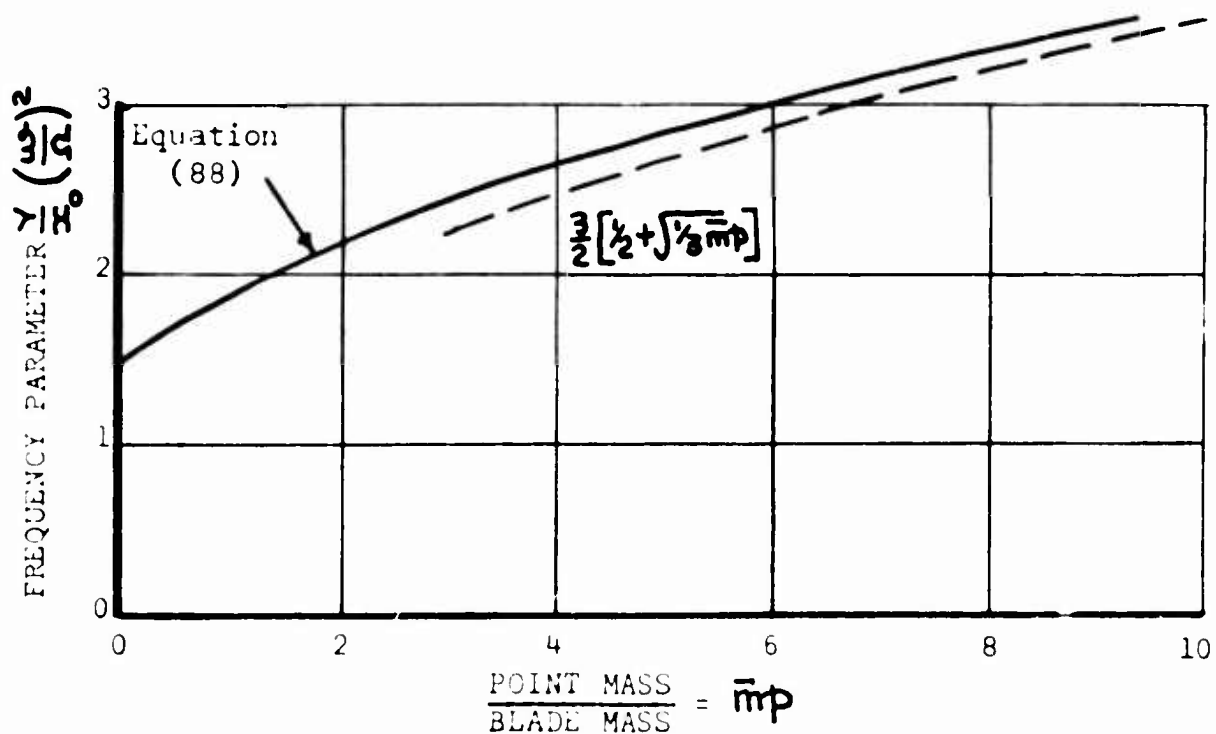
Figure 117. Optimum Frequency Variation With Mass Ratio.

169
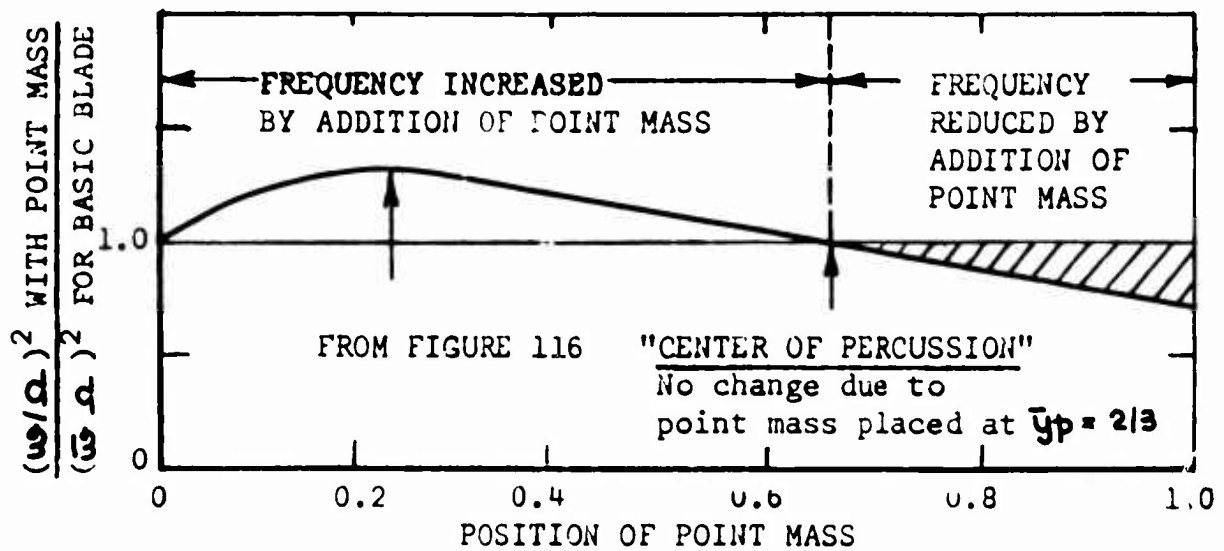
Figure 118. Effect of Radial Position of Point
Mass on Blade Frequency for $\overline{m}_p$ = 1.0.

Effect of Mass-Balancing A Blade

From equation (150a) we can see that the frequency parameter (ω/Ω)
is more or less fixed by blade geometry, in the absence of a large
point mass. It can be reduced by the addition of mass balance, how-
ever, as shown in Figure
119. When this is done,
equation (150a) becomes

$$\left(\frac{\omega}{\Omega}\right)^2 = \frac{3}{2}\frac{x_g}{Y}\frac{1-2\overline{m}_B\overline{y}_B}{1+3\overline{m}_B\overline{y}_B^2}$$ (102)

Where $\overline{m}_B = \dfrac{m_B}{m_b}$

$\overline{y}_B = \dfrac{y_B}{Y}$

This is plotted in Figure
120 for two balance weight
positions, and the effect
on C.F. torque is plotted
in Figure 121.
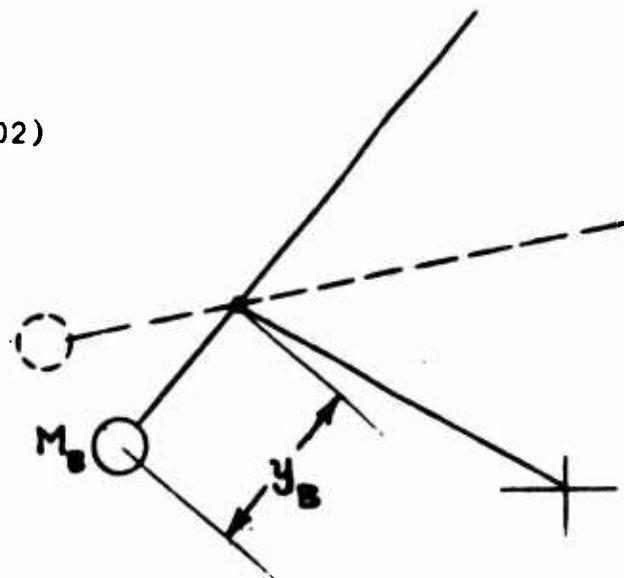
Figure 119. Mass-Balanced Blade.

170
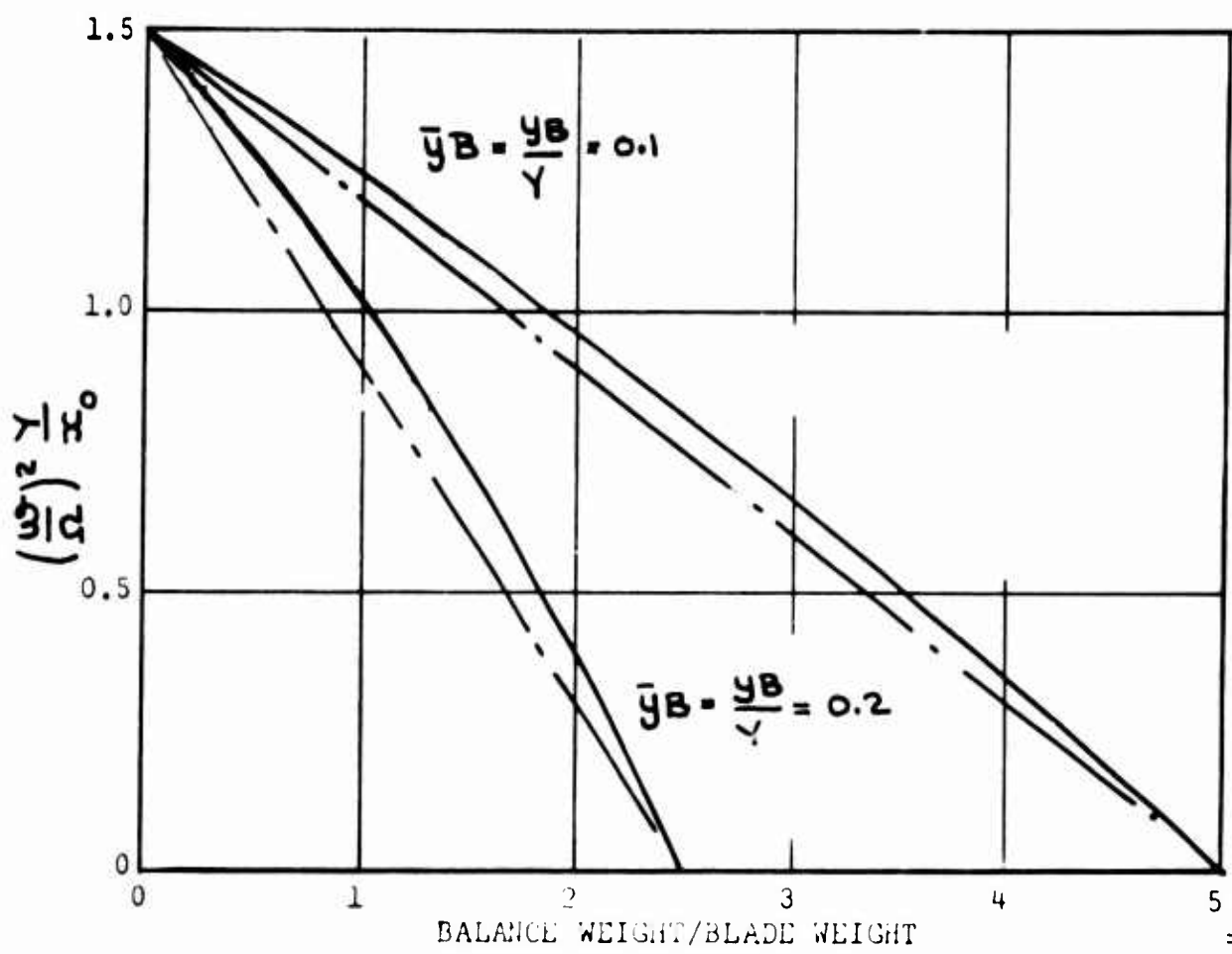
Figure 120. Effect of Balance Weight on Blade Frequency.
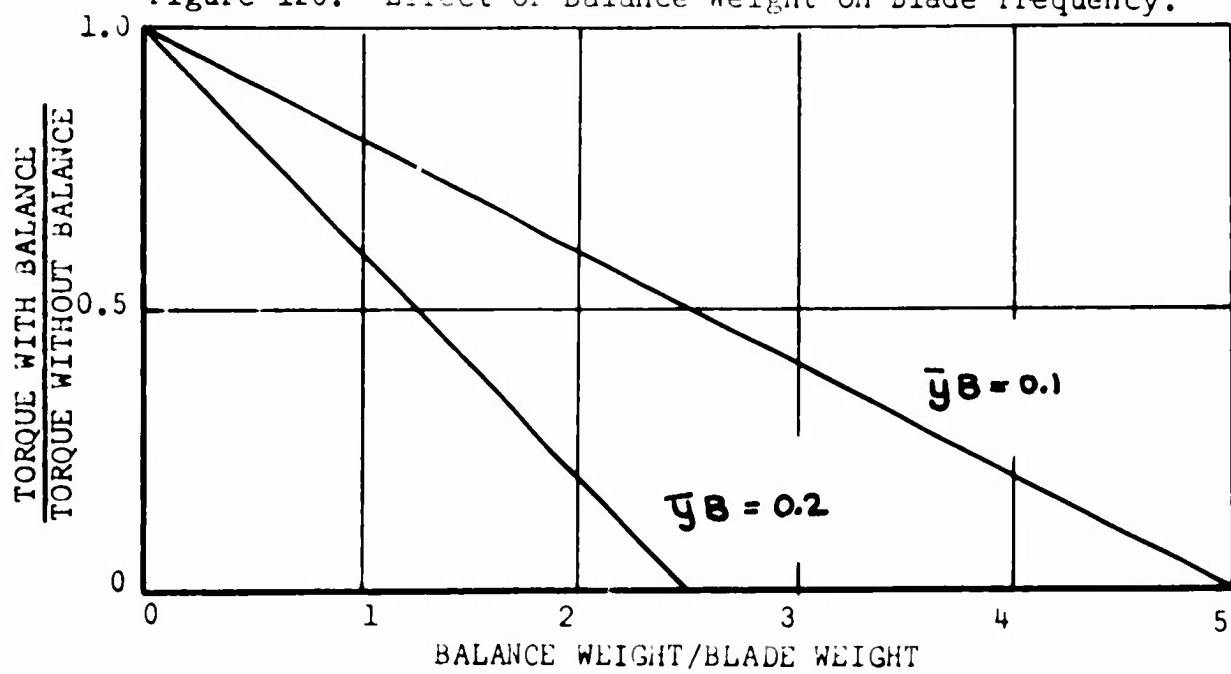
Figure 121. Effect of Balance Weight on Torque.

171

RECOMMENDATIONS FOR FURTHER ANALYTICAL WORK

Influence Of A Pressure Differential Across The Jet

In this report we have studied the problem of exhausting to a constant back-pressure Δp_j. In a practical ground effect machine the static pressure on the cushion side of the jet will be higher than on the opposite side, as indicated in Figure 122. Naturally, we can approximate to this condition by assuming that the jet static pressure is everywhere equal to the mean of the static pressure on either side of it, as is the case for "thin-jet" theory. The limitations of this assumption at low height/jet thickness ratios are well known, however, and "layered jet" theory will have to be developed for the Frost Fan. Since we are here concerned with essentially a positive displacement device, rather than a constant total head generator such as an axial fan, the theoretical attack will have to be somewhat different to the treatments so far published.
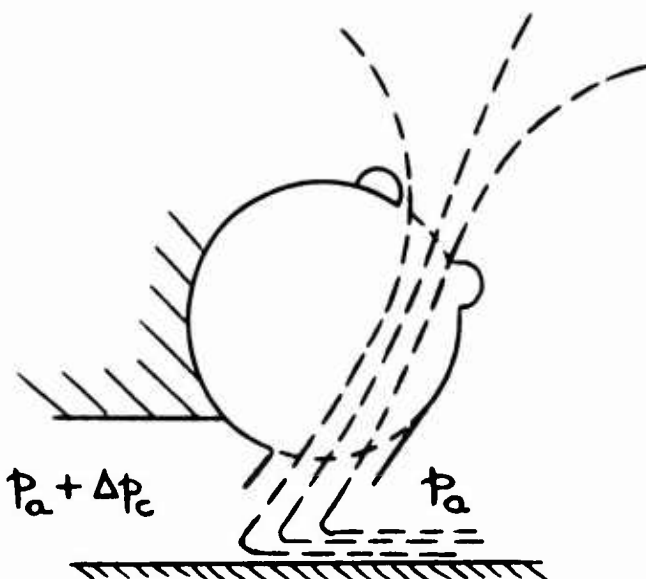
Figure 122. Differential Static Pressure at Jet Exit.

Control Power and Control Surface Loads

The most obvious method of applying pitch and roll control moments to a vehicle equipped with Frost fans is to vary the exit area, by means of a hinged plate, as was done with the model described in Reference 24, for example. Other methods involve dumping some of the jet horizontally into the cushion, the use of spoilers, and partial closure of the intake. These methods should be investigated theoretically in order to discover the most promising solution, followed by an experimental program, utilizing the existing fan test rigs, in order to check the theoretical findings.

As part of this work the control loads should be measured and compared with theoretical values, so that a logical basis for predicting and minimizing the driver's control forces can be developed.

Static and Dynamic Stability

The static stability derivatives in heave, pitch and roll should be examined theoretically for a constant fan speed and for constant fan torque. A Theoretical treatment should be developed to permit experimental observations of dynamic response to heave and pitch perturbations to be analyzed, and the performance of free-flight vehicles to be estimated.

A number of investigations of the dynamic stability of annular jet machines have already been published, but none of them include the fan coupling effects which are felt to be of dominant importance in a GEM equipped with Frost Fans - or indeed, in any annular jet vehicle.

Optimum Case Profile

The non-sinusoidal nature of the blade flapping function

$$\zeta = f(\theta)$$

- which is obtained when the case is circular, gives rise to very large local tip loads, as shown in Figure 108, for example. These high loads can be expected to have a detrimental effect upon the life of the tip rollers, to introduce some noise and vibration problems, and most importantly, to increase the frictional losses.

To avoid these disadvantages it is desirable to work out a case geometry which gives a sinusoidal variation of the blade flapping angle as the fan shaft is rotated.

SECTION FIVE

FULL-SCALE MEASUREMENTS WITH A FROST FAN

INTRODUCTION

This section together with Appendix IX contains the results obtained
from various investigations with two full-scale Frost Fans. During the
test program it was found necessary to substitute redesigned blades to
cure structural deficiencies found in the original ones, but the basic
fan configuration remained essentially unchanged. As usual in initial
development, results showed that this original fan design was non-
optimum. As this became apparent, additional theory was developed that
seems to give satisfactory explanation.

For example, the tip clearance between the blade and the case was
thought originally to be quite unimportant. For production reasons the
full-scale fans were designed with a large tip clearance and it was
difficult to remedy this after the theory of Reference 28 showed that
tip losses in fact, next to friction losses, were the major source of
inefficiency.

In general, the results of these tests are considered to be quite sat-
isfactory, bearing in mind the problem encountered with tip roller
friction and the additional problems of blade leakage and end loss.
The highest efficiencies measured - around 55 per cent - are signifi-
cantly better than the system efficiencies of existing annular-jet
GEM's.

Applying the theory developed in Reference 28 to test results obtained
indicates that the anticipated efficiency figures should be achievable
with a revised configuration of the Frost Fan that incorporates the
lessons learned. Even allowing for performance decrements in this next
evolutionary phase, it is expected that an efficiency in the range of
70 to 80 per cent will still be attained.

CALCULATED PERFORMANCE

The theory of Reference 28 has been used to calculate the performance
of the prototype Frost Fan. Figure 123 shows one of the fans with its
end bell removed. Contrary to the expectations expressed in Reference
26, the influence of blade edge clearance (and the resultant leakage)
is found to be of overriding importance.

Figure 123. Frost Fan With End-Bell Removed.

In Figures 124 and 125 the air mass flow is plotted as a function of the leakage area (the nominal leakage area A_{LN} corresponding to $t_L = 0.02275$, the geometric value measured under static conditions) and the back-pressure parameter $\Delta p_j / q_T$, Δp_j being the mean (gauge) static pressure in the jet, and q_T the dynamic pressure associated with the maximum peripheral velocity of the fan blades. It is evident that even the nominal leakage area accounts for a very severe drop in air mass flow. In practice, this is accentuated by case and blade deflections during operation of the fan. Certain minor improvements to correct these conditions were made, but the real solution lies in taking these lessons into account and incorporating appropriate revisions in designing the next generation of the Frost Fan configuration.

It is of interest to note, in Figure 124, the limitations of the cross-flow fan in comparison with the Frost Fan. If we assume a steady-state cushion pressure of 50 lb./ft.^{2}, for example, $(\Delta p_j / q_T)_{MAX} = 1.1$ for the crossflow fan (allowing for dynamic increases when perturbed) so that a tip speed of $V_T = 200$ ft./sec. is required. This presents serious problems in the design of blading to withstand the high bending forces due to centrifugal acceleration.

For the Frost Fan, back-pressure is almost immaterial, and a mass flow parameter of

$$\frac{\dot{m}_j}{\rho A_j V_T} = 1.5 \text{ to } 1.6$$

- should be easily realizable.

The efficiency of the present Frost Fan configuration, with zero leakage, is plotted in Figure 126. It is evident that the largest single source of inefficiency is the rolling friction associated with the tip rollers, even with the quite low rolling friction coefficient of $\mu_R = 0.01$.
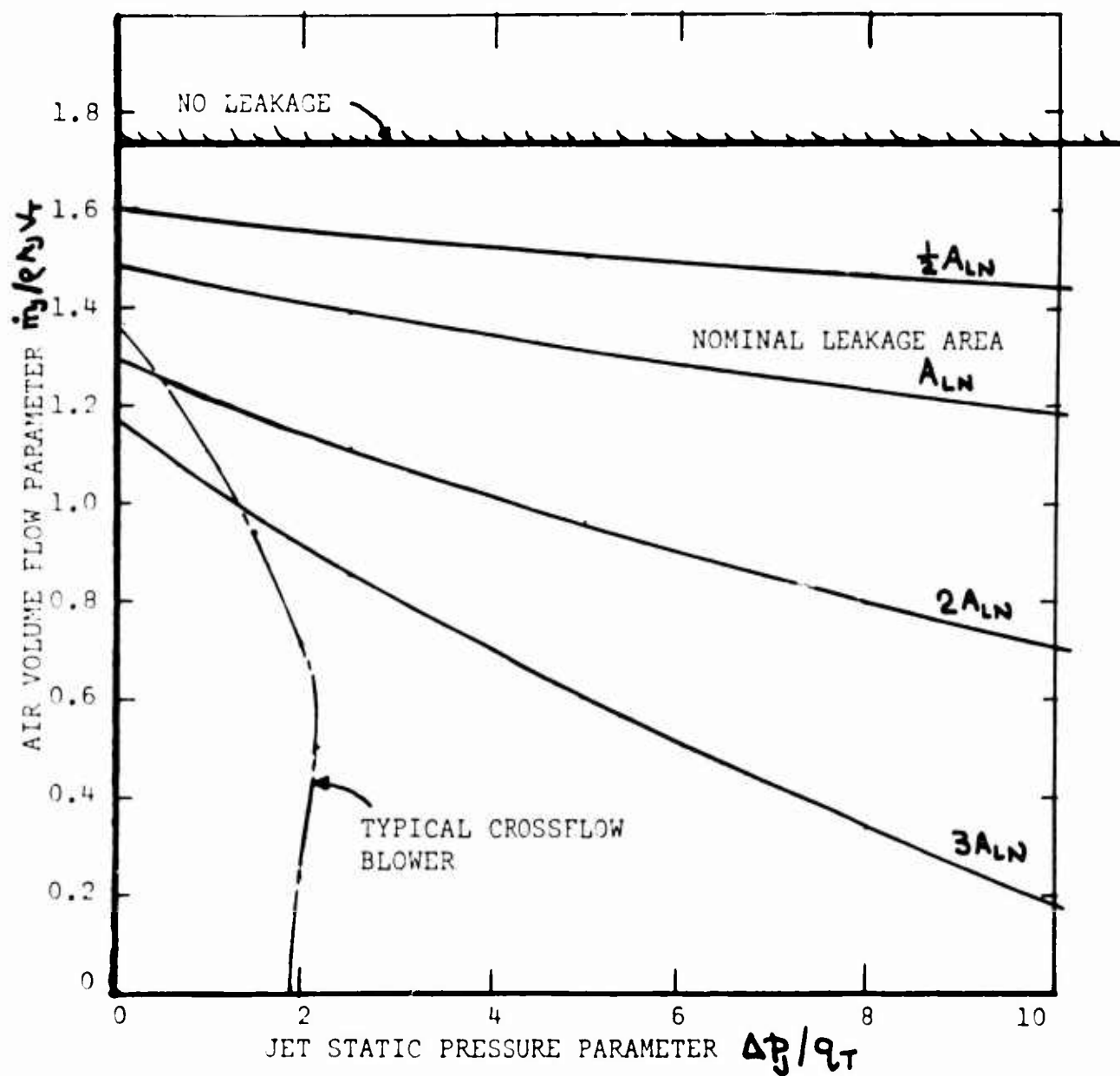
Figure 124. Variation of Air Volume Flow With Back-Pressure For Frost Fan No. 1 (Full Scale).
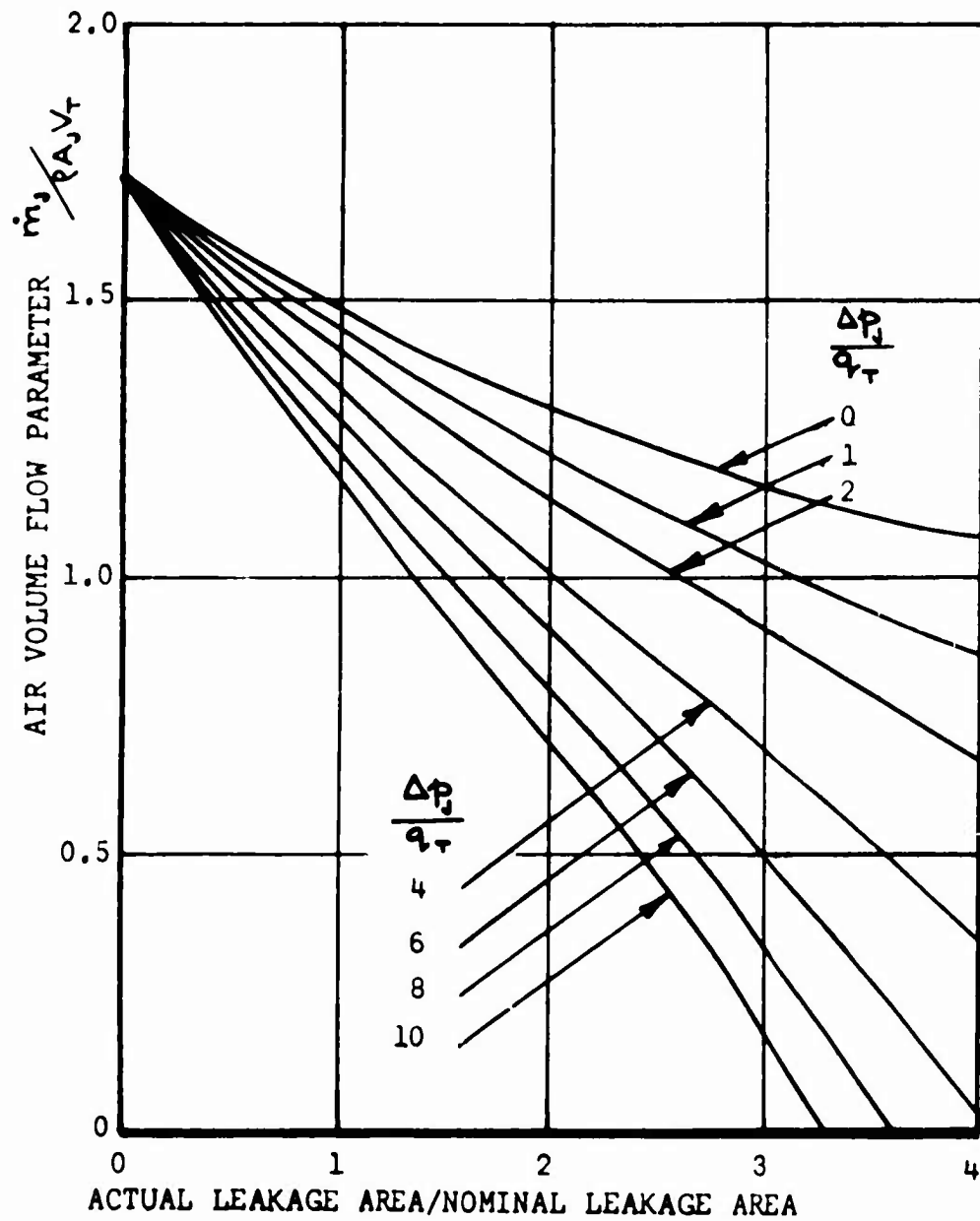
Figure 125. Variation of Air Volume Flow
With Leakage Area For Frost Fan No. 1.
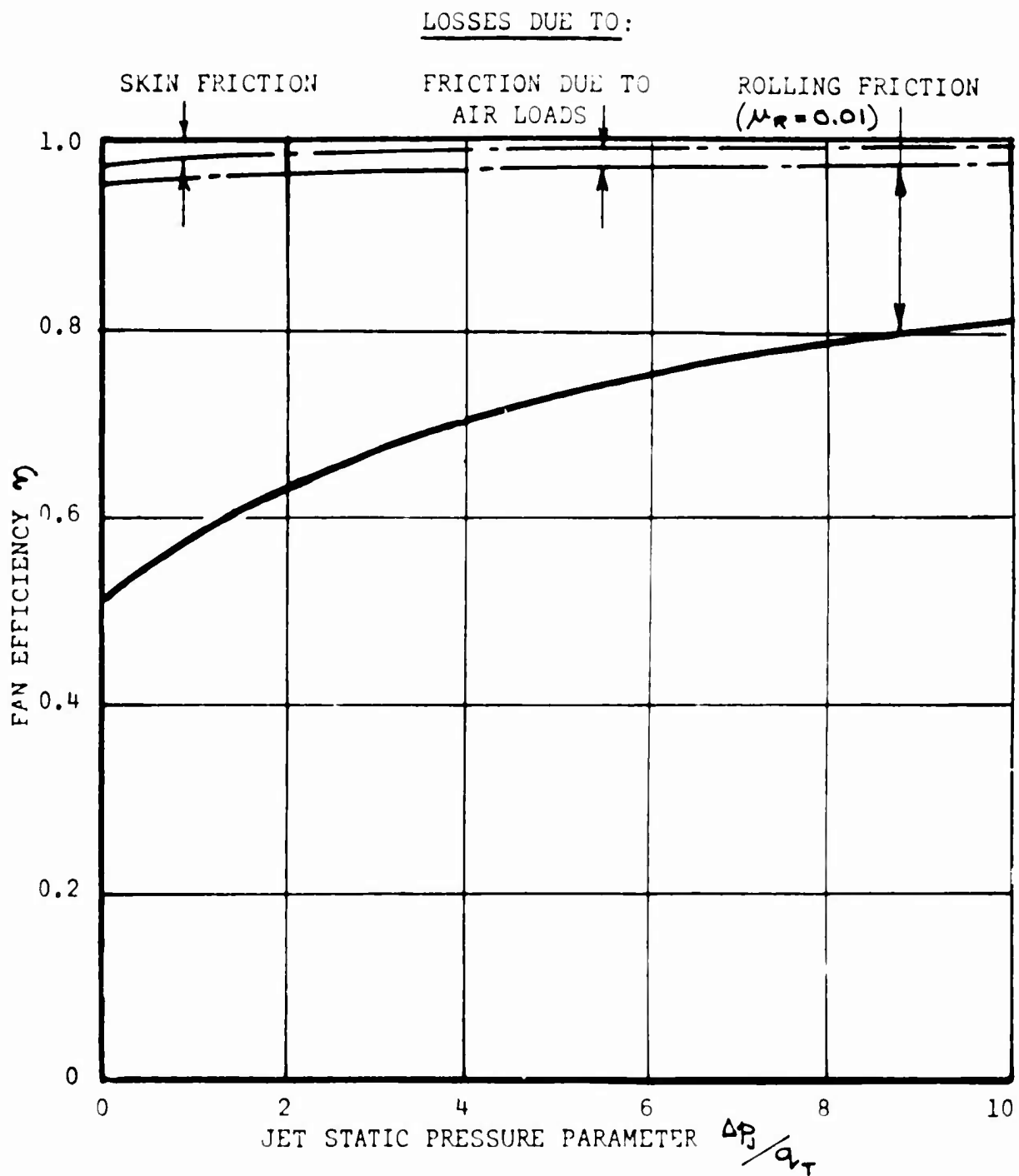
Figure 126. Efficiency of Fan No. 1 With Zero
Leakage Losses (Partially Balanced Blade).
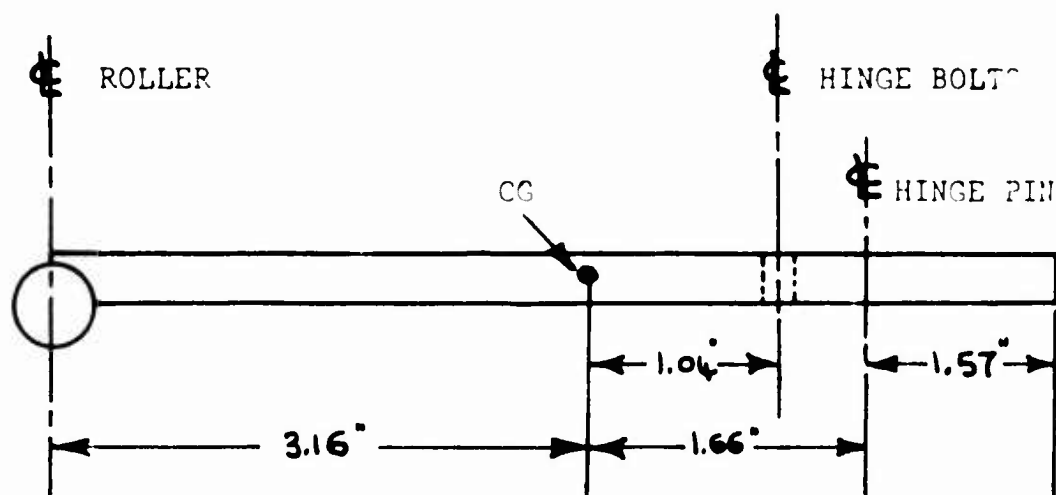
MASS OF BLADE   = 0.053 SLUGS
MASS OF ROLLER
   ASSEMBLY   = 0.002 SLUGS
MASS OF HINGE BOLTS   = 0.004 SLUGS

Figure 127.   Fan Blade Center of Gravity and Mass Distribution.

The Influence of Leakage Upon Efficiency

The theory of Reference 28 has been used to calculate the efficiency of the Frost Fan, as a function of back-pressure, for various values of leakage, and the results are shown in Figures 128 - 131 for the fan blade geometry and mass distribution shown in Figure 127. The summary curves in Figure 131 indicate very clearly the powerful effect of quite small leakage ratios in reducing efficiency. Obviously, an efficient fan will be designed with the reduction of leakage as a prime design objective.

The general theory of Reference 28 treats the problem of leakage as a gross phenomenon, in that all leakage paths are lumped together as a "total mean effective leakage area" (A_L) across which the pressure differential ΔP_J is assumed to act. In practice, of course, the flow picture is much more complicated than this simple model would indicate, so that there is no simple way of relating A_L to the actual area measured. Moreover, it is obvious that case and blade deflections can substantially modify the leakage area when the fan is running, thus further complicating the picture.

180
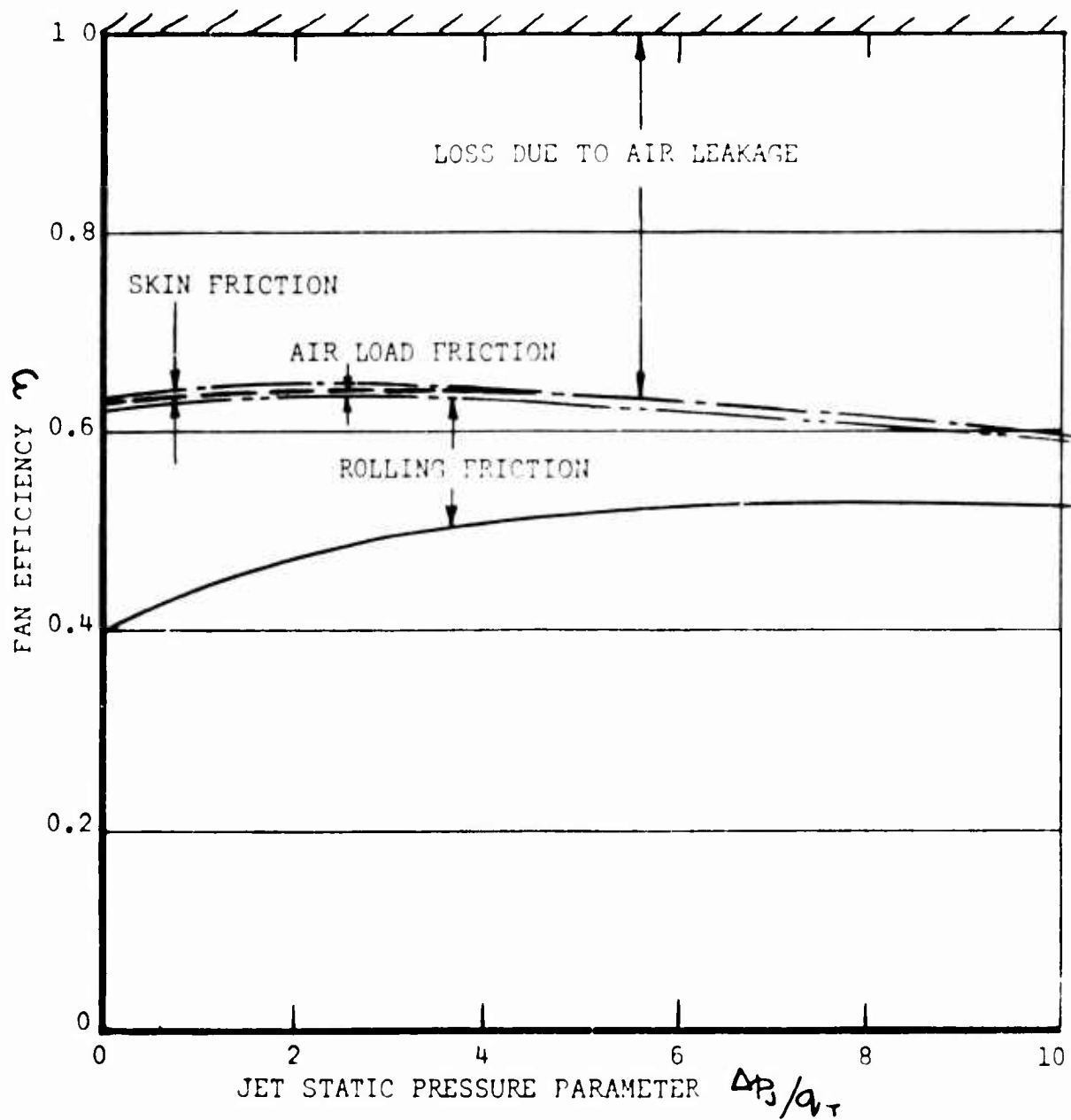
Figure 128. Efficiency of Fan No. 1 With Nominal
Leakage Area (Partially Balanced Blade).

181
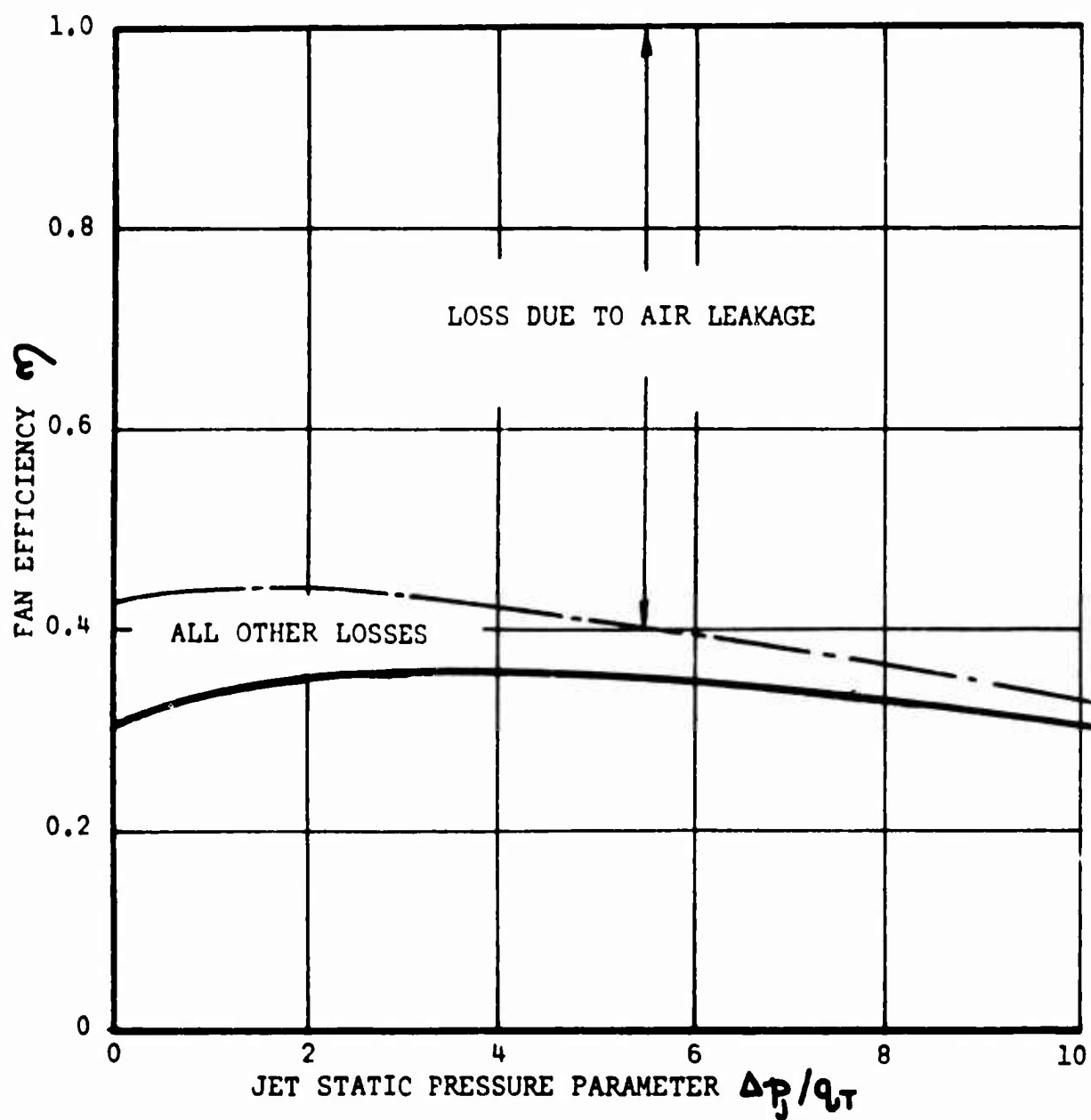
Figure 129. Efficiency of Fan No. 1 With Twice
Nominal Leakage Area (Partially Balanced Blade).
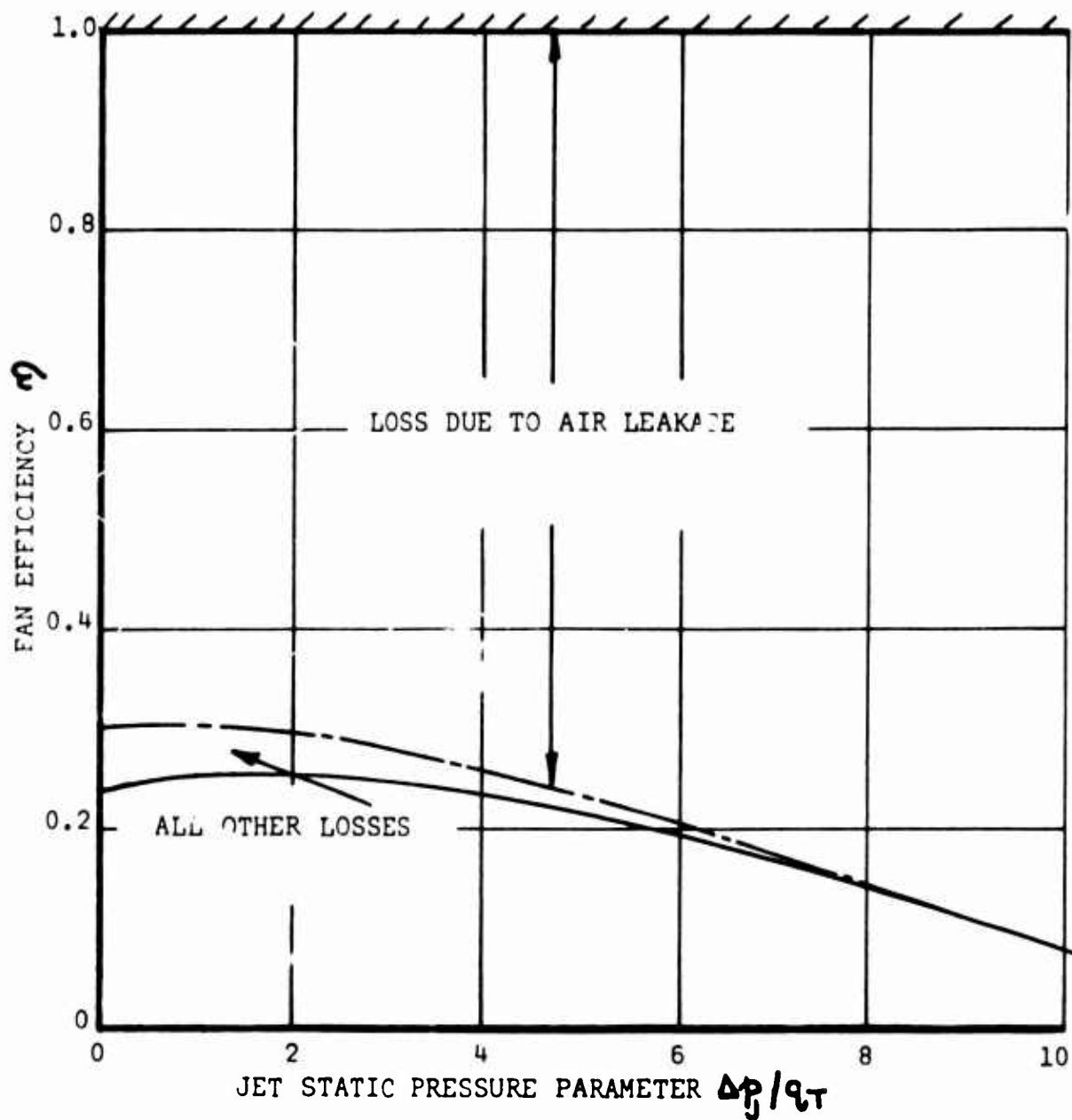
Figure 130. Efficiency of Fan No. 1 With Three Times
Nominal Leakage Area (Partially Balanced Blade).
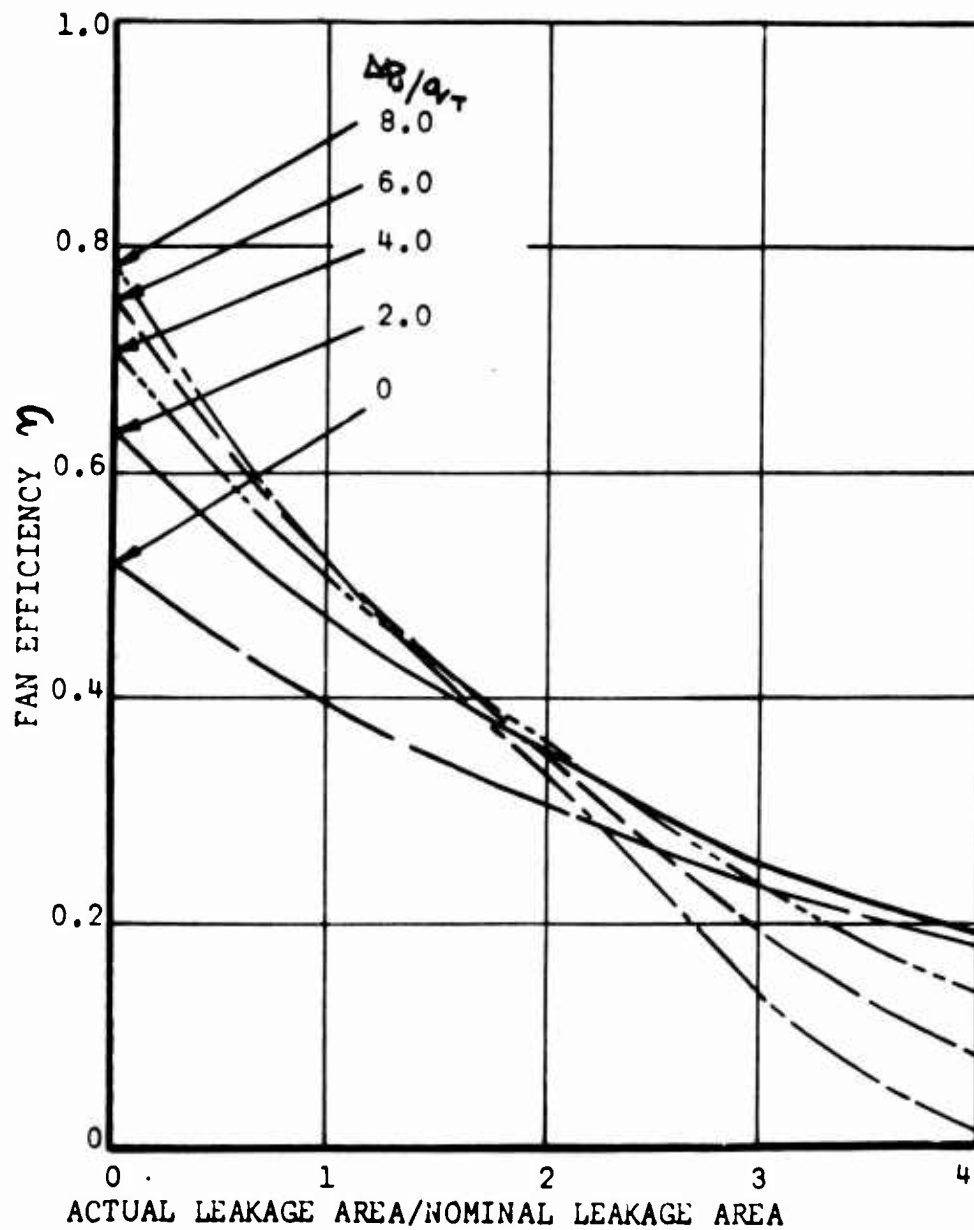
(NOMINAL $\hat{\mathcal{E}}_L$ = 0.02275)

Figure 131. Variation of Efficiency of Fan No. 1 With Leakage Area (Partially Balanced Blade).

184

One interesting manifestation of leakage is indicated by the exit velocity profiles given in Appendix IX. A characteristic of all these surveys is that V_J falls off markedly towards either end of the fan case; much more so than could be expected from normal skin-friction and end bell turbulence losses. It was first thought that the rig end plates were stalling the ends of the intake, but removal of these end plates and the provision of three-dimensional intake fairings were found to have no influence upon this distribution. Subsequently, it was realized that the only factor important enough to cause such a large reduction in velocity was the leakage occurring between the end bells and the ends of the fan blades.

The Influence of Rolling Friction Upon Efficiency

The effect of increasing the rolling friction coefficient μ_R is shown in Figure 132. Evidently μ_R has a very powerful effect, and since in practice the value is found to be .03 - .04 (Reference 4) instead of the originally assumed value of .01, this factor accounts for more than half the loss observed in the experimental fans.

Blade Angle of Attack At The Intake

The theory developed in Reference 28 is here extended slightly.

From equations (44) and (46) of Reference 28, the angle of attack at the entry plane for constant velocity distribution and neglecting pre-swirl is

$$\alpha = \phi - \tan^{-1}\left(\frac{\dot{m}_J}{\rho A_i V_T}\right)\frac{1}{\xi}$$

$$= \phi - \tan^{-1}\left(\frac{\dot{m}_J}{\rho A_J V_T}\frac{A_J}{A_i}\right)\frac{1}{\xi} \qquad (152)$$

where ξ = ratio of local peripheral tip speed to V_T .

It would seem to be desirable for $\alpha < 10°$ if turbulence is to be minimized inside the fan case. In flow visualization studies, no appreciable pre-swirl has so far been detected.

Naturally no quantitative information yet exists on the relationship between efficiency and blade angle of attack, but we might anticipate some general trends. Since mass flow diminishes with increasing back-pressure, blade angle of attack must increase with ΔP_J
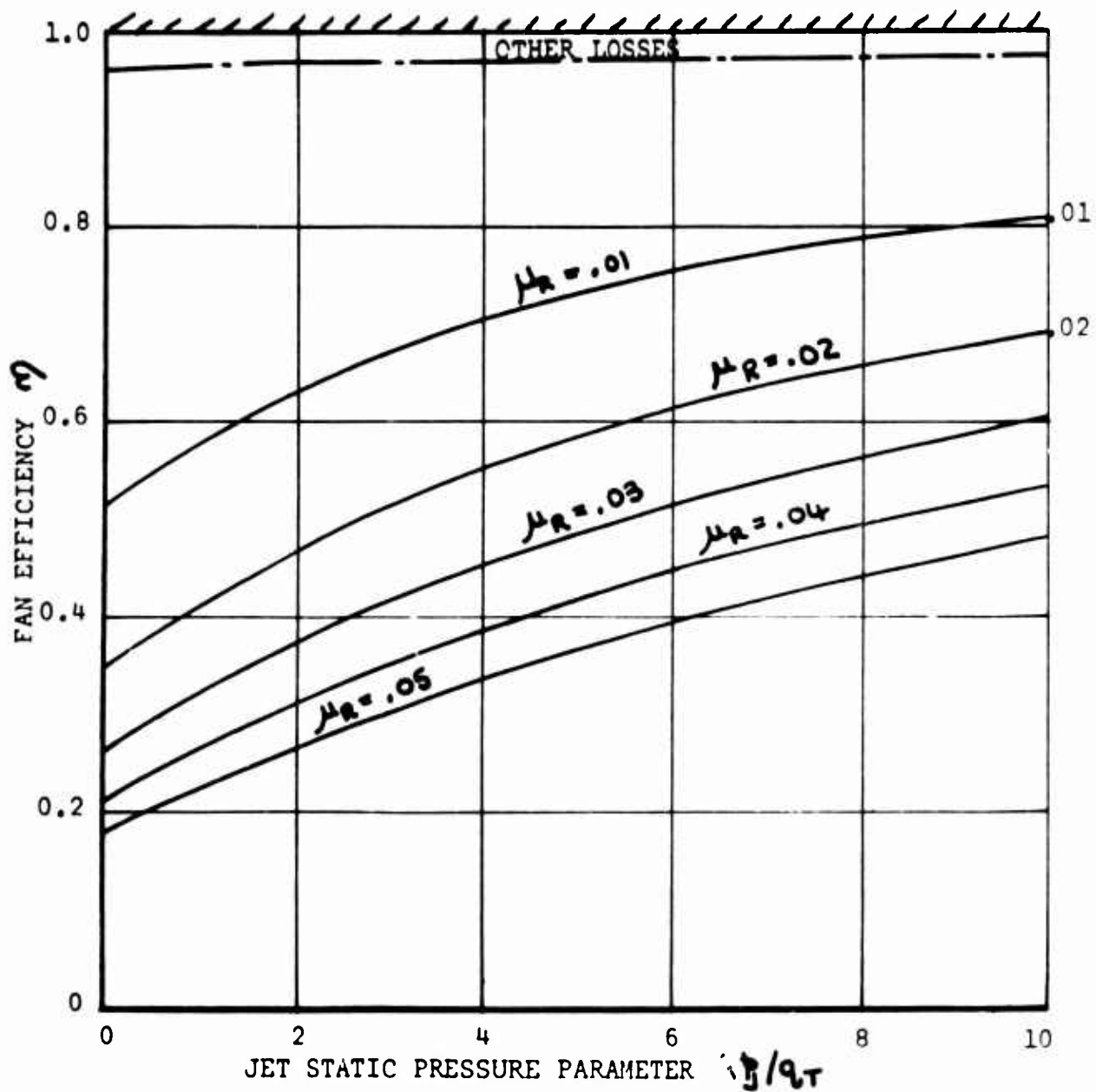
Figure 132. Efficiency of Fan No. 1 As A Function of Rolling
Friction Coefficient. Zero Leakage Losses, Partially Balanced
Blade.
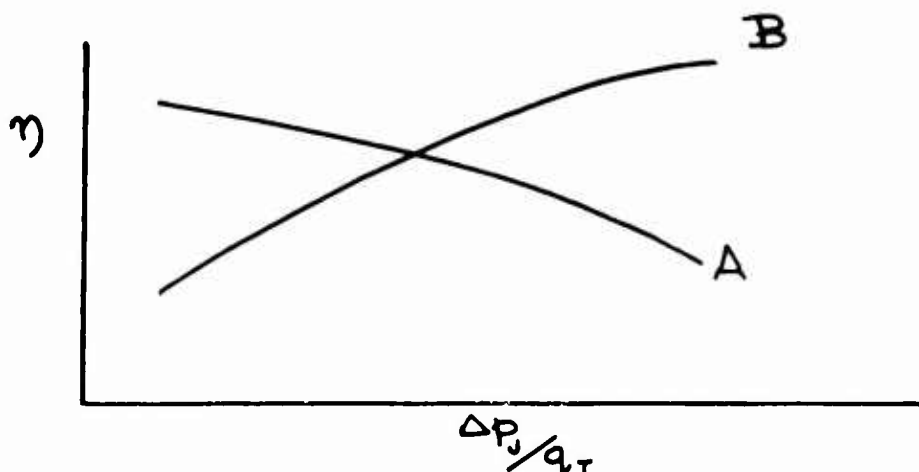
Figure 133. Effect of Blade Stall on Efficiency.

If the blade is stalled, or partly stalled, then increasing ΔP_J should cause a fall-off in efficiency, as for curve "A" in Figure 133. This contrasts with curve "B" which shows the theoretical variation when the blade is either unstalled or so fully stalled that the flow pattern is insensitive to ΔP_J changes.

A second logical hypothesis is that the airflow velocity should be comparable with or less than the mean effective velocity through the fan case, in order to avoid unnecessary diffusion losses. Obviously, the mean case velocity is

$$U_c = \frac{\dot{m}_J}{\rho A_c} \tag{153}$$

so that

$$\begin{aligned}
\frac{U_c}{U_i} &= \frac{A_i}{A_c} \cdot \frac{t_i}{R-r} = \frac{\hat{t}_i}{1-r/R} \\
&= \frac{\hat{t}_i}{\sqrt{1-\sqrt{1-\mu}}}
\end{aligned} \left.\rule{0pt}{36pt}\right\} \tag{154}$$

where

$$\hat{t}_i = \frac{t_i}{R}$$

187

If the flow is uniform over the inlet area

$$V_i A_i \rho = \dot{m}_J$$

$$\therefore \frac{V_i}{V_T} = \frac{\dot{m}_J}{\rho A_i V_T} = \frac{\dot{m}_J}{\rho A_J V_T} \frac{A_J}{A_i}$$

$$= \left(\frac{\dot{m}_J}{\rho A_J V_T} \right) \frac{\hat{\epsilon}_J}{\hat{\epsilon}_i} \tag{155}$$

In general it is easy to observe ...e requirement $V_c/V_i > 1.0$.

For the existing Frost Fan No. 1,

$$\mu = 0.485; \qquad 1-\sqrt{1-\mu} = 0.282$$

$$\hat{\epsilon}_J = 0.14$$

$$\hat{\epsilon}_i = 0.02275; \qquad \hat{\epsilon}_J/\hat{\epsilon}_i = 0.194$$

For the standard inlet $\qquad \hat{\epsilon}_i = 0.721$

$$\therefore V_c/V_i = \frac{0.721}{0.282} = 2.555$$

- a figure which obviously indicates that the intake is not running "full".

The blade geometric angles and tip speed variation across the standard intake are plotted in Figure 134.

The variations are small enough for us to take the mean values

$$\phi = 48°$$

$$\zeta = 0.9$$

For a range of mass flow values, the blade angle of attack is then as plotted in Figure 135, for various intake areas.
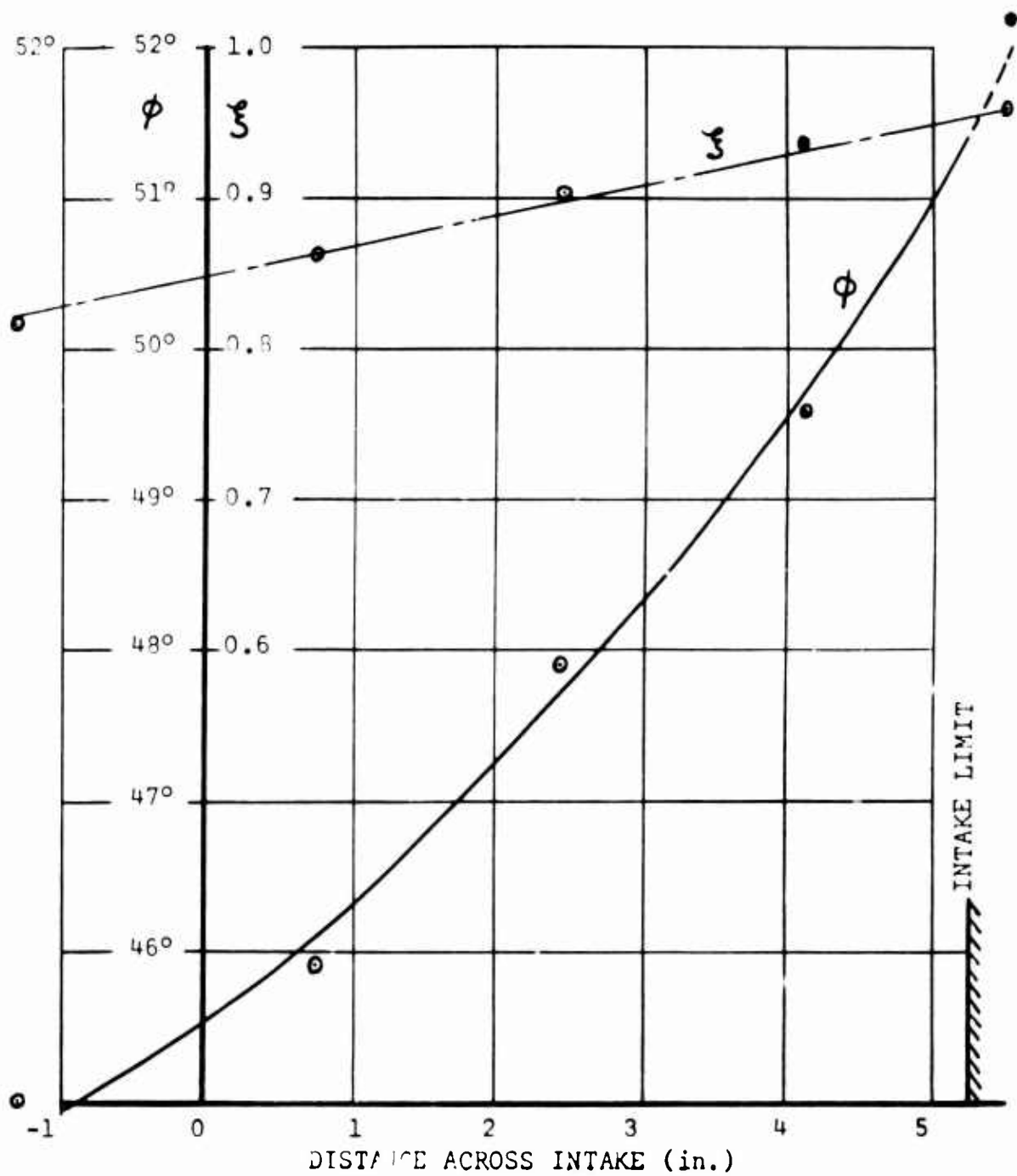
Figure 134. Variation of ϕ and ζ Across The Standard Frost Fan Intake.

189
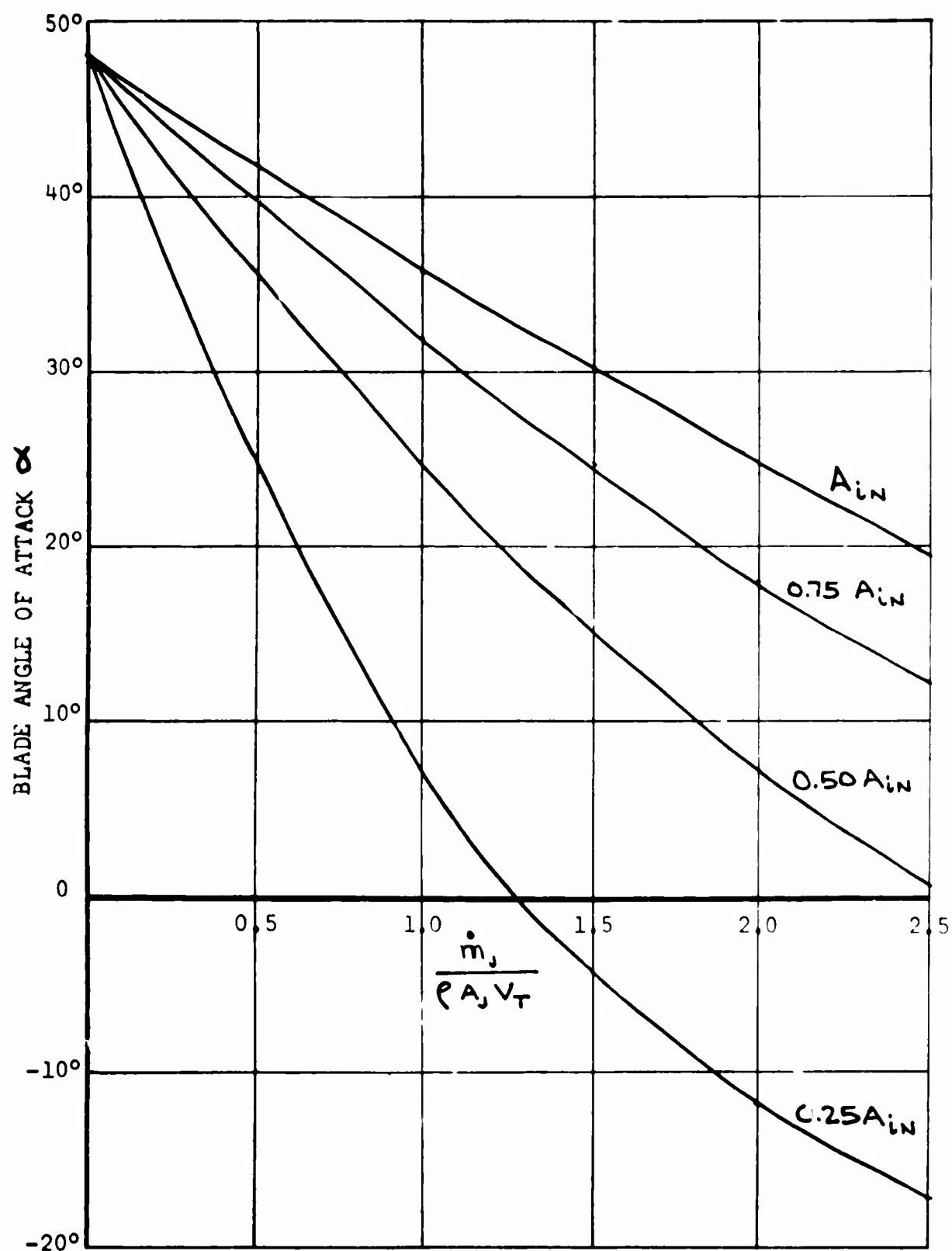
Figure 135. Theoretical Blade Angle of Attack in
Inlet (A_{iN} = Standard [5.25"] Intake).

190

From the curves plotted in Figure 135, we would suspect that a 60 per cent reduction from the nominal intake area would result in improved mass flow and efficiency for the No. 1 Frost Fan. In fact, during Series C runs, the intake area was progressively reduced down to 30 per cent of the nominal value without causing any significant variation in either mass flow or efficiency.
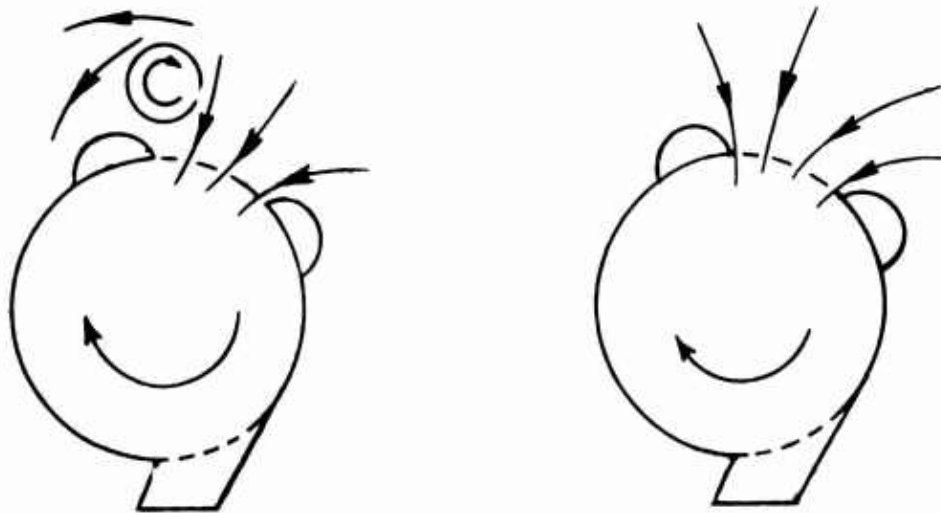
(a) Nominal (5.1" Intake.   (b) Small Intake.

Figure 136.   Intake Flow Patterns With the Frost Fan.

Studies of the intake airflow which actually occurred indicated that the theory applied only if the intake area was small enough to run "full". Increasing the intake area above this value did not affect the flow into the fan, which still entered through about the same area, but of course secondary vorticity developed over the portion of the intake area which was not being utilized by the in-flowing air, see Figure 136.

In short, the impression was gained that the fan made its own intake area, and ignored any excess area provided. Thus the fan appears to be completely insensitive to blade angle of attack - a conclusion which is strengthened by the fact that the efficiency was not influenced by running the blades backwards in the Series B tests.

191

The Influence of Blade Shape

No attempt has been made to investigate the influence of blade shape experimentally, and the theoretical analysis of inlet conditions, for example, has so far been singularly unrewarding, as indicated in the previous section.

It is reasonable to expect that blade shape is of importance however, and that under ideal conditions, some of the pressure rise could occur from aerodynamic reaction at the inlet. In fact, the Frost Fan can be regarded as a type of reaction device, similar to the crossflow fan, so that the theory of Reference 29 could be applied if suitably modified and might prove to be very instructive. The similarities of the two approaches are brought out more clearly in Figure 137.

Thus, in this (reaction) analogy, the Frost Fan is a transverse blower with internal sealing, leading to a much smaller sensitivity to back-pressure.

Methods exist for determining the optimum blade profile, which does not now appear to be the flat shape (with pronounced surface protuberances) hitherto used on the Frost Fan. Unfortunately, budgetary limitations did not permit an investigation of this aspect during the course of the present contract.
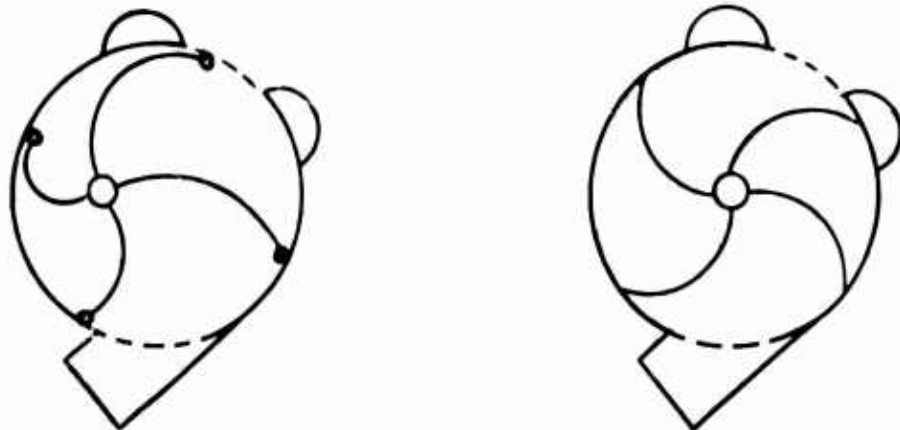
(a) Frost Fan With Curved Blades   (b) Transverse Blower

Figure 137. Similarities Between the
Transverse Blower and the Frost Fan.

Variability of Measured Performance

For any given configuration tested experimentally, the variability in the air mass flow measurements is within the limits of the anticipated experimental accuracy, but the reduced mass flow parameter $\dot{m}_1/\rho A_1 v_1$ is not. This is attributable to case deflections, however, which increase with increasing fan speed and back-pressure, resulting in greater leakage.

The experimental scatter in measured efficiency is much greater, however, and this is attributed primarily to the variability in the rolling friction coefficient of the tip rollers. This variability is caused by inherent variability in μ_R from test to test, a steady deterioration in both bearings and tracks with running time, and the temporary presence of small metal particles on the tracks.

Calculation of Induction Parameter μ

In Reference 28, two methods were given for calculating μ. The equation giving best agreement with experiment at the time Reference 28 was written was

$$\mu = 1 - \left(r_D/R\right)^2$$

$= 0.485$ for the prototype fan.

An alternative method, based on volume change, was also postulated. Since the mass flow of the fan is now found to be invariant with intake size, however, this second method is now assumed to be inapplicable.

SOME EXPERIMENTAL RESULTS

Although the reporting of raw data is not particularly useful under normal conditions, the fact that the Frost Fan is a novel device makes such a procedure advisable, and this is done for a series of twenty-three runs in Appendix IX. The clear indication of end-clearance leakage is obvious in all these runs.

Two blade configurations have so far been used, being illustrated in Figures 138(a) and 138(b), respectively, both of which are underbalanced. The efficiencies measured with the 138(a) blades were higher than with the 138(b) blades, presumably because the rollers and roller tracks were newer, although the cleaner aerodynamic form of the blades may have been a contributing factor.
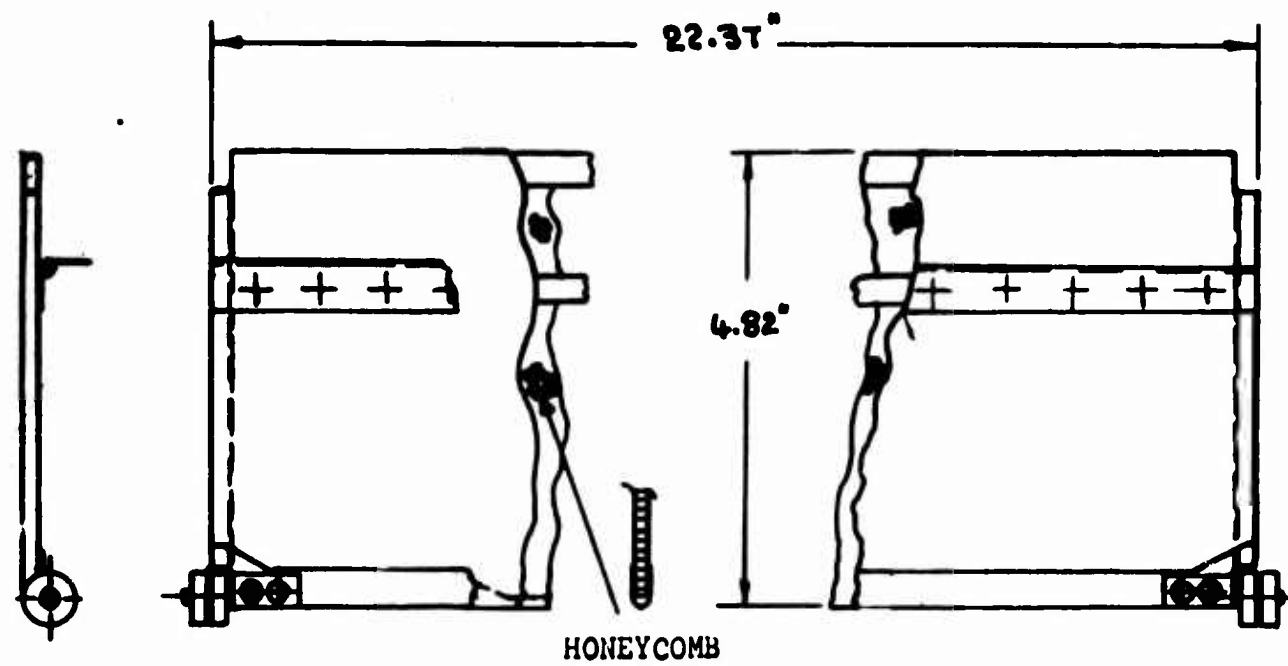
22.37"

4.82"

HONEYCOMB

Figure 138(a).   General Arrangement of "Old" Fan Blade.

FOAM
RUBBING
STRIP

22.37"
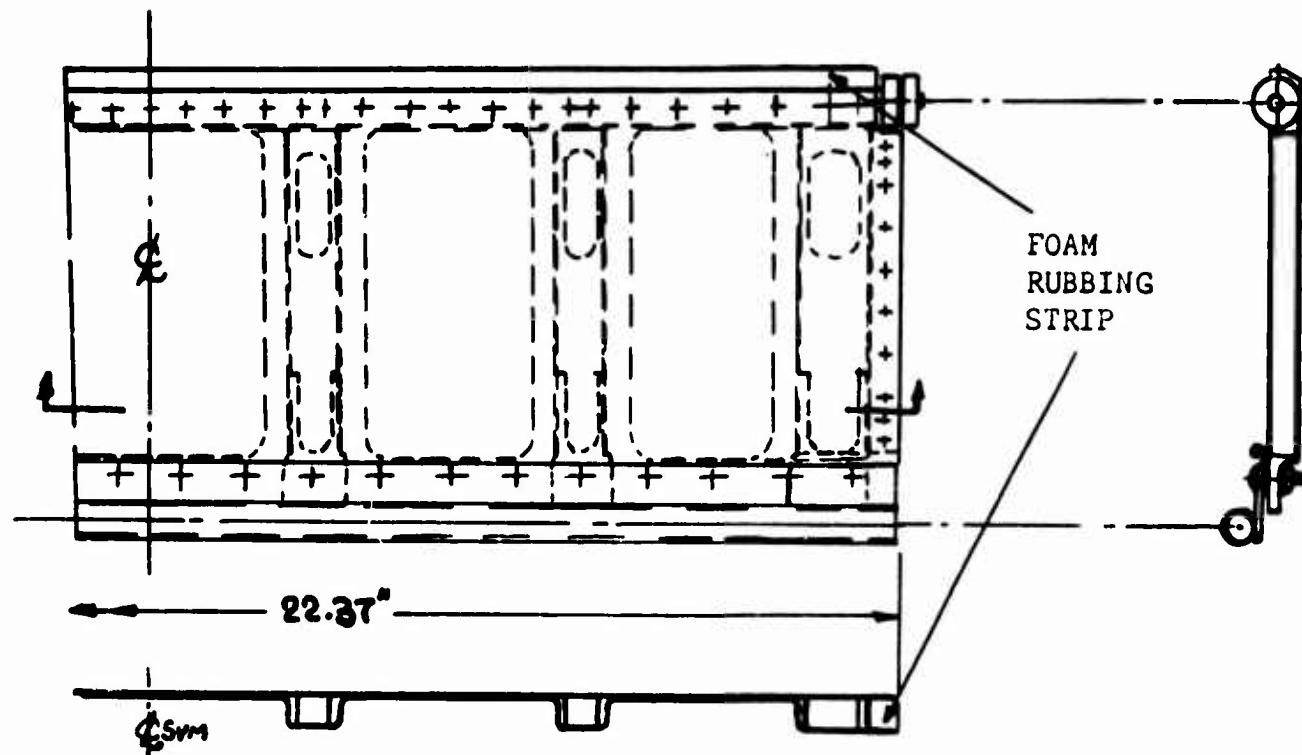
Figure 138(b).   General Arrangement of "New" Fan Blade.

The air mass flow parameter was lower with the 138(a) blades, however, because of their greater leakage area. Typical results for these first blades are given in Figures 139 and 140, with and without correction for end-plate leakage. It is seen that, with a good end-plate seal, the leakage area is about three times the nominal (measured) value. The highest efficiency is 60 per cent, and the scatter is presumed to be due to variability in the rolling friction coefficient of the tip rollers. Thus, since the nominal experimental accuracy is $\pm$5 per cent, the measured figure of 60 per cent can hardly be less than $\overline{57}$ per cent and probably corresponds to a value of μ_R near the originally assumed value of μ_R = .01.

The Series C runs summarized in Figures 141 and 142 were made with the blades illustrated in Figure 138(b). Due to the smaller leakage area, the mass-flow parameter is somewhat higher at low values of $\overline{\Delta P_J}$ and substantially higher at the higher values. This apparent reduction in leakage area with high back-pressure was also observed mechanically, and is undoubtedly due to the greater flexibility of the 138(b) blades.

The uncorrected efficiencies plotted in Figure 142 are substantially lower than for the Series A runs, due presumably to the track and roller deterioration which had occurred with increased running time. The different configurations used in the Series C runs did not have any important effect upon efficiency, although trends might have been detected if the large friction losses had not swamped all other effects.

Some indication that $\mu_R \approx$ .04 for the Series C runs is given by Figure 143, the uncorrected results for the Series A runs also being plotted for comparison. When μ_R = .04 in the theoretical calculations, both the mass flow (Figure 141) and the efficiency correspond to a leakage area of three times the nominal at low values of $\overline{\Delta P_J}$ and show a trend towards reduced leakage area as $\overline{\Delta P_J}$ increases.

Figure 139. Variation of Air Volume Flow With Back-Pressure For Frost Fan No. 1 (Full Scale) (Obstructed Inlet).

Figure 140. Efficiency of Fan No. 1 With Nominal Leakage Area.
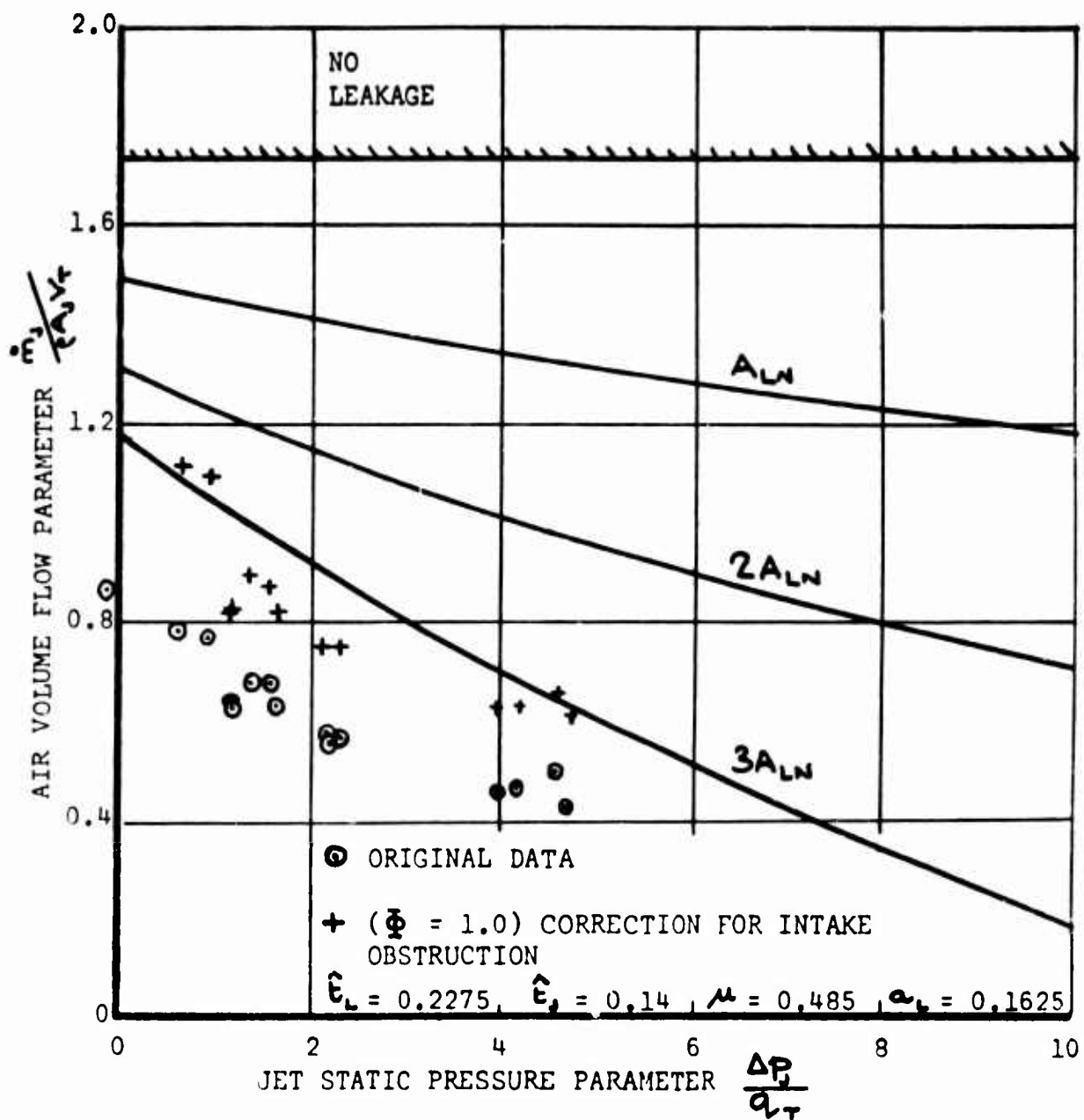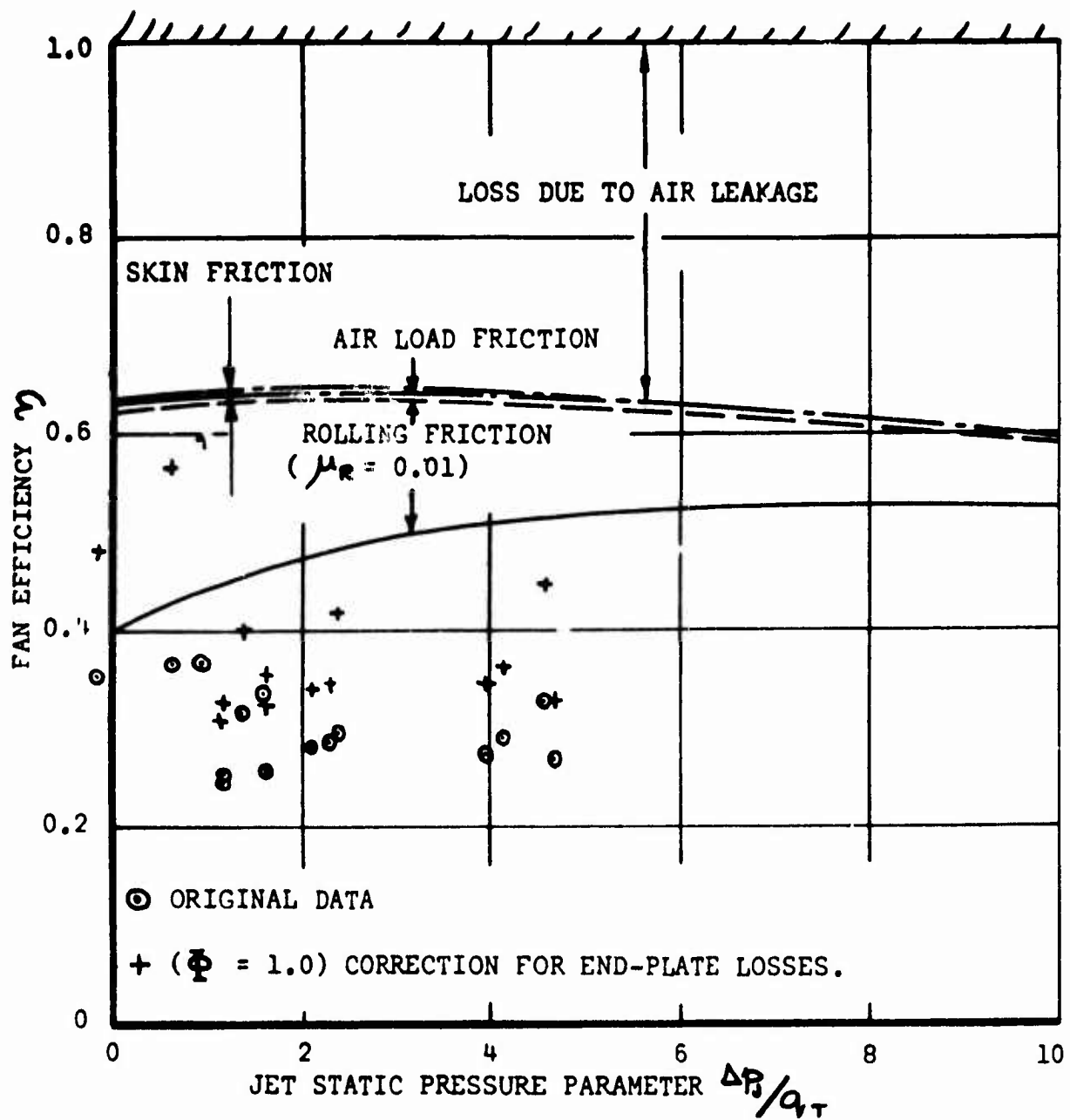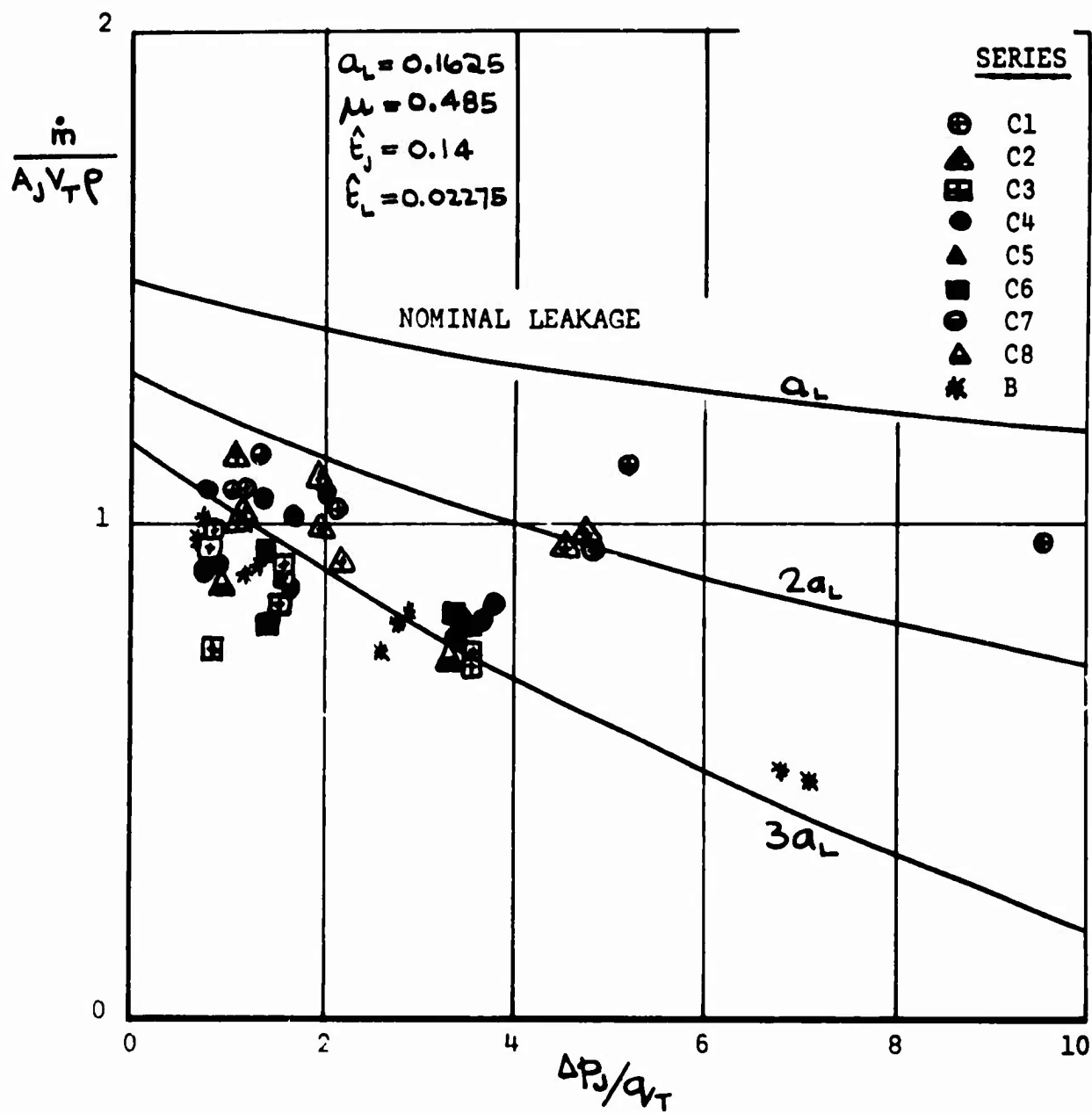
Figure 141.   Summation of Data From Series C Runs.
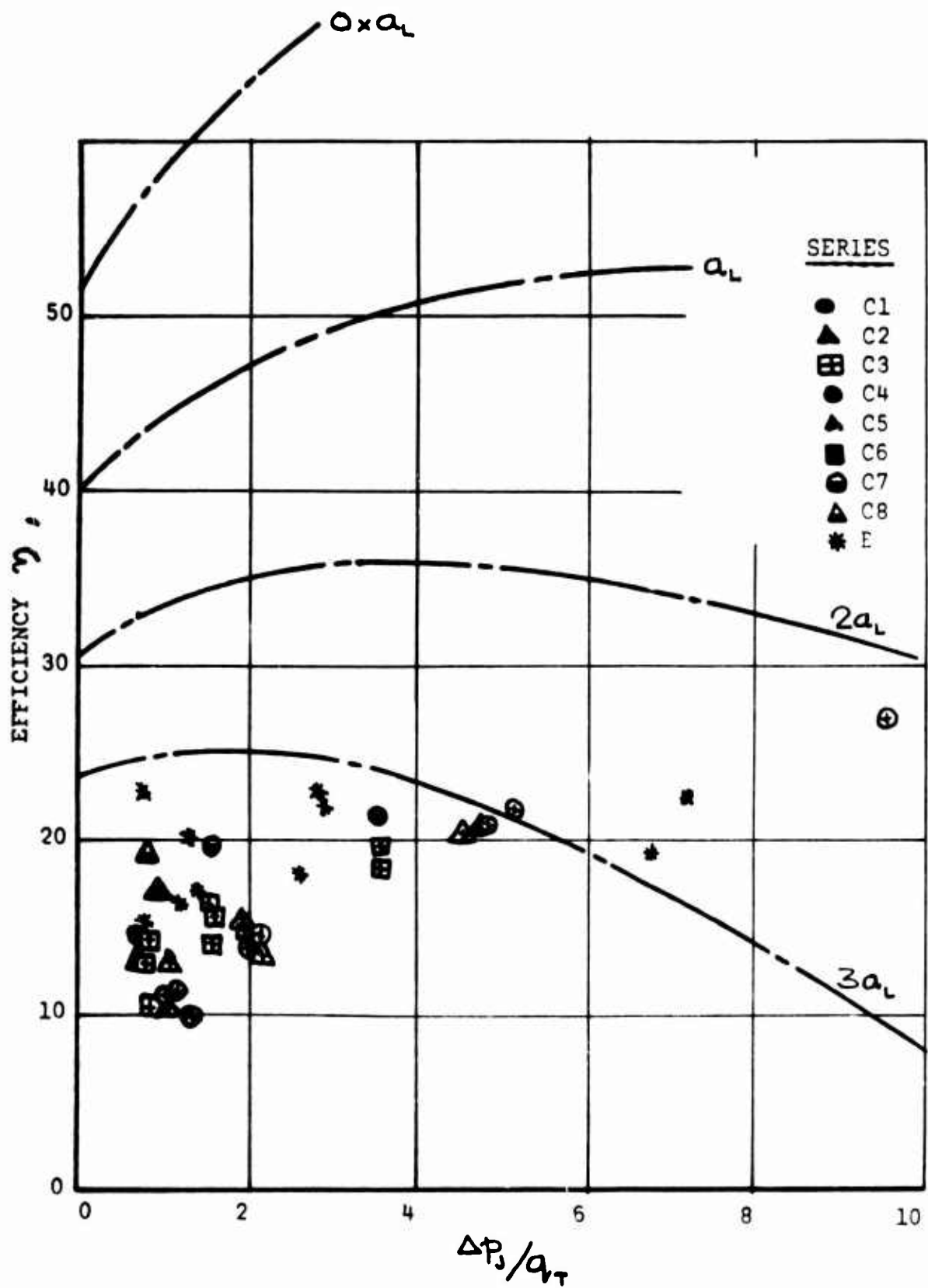
Figure 142. Summation of Data From Series C Runs.
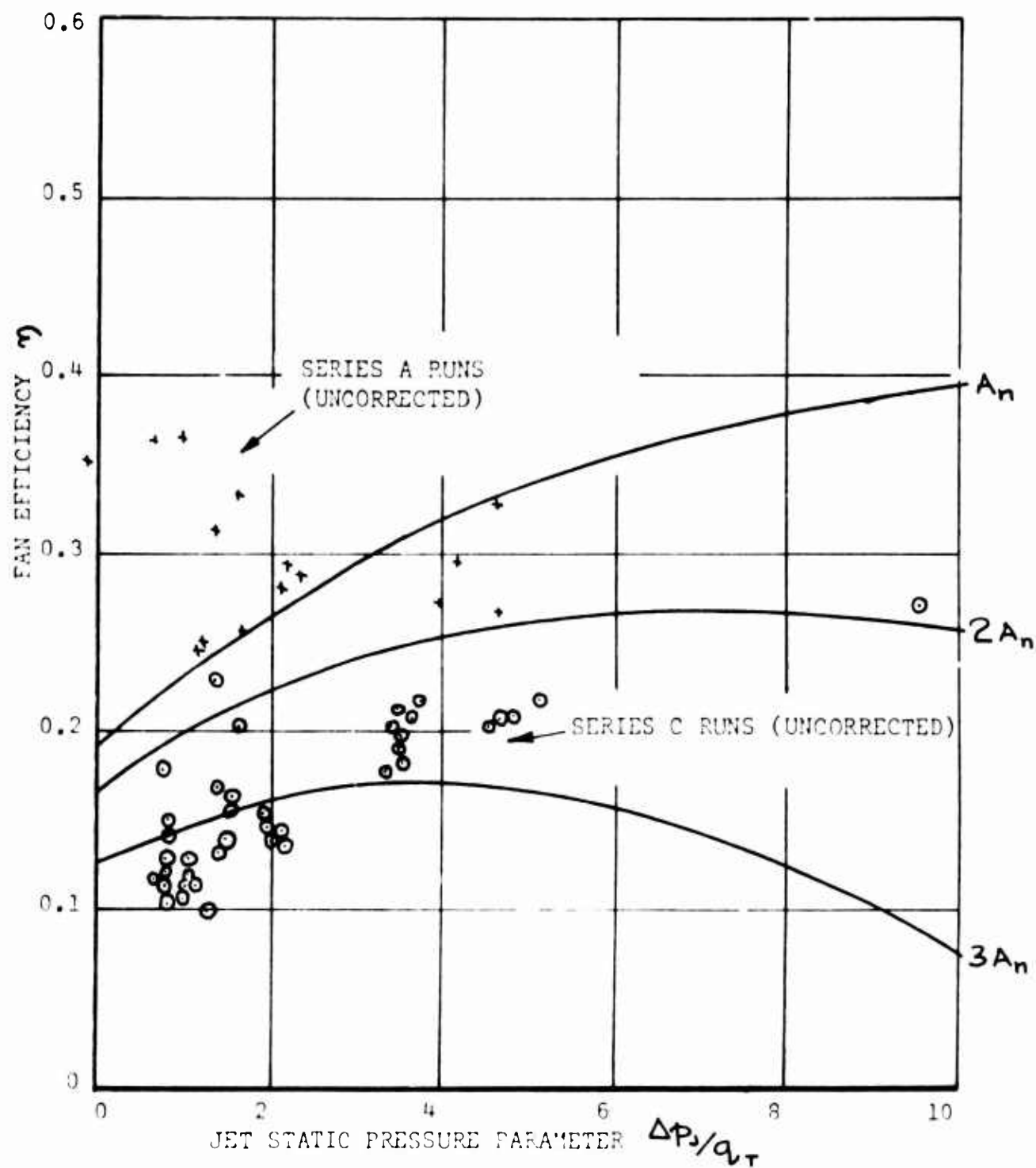
Figure 143. Comparison of Efficiency Measured In
Series A and C Runs With Theoretical Values (μ_R = .04).

201

BIBLIOGRAPHY

1. Payne, Peter R., Effect of Varying the Chord of the Fan on the Search Head Carrier, Frost Engineering Report No. 152-3, Contract DA 44-177-AMC-6(T), Frost Engineering Development Corporation, Englewood, Colorado, December 1962.

2. Payne, Peter R., The Effects of Altitude and Ambient Temperature on the Performance of the Mine Search Head Carrier, Frost Engineering Report No. 152-7, Contract DA 44-177-AMC-6(T), Frost Engineering Development Corporation, Englewood, Colorado, September 1963.

3. Payne, Peter R., The Theory of Heave Stability of an Annular Jet GEM, Frost Engineering Report No. 142-15, Contract DA 44-177-AMC-5(T), Frost Engineering Development Corporation, Englewood, Colorado, September 1963.

4. Payne, Peter R. and Smith, I., Measurement of Roller Friction on the Frost Fan, Frost Engineering Report No. 142-12, Contract DA 44-177-AMC-5(T), Frost Engineering Development Corporation, Englewood, Colorado, August 1963.

5. Payne, Peter R., Observations of Some Recirculating Flow Phenomena, Frost Engineering Report No. 142-16, Contract DA 44-177-AMC-5(T), Frost Engineering Development Corporation, Englewood, Colorado, September 1963.

6. Payne, Peter R., A Note on the Optimum Thickness and Angle of an Annular Jet with Zero Translational Velocity, Frost Engineering Report No. 142-5, Contract DA 44-177-AMC-5(T), Frost Engineering Development Corporation, Englewood, Colo., March 1963.

7. Payne, Peter R., A Method of Assessing the Performance of a Ground Effect Machine Configuration, Frost Engineering Report No. 142-14, Contract DA 44-177-AMC-5(T), Frost Engineering Development Corporation, Englewood, Colorado, August 1963.

8. Payne, Peter R., A Note on the Comparative Hover Performance of Annular Jet-and-Plenum Chamber Ground Effect Machines, Frost Engineering Report No. 142-9, Contract DA 44-177-AMC-5(T), Frost Engineering Development Corporation, Englewood, Colorado, May 1963.

9.   Payne, Peter R., *Preliminary Performance Measurements with a Frost Fan Model Exhausting to Ambient*, Frost Engineering Report No. 142-4, Contract DA 44-177-AMC-5(T), Frost Engineering Development Corporation, Englewood, Colorado, February 1963.

10. Payne, Peter R., *A Note on Viscous Mixing of Annular Jets*, Frost Engineering Report No. 142-6, Contract DA 44-177-AMC-5(T), Frost Engineering Development Corporation, Englewood, Colorado, February 1963.

11. Payne, Peter R., *Introduction to Ground Effect Recirculation Theory*, Frost Engineering Report No. 142-2, Contract DA 44-177-AMC-5(T), Frost Engineering Development Corporation, Englewood, Colorado, January 1963.

12   Cossairt, Keith R., *A Recirculation Concept, Proceedings of the National Meeting on Hydrofoils and Air Cushion Vehicles*, Washington, D.C., September 1962.

13. Ortell, A., *Recirculation Principle for Ground Effect Machine - Two Dimensional Tests*, TCREC Tech. Report 62-66, U. S. Army Transportation Research Command, Fort Eustis, Virginia, June 1962.

14. Payne, P. R., *A Contribution to the Theory of Thrust (Momentum) Augmentors*, Frost Engineering Report No. 137-2, Contract DA 44-177-AMC-71(T), Frost Engineering Development Corporation, Englewood, Colorado, August 1963.

15   Black, J. and Foster, D. M., "Study of a Recirculation System", paper delivered at the Southampton University Symposium, England, reported in *Air Cushion Vehicles*, Iliffe Transport Publications, Ltd., London, England, May 23, 1963.

16. Vinson, P., *Recirculation Principle for Ground Effect Machines Man-Carrying Test Vehicle, Preliminary Flight Test Results*, TCREC Tech. Report 62-100, U. S. Army Transportation Research Command, Fort Eustis, Virginia, December 1962.

17. Wallis, R. A., *Axial Flow Fans; Design and Practice*, Academic Press, New York, 1961.

18. Merz, Kenneth A., "An Unusual Type of Blower Transverse Flow Fan", *Product Engineering*, McGraw-Hill Publishing Co., Inc., New York City, New York, April 1, 1963.

19.   Atalla, Anwar A., "Propeller Fan Orifice Design", *Electrical Manufacturing*, McGraw-Hill Publishing Co., Inc., New York, December 1956.

20.   Hajer, Richard G., "Moving Air Through High Resistance Systems", *Electro-Technology*, Conover-Mast Publications, Inc., New York, October 1962.

21.   Hathaway, Charles A., "Mixed-flow Impellers Enter Air Moving Field", *Product Engineering*, McGraw-Hill Publishing Co., Inc., New York, January 5, 1959.

22.   Hathaway, Charles A., "Air Impellers for Optimum Performance", *Machine Design*, Penton Publications Co., Cleveland, Ohio, October 4, 1956.

23.   Cohen, H. and Rogers, G. F. C., *Gas Turbine Theory*, Longmans, Green & Company, London, England, 1951.

24.   Barrett, S., *Performance Measurements with a Frost Fan Model*, Frost Engineering Report No. 142-7, Contract DA 44-177-AMC-5(T), Frost Engineering Development Corporation, Englewood, Colorado, February 1963.

25.   Payne, P. R., *Introduction to Theory of the Crossflow Fan*, Frost Engineering Report No. 142-3, Contract DA 44-177-AMC-5(T), Frost Engineering Development Corporation, Englewood, Colorado, January 1963.

26.   Payne, P. R., *Proposal Relating to the Development of the Frost Fan for Ground Effect Machines*, Frost Engineering Report No. 142-1, Contract DA 44-177-AMC-5(T), Frost Engineering Development Corporation, Englewood, Colorado, July 1962.

27.   *Mechanical Engineers' Handbook*, McGraw-Hill Publishing Co., Inc., New York, 1958.

28.   Payne, Peter R., *Aerodynamic Theory of the Hinged-Blade Frost Fan for Annular Jet Ground Effect Machines*, Frost Engineering Report No. 142-8, Contract DA 44-177-AMC-5(T), Frost Engineering Development Corporation, Englewood, Colorado, March 1963.

29.   Payne, Peter R. and Barrett, Stanley, *An Introduction to the Theory of the Crossflow Fan*, Frost Engineering Report No. 142-10, Contract DA 44-177-AMC-5(T), Frost Engineering Development Corporation, Englewood, Colorado, June 1963.

BERNOULLI-FLOW REGIME, TWO-DIMENSIONAL
THEORY FOR CONSTANT MOMENTUM FLUX

Figure 144. Bernoulli-Flow Geometry.
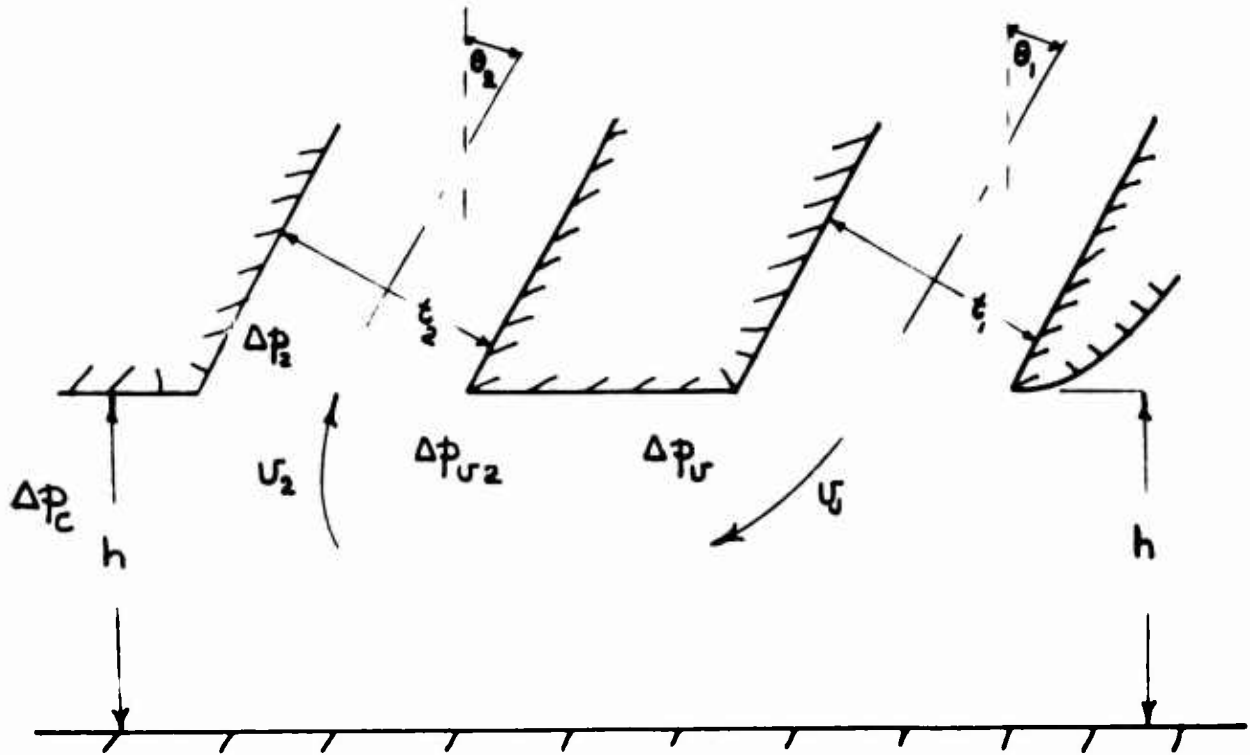
The conventional method of analysis, based on equality of horizontal momentum and ignoring intake suction, would give

$$\Delta P_c = \frac{J_1}{hC}\left(\sin\theta_1 + \frac{t_1}{t_2}\sin\theta_2\right) \tag{156}$$

- implying static stability at all heights. When we allow for pressure losses in the cavity region, however, we have from Bernoulli

$$P_2 = P_J - P_\sigma \tag{157}$$

or $\quad \Delta P_2 + \frac{1}{2} \rho \, U_2^2 = \Delta P_j + \frac{1}{2} \rho \, U_j^2 - \Delta P_v$ $\qquad$ (158)

From continuity,

$$t_2 \, U_2 = t_1 \, U_j \quad \therefore \, U_2 = U_j \frac{t_1}{t_2} \qquad (159)$$

Substituting in (158),

$$\Delta P_2 = \Delta P_j + \frac{1}{2} \rho \, U_j^2 \left\{ 1 - \left(\frac{t_1}{t_2} \right)^2 \right\} - \Delta P_v \qquad (160)$$

or, writing $\Delta P_v = \phi \, \frac{1}{2} \rho U_j^2$

$$\Delta P_2 = \Delta P_j + \frac{1}{2} \rho \, U_j^2 \left\{ 1 - \left(\frac{t_1}{t_2} \right)^2 - \phi \right\} \qquad (161)$$

$$= \Delta P_j + \frac{J_1}{2 t_1 \, \mathcal{C}} \left\{ 1 - \left(\frac{t_1}{t_2} \right)^2 - \phi \right\} \qquad (162)$$

When:

$$h \ll t \quad \Delta P_j \approx 0 \quad \Delta P_2 \approx \Delta P_c$$

$$\therefore \Delta P_c = \frac{J_1}{2 t_1 \, \mathcal{C}} \left\{ 1 - \left(\frac{t_1}{t_2} \right)^2 - \phi \right\} \qquad (163)$$

and $\quad \phi = f\left(\frac{h}{t} \right)$

At large values of h/t we can use the thin jet assumption, but for the intermediate values of real interest, layered-jet theory must be employed.

The initial cavity pressure ΔP_v can be calculated from equating horizontal momentum to the external pressure forces.

That is, $-\Delta P_{v} h \mathcal{C} = \rho h \mathcal{C} u_{v}^{2} - \rho t_{1} \mathcal{C} u_{j}^{2} \sin\theta_{1}$

$$-\Delta P_{v} = \rho u_{v}^{2} - \rho \frac{t_{1}}{h} u_{j}^{2} \sin\theta_{1}$$

$$= \rho u_{j}^{2} \left\{ \left(\frac{u_{v}}{u_{j}}\right)^{2} - \left(\frac{t_{1}}{h}\right) \sin\theta_{1} \right\} \qquad (164)$$

From continuity, $h U_{v} = t_{1} U_{j}$, so that

$$\frac{U_{v}}{U_{j}} = \frac{t_{1}}{h}$$

$$-\Delta P_{v} = \rho u_{j}^{2} \left(\frac{t_{1}}{h}\right) \left\{ \left(\frac{t_{1}}{h}\right) - \sin\theta \right\} \qquad (165)$$

This is a different result from the derivation for constrained vortex flow [equation (11)] which gives

$$-\Delta P_{v} = \frac{J_{1}}{h \mathcal{C}} (1 - \sin\theta)$$

$$= \rho u_{j}^{2} \left(\frac{t_{1}}{h}\right) (1 - \sin\theta) \qquad (166)$$

-although obviously both (165) and (166) give the same result for $t_{1}/h = 1.0$, indicating that the boundary between two flow regimes is delineated by $t_{1} = h$. Equations (165) and (166) are plotted in Figure 145, using this assumption.
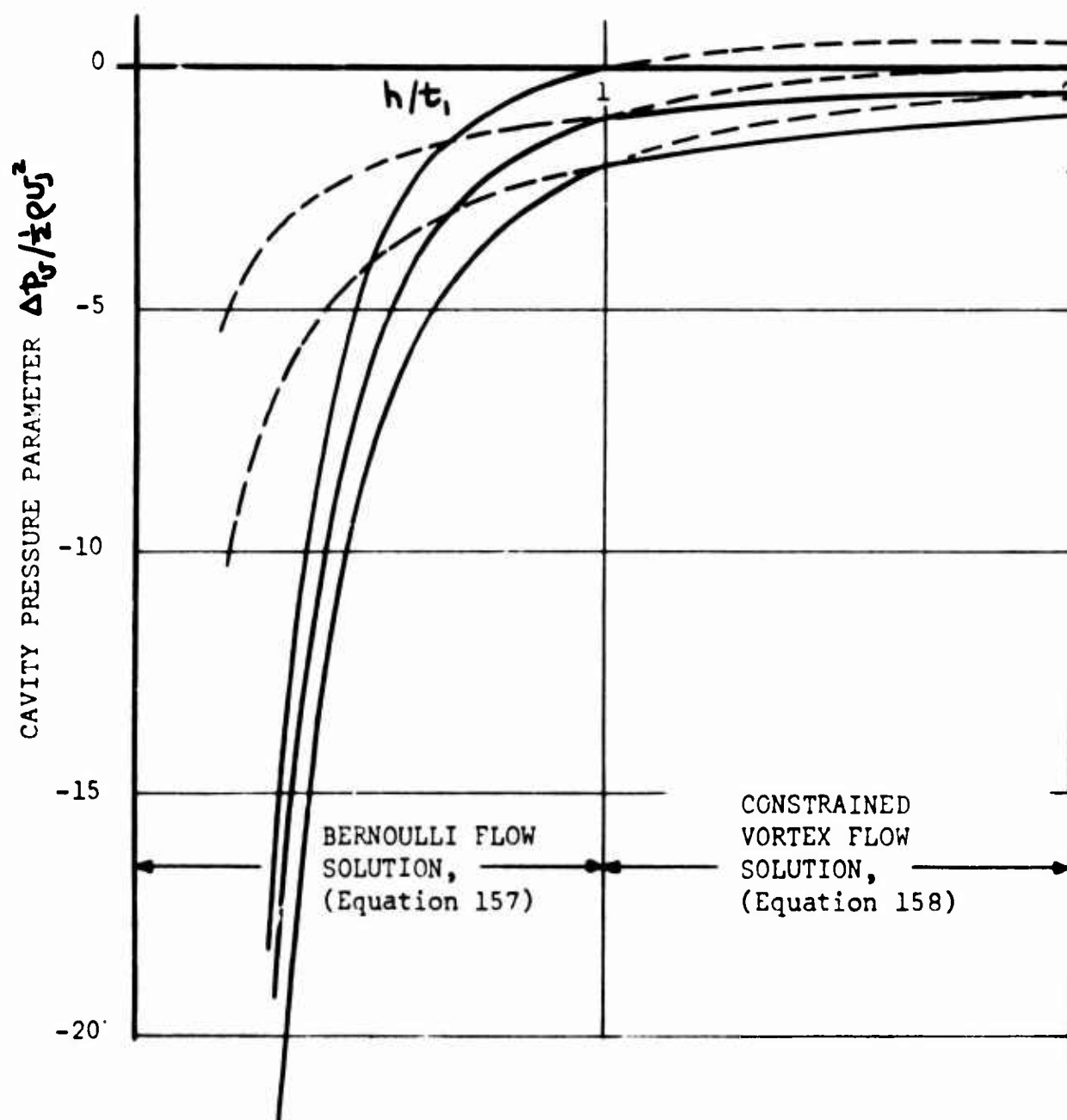
Figure 145. Cavity Pressure As A Function of Hover Height.

INFLUENCE OF EXPANSION LOSS ON
PERFORMANCE IN THE BERNOULLI-FLOW REGIME
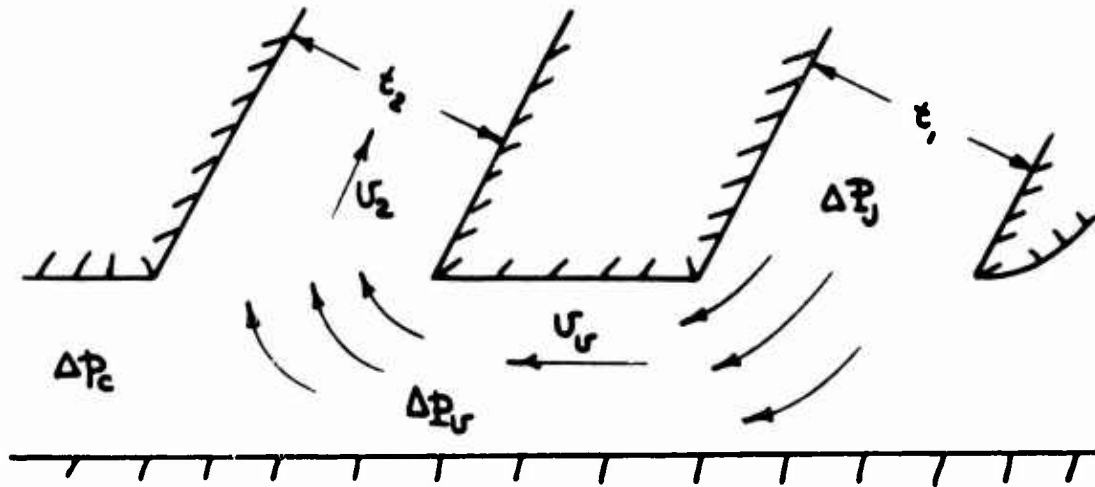
Figure 146. Bernoulli-Flow Geometry.

If the hover height is very small in relation to the jet thickness, then the airflow in the entry and exit ducts will be moving very slowly and can be considered to be at an essentially static "reservoir" state. Considering the case where all the flow recirculates, we have

$$\Delta P_j = \Delta P_c + \frac{1}{2} \rho U_2^2 + \Delta P_\sigma \qquad (167)$$

- where ΔP_σ is the total head loss involved in flowing through the cavity restriction and in suddenly diffusing from a pressure ΔP_σ to ΔP_c .

$$\therefore U_2 = \sqrt{\frac{2}{\rho} \left(\Delta P_j - \Delta P_c - \Delta P_\sigma \right)} \qquad (168)$$

For continuity,

$$u_{\sigma} h C_{\sigma} = u_2 C_2 t_2$$

so that $\quad U_{\sigma} = u_2 \left(\dfrac{t_2}{h}\right) \dfrac{C_2}{C_{\sigma}}$ (169)

The horizontal momentum flux is

$$J_H = \dot{m} U_{\sigma} = h C_{\sigma} \rho U_{\sigma}^2$$

$$= h C_{\sigma} (\rho u_2^2) \left(\dfrac{t_2}{h}\right)^2 \left(\dfrac{C_2}{C_{\sigma}}\right)^2$$ (170)

$$= 2 h C_{\sigma} \left(\dfrac{t_2}{h}\right)^2 \left(\dfrac{C_2}{C_{\sigma}}\right)^2 (\Delta P_J - \Delta P_c - \Delta P_{\sigma})$$ (171)

This must be equal to the cushion pressure for $\Delta P_c \, h \, C_2$

That is $\quad \Delta P_c \, h C_2 + 2 h C_{\sigma} \left(\dfrac{t_2}{h}\right)^2 \left(\dfrac{C_2}{C_{\sigma}}\right)^2 = 2 h C_{\sigma} \left(\dfrac{t_2}{h}\right)^2 \left(\dfrac{C_2}{C_{\sigma}}\right)^2 (\Delta P_J - \Delta P_{\sigma})$

or $\quad \dfrac{\Delta P_c}{\Delta P_J} = \dfrac{2 \left(\dfrac{t_2}{h}\right)^2 \dfrac{C_2}{C_{\sigma}} \left(1 - \dfrac{\Delta P_{\sigma}}{\Delta P_J}\right)}{1 + 2 \left(\dfrac{t_2}{h}\right)^2 \dfrac{C_2}{C_{\sigma}}}$ (172)

Using normal diffuser terminology, we define the pressure loss due to diffusion as

$$\Delta P_{\sigma D} = (1 - \eta) \tfrac{1}{2} \rho U_{\sigma}^2$$

$$= (1 - \eta) \tfrac{1}{2} \rho u_2^2 \left(\dfrac{t_2}{h}\right)^2 \left(\dfrac{C_2}{C_{\sigma}}\right)^2$$ (173)

210

Therefore, from (168),

$$\frac{1}{2}\rho u_2^2 = \Delta P_j - \Delta P_c - (1-\eta)\frac{1}{2}\rho u_2^2 \left(\frac{t_2}{h}\right)^2 \left(\frac{c_2}{c_v}\right)^2$$

$$= \frac{(\Delta P_j - \Delta P_c)}{\left\{1 + (1-\eta)\left(\frac{t_2}{h}\right)^2 \left(\frac{c_2}{c_v}\right)^2\right\}} \tag{174}$$

Thus equation (170) becomes

$$J_H = 2hc_v\left(\frac{t_2}{h}\right)^2\left(\frac{c_2}{c_v}\right)^2 \frac{(\Delta P_j - \Delta P_c)}{\left\{1 + (1-\eta)\left(\frac{t_2}{h}\right)^2\left(\frac{c_2}{c_v}\right)^2\right\}}$$

$$\frac{\Delta P_c}{\Delta P_j} = \frac{2\left(\frac{t_2}{h}\right)^2\left(\frac{c_2}{c_v}\right)}{1 + (1-\eta)\left(\frac{t_2}{h}\right)^2\left(\frac{c_2}{c_v}\right)^2 + 2\left(\frac{t_2}{h}\right)^2\left(\frac{c_2}{c_v}\right)} \tag{175}$$

In simplifying this equation, we restrict the analysis to the two-dimensional case, where $c_v = c_2$.

Thus, $\quad \dfrac{\Delta P_c}{\Delta P_j} = \dfrac{2\left(\frac{t_2}{h}\right)^2}{1 + 3\left(\frac{t_2}{h}\right)^2 - \eta\left(\frac{t_2}{h}\right)^2}$

$$= \frac{2}{\left(\frac{h}{t_2}\right)^2 + 3 - \eta} \tag{176}$$

If $\eta = 1.0$, then $\dfrac{\Delta P_c}{\Delta P_j} \longrightarrow 1.0$ as $h \longrightarrow 0$, as we should expect.

211

For a sudden expansion from U_v to U_2 ,

$$\eta = 2\frac{U_2}{U_v} - \left(\frac{U_2}{U_v}\right)^2 \tag{177}$$

But from (169)

$$\frac{U_2}{U_v} = \frac{h}{t_2}$$

$$\therefore \; \eta = 2\left(\frac{h}{t_2}\right) - \left(\frac{h}{t_2}\right)^2 \tag{178}$$

Substituting into (176) for η ,

$$\frac{\Delta P_c}{\Delta P_j} = \frac{2}{\left(\frac{h}{t_2}\right)^2 + 3 - 2\left(\frac{h}{t_2}\right) + \left(\frac{h}{t_2}\right)^2}$$

$$= \frac{1}{\frac{3}{2} + \left(\frac{h}{t}\right)^2 - \left(\frac{h}{t}\right)} \tag{179}$$

Equation (179) is plotted in Figure 147, and it is seen that a simple expansion loss alone is sufficient to cause a negative cushion stiffness below $h/t_2 = 0.5$. When all losses are taken into account, the cushion pressure will obviously be much less as $h \longrightarrow 0$ and will follow a curve similar to the lower one sketched in Figure 147. It should also be remembered that in most practical systems ΔP_j will fall off as the losses increase, thus further contributing to heave instability.

As an example of this latter case, consider a system which, instead of maintaining ΔP_j at a constant value, adds a fixed total head increment ΔH. This might be regarded as a useful approximation to an eductor or a conventional fan.

$$\Delta P_j = \Delta P_2 + \Delta H = \Delta P_j - \Delta P_v + \Delta H$$

That is, $(1 - \eta)\frac{1}{2}\rho U_v^2 = \Delta H$

Under these conditions the velocity will be such that the losses through the cavity region will always balance the input total pressure.

That is, $(1 - \eta) \frac{1}{2} \rho U_U^2 = \Delta H$ (180)

or, from (170),

$$J_H = h \mathcal{C} \frac{2 \Delta H}{(1 - \eta)}$$ (181)

$$\therefore \quad \frac{\Delta P_c}{\Delta H} = \frac{2}{(1 - \eta)}$$ (182)

Substituting equation (178) for η,

$$\frac{\Delta P_c}{\Delta H} = \frac{2}{1 - 2\left(\frac{h}{t_2}\right) + \left(\frac{h}{t_2}\right)^2}$$ (183)

Obviously, $\Delta P_c / \Delta H$ increases rapidly with h/t_2, becoming infinite at $h/t_2 = 1.0$, since we have considered only the diffusion loss.
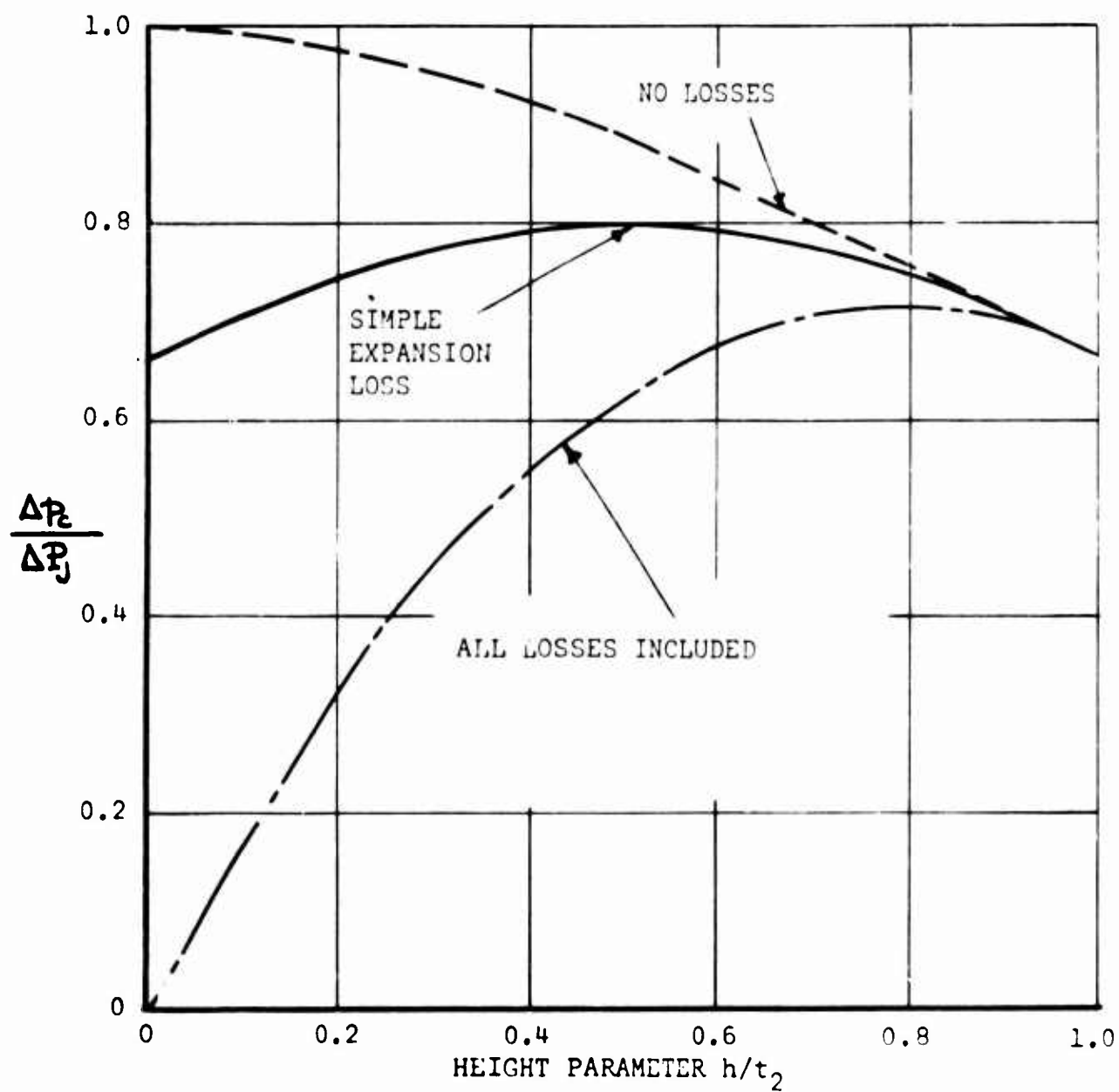
Figure 147. Variation of Cushion Pressure
With Hover Height (Constant Total Head).

214

APPENDIX III

APPROXIMATE EQUATIONS FOR THE RECIRCULATION CUSHION PRESSURE

CONSTANT TOTAL HEAD SOLUTION

The previous analysis of Reference 11 assumed that the total pressure was constant throughout the vortex. More refined treatment, including viscous mixing effects, indicates that this assumption is invalid. Moreover, total head measurements in the intake plane of the Frost Fan recirculation rig indicate that a marked drop in pressure occurs between exit and intake. Since the intake momentum J_2 is in any case smaller than the exit momentum flux J_1, an appropriate approximation would seem to be obtained by assuming $J_2 = 0$. Then from equations (51) and (73) of Reference 11, the cavity pressure is

$$\frac{\Delta P_\sigma}{\Delta P_j} = 1 - e^{2x_1} \tag{184}$$

and

$$\frac{J_1}{C\Delta P_j} = \frac{t_1}{x_1} \left\{ e^{2x_1} - 1 \right\} \tag{185}$$

- where

$$x_1 = \frac{t_1}{h} \left(1 - \sin \theta_1 \right) \tag{186}$$

From the balance of horizontal momentum,

$$J_1 = h C \left(\Delta P_c - \Delta P_\sigma \right) \tag{187}$$

or

$$\Delta P_c = \frac{C \Delta P_j}{h C} \frac{t_1}{x_1} \left\{ e^{2x_1} - 1 \right\} + \Delta P_j \left\{ 1 - e^{2x_1} \right\}$$

$$\therefore \frac{\Delta P_c}{\Delta P_j} = \frac{t_1}{h x_1} \left(e^{2x_1} - 1 \right) + \left(1 - e^{2x_1} \right)$$

$$= \left\{ 1 - \frac{1}{(1 - \sin \theta_1)} \right\} - e^{2x_1} \left\{ 1 - \frac{1}{(1 - \sin \theta_1)} \right\}$$

215

$$\frac{\Delta p_c}{\Delta p_J} = \frac{\sin \theta_1}{(1 - \sin \theta_1)} \left(e^{2x_1} - 1 \right) \tag{188}$$

As $t_1 \rightarrow 0$, $\Delta p_c \rightarrow 0$.

CONSTANT MOMENTUM FLUX SOLUTION

If J_1 is constant, such as would be the case with a constant displacement fan,

$$- \Delta p_U = \frac{J_1}{h\,\mathcal{C}} (1 - \sin \theta_1) \tag{189}$$

$$\Delta p_c - \Delta p_U = \frac{J_1}{h\,\mathcal{C}}$$

$$\therefore \Delta p_c = \frac{J_1}{h\,\mathcal{C}} - \frac{J_1}{h\,\mathcal{C}} (1 - \sin \theta_1)$$

$$\frac{\Delta p_c}{J_1} = \frac{\sin \theta_1}{h\,\mathcal{C}} \tag{190}$$

The same result can be obtained by writing

$$\Delta p_J = \frac{\dfrac{J_1}{\mathcal{C}} \dfrac{x_1}{t_1}}{\left\{ e^{2x_1} - 1 \right\}} \tag{191}$$

and substituting for Δp_J in equation (188).

APPENDIX IV

IDEAL POWER REQUIRED TC ACHIEVE A TOTAL HEAD RISE

Consider a stream of fluid travelling at a velocity U_1 with a static pressure P_1 and a total head P_1 . If this is expanded to ambient pressure through a loss-free diffuser,

$$P_a + \tfrac{1}{2} \rho \, U_a^2 = P_1 + \tfrac{1}{2} \rho \, U_1^2 \tag{192}$$

$$U_{a1} = \sqrt{\frac{2}{\rho}(P_1 - P_a) + U_1^2} \tag{193}$$

- and the energy content is $\tfrac{1}{2} \dot{m} \, U_a^2$

If the total pressure is now increased by an amount ΔH ,

$$U_{a2} = \sqrt{\frac{2}{\rho}(\Delta H + P_1 - P_a) + U_1^2} \tag{194}$$

Thus the energy added is

$$\Delta E = \tfrac{1}{2} \dot{m}\left(U_{a2}^2 - U_{a1}^2\right) = \frac{\dot{m}}{\rho}\, \Delta H$$

$$= A_1 \, U_1 \, \Delta H \tag{195}$$

217

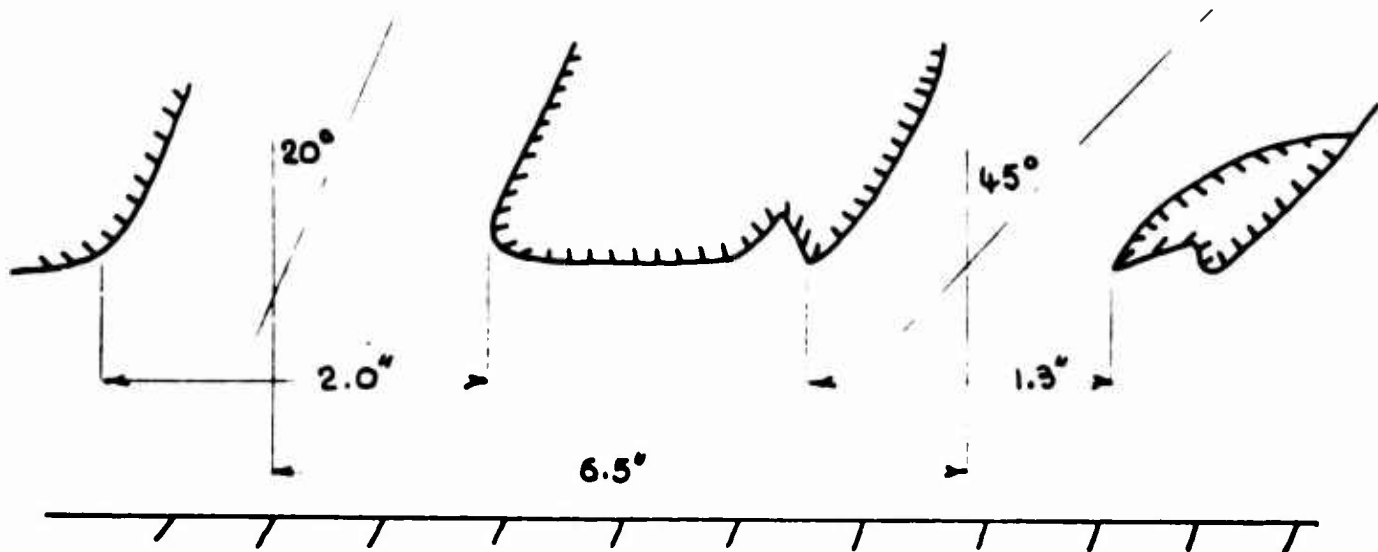GEOMETRY AND THEORETICAL PERFORMANCE OF FROST TEST RIG

Figure 148. Geometry of Two-Dimensional Test Rig.

Irrespective of back-pressure, the Frost Fan used in this rig had a
mass flow parameter value of about

$$\overline{m} = \frac{\dot{m}_J}{A_J V_T \rho} \approx 1.0 \qquad (196)$$

Thus the momentum flux is given by

$$J = \rho A_J V_J^2 = \frac{\dot{m}_J^2}{\rho A_J}$$

$$= \overline{m}^2 A_J \rho V_T^2 \qquad (197)$$

218

At 1000 r.p.m. $\quad\quad\quad\quad \frac{1}{2}\rho V_T^2 = 3.76$ lb./ft.

Also $\quad\quad\quad\quad\quad\quad\quad A_J = 0.2225$

$$\therefore J = (1.0)^2 \times 0.2225 \times 7.52 = 1.675 \text{ lb.}$$

At other speeds the momentum flux will be linearly proportional to the square of the r.p.m.

Since the jet momentum flux is known, we can calculate cushion pressure from equation (13)

That is, $\quad \Delta p_c = \dfrac{J_1}{hC}\left\{\sin\theta_1 + \dfrac{J_2}{J_1}\sin\theta_2\right\}$ $\hfill$ (198)

$$= 1.675\left(\frac{\text{r.p.m.}}{1000}\right)^2 \frac{144}{24.25 \times h}\left\{0.707 + \frac{J_2}{J_1}0.342\right\}$$

$$= \frac{9.95}{h}\left(\frac{\text{r.p.m.}}{1000}\right)^2\left\{0.707 + 0.342\frac{J_2}{J_1}\right\} \hfill (199)$$

 - where h is in inches.

The critical height will be given by

$$\frac{\ell_r}{h} \leq \frac{\cos\theta_1}{(1-\sin\theta_1)} + \frac{\cos\theta_2}{(1+\sin\theta_2)} \hfill (200)$$

$$= 3.11$$

$$\therefore h_{CRIT} = \frac{8.15}{3.11} = 2.62 \text{ inches.}$$

The cavity pressure is, from Appendix IV,

$$-\Delta p_v = \frac{J_i}{hc} (1 - \sin \theta_i)$$

$$= 1.675 \left(\frac{r.p.m.}{1000}\right)^2 \times \frac{0.293}{24.25} \times \frac{144}{h}$$

$$= \frac{2.92}{h} \left(\frac{r.p.m.}{1000}\right)^2 \qquad (201)$$

PERFORMANCE PARAMETERS FREQUENTLY USED BY FAN DESIGNERS

The segment of industry which is most concerned with the design of a wide variety of air moving devices, and which has the greatest amount of practical experience with them, is probably comprised of those companies which design and manufacture blowers for cooling electronic packages, central heating and cooling systems, and special blower applications.

The parameters used by workers in this field are foreign to the aerodynamicist; in this appendix we shall relate them to the more widely understood parameters of general aerodynamics.

SPECIFIC SPEED

Specific speed is defined as

$$N_s = \frac{N\sqrt{Q}}{P_s^{3/4}} \qquad (N \text{ in r.p.m.}) \qquad (202)$$

$$= \frac{(\text{r.p.m.}) \times \text{Flow rate in feet}^3/\text{minute}}{(\text{static back-pressure in inches of water})^{3/4}}$$

It is difficult to give a rationalization of specific speed, which is an empirical concept generated in the early days of water turbine design. It is found empirically that the efficiency of a particular type of fan cor_lates quite closely with N_s , irrespective of the sizes of the test articles.

We can, of course, reduce N_s to aerodynamic units

$$= \frac{(V_T/R)(60/2\pi)\sqrt{(A_j \, U_j) \times 60}}{(\Delta p_j /5.19)^{3/4}}$$

$$= \frac{60 \times 7.75 \times 3.436}{2\pi} \, V_T \, \frac{\sqrt{\dfrac{A_j \, U_j}{R^2}}}{(\Delta p_j)^{3/4}}$$

221

$$= 254.5 \frac{V_T}{R(\Delta P_J)^{3/4}} \sqrt{A_J U_J} \qquad (203)$$

STATIC EFFICIENCY

Static efficiency is given by the equation

$$\eta_s = \frac{Q P_s}{6356 \, (BHP)}$$

$$= \frac{(\text{Flow rate}) \times (\text{Static pressure})}{6356 \, (\text{shaft BHP})} \qquad (204)$$

- where

Q = Flow rate is measured in cubic feet per minute,

P_s = Static pressure is measured in inches of water.

Obviously this equation neglects the kinetic energy content of the exhaust air. The equation for absolute efficiency, in aerodynamic terms, is

$$\eta = \frac{E_J}{E_T} = \frac{\tfrac{1}{2} \dot{m} U_J^2 + A_J U_J \Delta P_J}{E_T}$$

$$= \frac{\tfrac{1}{2} \rho A_J U_J^3 + A_J U_J \Delta P_J}{E_T}$$

$$= \frac{\rho}{2 A_J^2} \frac{(A_J U_J)^3}{E_T} + \frac{(A_J U_J) \Delta P_J}{E_T} \qquad (205)$$

- where the second term is the "static efficiency".

In order to convert from "static efficiency" to absolute efficiency, we need additional information which, in general, is not available.

PRESSURE COEFFICIENT, ψ

Pressure coefficient is defined as

$$\psi = \frac{2.341 \times 10^8 \, P_s}{(ND)^2} \qquad (206)$$

$$= \frac{2.341 \times 10^8 \times \text{(static back-pressure in inches of water)}}{[\text{r.p.m.} \times \text{diameter of fan in inches}]^2}$$

Obviously this is analogous to the aerodynamic parameter $\Delta p_j / q_T$

That is, $\dfrac{\Delta p_j}{q_T} = \psi \times \dfrac{5.19 \times \left(\dfrac{120}{2\pi}\right)^2 \times 144}{2.341 \times 10^8 \times \frac{1}{2}\rho}$

- which at standard sea level becomes

$$\frac{\Delta p}{q_T} = \psi \times \frac{5.19 \times 365 \times 144}{2.341 \times 10^4 \times 11.5} = \psi \qquad (207)$$

Thus, the pressure coefficient ψ is identical numerically with $\dfrac{\Delta p}{q_T}$

FLOW COEFFICIENT, ϕ

The flow coefficient, ϕ, is defined as

$$\phi = \frac{550\, Q}{ND^2 L} \qquad (208)$$

$$= \frac{550 \times \text{(flow rate in feet}^3/\text{minute)}}{\text{r.p.m.} \times \text{(diameter of fan in inches)}^2 \times \text{(fan length in inches)}}$$

Thus the flow coefficient gives the ratio of the actual airflow velocity to the fan's peripheral speed. The corresponding aerodynamic term is $\dot{m}_j / A_j V_T \rho$

That is, $\dfrac{\dot{m}_j}{A_j V_T \rho} = \phi\, \dfrac{120 \times 12 \times 144}{550 \times 60 \times 2}\left(\dfrac{DL}{A_j}\right)$

- which at standard sea level becomes

$$\frac{\dot{m}_j}{A_j V_T \rho} = \phi\left(\frac{DL}{A_j}\right) \qquad (209)$$

Thus, the flow coefficient is also seen to be compatible with an equivalent aerodynamic term.

APPENDIX VII

A NOTE ON THE HISTORY OF TRANSVERSE FANS

Reference (18) credits the first transverse flow fan to Mortier, who applied for a French patent in 1892. Later patents were taken out in the 1930's by the Americans, Anderson and Buck; while in Switzerland, Sprenger and Ackeret showed the nature of transverse flow.

After the last war Coester wrote his doctoral dissertation on the transverse-flow blowers and now designs and manufactures them in Switzerland. Another Swiss, Datwyler, developed a rather different configuration. The Torrington Manufacturing Company of Torrington, Connecticut, has a world-wide nonexclusive license under the Coester patents, and a world-wide license under the Datwyler patents which is exclusive except in certain parts of western Europe.

In Germany, Laing and Eck made certain fan developments in the late 1950's, and the world-wide rights to these are owned by Firth-Cleveland-Laing International, a licensee being its one-time subsidiary Solartron.

Standard Electrik Lorenz, a subsidiary of IT&T, was at one time also a licensee of Laing, but after developing its own fan is now a licensee of Datwyler.
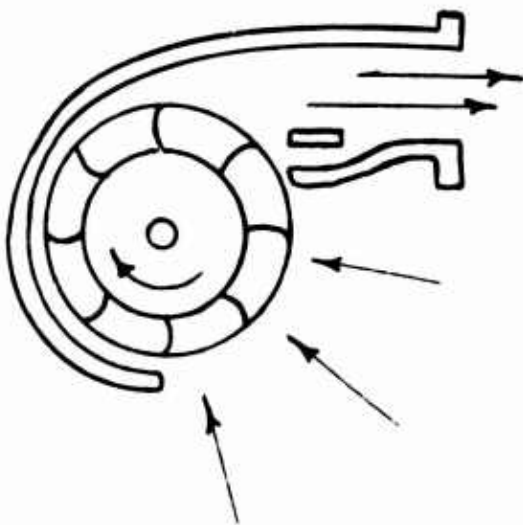
In Figure 149 the main aerodynamic characteristics of these different approaches are sketched diagramatically. Figure 150 gives typical mass-flow versus back-pressure curves.
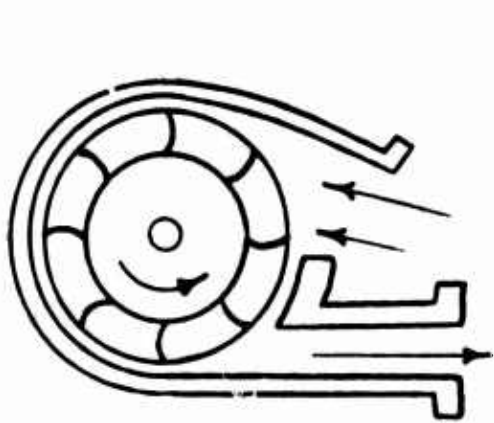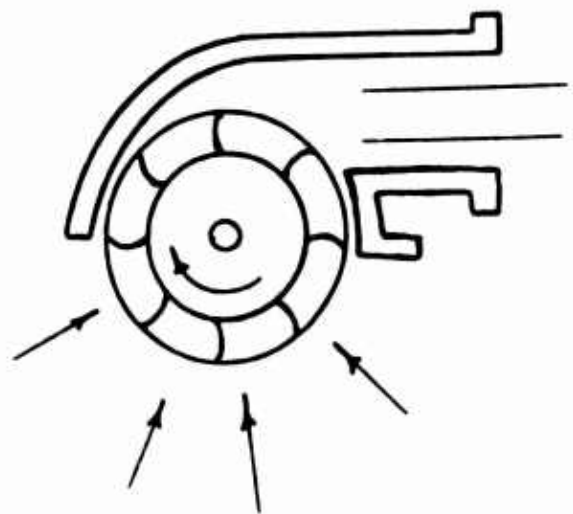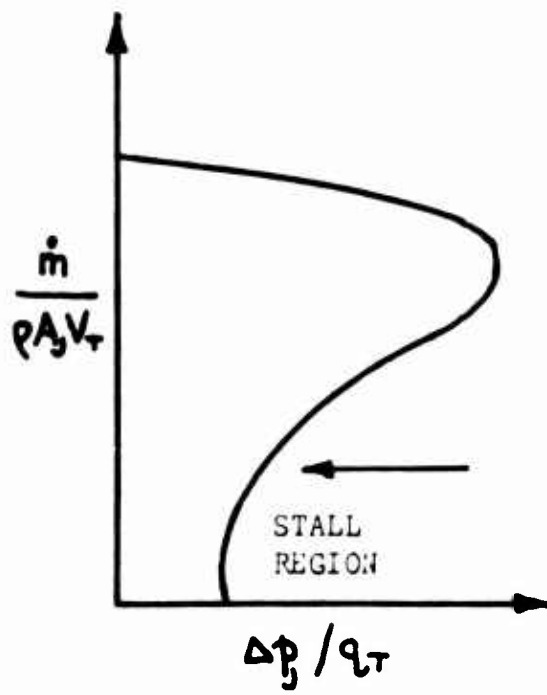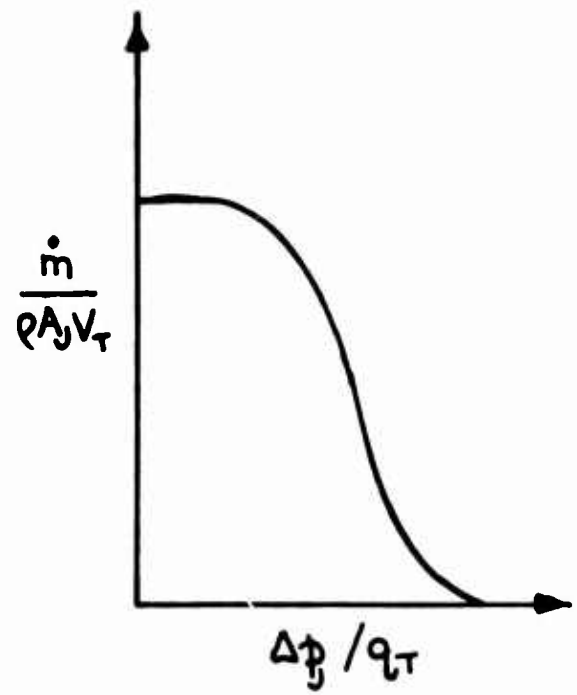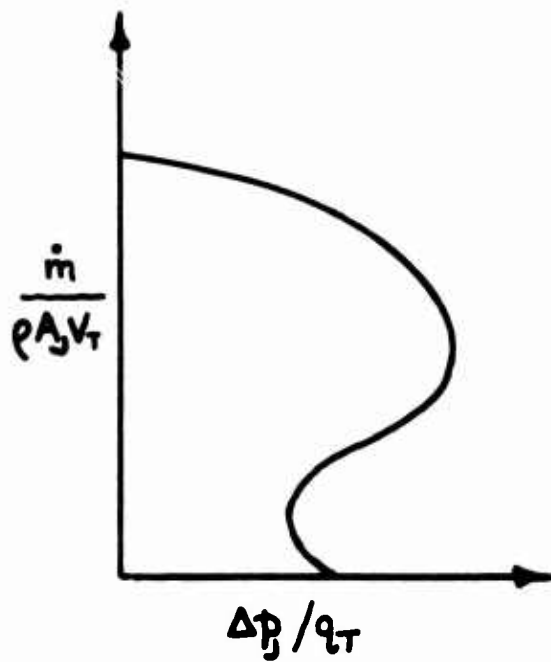
BUCK
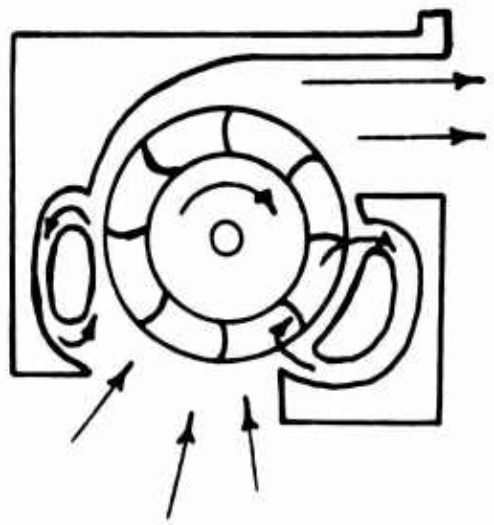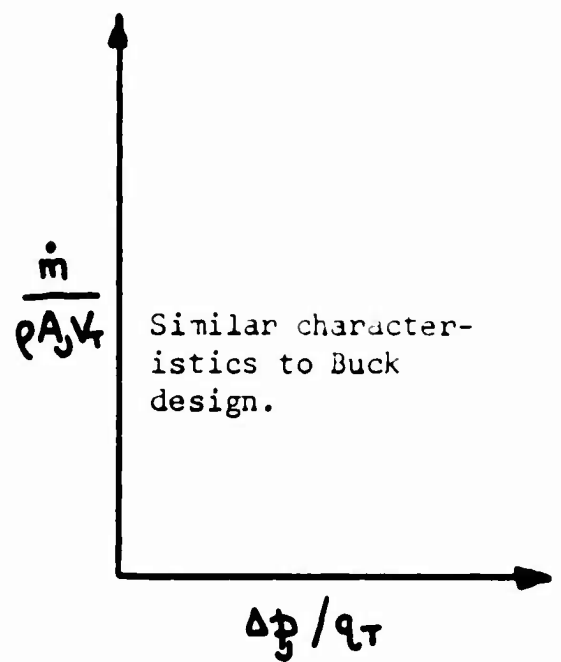
COESTER

DATWYLER

LAING

Figure 143. Types of Crossflow Fan.

Figure 150. Typical Mass-Flow Versus Back-Pressure Curves.

226

APPENDIX VIII

PERFORMANCE CALCULATIONS

INTRODUCTION

The performance calculations presented in this appendix were made with the data obtained from the series of tests discussed in Section Three.

MODEL FAN GEOMETRY

The geometry for the model is as follows:

$$\sigma = \frac{46 \times 0.1875}{2 \times 3.1875} = 0.431$$

$$\frac{A_3}{A_1} = 0.684 \quad \left(\frac{A_3}{A_1}\right)^2 = 0.468$$

$$\beta_1 \approx 58° \quad \beta_2 \approx 0°$$

$$\alpha_2 = 24.7° \quad \frac{2a}{c} = 1.0 \text{ (circular arc)}$$

$$\tan \alpha_2 = 0.46 \quad \text{and we assume zero slip, } \zeta = 1.0.$$

PHYSICAL PROPERTIES OF FAN BLADES

Weight of one blade/roller assembly = 0.117 lb.

Distance of center of gravity from hinge = 2.36 inches

First moment of mass about hinge = 0.713×10^{-3} slugs/ft.

Second moment of mass about hinge = 0.230×10^{-3} slugs/ft.^{2}.

TABLE 9

CALCULATION OF $\Delta p_j/q_T$ FOR $\beta_1 \approx 58°$ AND $\alpha_2 = 24.7°$

v_j/v_T	1.6	1.4	1.2	1.0	0.8	0.6	0.4	0.2	0
$\left(\dfrac{v_j}{v_T}\right)\left(\dfrac{A_j}{A_1}\right)$	1.093	.957	.82	.684	.547	.41	.2735	.1368	0
$\tan\alpha_1 = \dfrac{v_T}{v_j}$	.914	1.043	1.22	1.462	1.826	2.44	3.66	7.31	—
α_1	42.43	46.2	50.66	55.63	61.29	67.71	74.72	82.21	90°
$\alpha_1 - \alpha_2$	17.73	21.5	25.96	30.93	36.59	43.01	50.02	57.51	65.3
$\tan\alpha_1 + \tan\alpha_2$	1.374	1.503	1.68	1.922	2.286	2.90	4.12	7.77	—
$\cot\phi_r$	.687	.7515	.84	.961	1.143	1.45	2.06	3.885	—
ϕ_r	55.51	53.07	49.97	46.14	41.18	34.59	25.89	14.42	0
$\sin\phi_r$	.8242	.7994	.7657	.721	.6584	.5677	.4366	.249	0
$\tan\alpha_1 - \tan\alpha_2$	.454	.583	.76	1.002	1.366	1.98	3.20	6.85	—
σC_L	.374	.466	.574	.724	.9	1.124	1.398	1.705	—
$\left\{1+\left(\dfrac{A_j}{A_1}\right)^2\left(\dfrac{v_j}{v_T}\right)^2\right\}$	2.195	1.917	1.673	1.467	1.3	1.168	1.0747	1.0187	—
$\left\{\zeta^2+\sigma C_L\right\}^{1/2}$	1.555	1.646	1.743	1.878	2.028	2.218	2.45	2.725	—
$(v_j/v_T)^2$	2.55	1.96	1.44	1.0	.64	.36	.16	.04	—
$\Delta p_j/q_T$	-.995	-.314	.303	.878	1.388	1.858	2.29	2.685	—

TABLE 10

CALCULATION OF $\Delta p_J/q_T$ FOR $\beta_1 = 64°$ AND $\alpha_2 = 27.9°$

v_J/v_T	1.6	1.4	1.2	1.0	0.8	0.6	0.4	0.2	0
$\tan \alpha_1$	.914	1.043	1.22	1.462	1.826	2.44	3.66	7.31	-
$\tan \alpha_1 + \tan \alpha_2$	1.444	1.573	1.75	1.992	2.356	2.97	4.19	7.84	-
$\cot \phi_r$	.722	.7865	.875	.996	1.178	1.485	2.095	3.92	-
ϕ_r	54.17	51.81	48.81	45.11	40.33	33.96	25.52	14.31	-
$\sin \phi_r$	.8108	.786	.7525	.7085	.6472	.5586	.4308	.2472	-
$\tan \alpha_1 - \tan \alpha_2$	.384	.513	.69	.932	1.296	1.91	3.13	6.78	-
$\sigma\, C_L$	.312	.404	.519	.66	.84	1.067	1.35	1.677	-
$\left\{1+\left(\frac{A_1}{A_1}\right)^2\left(\frac{v_J}{v_T}\right)^2\right\}$	2.195	1.917	1.673	1.467	1.3	1.168	1.0747	1.0187	-
$f^2 + \sigma\, C_L \left\{\ \ \right\}^{1/2}$	1.463	1.56	1.672	1.801	1.96	2.154	2.4	2.693	-
$(v_J/v_T)^2$	2.55	1.96	1.44	1.0	.64	.36	.16	.04	-
$\Delta p_J/q_T$	-1.087	-.40	.232	.801	1.32	1.794	2.24	2.653	-

229

TABLE 11

COMPARISON OF SCALE READINGS FOR 20, 33 and 45 PER CENT OF MAXIMUM EXIT AREAS

Fan Speed (r.p.m.)	Exit Area 20% of Max. Density = 20.2×10^{-4} slugs/cu. ft.		Exit Area 33% of Max. Density = 21.5×10^{-4} slugs/cu. ft.		Exit Area 45% of Max. Density = 19.8×10^{-4} slugs/cu. ft.	
	Scale Reading* (ounces)	Manometer Reading* (inches of water)	Scale Reading (ounces)	Manometer Reading (inches of water)	Scale Reading (ounces)	Manometer Reading (inches of water)
300	2.00	.060	2.2	.056	2.2	.040
400	2.75	.109	3.3	.099	2.8	.070
450	3.75	.137	4.0	.136	3.4	.088
500	5.50	.168	5.0	.160	4.1	.110
550	6.60	.199	5.5	.205	5.5	.133
600	8.25	.240	8.0	.220	7.0	.160
650	10.25	.280	9.0	.260	9.0	.184
700	12.00	.320	10.0	.290	10.25	.210
750	14.25	.370	12.5	.340	12.0	.245
800	16.50	.416	14.5	.380	12.5	.275

*Average of four runs

230

TABLE 12

COMPARISON OF SCALE READINGS FOR 57, 80 and 100 PER CENT OF MAXIMUM EXIT AREAS

Fan Speed (r.p.m.)	Exit Area 57% of Max. Density = 20.5 X 10⁴ slugs/cu. ft.		Exit Area 80% of Max. Density = 20.3 X 10⁻⁴ slugs/cu. ft.		Exit Area 100% of Max. Density = 20.75 X 10⁴ slugs/cu. ft.	
	Scale Reading (ounces)	Manometer Reading (inches of water)	Scale Reading (ounces)	Manometer Reading (inches of water)	Scale Reading (ounces)	Manometer Reading (inches of water)
300	1.25	.031	2.5	.019	1.6	.013
400	1.6	.052	3.0	.034	2.0	.022
450	2.25	.065	4.0	.042	2.5	.027
500	3.5	.081	4.6	.051	3.8	.036
550	4.75	.098	6.0	.062	3.8	.040
600	6.25	.115	7.0	.073	6.4	.050
650	8.10	.136	8.6	.085	7.6	.059
700	10.0	.160	9.7	.099	9.3	.068
750	11.75	.180	11.7	.114	10.3	.076
800	13.0	.199	12.5	.128	13.0	.086

TABLE 13

HORIZONTAL TRAVERSE MANOMETER READINGS FOR 20, 33, AND 45 PER CENT OF MAXIMUM EXIT AREAS

Distance From Nozzle Wall (inches)	Exit Area 20% of Max. Density = 20.2×10^{-4} slugs/cu. ft. Manometer Reading* (inches of water)	Exit Area 33% of Max. Density = 21.5×10^{-4} slugs/cu. ft. Manometer Reading (inches of water)	Exit Area 45% of Max. Density = 19.8×10^{-4} slugs/cu. ft. Manometer Reading (inches of water)
0	.033	.033	.045
.125	.087	.087	.060
.250	.099	.099	.065
.375	.111	.111	.065
.50	.122	.122	.065
.75	.147	.147	.063
1.25	.123	.129	.060
2.00	.123	.123	.063
2.375	.133	.133	.067
2.75	.141	.141	.069

*Average of three runs.   Constant speed (400 r.p.m.).

232

TABLE 14

HORIZONTAL TRAVERSE MANOMETER READINGS FOR 57, 80 AND 100 PER CENT OF MAXIMUM EXIT AREAS

Distance From Nozzle Wall (inches)	Exit Area 57% of Max. Density = 20.5×10^4 slugs/cu. ft. Manometer Reading (inches of water)	Exit Area 80% of Max. Density = 20.3×10^{-4} slugs/cu. ft. Manometer Reading (inches of water)	Exit Area 100% of Max. Density = 20.75×10^4 slugs/cu. ft. Manometer Reading (inches of water)
0	.041	.017	.010
.125	-	.028	.015
.25	.044	.032	.019
.375	.042	.033	.020
.50	.040	.032	.019
.75	.039	.031	.018
1.25	-	.031	.016
2.00	.052	.032	.020
2.375	-	.035	-
2.75	.052	.034	.020

Constant speed (400 r.p.m.).

233

TABLE 15

VERTICAL TRAVERSE MANOMETER READINGS FOR 20, 33, AND 45 PER CENT OF MAXIMUM EXIT AREAS

Vertical Position	Exit Area 20% of Max. Density = 20.2×10^{-4} slugs/cu. ft. Manometer Reading* (inches of water)	Exit Area 33% of Max. Density = 21.5×10^{-4} slugs/cu. ft. Manometer Reading (inches of water)	Exit Area 45% of Max. Density = 19.8×10^{-4} slugs/cu. ft. Manometer Reading (inches of water)
1	.010	.050	.025
2	.040	.089	.058
3	.045	.100	.070
4	.105	.100	.068
5	.092	.090	.063
6	.160	.064	.055
7	.172	.039	.040
8	.128	−	−
9	.006	−	−

*Average of Three Runs.   Constant speed (400 r.p.m.).

TABLE 16

VERTICAL TRAVERSE MANOMETER READINGS FOR 57, 80 AND 100 PER CENT OF MAXIMUM EXIT AREAS

Vertical Position	Exit Area 57% of Max. Density = 20.5×10^4 slugs/cu. ft. Manometer Reading (inches of water)	Exit Area 80% of Max. Density = 20.3×10^{-4} slugs/cu. ft. Manometer Reading (inches of water)	Exit Area 100% of Max. Density = 20.75×10^4 slugs/cu. ft. Manometer Reading (inches of water)
1	.015	.023	.016
2	.049	.035	.022
3	.060	.035	.029
4	.056	.034	.030
5	.050	.033	.028
6	.042	.029	.024
7	.029	.028	.020
8	.013	.027	.019
9	.005	.024	.018
10	-	.020	.016
11	-	.020	.014
12	-	-	.010
13	-	-	.009

Constant speed (400 r.p.m.).

235

TABLE 17

VARIATION OF U_{Jc}, $\dot{m}_J$ AND E_J FOR 20, 33, AND 45 PER CENT OF MAXIMUM EXIT AREAS

Fan Speed	Exit Area 20% of Max.			Exit Area 33% of Max.			Exit Area 45% of Max.		
	U_{Jc}	$\dot{m}_J$	E_J	U_{Jc}	$\dot{m}_J$	E_J	U_{Jc}	$\dot{m}_J$	E_J
300	17.58	3.49	.0370	16.44	5.91	.0606	14.49	6.70	.0538
400	23.66	4.69	.0906	21.86	7.85	.1423	19.19	8.87	.1245
450	26.43	5.25	.1266	26.15	9.07	.2350	21.47	9.94	.1705
500	29.39	5.83	.1739	27.79	9.96	.2920	24.00	11.12	.2380
550	32.01	6.36	.2248	32.17	11.01	.4330	26.40	12.25	.3150
600	36.00	7.15	.3040	32.65	11.71	.4750	28.98	13.40	.4200
650	37.95	7.53	.3740	35.43	12.72	.6060	31.02	14.37	.5140
700	40.56	8.06	.4575	37.47	13.45	.7175	33.17	15.37	.6300
750	43.63	8.66	.5700	40.50	14.54	.9060	35.81	16.60	.7930
800	46.26	9.18	.6780	42.33	15.20	1.0350	37.92	17.55	.9400

Velocity at center of jet exit, U_{Jc} (ft./sec.).
Mass flow, $\dot{m}_J$, (slugs/sec. X 10^{-4}).
Jet Power, E_J, (ft.lb./sec.).

TABLE 18

VARIATION OF U_{Jc}, $\dot{m}_J$ AND E_J FOR 57, 80, AND 100 PER CENT OF MAXIMUM EXIT AREAS

Fan Speed	Exit Area 57% of Max.			Exit Area 80% of Max.			Exit Area 100% of Max.		
	U_{Jc}	$\dot{m}_J$	E_J	U_{Jc}	$\dot{m}_J$	E_J	U_{Jc}	$\dot{m}_J$	E_J
300	12.53	6.22	.0256	9.98	7.78	.0276	8.06	7.20	.0128
400	16.31	8.09	.0565	13.34	10.42	.0660	10.49	9.37	.0280
450	18.14	9.00	.0777	14.80	11.55	.0925	11.75	10.50	.0393
500	20.27	10.05	.1083	16.34	12.75	.1210	13.42	12.00	.0588
550	22.27	11.05	.1439	18.03	14.09	.1628	14.25	12.75	.0705
600	24.15	11.97	.1765	19.55	15.25	.2070	15.81	14.15	.0960
650	26.25	13.06	.2360	21.10	16.95	.2680	17.19	15.36	.1230
700	28.46	14.14	.3010	22.76	17.75	.3270	18.44	16.50	.1525
750	30.18	14.94	.3580	24.43	19.10	.4050	19.49	17.41	.1800
800	31.82	15.80	.4210	25.90	20.20	.4820	20.73	18.55	.2168

Velocity at center of jet exit, U_{Jc} (ft./sec.).
Mass flow, $\dot{m}_J$, (slugs/sec. X 10^{-4}).
Jet Power, E_J, (ft.lb./sec.).

TABLE 19

VARIATION OF SHAFT BHP, η , AND M FOR 20, 33, AND 45 PER CENT OF MAXIMUM EXIT AREAS

Fan Speed	Exit Area 20% of Max. Shaft BHP	η	M	Exit Area 33% of Max. Shaft BHP	η	M	Exit Area 45% of Max. Shaft BHP	η	M
300	15.54	4.33	3.28	17.09	6.46	4.95	17.10	5.73	4.97
400	28.48	5.78	3.25	34.20	7.57	4.37	29.40	7.73	5.06
450	43.70	5.27	2.65	46.60	9.17	4.43	37.85	8.20	4.93
500	71.25	4.45	2.00	64.75	8.19	3.72	53.20	8.15	4.40
550	93.90	4.36	1.81	78.30	8.01	3.31	78.30	7.33	3.62
600	128.40	4.30	1.67	125.70	6.88	2.65	108.90	7.03	3.12
650	171.00	3.98	1.39	153.00	7.20	2.50	151.	.20	2.59
700	217.50	3.83	1.25	183.00	7.14	2.40	186.00	6.15	2.40
750	276.00	3.75	1.14	242.80	6.79	2.11	233.00	6.18	2.24
800	342.00	3.60	1.03	300.50	6.18	1.87	259.00	6.37	2.25

Shaft brake horsepower of motor (b.h.p. X 10^{-4}).
Efficiency, η (percentage).
Momentum flux per shaft brake horsepower, M (pounds/b.h.p.).

TABLE 20

VARIATION OF SHAFT BHP, η , AND M FOR 57, 80, AND 100 PER CENT OF MAXIMUM EXIT AREAS

| Fan Speed | Exit Area 57% o. Max. | | | Exit Area 80% of Max. | | | Exit Area 100% of Max. | | |
	Shaft BHP	η	M	Shaft BHP	η	M	Shaft BHP	η	M
300	9.70	4.80	5.82	19.45	2.59	3.53	12.45	1.87	3.43
400	16.55	6.20	5.78	31.10	3.86	3.77	20.72	2.45	3.48
450	26.20	5.38	4.52	46.60	3.61	3.10	29.10	2.46	3.12
500	45.25	4.35	3.27	59.60	3.73	2.95	48.75	2.19	2.43
550	67.60	3.86	2.64	85.50	3.45	2.51	54.20	2.36	2.47
600	97.00	3.31	2.16	108.80	3.55	2.31	99.50	1.76	1.66
650	136.20	3.14	1.83	144.50	3.37	2.09	128.00	1.75	1.52
700	181.00	3.02	1.62	175.80	3.38	1.94	168.60	1.65	1.33
750	226.80	2.88	1.52	227.00	3.25	1.73	187.50	1.75	1.33
800	269.00	2.84	1.36	259.00	2.99	1.70	269.20	1.46	1.05

Shaft brake horsepower of motor (b.h.p. X 10^{-4}).
Efficiency, η (percentage).
Momentum flux per shaft brake horsepower, M (pounds/b.h.p.).

TABLE 21

FLOW FACTOR, Φ, EVALUATED AT 400 RPM FOR VARIOUS EXIT AREAS

Jet Exit Area (Percentage of Maximum)	Φ
20	.830
33	.870
45	.875
57	.725
80	.844
100	.738

In the tables which follow, for all cases, jet exit area was 57 per cent of maximum. Also, atmospheric density was 19.5×10^{-4} slugs/cu. ft.

BLANK PAGE

TABLE 22

COMPARISON OF SCALE READINGS FOR PLENUM CHAMBER PRESSURES
OF 0.277, 0.416 AND 0.554 POUNDS PER SQUARE FOOT

Fan Speed (r.p.m.)	Plenum Chamber Pressure = 0.227 lb./sq. ft.		Plenum Chamber Pressure = 0.416 lb./sq. ft.		Plenum Chamber Pressure = 0.554 lb./sq. ft.	
	Scale Reading (ounces)	Manometer Reading (inches of water)	Scale Reading (ounces)	Manometer Reading (inches of water)	Scale Reading (ounces)	Manometer Reading (inches of water)
300	1.75	.0155	1.85	.026	1.25	.0155
400	2.35	.0415	2.00	.038	2.00	.0310
500	4.00	.0700	3.75	.071	3.40	.0585
600	6.50	.1120	6.00	.110	5.75	.0910
700	10.25	.1640	9.25	.158	9.00	.1480
800	13.75	.2200	13.00	.205	13.10	.1970

TABLE 23

COMPARISON OF SCALE READINGS FOR PLENUM CHAMBER PRESSURES
OF 0.831 AND 1.108 POUNDS PER SQUARE FOOT

Fan Speed (r.p.m.)	Plenum Chamber Pressure = 0.831 lb./sq. ft.		Plenum Chamber Pressure = 1.108 lb./sq. ft.	
	Scale Reading (ounces)	Manometer Reading (inches of water)	Scale Reading (ounces)	Manometer Reading (inches of water)
400	2.75	.0245	2.30	.0200
500	4.00	.0505	4.00	.0405
600	6.25	.0800	6.60	.0695
700	9.00	.1305	8.85	.1120
800	12.00	.1780	12.00	.1550

TABLE 24

HORIZONTAL TRAVERSE MANOMETER READINGS FOR VARIOUS PLENUM CHAMBER PRESSURES

Distance From Nozzle Wall (inches)	Plenum Chamber Pressure = 0.277 lb./sq. ft. Manometer Reading (inches of water)	Plenum Chamber Pressure = 0.554 lb./sq. ft. Manometer Reading (inches of water)	Plenum Chamber Pressure = 0.831 lb./sq. ft. Manometer Reading (inches of water)	Plenum Chamber Pressure = 1.108 lb./sq. ft. Manometer Reading (inches of water)
0	.040	.030	.009	.025
.125	.040	.034	.012	.025
.25	.039	.034	.015	.025
.375	.038	.031	.014	.025
.50	.036	.030	.012	.023
.75	.034	.028	.015	.020
1.25	.030	.025	.015	.020
2.00	.036	.025	.020	.023
2.375	.040	.029	.025	.028
2.75	.040	.030	.025	.029

Constant speed (400 r.p.m.), horizontal traverse.

TABLE 25

VERTICAL TRAVERSE MANOMETER READINGS FOR VARIOUS PLENUM CHAMBER PRESSURES

Vertical Position	Plenum Chamber Pressure = 0.277 lb./sq. ft. Manometer Reading (inches of water)	Plenum Chamber Pressure = 0.554 lb./sq. ft. Manometer Reading (inches of water)	Plenum Chamber Pressure = 0.831 lb./sq. ft. Manometer Reading (inches of water)	Plenum Chamber Pressure = 1.108 lb./sq. ft. Manometer Reading (inches of water)
1	.030	.018	.017	.020
2	.036	.022	.021	.026
3	.040	.025	.024	.030
4	.039	.025	.024	.029
5	.040	.023	.022	.030
6	.038	.022	.021	.028
7	.031	.020	.019	.021

Constant speed (400 r.p.m.), vertical traverse.

244

TABLE 26

VARIATION OF U_{Jc}, $\dot{m}_J$ AND E_J FOR PLENUM CHAMBER PRESSURES
OF 0.277, 0.416 AND 0.554 POUNDS PER SQUARE FOOT

Fan Speed (r.p.m.)	Plenum Chamber Pressure = 0.277 lb./sq. ft.			Plenum Chamber Pressure = 0.416 lb./sq. ft.			Plenum Chamber Pressure = 0.554 lb./sq. ft.		
	U_{Jc}	$\dot{m}_J$	E_J	U_{Jc}	$\dot{m}_J$	E_J	U_{Jc}	$\dot{m}_J$	E_J
300	9.09	5.36	.0948	11.77	6.93	.1859	9.09	5.23	.1644
400	14.87	8.76	.2032	14.24	8.38	.2467	12.85	7.40	.2563
500	19.31	11.40	.3345	19.44	11.43	.4176	17.66	10.16	.4093
600	24.43	14.42	.5548	24.21	14.25	.6382	22.02	12.70	.5965
700	29.55	17.42	.8655	29.02	17.08	.9435	28.07	16.17	.9485
800	34.21	20.20	1.2485	33.06	19.43	1.2700	32.40	18.65	1.2840

Velocity at center of jet exit, U_{Jc} (ft./sec.).
Mass flow, $\dot{m}_J$ (slugs/sec. X 10-4).
Jet Power, E_J (ft.lb./sec.).

TABLE 27

VARIATION OF U_{Jc}, $\dot{m}_J$ AND $\mathcal{E}_J$ FOR PLENUM CHAMBER PRESSURES OF 0.831 AND 1.108 POUNDS PER SQUARE FOOT

Fan Speed (r.p.m.)	Plenum Chamber Pressure = 0.831 lb./sq. ft.			Plenum Chamber Pressure = 1.108 lb./sq. ft.		
	U_{Jc}	$\dot{m}_J$	$\mathcal{E}_J$	U_{Jc}	$\dot{m}_J$	$\mathcal{E}_J$
400	11.42	6.35	.2994	10.32	5.71	.3461
500	16.40	9.11	.4758	14.70	8.14	.5250
600	20.66	11.48	.6640	19.26	10.65	.7468
700	26.38	14.66	.9910	24.43	13.53	1.0575
800	30.79	17.10	1.3120	28.76	15.90	1.3750

Velocity at center of jet exit, U_{Jc} (ft./sec.).
Mass flow, $\dot{m}_J$ (slugs/sec. X 10^{-4}).
Jet Power, $\mathcal{E}_J$ (ft.lb./sec.).

TABLE 28

VARIATION OF SHAFT BHP AND η FOR VARIOUS PLENUM CHAMBER PRESSURES

Fan Speed (r.p.m.)	Plenum Chamber Pressure = 0.277 lb./sq. ft. Shaft BHP	η	Plenum Chamber Pressure = 0.416 lb./sq. ft. Shaft BHP	η	Plenum Chamber Pressure = 0.554 lb./sq. ft. Shaft BHP	η	Plenum Chamber Pressure = 0.831 lb./sq. ft. Shaft BHP	η	Plenum Chamber Pressure = 1.108 lb./sq. ft. Shaft BHP	η
300	13.5	12.70	14.3	23.50	9.7	30.80	-	-	-	-
400	24.3	15.20	20.7	21.70	20.7	22.80	28.5	19.10	23.8	26.4
500	51.8	11.75	48.5	15.70	44.0	16.90	51.8	16.70	51.8	18.45
600	101.0	10.30	93.1	12.45	89.3	12.15	97.1	12.40	102.5	13.22
700	185.6	8.50	167.5	10.23	163.0	10.60	163.0	11.05	160.8	11.95
800	284.9	8.05	269.0	8.60	271.0	8.62	248.4	9.60	248.8	10.05

Shaft brake horsepower of motor (b.h.p. X 10^{-4}).
Efficiency, η (percentage).

TABLE 29

FLOW FACTOR, $\bar{\Phi}$, EVALUATED AT 400 RPM
FOR VARIOUS PLENUM CHAMBER PRESSURES

Plenum Chamber Pressure (lb./sq.ft.)	$\bar{\Phi}$
.277	.902
.416	.898
.554	.880
.831	.850
1.108	.847

TABLE 30

LEAKAGE AREA AROUND BLADES

Blade Number	Average Tip Clearance (in.)	Tip Leakage Area (sq. in.)	Average Edge Clearance (in.)	Edge Leakage Area (sq. in.)
1	.047	.272	.047	.324
2	.055	.317	.047	.324
3	.055	.272	.047	.324
4	.055	.272	.047	.324

SUMMARY OF TESTS CONDUCTED WITH A FULL-SCALE FROST FAN

SUMMARY

In all, four series of tests have been conducted, using a single Frost Fan exhausting into a plenum chamber, in order to vary the back-pressure. These tests have been designated Series 1, Series A, Series B, and Series C. The purpose of this appendix is to present a brief description of each series in chronological sequence. Figure No. 151 shows the test rig and instrumentation set-up.
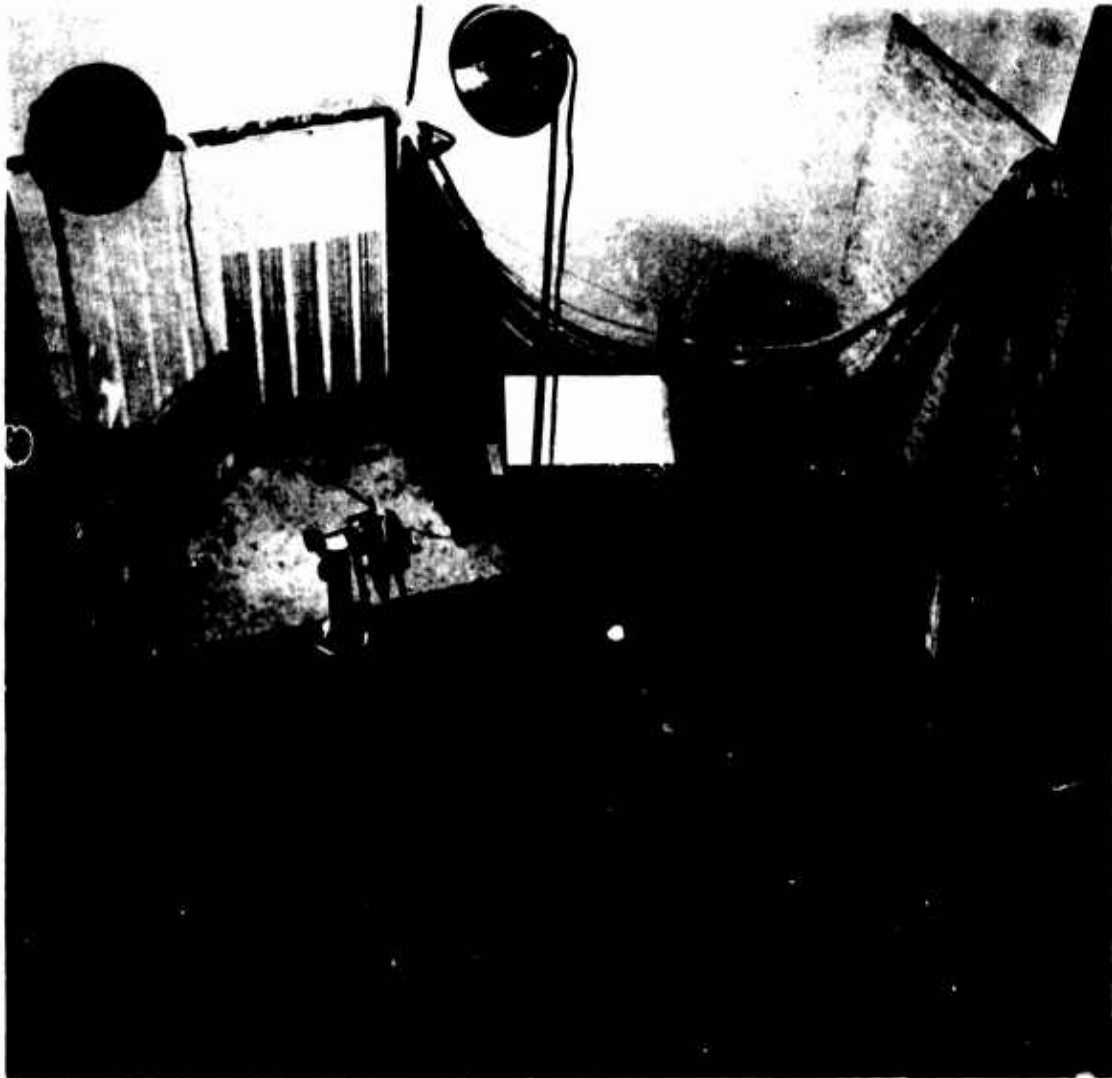
Figure No. 151. Frost Fan Test Rig and Instrumentation.

SERIES 1

This series was conducted in April 1963 and consisted of sixteen runs.
The fan configuration was as shown in Figure 103, and the blades as detailed in Figure 138(a). The test conditions are listed below in Table
31.

TABLE 31

FAN SPEED AND TEST RIG CONFIGURATION FOR SERIES 1 RUNS

Run No.	Fan Speed (r.p.m.)	Test Rig Configuration*
1	1000	Open
2	1000	Closed
3	1000	One Closed
4	1000	Two Closed
5	1000	Two and One-Half Closed
6	1000	Closed
7	1100	Closed
8	1000	Closed
9	1200	Closed
10	1300	Closed
11	1300	Two Closed
12	1200	Two Closed
13	1100	Two Closed
14	1100	One Closed
15	1200	One Closed
16**	1300	One Closed

*   Test rig configuration refers to the three 4-inch diameter
         holes in the rig and cover.

**   During this run, the fan blades failed.

Dismantling and inspection of the fan, after Run 16, revealed that the skin of one blade had torn open and that each blade had started to open up at the corners adjacent to the hinge.

The above-mentioned failures were attributed to the blades' flexing, which caused a progressive failure of the relatively rigid epoxy bond.

Figure 152 shows the location of the total head rake in relation to the fan exit. All of the pressures were measured on manometer tubes and recorded photographically.

LONGITUDINAL STATIONS   TRANSVERSE STATIONS

FAN CASING
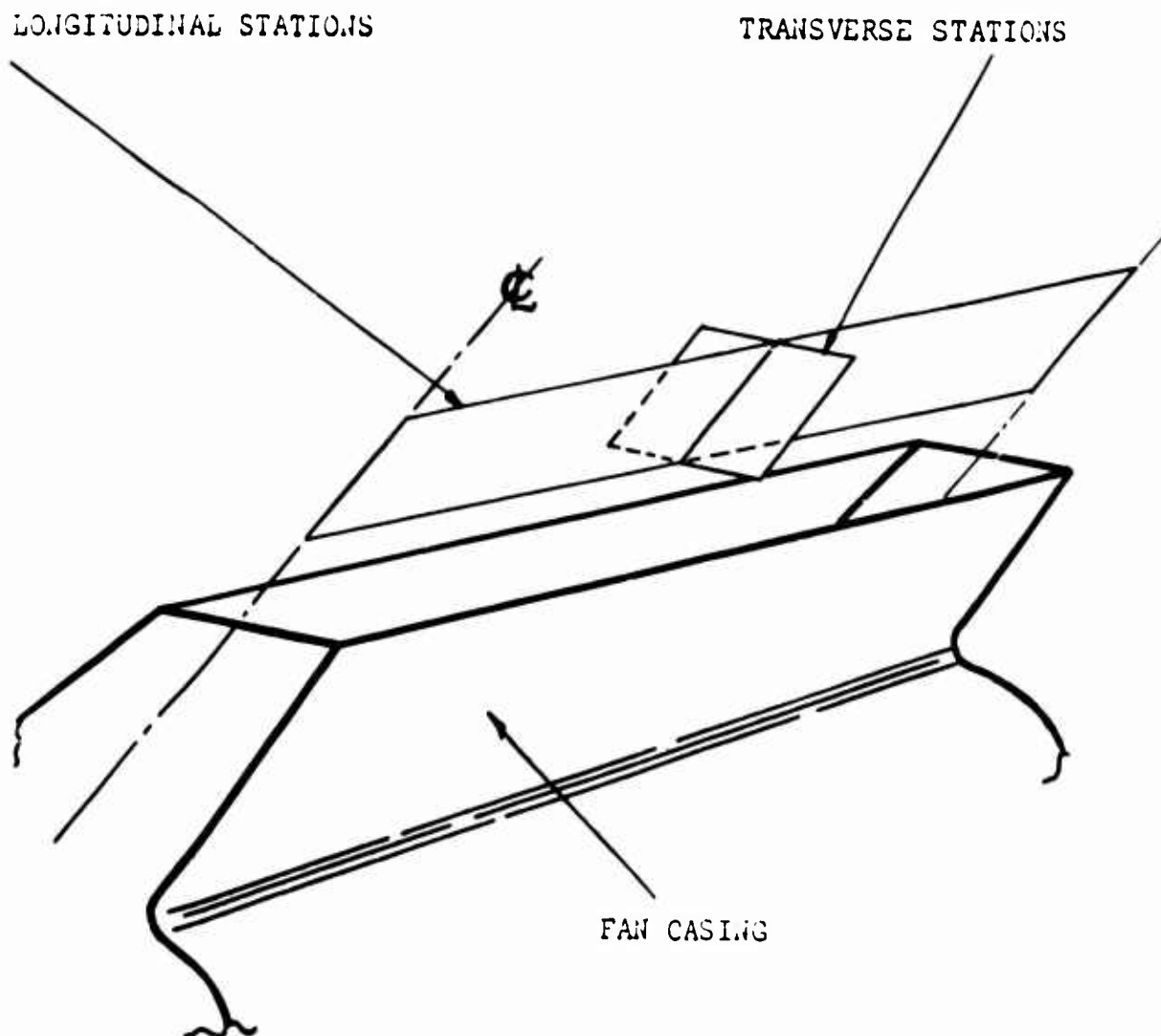
Figure 152.   Location of Total Head Rake.

Table 32 lists the exact location of the total head rake stations with reference to the edges of the fan exit.

251

TABLE 32

STATION LOCATIONS FOR TESTS WITH FULL-SIZE FROST FAN

Station No.	Distance From Edge of Fan Exit (in.)	Station No.	Distance From Edge of Fan Exit (in.)
Longitudinal		24	15.03
1	0.07	25	15.78
2	0.25	26	16.65
3	0.50	27	17.47
4	0.81	28	18.26
5	1.14	29	19.13
6	1.56	30	19.93
7	2.11	31	20.62
8	2.68	32	21.17
9	3.35	33	21.66
10	4.17	34	22.11
11	4.95	35	22.45
12	5.78	36	22.79
13	6.61	37	23.01
14	7.45	38	23.21
15	8.30	Transverse	
16	9.07	39	0
17	9.93	40	.093
18	10.73	41	.344
19	11.53	42	.563
20	11.77	43	.750
21	12.58	44	1.00
22	13.38	45	1.312
23	14.18		

From the test data obtained, the following velocity profiles were prepared.

BLANK PAGE
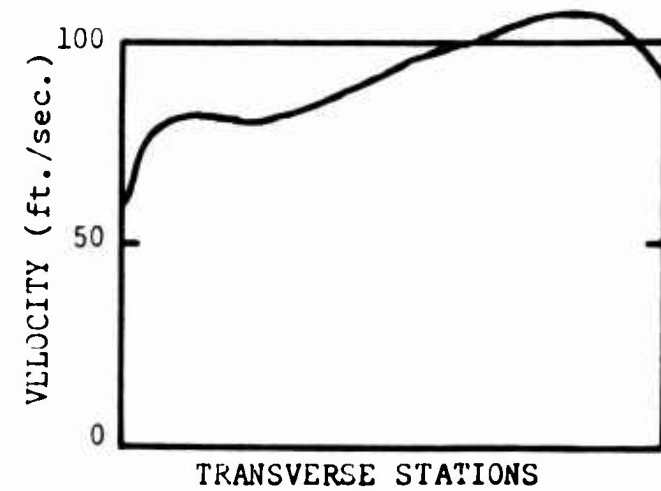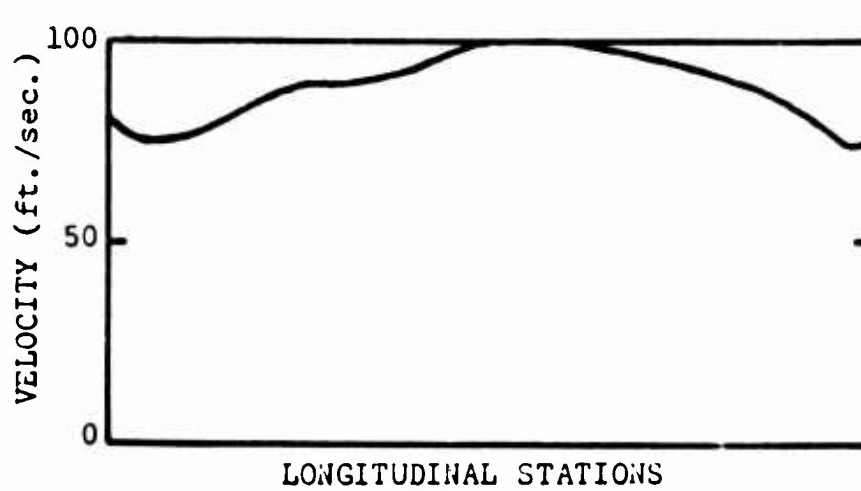
Figure 153.   Velocity Profile Test No. 1.   Configuration: All Open, Speed: 1000 RPM.
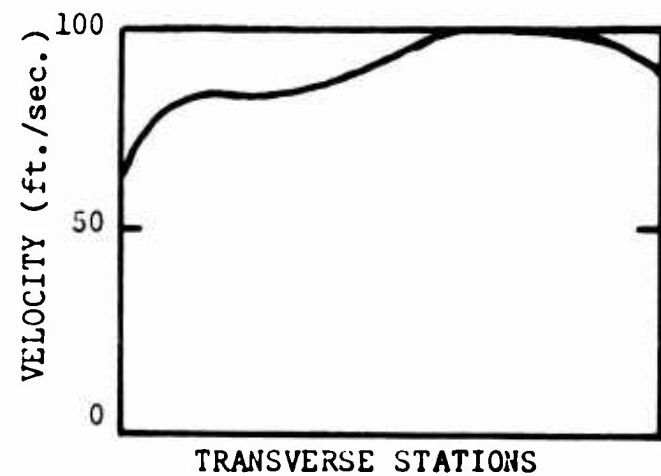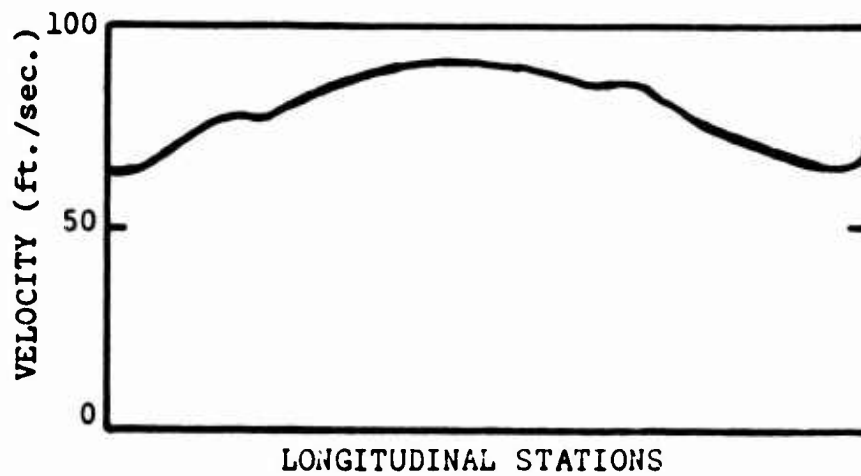
Figure 154.   Velocity Profile Test No. 2.   Configuration: All Closed, Speed: 1000 RPM.
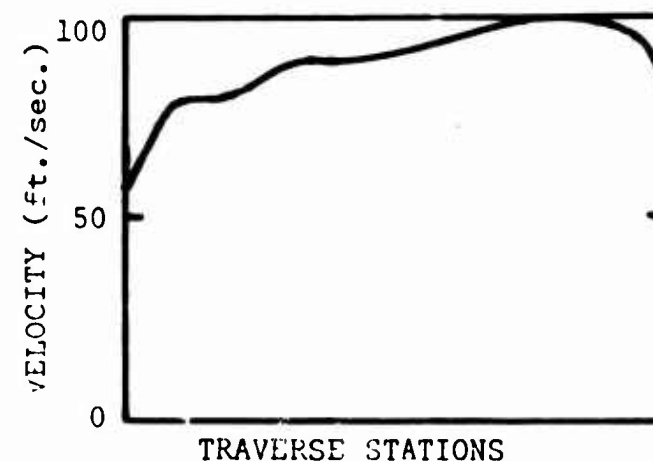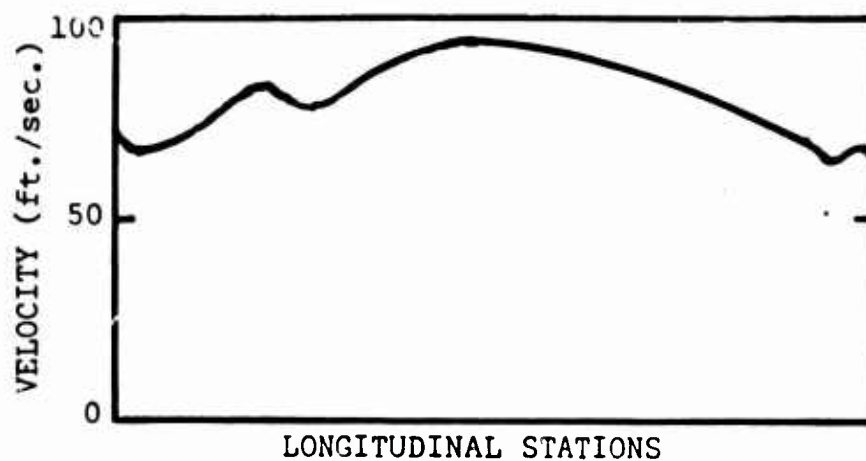
Figure 155. Velocity Profile Test No. 3. Configuration: One Closed, Speed: 1000 RPM.
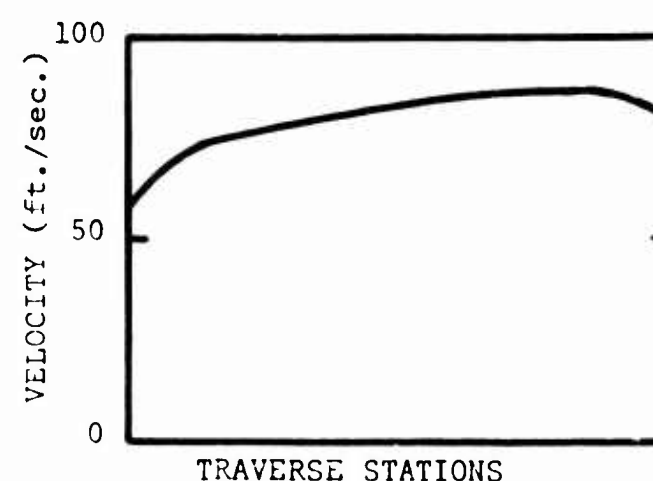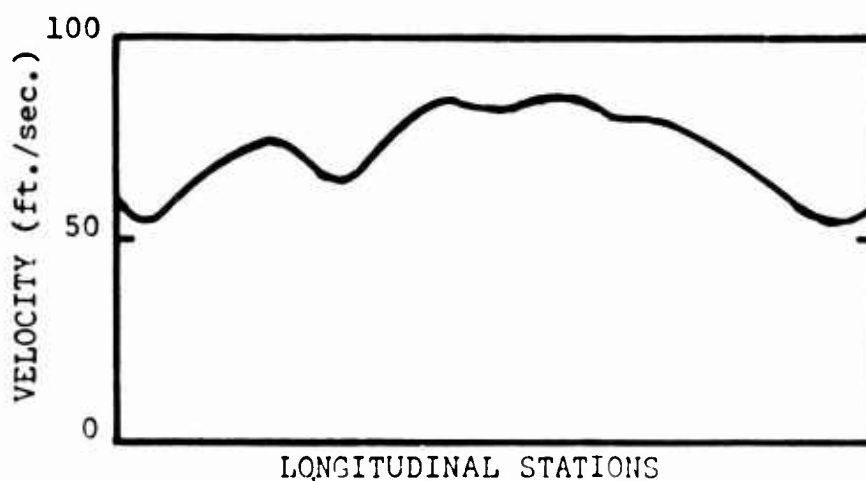
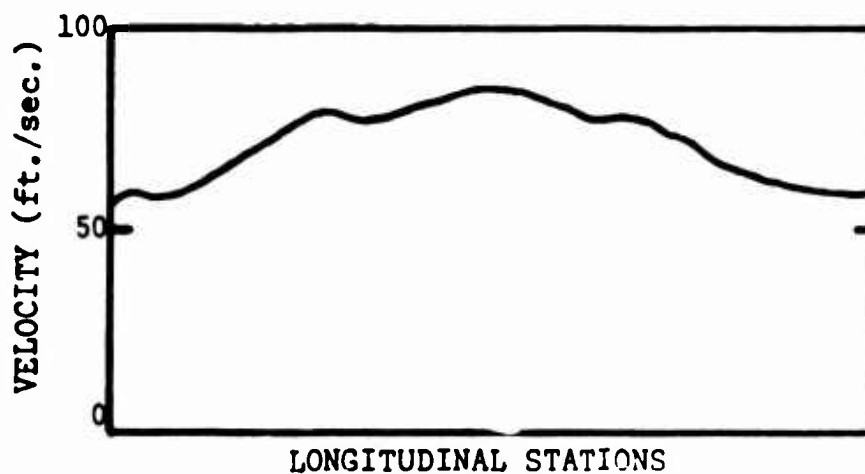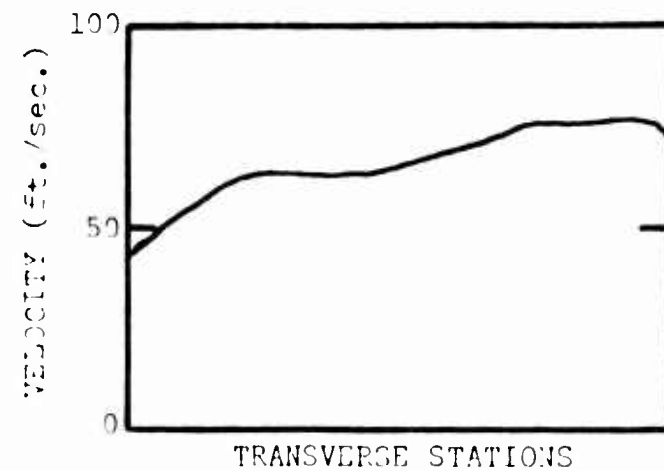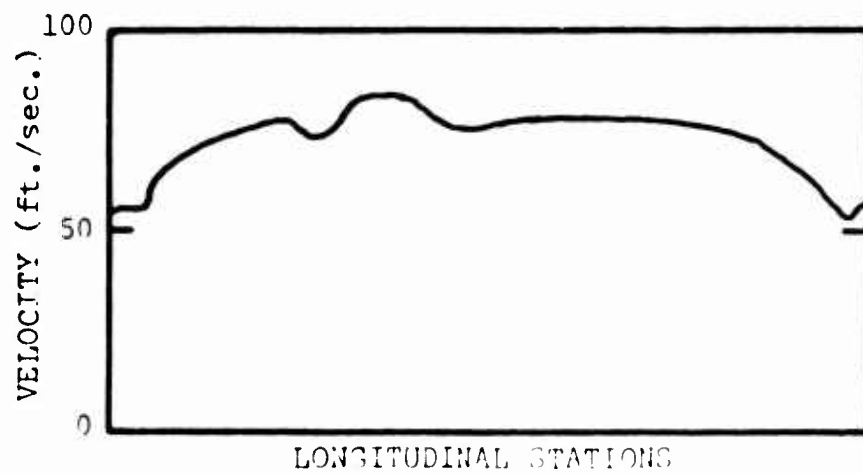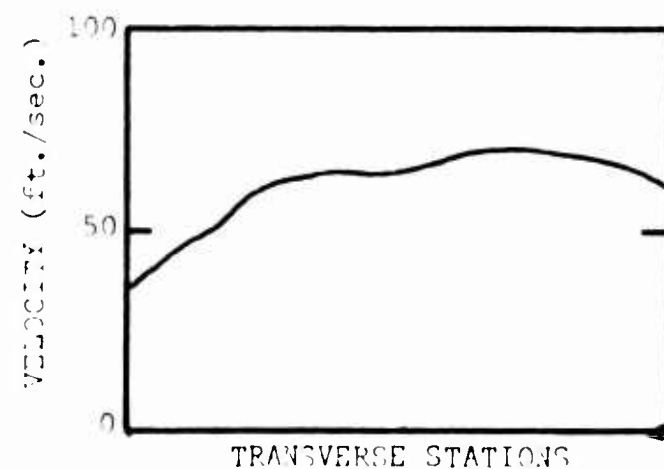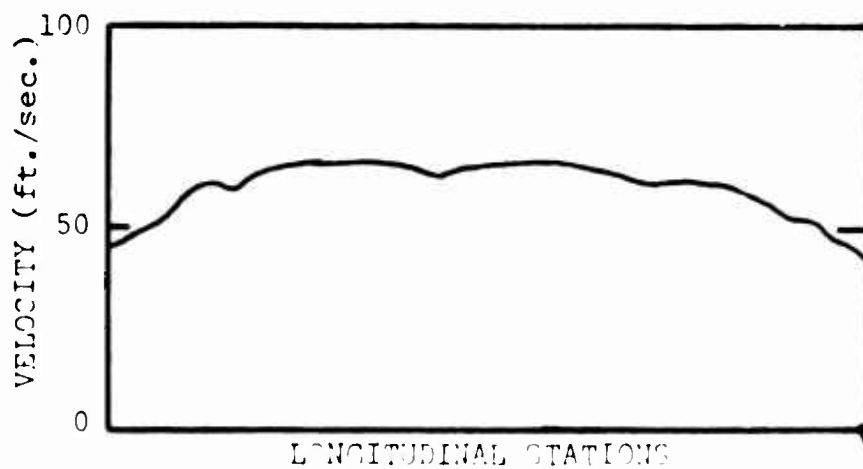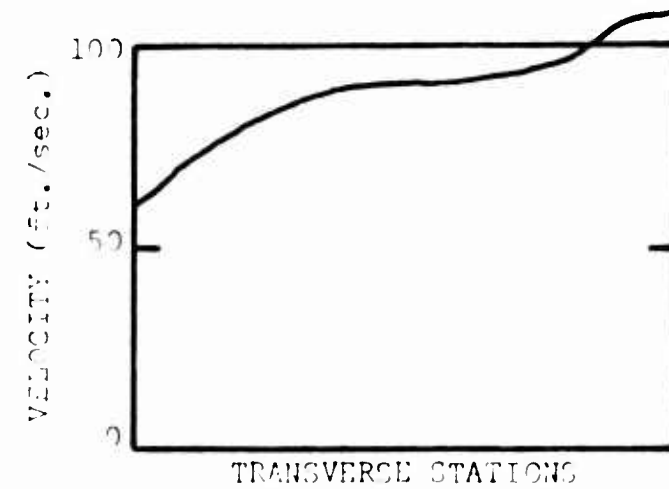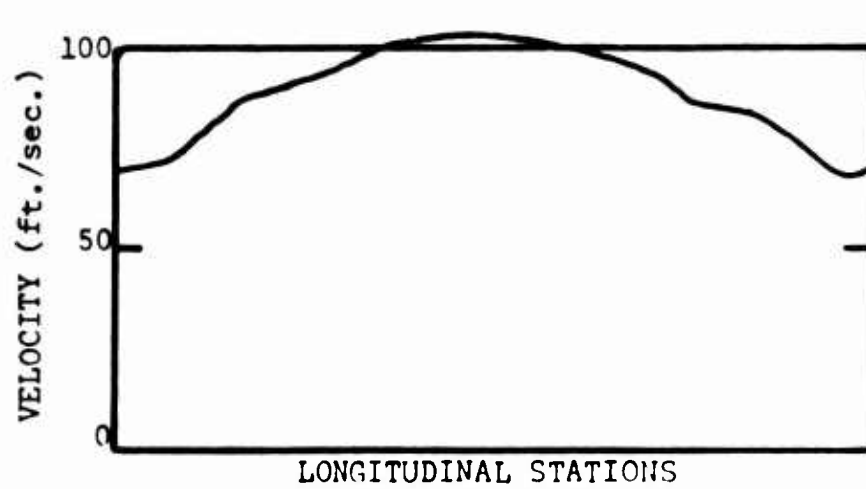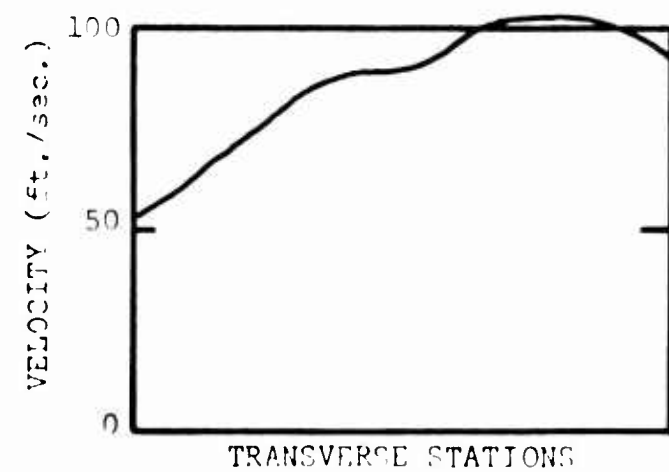Figure 156. Velocity Profile Test No. 4. Configuration: Two Closed, Speed: 1000 RPM.
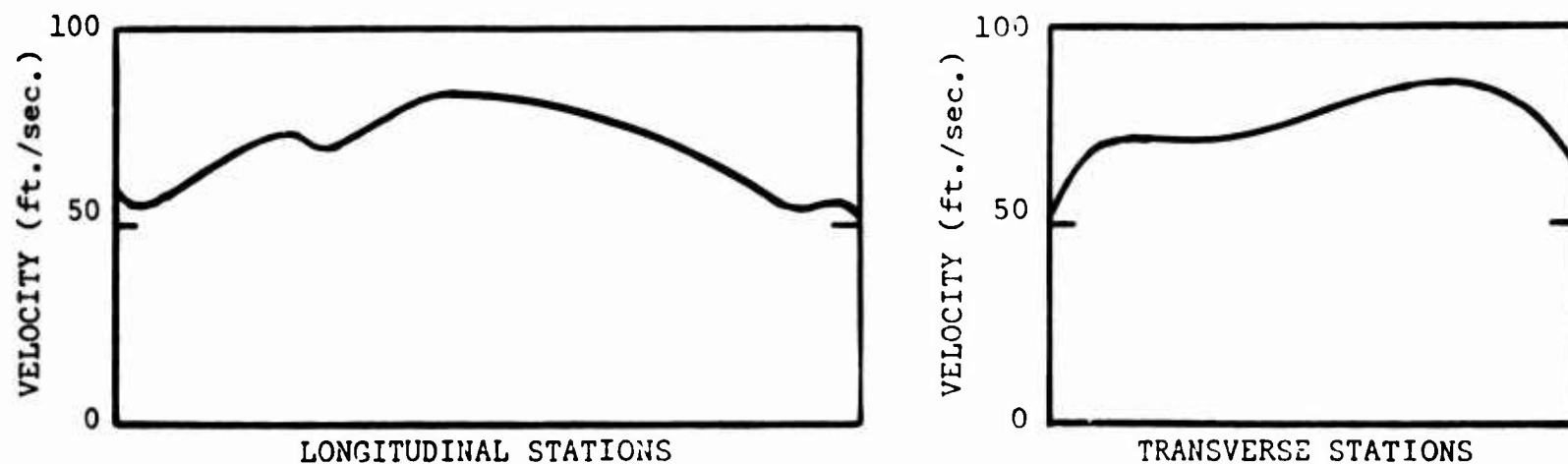
Figure 157. Velocity Profile Test No. 5. Configuration: Two and One-Half Closed, Speed: 1000 RPM.
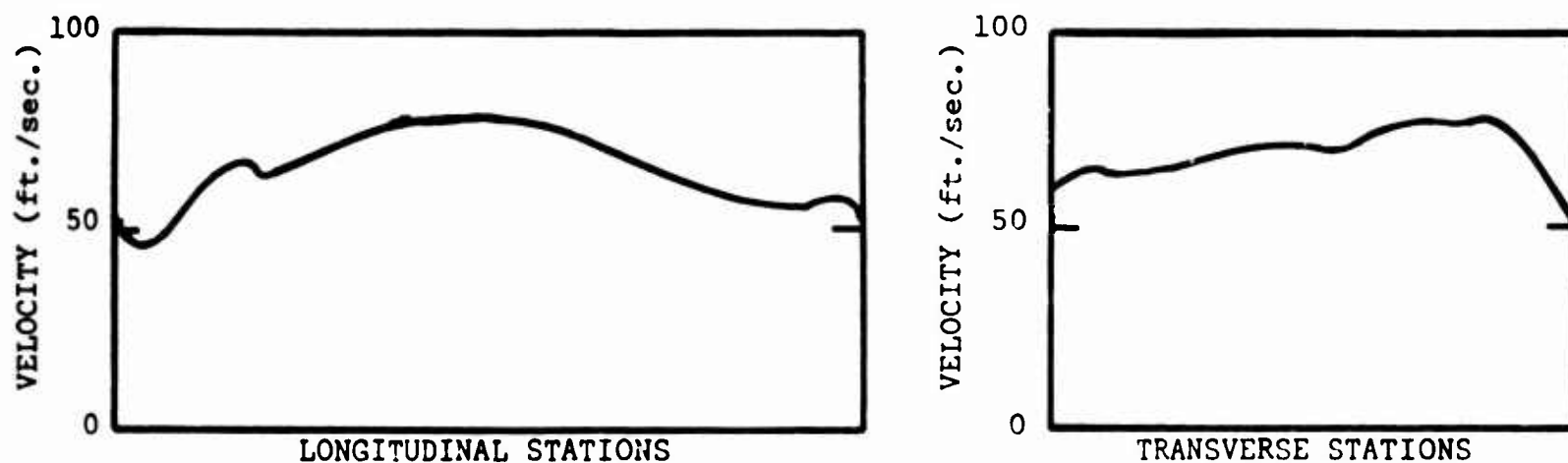
Figure 158. Velocity Profile Test No. 6. Configuration: All Closed, Speed: 1000 RPM.

255
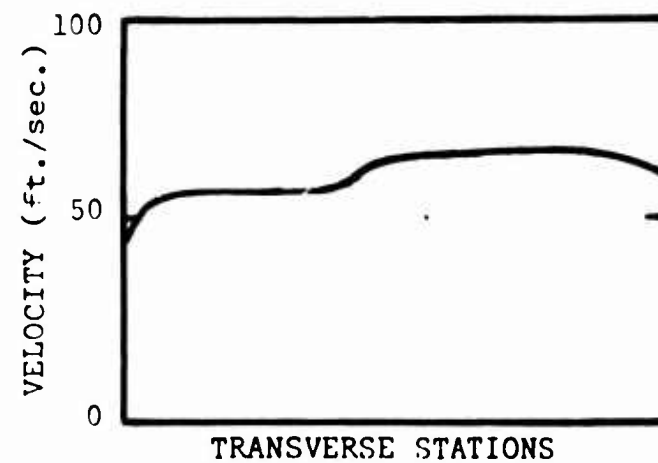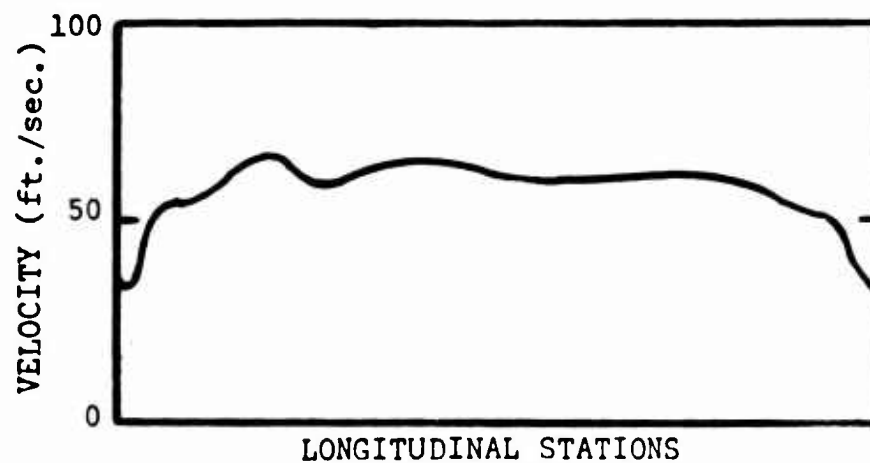
Figure 159. Velocity Profile Test No. 7. Configuration: Closed, Speed: 1100 RPM.
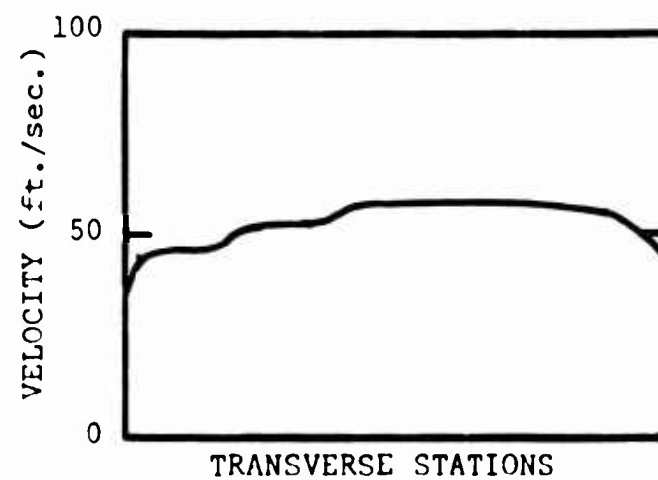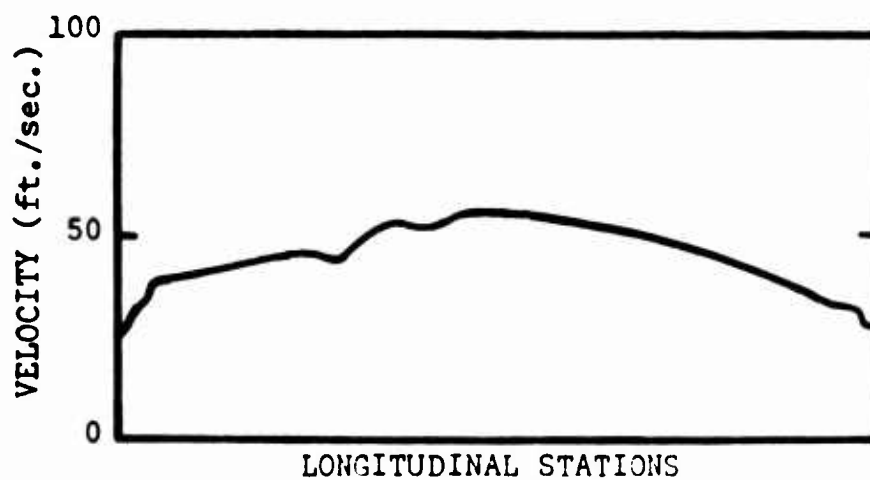
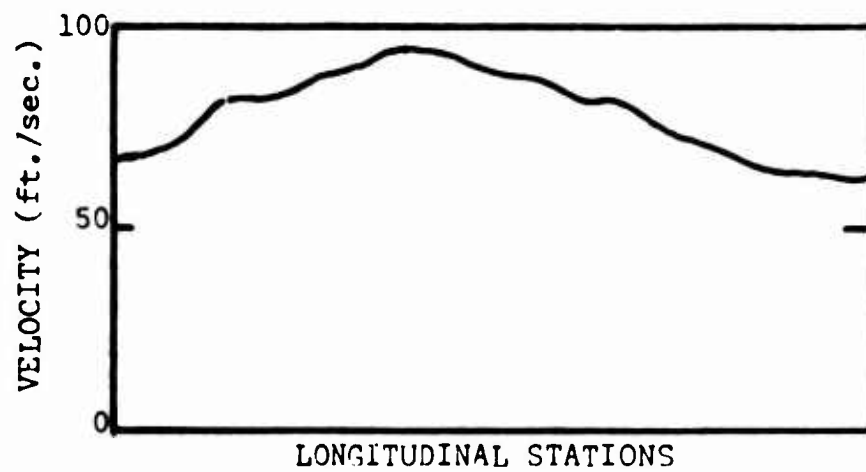Figure 160. Velocity Profile Test No. 8. Configuration: Closed, Speed: 1000 RPM.
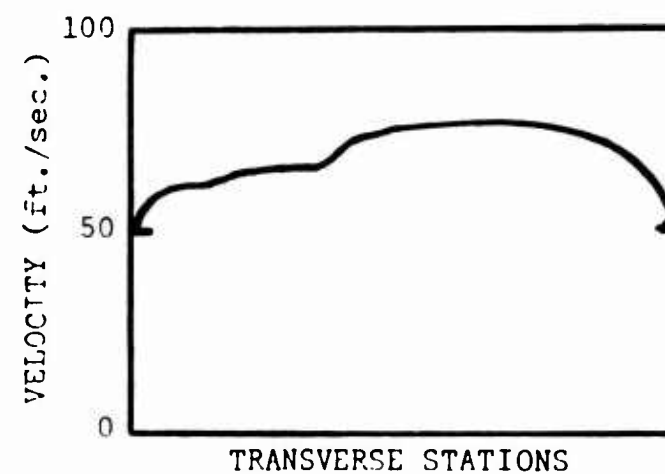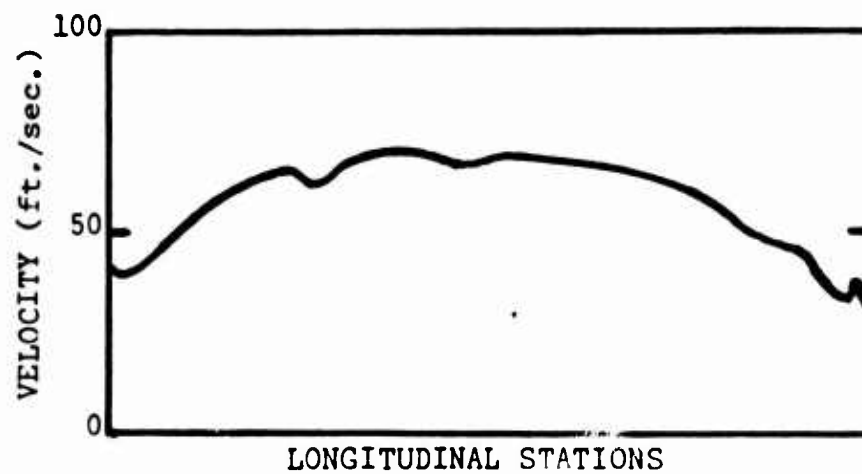
Figure 161.   Velocity Profile Test No. 9.   Configuration: Closed, Speed: 1200 RPM.
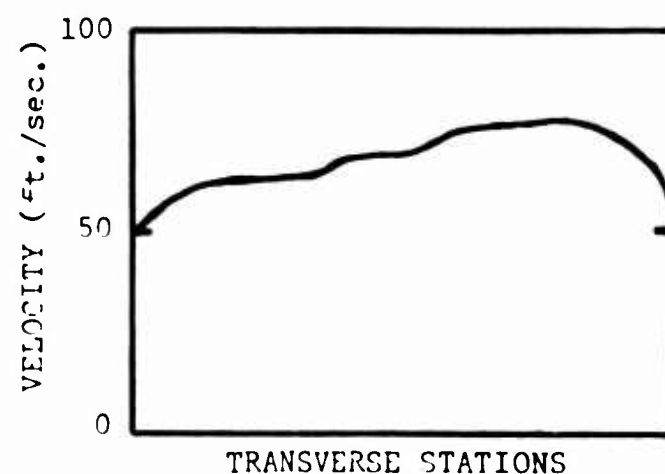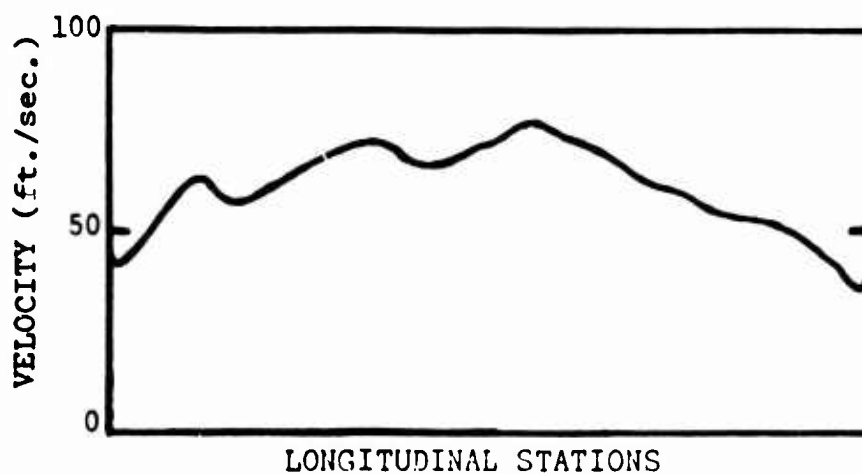
Figure 162.   Velocity Profile Test No. 10.   Configuration: Closed, Speed: 1300 RPM.
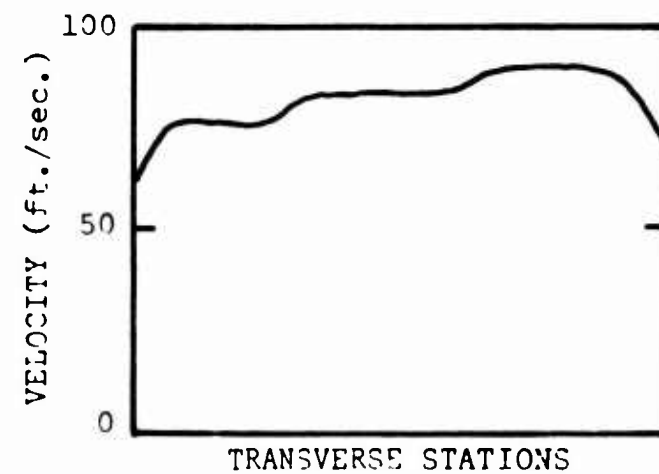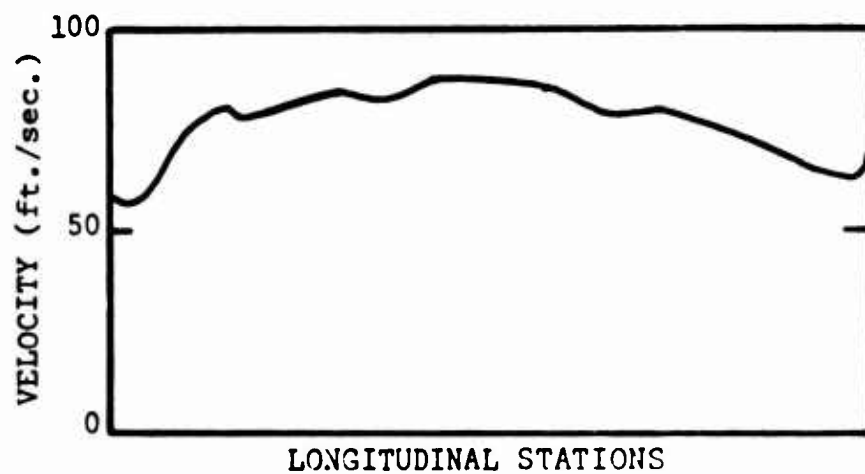
Figure 163. Velocity Profile Test No. 11. Configuration: One Open, Speed: 1300 RPM.
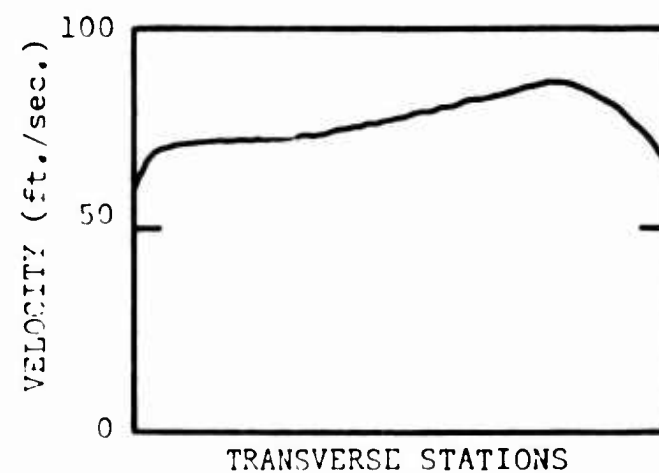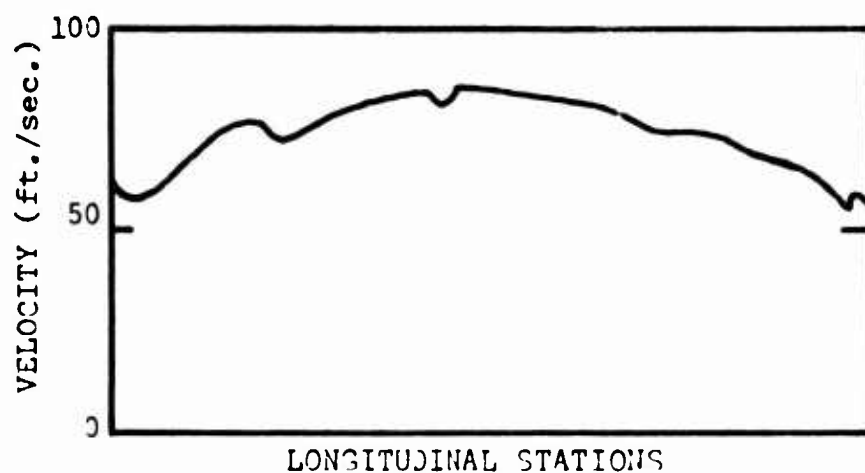
Figure 164. Velocity Profile Test No. 12. Configuration: One Open, Speed: 1200 RPM.
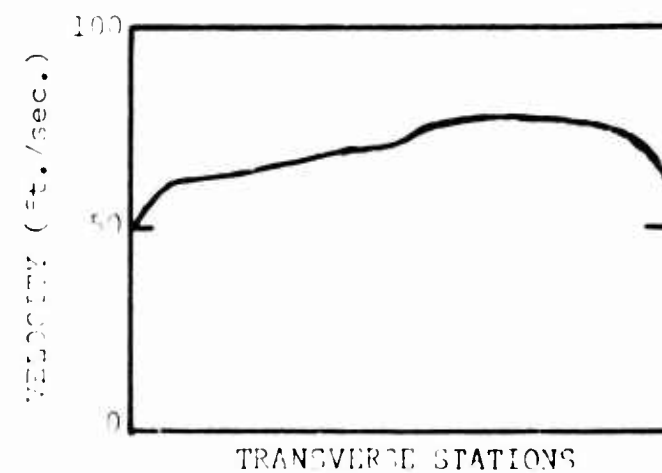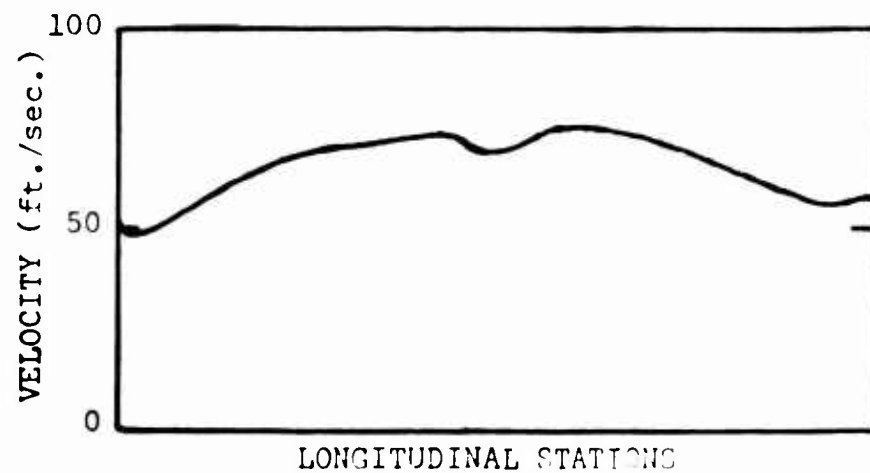
Figure 165. Velocity Profile Test No. 13. Configuration: One Open, Speed: 1100 RPM.
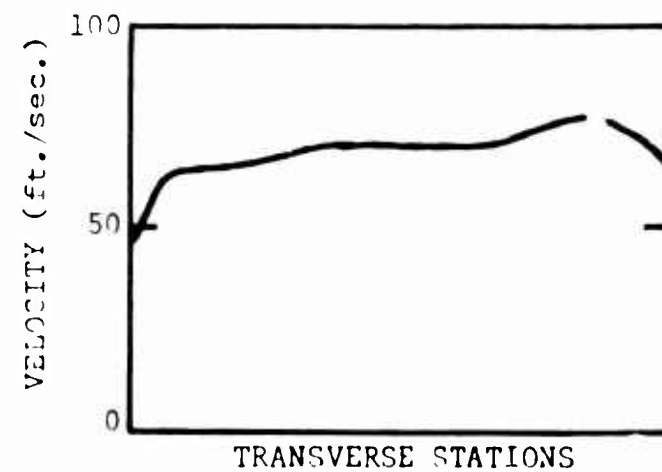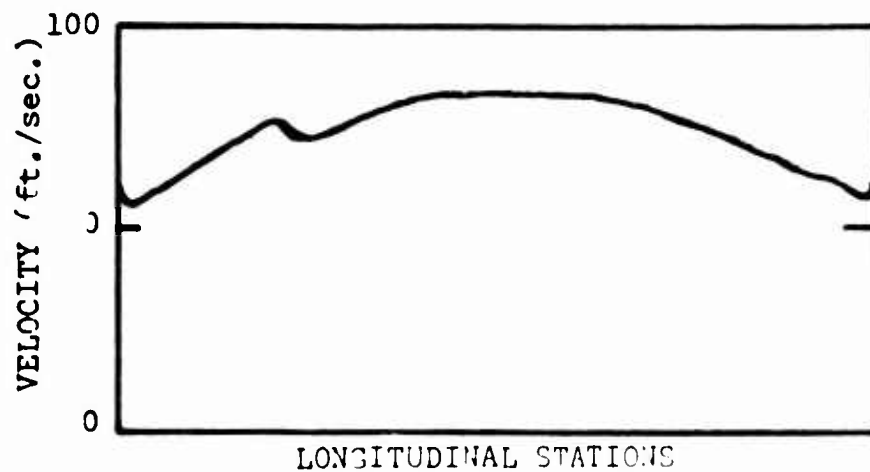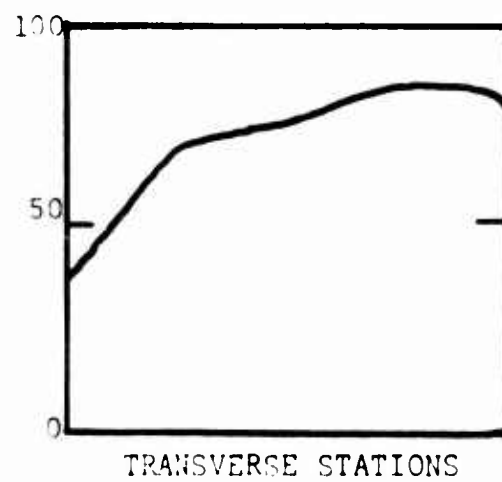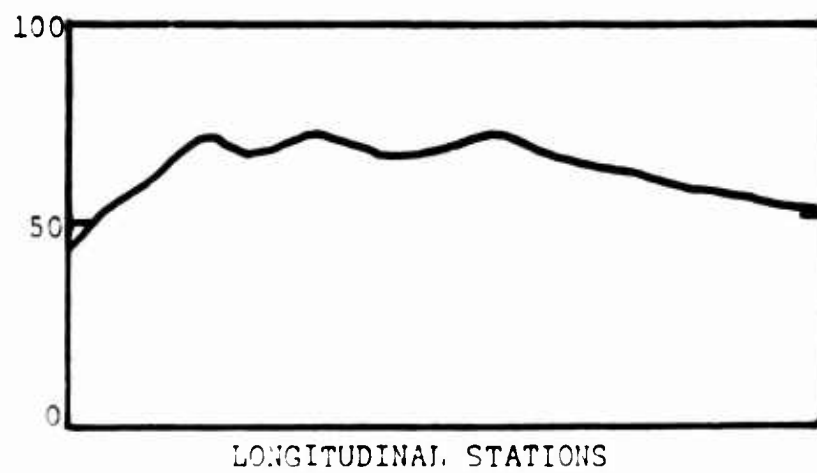
Figure 166. Velocity Profile Test No. 14. Configuration: Two Open, Speed: 1100 RPM.
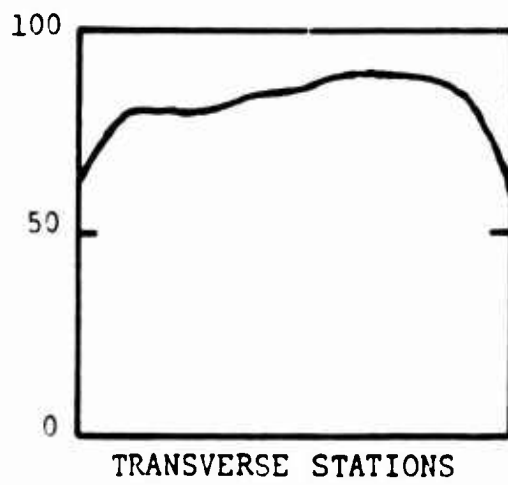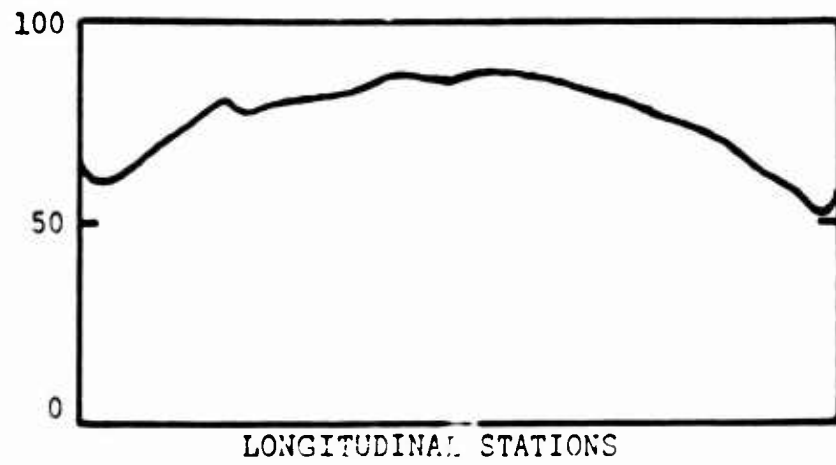
Figure 167. Velocity Profile Test No. 15.
Configuration: Two Open, Speed: 1200 RPM.

SERIES A

Three of the blades used in Series 1, together with one new blade, were
modified by adding stiffeners and a reinforcing strip to the corners
adjacent to the hinge. These blades were then installed into a fan cas-
ing, and Series A runs were conducted.

This series consisted of ten runs designated 1A through 10A and were
conducted in May 1963. Table 33 lists the test conditions.

TABLE 33

LIST OF TEST CONDITIONS FOR SERIES A RUNS

Run No.	Fan Speed (r.p.m.)	Test Rig Configuration
1A	1000	Open
2A	1000	One Closed
3A	1000	Two Closed
4A	*	
5A	1200	Open
6A	1200	One Closed
7A	1200	Two Closed
8A	1400	Open
9A	1400	One Closed
10A	1400	Two Closed

*Run 4A was started at 1000 r.p.m. with all three holes closed but the
pressure build-up in the plenum chamber blew out the chamber sealing
strips. Prior to the sealing strips failing, the window in the plenum
chamber side cover was seen to deflect some four inches. The run was
stopped, and regarded as a no-test.

Inspection of the fan after the testing was completed revealed no struc-
tural damage. A number of score marks were noticed on the inside of the
fan case; these were attributed to particles of dust and foreign matter
being sucked up through the fan intake.

The following velocity profiles were prepared from the test data.
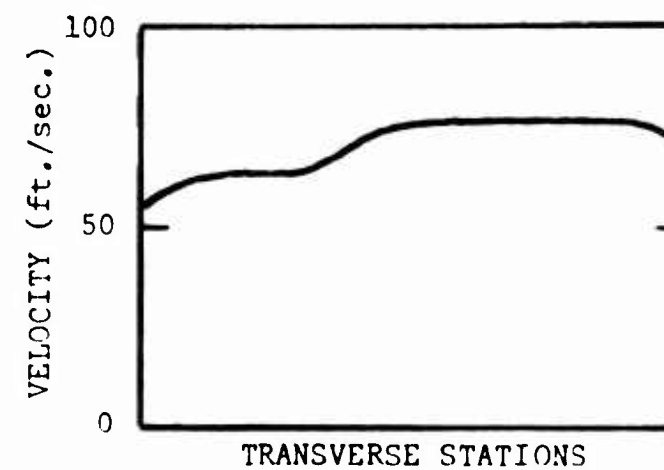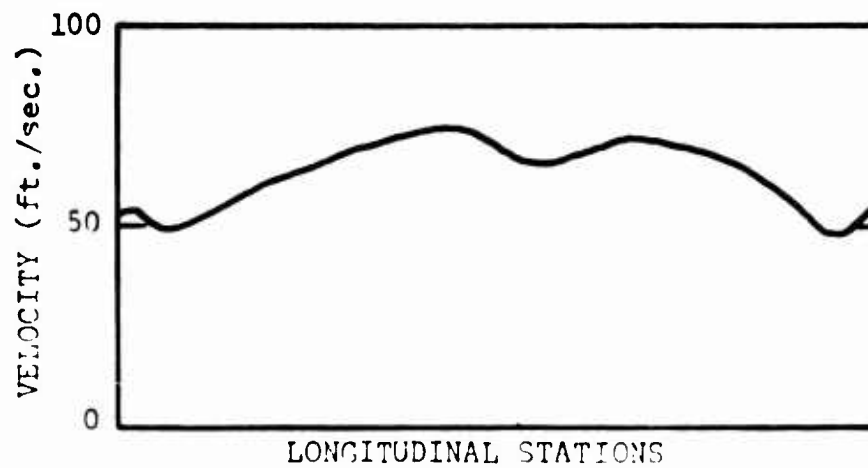
Figure 168. Velocity Profile Test No. 1A. Configuration: Fully Open, Speed: 1000 RPM.

262
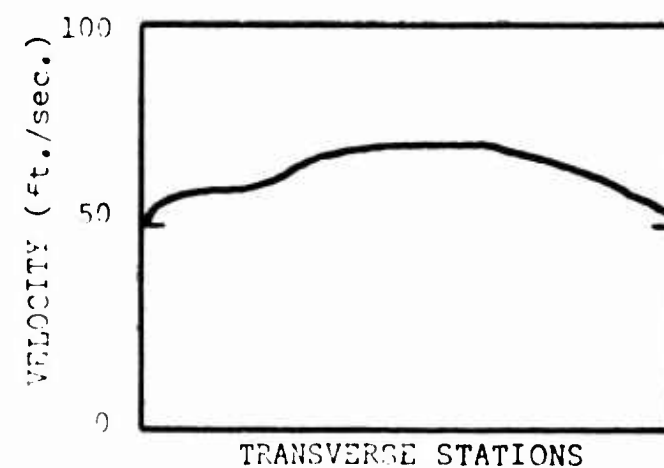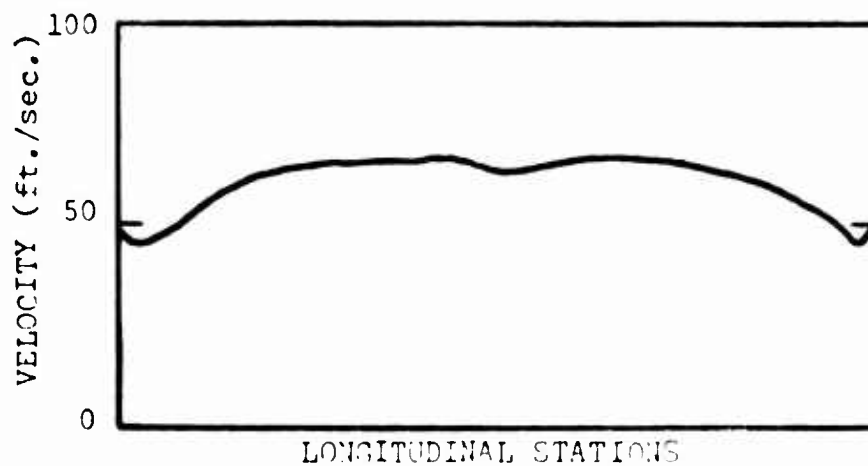
Figure 169. Velocity Profile Test No. 2A. Configuration: One Closed, Speed: 1000 RPM.
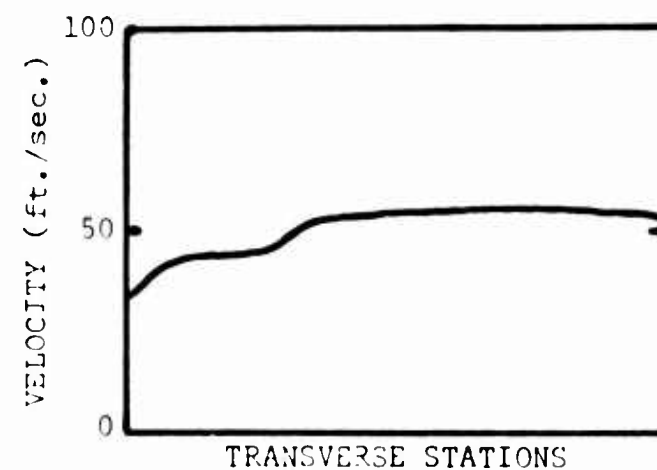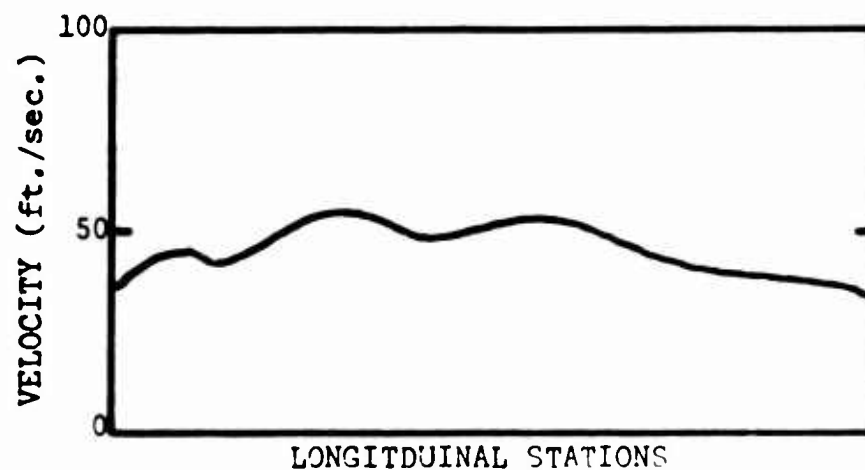
Figure 170. Velocity Profile Test No. 3A. Configuration: One and Two Closed, Speed: 1000 RPM.
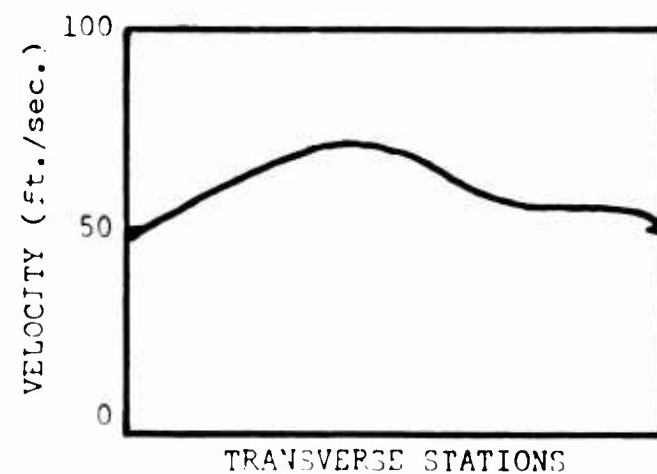
Figure 171. Velocity Profile Test No. 5A. Configuration: All Open, Speed: 1200 RPM.

263

Figure 172. Velocity Profile Test No. 6A. Configuration: One Closed, Speed: 1200 RPM.

Figure 173. Velocity Profile Test No. 7A. Configuration: One and Two Closed, Speed: 1200 RPM.

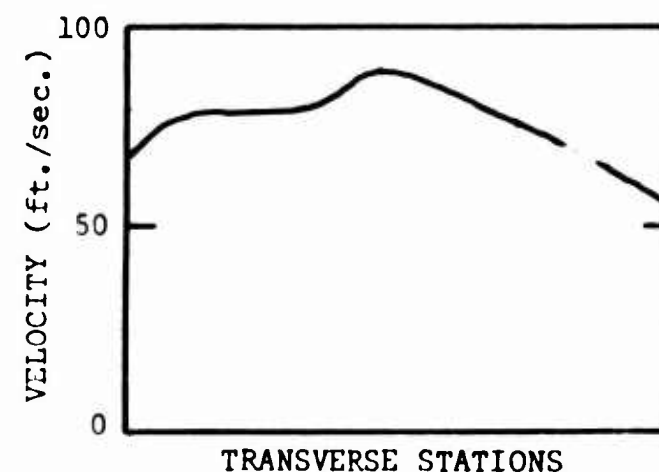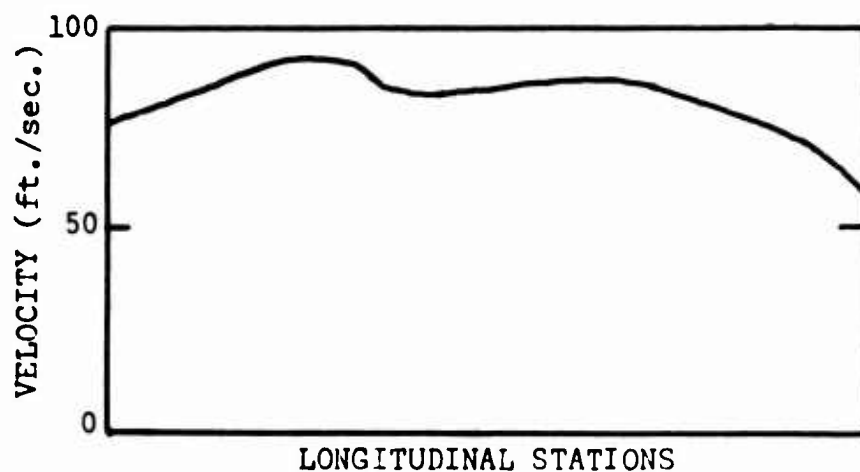**Figure 174.** Velocity Profile Test No. 8A. Configuration: Fully Open, Speed: 1400 RPM.

Figure 175. Velocity Profile Test No. 9A. Configuration: One Closed, Speed: 1400 RPM.

Figure 176. Velocity Profile Test No. 10A.
Configuration: One and Two Closed, Speed:
1400 RPM.

SERIES B

The fan case and blades used for Series A were assembled, but this time
the left-hand end of the rotor was fitted to the right-hand end bell.
This, in effect, caused the blades to run backwards.

In July 1963 twelve runs were made with the "backward" fan. Table 34
lists the test conditions.

TABLE 34

LIST OF TEST CONDITIONS FOR SERIES B RUNS

Run No.	Fan Speed (r.p.m.)	Test Rig Configuration
1	1000	Open
2	1000	One Closed
3	1000	Two Closed
4	1000	All Closed
5	1200	Open
6	1200	One Closed
7	1200	Two Closed
8	1200	All Closed
9	1400	Open
10	1400	One Closed
11	1400	Two Closed
12	1600	Open

As can be seen from Table 34, we were able to run the "backward" fan at
1000 and 1200 r.p.m. with the test rig completely closed.

The test data were reduced and velocity profiles plotted, but as explained in a previous section of this report, the data were of no significant value. The velocity profiles therefore are not presented in this appendix.

The fan was again dismantled for inspection, and no damage was visible. The blades at this time were discarded and new blades, per Figure 138(b) configuration, were fabricated.

Figure 177 is a photograph of the two blades and clearly shows the stiffeners added prior to the Series A tests.
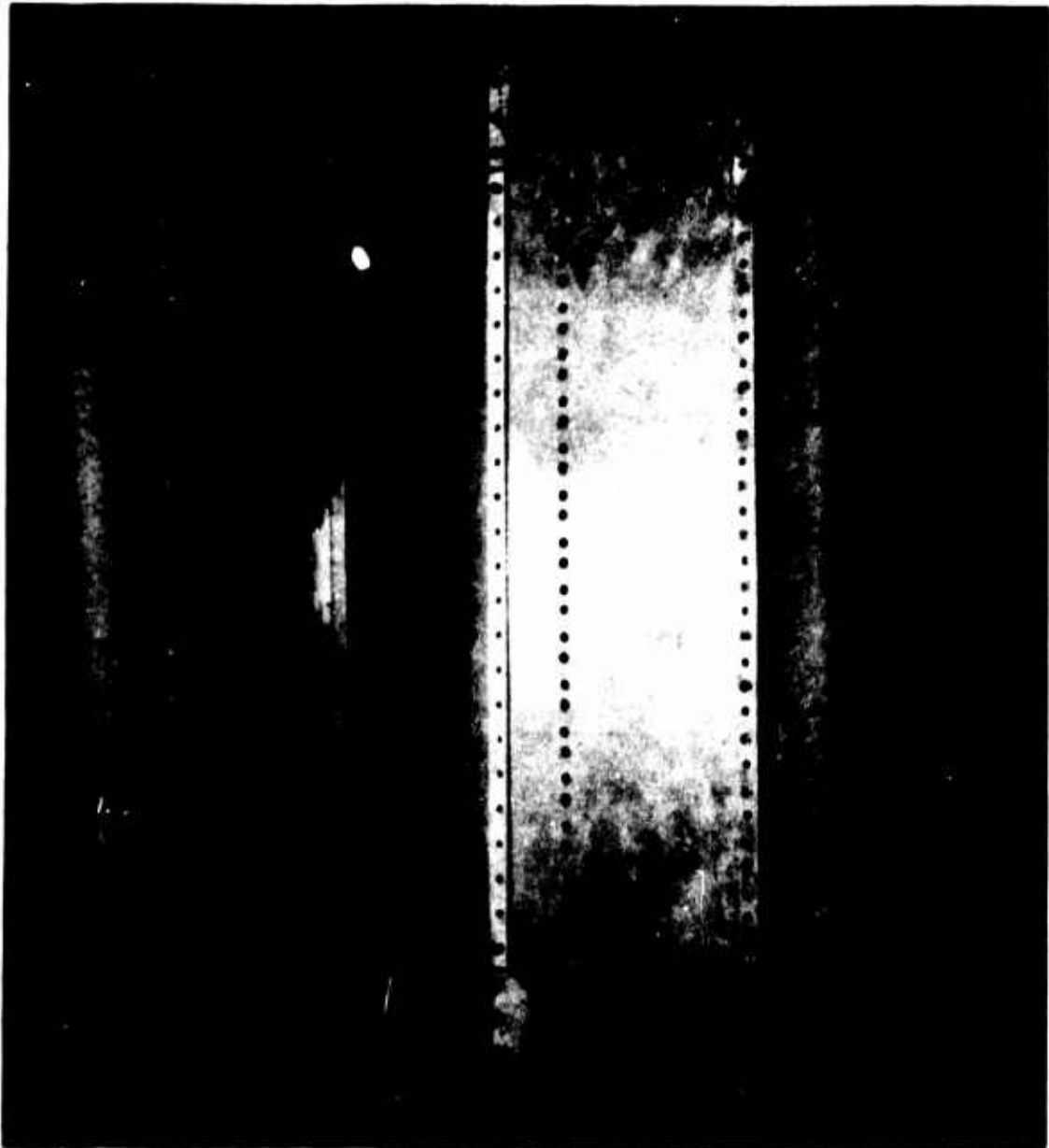
Figure 177. "Old" and "New" Fan Blades.

SERIES C

During this series with the new blade configuration, fan case modifications caused the series to be conducted in eight stages, designated C1 through C8.

SERIES C1

The fan case was the same configuration as for the Series 1, A, and B; the blades were as shown in Figure 138(b). In July 1963 ten runs were made with this new fan, designated Fan No. 2. The test conditions are listed in Table 35.

TABLE 35

TEST CONDITIONS FOR SERIES C1 RUNS

Run No.	Fan Speed (r.p.m.)	Test Rig Configuration
1	1000	Open
2	1000	One Closed
3	1000	Two Closed
4*	800	All Closed
5	1200	Open
6	1200	One Closed
7	1200	Two Closed
8	1400	Open
9	1400	One Closed
10**	1480	Open

* 800 r.p.m. was the maximum speed obtainable, that is, the peak output of the dynamometer motor/belt drive combination used to drive the fan.

** Here again, 1480 r.p.m. was the maximum speed obtainable.

Inspection of the fan revealed no damage from this set of runs.

SERIES C2

For the eight runs constituting this series, the fan blades were the
same ones used for Series C1, and the fan case was modified by cutting
three relief holes in the area between the exit and intake slots per
Figure 178.
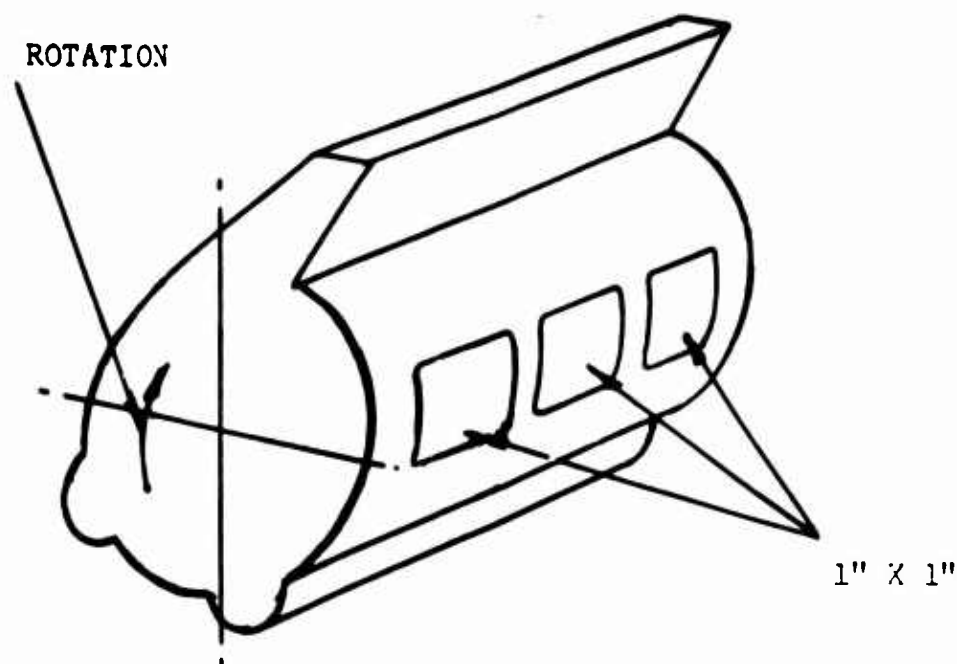
Figure 178.   Location of Relief Holes.

The remainder of the Series C tests, C3 through C8, were conducted
under the same conditions as listed in Table 36, with various fan case
modifications as listed in Table 37.

The data obtained from all of the Series C runs have been discussed in
a previous section of this report and as the velocity profiles were
quite similar, only those plotted from Series C1 data appear in this
appendix.

Throughout the Series C runs, the blades were not changed, apart from
the foam tip rubbing strip. Subsequent inspection of the blades and
case revealed no structural damage.

The complete set of Series C runs were conducted in July and Aug. 1963.

TABLE 36

TEST CONDITIONS FOR SERIES C2

Run No.	Fan Speed (r.p.m.)	Test Rig Configuration
1	1000	Open
2	1000	One Closed
3	1000	Two Closed
4	1200	Open
5	1200	One Closed
6	1200	Two Closed
7	1400	Open
8	1400	One Closed

TABLE 37

FAN CASE CONFIGURATION FOR SERIES C3 THROUGH C8

Series	Relief Configuration	Inlet Configuration
C3	Three holes used for Series C1 were cut into a slot. Slot dimensions 1-1/2" X 21"	No change
C4	C3 slot reduced in width from 1-1/2" to 3/4"	No change
C5	1-inch-wide slot	Width reduced to 2 inches
C6	Same as C5	Width increased to 3 inches
C7	2-1/2 inches wide	Width reduced to 1-1/2 inches
C8	No relief	Same as C7

Figure 179. Velocity Profile Test No. 1C1. Configuration: All Open, Speed: 1000 RPM.
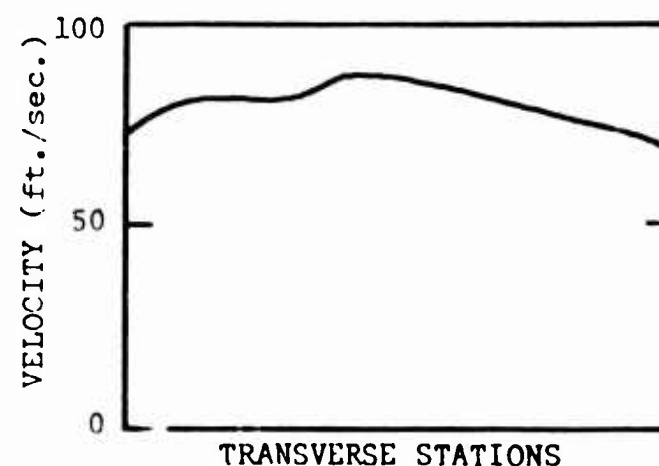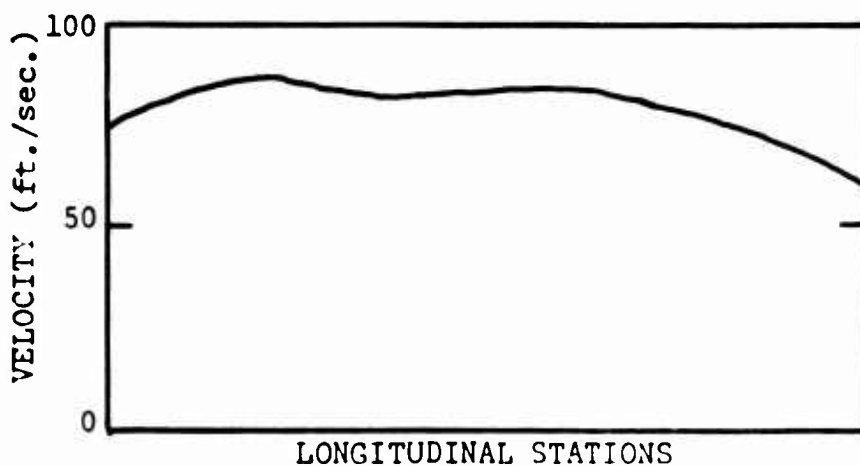
Figure 180. Velocity Profile Test No. 2C1. Configuration: One Closed, Speed: 1000 RPM.
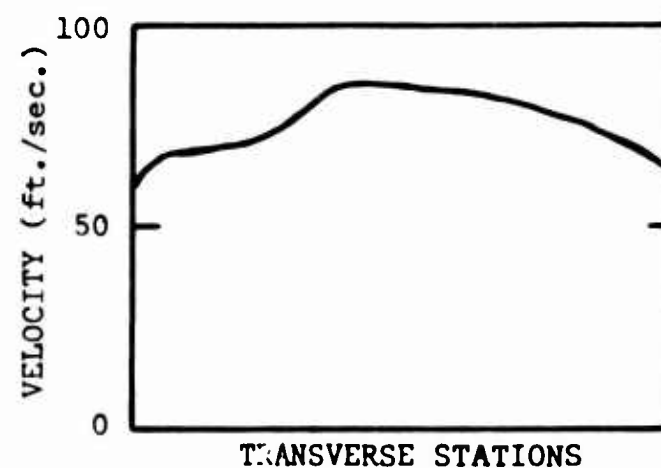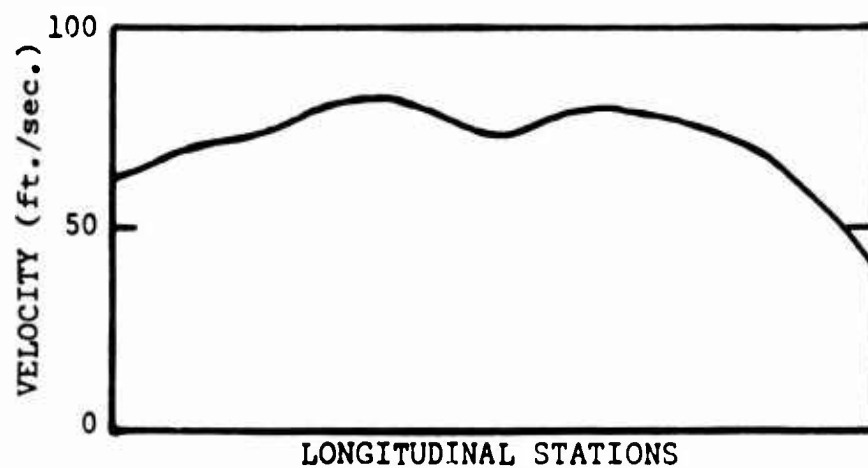
Figure 181. Velocity Profile Test No. 3C1. Configuration: Two Closed, Speed: 1000 RPM.
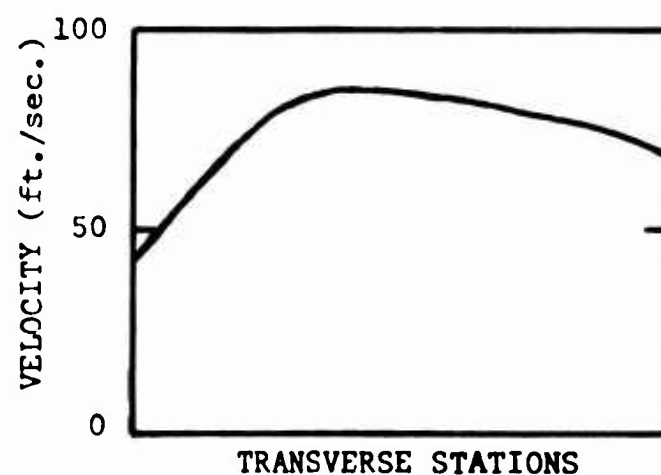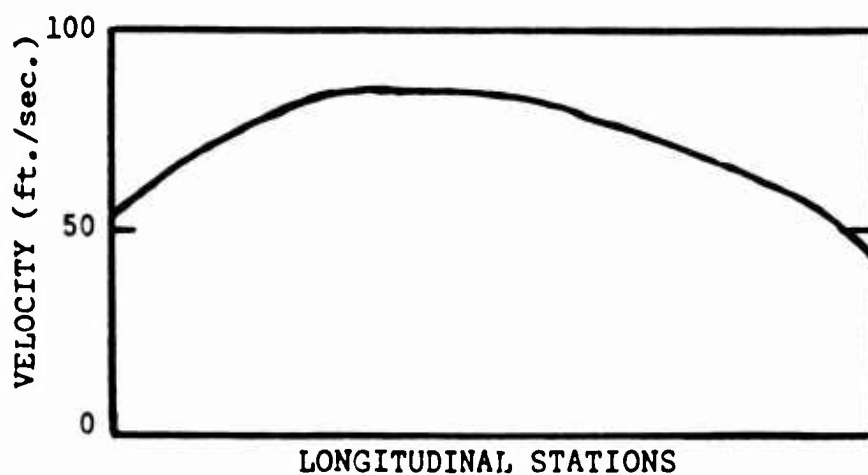
Figure 182. Velocity Profile Test No. 4C1. Configuration: All Closed, Speed: 800 RPM.
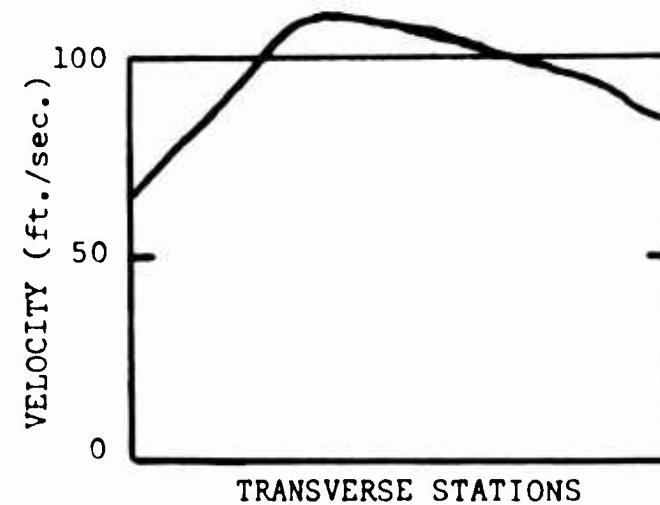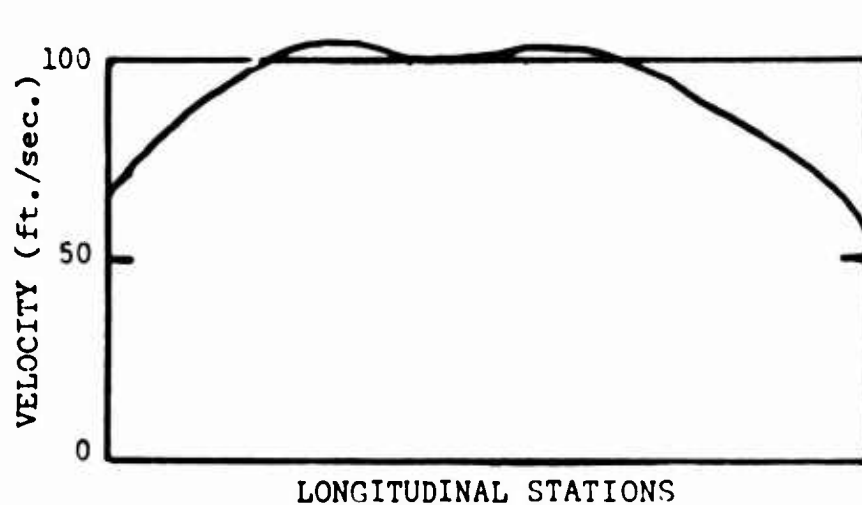
Figure 183.   Velocity Profile Test No. 5Cl.   Configuration: All Open, Speed: 1200 RPM.
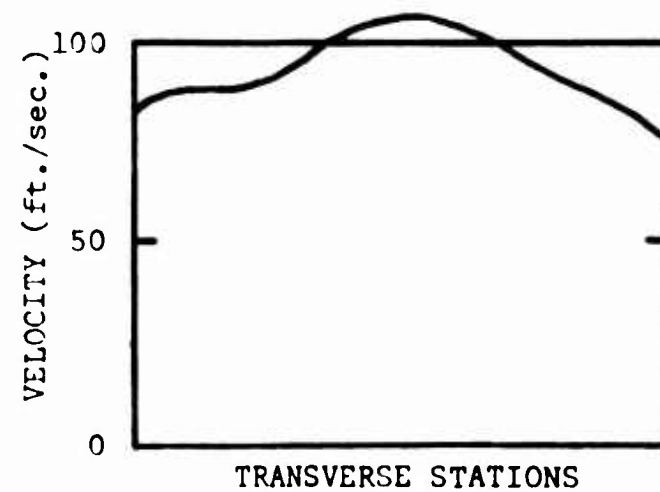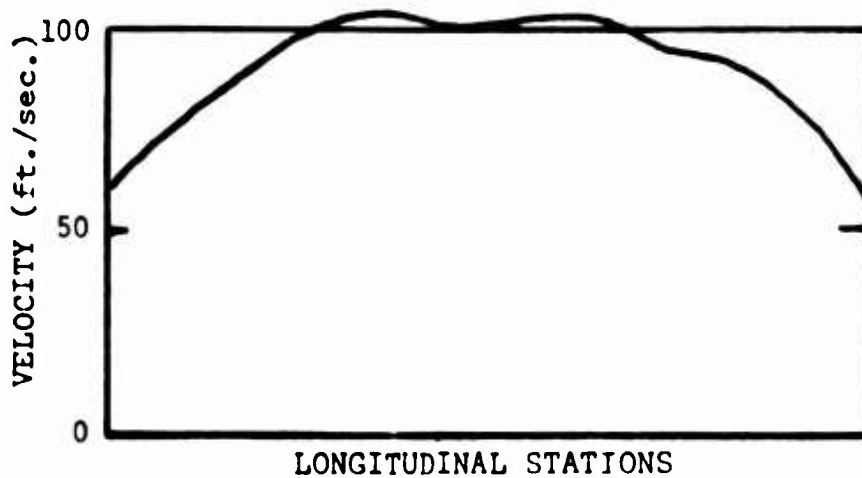
Figure 184.   Velocity Profile Test No. 6Cl.   Configuration: One Closed, Speed: 1200 RPM.

274
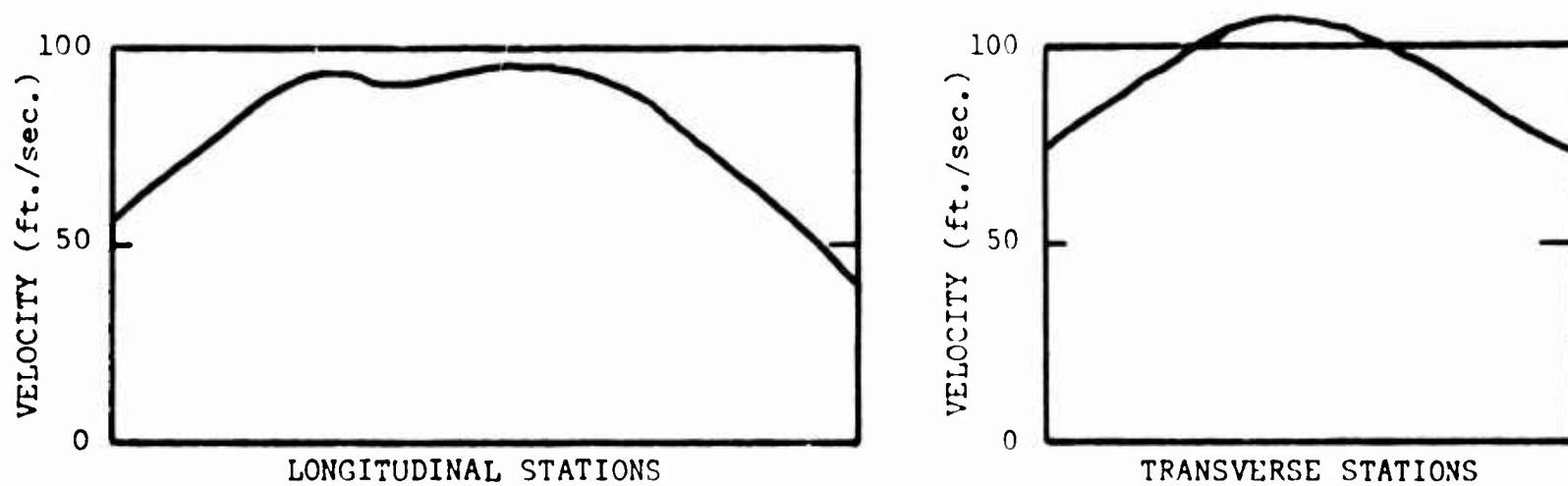
Figure 185.   Velocity Profile Test No. 7C1.   Configuration: Two Closed, Speed: 1200 RPM.
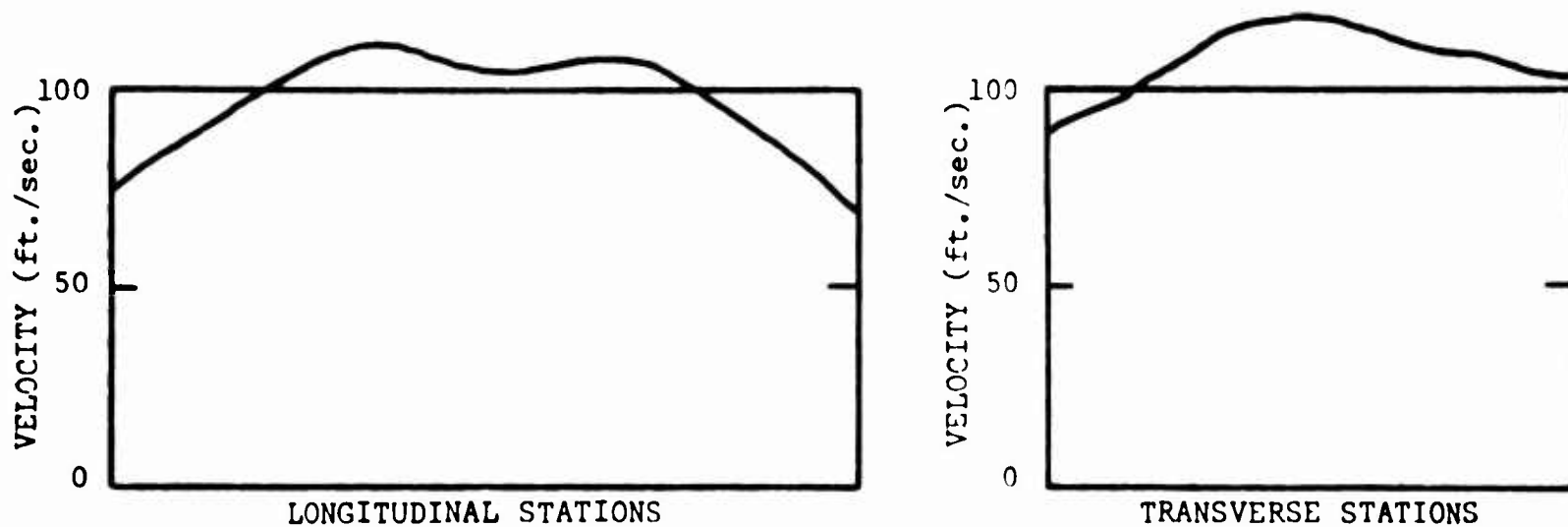
Figure 186.   Velocity Profile Test No. 8C1.   Configuration: All Op , Speed: 1400 RPM.
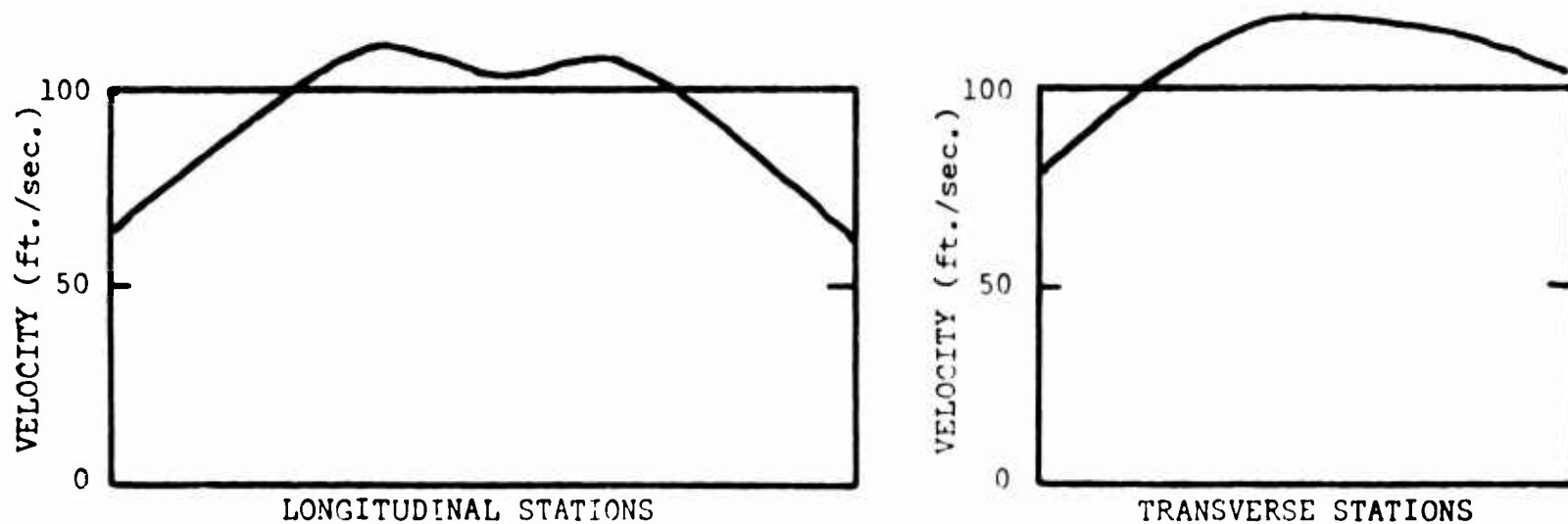
Figure 187. Velocity Profile Test No. 9C1. Configuration: One Closed, Speed: 1400 RPM.
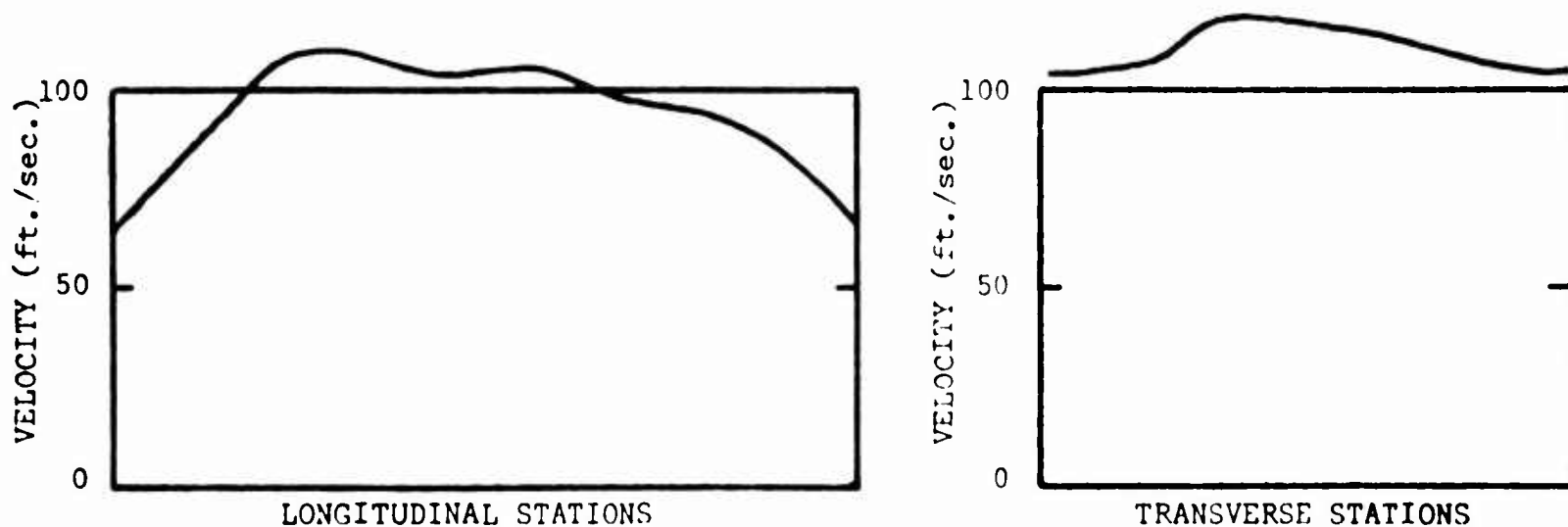
Figure 188. Velocity Profile Test No. 10C1. Configuration: All Open, Speed: 1480 RPM.

BLANK PAGE

DISTRIBUTION

U. S. Army Materiel Command	7
U. S. Army Mobility Command	3
U. S. Strike Command	1
Office of Chief of R&D, D/A	2
Chief of R&D, D/A	1
U. S. Army Transportation Research Command	66
U. S. Army Research and Development Group (Europe)	2
U. S. Army Combat Developments Command	1
U. S. Army Human Engineering Laboratories	1
Army Research Office, Durham	2
U. S. Army Polar Research and Development Center	1
U. S. Army Medical Research and Development Command	1
U. S. Army Combat Developments Command Transportation Agency	1
U. S. Army War College	1
U. S. Army Aviation and Surface Materiel Command	1
U. S. Army Airborne, Electronics and Special Warfare Board	1
Office of the United States Army Attache′	1
Chief of Naval Operations	1
Bureau of Naval Weapons	1
Bureau of Supplies and Accounts, N/D	1
U. S. Naval Supply Research and Development Facility	1
U. S. Naval Postgraduate School	1
U. S. Naval Ordnance Test Station	1
David Taylor Model Basin	1
Marine Corps Landing Force Development Center	1
Marine Corps Educational Center	1
Ames Research Center, NASA	2
NASA-LRC, Langley Station	2
Lewis Research Center, NASA	2
NASA Representative, Scientific and Technical Information Facility	2
Human Resources Research Office	2
U. S. Army Standardization Group, Canada	1
Canadian Liaison Officer, U. S. Army Transportation School	3
British Army Staff, British Embassy	4
U. S. Army Standardization Group, U. K.	1
Defense Documentation Center	10

BLANK PAGE

Frost Engineering Development Corp.,
Englewood, Colorado, PRELIMINARY
STUDIES OF THE APPLICATION OF
PERIPHERAL FANS TO GROUND EFFECT
MACHINES - P. R. Payne

1. Ground Effect
   Machine
   Literature

TRECOM Technical Report No. 64-10,
April 1964, 277 pp. Contract DA 44-
177-AMC-5(T)
USATRECOM Task 1D021701A04814

2. Contract DA 44-
   177-AMC-5(T)

Unclassified Report
This report describes the concept,
development of applicable theory, and
experiments performed to date with
the Frost Fan. Essentially a rotary
vane air pump, the Frost Fan lends

Frost Engineering Development Corp.,
Englewood, Colorado, PRELIMINARY
STUDIES OF THE APPLICATION OF
PERIPHERAL FANS TO GROUND EFFECT
MACHINES - P. R. Payne

1. Ground Effect
   Machine
   Literature

TRECOM Technical Report No. 64-10,
April 1964, 277 pp. Contract DA 44-
177-AMC-5(T)
USATRECOM Task 1D021701A04814

2. Contract DA 44-
   177-AMC-5(T)

Unclassified Report
This report describes the concept,
development of applicable theory, and
experiments performed to date with
the Frost Fan. Essentially a rotary
vane air pump, the Frost Fan lends

itself to installation around the periphery of ground
effect machines for generation of the lifting cushion
pressure. Structural and space utilization advantages
are inherent in this concept, and enhance the potentially
high overall efficiency gained through almost complete
elimination of duct losses.

Test data and theory are also presented on the applica-
tion of crossflow blowers to the peripheral fan concept.
Similar information on energy recovery through recircula-
tion of lift cushion air is included, with indication of
shortcomings in practical applications of recirculation.